

Synthesis, characterization and oxidation of Mo-W and Mo-Cr-Si alloys

By

Bhaskar Paul

Registration No. –ENGG01200904033

BHABHA ATOMIC RESEARCH CENTRE

*A thesis submitted to the
Board of Studies in Engineering Sciences Discipline*

In partial fulfillment of requirements

For the Degree of

DOCTOR OF PHILOSOPHY

of

HOMI BHABHA NATIONAL INSTITUTE



*Guide: Prof. (Dr.) R. C. Hubli (2013 onwards)
Prof. (Dr.) A. K. Suri, (2009-2013)*

STATEMENT BY AUTHOR

This dissertation has been submitted in partial fulfillment of requirements for an advanced degree at Homi Bhabha National Institute (HBNI) and is deposited in the library to be made available to borrowers under rules of the HBNI.

Brief quotations from this dissertation are allowable without special permission, provided that accurate acknowledgement of source is made. Requests for permission for extended quotation from or reproduction of this manuscript in whole or in part may be granted by the Competent Authority of HBNI when in his or her judgment the proposed use of the material is in the interests of scholarship. In all other instances, however, permission must be obtained from the author.

(Bhaskar
Paul)

DECLARATION

This is to certify that the thesis titled, “Synthesis, characterization and oxidation of Mo-W and Mo-Cr-Si alloys” submitted by Shri Bhaskar Paul to Homi Bhabha National Institute, Mumbai for the award of the degree of Doctor of philosophy is a bona fide record of the research work carried out by him under my (our) supervision and guidance. The content of the thesis, in full or parts have not been submitted to any other Institute or University for the award of any other degree or diploma.

(Bhaskar Paul)

Place:

Signature of guide

Date:

Name of guide: Prof. R. C. Hubli

Dedicated

To my

Wife, Parents and Daughter

Title	Page No.
<i>Acknowledgements</i>	(i)
<i>Abstract</i>	(ii)
<i>List of Figures</i>	(iv)
<i>List of Tables</i>	(xi)
<i>List of abbreviations</i>	(xiii)
<i>List of symbols</i>	(xv)
Chapter 1: Introduction	
1.1 Introduction	1
1.2 Roadmap of the thesis	3
1.3 References	5
Chapter 2: Literature review	
2.1 Introduction	8
2.2 Refractory metals and alloys	8
2.2.1 Mo and Mo based alloys	12
2.2.1.1 Extraction of Mo	12
2.2.1.2 Properties vis-à-vis Applications	13
2.2.1.3 Types of Mo based alloy	15
2.2.1.3.1 Carbide strengthened alloys	15
2.2.1.3.2 Solid solution strengthened alloys	21
2.2.1.3.3 Dispersion- strengthened alloys	23
2.2.1.4 Processing	24
2.2.1.5 Limitations <i>w.r.t.</i> application and remedies	25
2.2.1.5.1 Mo based oxidation resistant alloys	26
2.2.1.5.1.1 Reservoir phases approach	27
2.2.1.5.1.2 Composite approach	29
2.2.1.5.2 Oxidation resistant coating	32
2.3 Summary	40
2.4 Reference	41
Chapter 3 : Experimental Procedure	

3.1 Introduction	52
3.2 Equipment and Instruments	52
3.3 Preparation of Mo–30W alloy	59
3.3.1 Mechanical Alloying	59
3.3.2 Sintering	59
3.4 Preparation of Mo–Cr–Si–Ti composite alloys	61
3.4.1 Hot pressing	61
3.4.2 Silicothermic co–reduction	61
3.5 Pack cementation coating process	63
3.6 Characterization of prepared alloys and coatings	64
3.6.1 Compositional, phase and microstructural characterization	64
3.6.2 Mechanical property evaluation	65
3.6.3 Oxidation Studies	66
3.6.4 Wear tests	67
Chapter–4: Preparation of Mo–30W alloy and development of oxidation resistant coatings	
4.1 Introduction	70
4.2 Studies on preparation of Mo–30W alloy powder	72
4.2.1 Mechanical alloying	72
4.3 Sintering studies	75
4.3.1 Sintering kinetics using constant rate of heating (CRH) method	77
4.3.2 Sintering kinetics using Stepwise Isothermal Dilatometry (SID)	81
4.4 Pack siliconisation studies	87
4.4.1 Evolution of microstructure, phase and interface	88
4.5 Hardness studies	94
4.6 Friction and Wear Behavior	95
4.7 Oxidation test	99
4.8 Summary	100
4.9 References	101
Chapter–5: Preparation of Mo–Cr–Si composite alloy and	

development of oxidation resistant coatings	
5.1 Introduction	106
5.2 Studies on hot pressing	110
5.3 Studies on silicothermic co–reduction	114
5.3.1 Kinetics of silicothermic reduction	120
5.3.2 Composition and Microstructural characterisation	128
5.3.2.1 Bulk compositional analysis	128
5.3.2.2 Microstructure and Micro compositional analysis	128
5.4 Mechanical property	133
5.4.1 Hardness test	133
5.4.2 Room temperature fracture toughness test	135
5.5 Oxidation studies	137
5.6 Effect of different alloying additions on different properties	140
5.6.1 Oxidation behavior	140
5.6.1.1 Kinetics of oxidation	
5.6.2 Fracture toughness	156
5.6.3 Effect of addition Ti on Mo–16Cr–4Si alloy	159
5.7 Pack siliconisation	163
5.7.1 Kinetics of growth of coating	166
5.7.2 Performance evaluation	169
5.8 Summary	171
5.9 Reference	173
Chapter–6: Concluding Remark and scope for further research	180
Scope for further research	183
Publications through this thesis	184

Acknowledgments

The author is grateful to his advisors Dr. A.K. Suri, Former director, Materials Group, BARC and Dr. R.C Hubli, Head, Material processing Division for their continuous encouragements and invaluable guidance, and fruitful discussions during the course of this research. The author is very much thankful to Dr. I.G. Sharma, Dr. A.C. Bidaye, Dr. A. Awasthi, Dr. S.P. Chakraborty, Dr. P. Alex, Dr. S. Majumdar, Dr. T. Mahata, Shri Jugal Kishor, Shri R. Fotedar, Shri P.K. Limaye, Shri T.S.R.Ch. Murthy, Shri Jitendra Sonber for their diversified support, guidance and encouragements throughout the work. Thanks are extended to Mrs. Archana Prajapat, Mr. V.S. Bhave, Mr. S.K. Gavai, Mr. S.N. Kamble and Mr. D.D. Gaoankar for their numerous helps in conducting experiments.

It gives me immense pleasure to thank the members of the doctoral committee Prof. P.K.Tewari (Chairman), Prof. R.C.Hubli (Member), Prof. Dinesh Srivastava (Member) and Dr. (Smt.) Sulekha Mukhopadhyay for their critical reviews and suggestions during the progress review, credit seminars and pre-synopsis viva-voce.

The author is grateful to Dr. J.K. Chakravartty, Director, Materials Group, BARC; for his keen interest and encouragement in his work. Finally, the author wishes to thank his wife, Mousumi, and his parents for their understanding and support during the course of the work.

ABSTRACT

The thesis deals with the studies carried out to overcome the inherent problem of pure molybdenum, which restricts its wide spread application at high temperature by alloying and coating. Two Mo based alloys were studied, which are Mo-30 wt.% W and Mo-(16-20) Cr-(4-6) Si (wt.%) alloys. W was added to enhance the re-crystallization temperature, whereas Cr and Si were added to prevent catastrophic oxidation of the Mo. The scientific and technological challenges of preparation of these alloys were also studied. The principle objective was (i) preparation of Mo-30 wt.% W alloy by powder metallurgical route (ii) preparation of Mo-(16-20) Cr-(4-6) Si (wt.%) alloys by different routes such as powder metallurgy, silicothermic reduction of mixed oxide, co-precipitation followed by reduction etc. (iii) characterization of synthesized alloys with respect to composition, microstructure, mechanical properties, oxidation characteristics etc. (iii) study the effect of alloying elements, associated microstructure and mode of synthesis on the properties of alloys (iv) development of silicide based oxidation resistant coating over the synthesized alloy by pack cementation technique and performance evaluation of the coated specimens with respect to oxidation and wear.

Mo-30W alloy powder was prepared by mechanical alloying technique (MA) and co-precipitation of Mo and W tri-oxide followed by co-reduction route. The phase and morphological evolution of synthesized powder was studied by X-ray diffraction (XRD) and Scanning electron microscopy (SEM). Sintering kinetics studies were conducted on Mo-30W alloy powders prepared through mechanical alloying route. Both, constant rate of heating method as well as stepwise isothermal dilatometry (SID) technique were used for studying the sintering kinetics. Step-wise isothermal shrinkage data were measured and analyzed using Mkipritti-Meng method. The shrinkage data was found to fit well with the rate equation proposed in this method and its validity was established for mechanically alloyed systems. Kinetic parameters were evaluated and sintering was found to occur through two major mechanisms operative successively, which are grain boundary diffusion and lattice diffusion with corresponding energies of activation as 230 and 480 kJ/ mol, respectively. The results have been well supported by micro structural evaluation of specimens at different stages of sintering.

Studies were carried out to develop silicide based oxidation resistant coatings over Mo-30 W alloy substrate employing halide activated pack cementation coating process. Effect of activator content and temperature on coating was studied in detail. The microstructure of the coating revealed that the coating was free of cracks or pores, adherent to the substrate and comprised of either single layer or double layer depending on the coating temperature. SEM coupled with energy dispersive spectroscopy (EDS) was used to determine diffusion profiles for Mo, W and Si. Reciprocating sliding wear and friction experiments were performed on the uncoated and coated alloy. Double layer coating showed an improved friction coefficient as compared to base alloy as well as a single layer coated alloy. The wear tests also showed a marked improvement of wear resistance of coated alloy as compared to uncoated alloy. The coating was found to be wear resistant at 7N. Cyclic oxidation tests on coated alloy were performed at 1000° C up to 50 h. The coating was found to be protective and no peeling off or cracking was observed.

Mo-(16-20) Cr-(4-6) Si (wt.%) alloy was prepared by reactive hot pressing method. The primary objective of the present study was to develop Mo-Cr-Si alloys, which exhibit improved oxidation resistance at elevated temperature, coupled with adequate room temperature fracture toughness. The microstructure of the synthesized alloy consisted of $(\text{Mo, Cr, Ti})_3\text{Si}$, and the discontinuous $\alpha\text{-(Mo, Cr, Ti)}_{\text{ss}}$ phases with varying phase ratio depending on the composition of the alloy. Effects of concentrations of Cr and Si on the evolution of microstructure, oxidation resistance, room temperature fracture toughness and mode of failure of the Mo-Cr-Si alloys have been studied. The Mo-16Cr-4Si was found to be the optimum alloy composition having highest room temperature fracture toughness along with adequate oxidation resistance amongst the other synthesized alloys. Besides, effect of addition of Ti on different properties has been studied for Mo-16Cr-4Si alloy.

The Mo-16Cr-4Si alloy was also prepared from the oxides of molybdenum and chromium by their co-reduction with Si metal powder as a reductant. Exothermic nature of these reactions resulted in the formation of consolidated composite as a product in a single step. Differential thermal analysis (DTA) studies were conducted to find out the onset temperature for silicothermic reduction. The reaction kinetics of Si-MoO₂ system has been analyzed by a model-free Kissinger method. The activation energy for silicothermic reduction of MoO₂ to Mo was evaluated to be 309 kJ/mole. The alloys produced by silicothermy were re-melted by arc melting

and heat treated to get a homogenous microstructure. Evolution of phases and microstructures were studied by means of XRD, SEM, and EDS analysis. The multiphase alloy was consisted of Mo₃Si and discontinuous (Mo, Cr) (ss) phase with volume percentage of 28%. The synthesized alloys were characterized with respect to composition, phases, microstructure, hardness and their oxidation behavior.

The isothermal oxidation behavior of the Mo-16Cr-4Si alloy was investigated in air at 1000°C for 50h. The alloy exhibited superior oxidation behavior in comparison with single phase molybdenum alloys, because of the formation of SiO₂ and Cr₂O₃ over the alloy surface. The flexural strength and the fracture toughness determined from three-point bend testing of single edge notch bend specimens were 615±15 MP and 10.7 ± 0.5 MPa.m^{1/2}, respectively. The dominant mechanism of fracture was identified as transgranular mode of crack propagation.

An alternative method was developed for measuring the kinetics of oxidation. In this method, apparent activation energy and the exponent related to the oxidation phenomena can be evaluated by conducting a single experiment. The method was tested for its applicability by measuring the activation energy for oxidation of pure Mo. It was found that the isothermal weight change data of Mo from stepwise isothermal thermo-gravimetry (SITG) could be well analyzed to get kinetics parameters according to the empirical rate equation.

$$\frac{dY}{dt} = nk(T)Y(1-Y)\left(\frac{1-Y}{Y}\right)^{1/n}$$

Further, the method was extended for evaluating the oxidation kinetics parameters for different Mo-Cr-Si alloys. Effects of varying concentration of Si on the oxidation behavior of the alloys were also studied.

To extend the life of the Mo-16Cr-4Si-0.5Ti alloy under oxidizing atmosphere, silicide based oxidation resistant coatings were developed, using halide activated pack cementation process. The kinetic behavior of growth of the coating was established and the activation energy of the coating process was determined to be 52.5kJ/mol. Isothermal oxidation tests of the coated alloy at 1273K for 50h, revealed a small weight gain at the initial stages of oxidation followed by no change of weight.

Therefore, with proper alloying addition coupled with formation of silicide based coatings could prevent catastrophic oxidation of the Mo based alloys at high temperature.

Key words: Sintering, Hot press, Silicothermic Reduction, Co-reduction, Oxidation resistance, Fracture toughness, Pack cementation, Wear, Sintering Kinetics, Activation energy

Figure No.	Figure Caption	Page No.
2.1	Recommended operating temperature range of structural materials in space nuclear power systems	11
2.2	Comparison of yield strengths of refractory metals and alloys	11
2.3	Ternary phase diagram of Mo-Ti-Zr system, isothermal section at 873K	15
2.4	Plot of fracture toughness results as a function of temperature for TZM obtained using the J-integral method: (a) transverse (T–L) orientation and (b) longitudinal (L–T) orientation. Each symbol represents the results of a single test, and the lines connect the points for each data set	16
2.5	Recession rates of TZM when oxidized in air	17
2.6	Fraction of oxidized molybdenum that volatilizes	18
2.7	Oxidation pattern of uncoated TZM alloy	19
2.8	Solubility of the elements in mercury at different temperatures	20
2.9	Phase diagram of Mo-W system	22
2.10	The weight change during oxidation for two Mo-15Si ₃ N ₄ -6Si, oxidized for 50 hours at 1073K and 20 hours at 1273K	24
2.11	SEM micrographs of (a) Mo-12Si-8.5B, arc-cast followed by annealing for 24 h at 1600 °C; and (b) Mo-Si-B consolidated from vacuum annealed Mo-20Si-10B powders by hipping for 4 h at 1600 °C and 207 MPa (30 ksi). The α -Mo volume fractions (bright phase) are 42 and 34 vol.% respectively	28
2.12	Cyclic oxidation of Mo-Si-B alloys with different α -Mo volume fractions, at a temperature of 1473K and for 1-h cycles. The alloys were hipped Mo-20Si-10B powders (45 to 90 μ m) that were vacuum annealed for different times to produce different α -Mo volume fractions	30
2.13	Room-temperature fracture toughness as a function of the α -Mo volume fraction. Full and open symbols denote standard and nonstandard tests,	31

	respectively	
2.14	Schematic illustration of aluminide coating obtained by pack cementation	34
2.15	Arrhenius plot of parabolic growth rate as a function of the reciprocal temperature for (a) Mo_5Si_3 and (b) Mo_3Si	37
2.16	Estimated lifetime of MoSi_2 based coatings on three phases ($\text{Mo}_{\text{ss}}+\text{Mo}_3\text{Si}+\text{T}_2$) alloy.	38
3.1	(a) Schematic view of the motion of the ball and powder mixture (b) Actual photograph of the planetary ball mill used	55
3.2	Hydraulic Press	56
3.3	Arc melting furnace	57
3.4	(a) Schematic of hot press and (b) Actual photograph of the equipment	58
3.5	Schematic of controlled atmosphere furnace	59
3.6	Experimental set-up for conducting co-reduction experiments	63
3.7	Schematic of method of pack cementation experiment	64
3.8	Schematic of 3-point single edge notched bend (SENB) sample geometry	66
3.9	Schematic of wear test set-up	68
4.1	Vapour pressure plot of Mo and W	72
4.2	XRD pattern of Mo-30 wt.% W powder prepared by mechanical alloying for 15 h. Inset shows the Mo (110) peak variation as a function of milling duration	74
4.3	SEM image of Mo-30 wt.% W powder prepared through mechanical alloying (25 h milling). Inset shows the higher magnification image of agglomerated particles to show the sub-micron nature of the powder	75
4.4	EDS Spectra of mechanically alloyed Mo-30 wt.% W powder	76
4.5	XRD patterns of Mo (110) peak for (a) Mo-30 wt.% W green compact, (b) sample sintered up to 1173 K and (c) sample sintered up to 1373 K	76
4.6	Plot of sintered density with respect to sintering temperature for fixed sintering time of 3h for green compacts prepared from mechanically alloyed	77

	powder and co-precipitated cum reduced powder	
4.7	Shrinkage profiles of Mo-30% W alloy powder compacts sintered at different temperatures with constant rate of heating (20 K/min). Inset shows the variation in shrinkage profile in different experiment	79
4.8	Plot of $\ln(yT dy/dT)$ and $\ln(y^2T dy/dT)$ versus $1/T$. Grey line curve shows the least-squares linear fit of the evaluated data	80
4.9	SID shrinkage profile of Mo-30 wt.% W alloy green compact along with the temperature program followed for the SID experiment. The Curve in grey color show the shrinkage rate $\{d(l/l_0)/dt\}$ as a function of time	83
4.10	Plot of $\log(dy/dt)$ vs $\log t$ at different isothermal steps	84
4.11	Plots of $\ln\{(dY/dt)/Y/(1-Y)\}$ versus $\ln\{(1-Y)/Y\}$ according to Mekipritti-Meng equation. Variation of temperature with time is also shown on the right hand scale	86
4.12	Arrhenius plot of $\ln k(T)$ versus $1/T$ based on the data in Table 4	86
4.13	SEM micrographs of Mo-30 wt% W alloys sintered at temperatures (a) 1173K (b) 1273K (c) 1373K (d) 1523K	87
4.14	Fig. 4.14a and 4.14b BSE images of the cross-sections of the coated specimen, heat treated at 1173K and 1573K	90
4.15	Shows the BSE image and corresponding EDS line scan over the interface of sample coated at 1573K, which shows the formation of double layer of $(Mo,W)_2Si$ coating	91
4.16	Concentration profile along the interface determined from point analysis for the sample coated at 1173K	91
4.17	Concentration profile along the interface determined from point analysis for the sample coated at 1573K	92
4.18	Spectrum of coating region	92
4.19	Crystal structure of disilicides	94
4.20	Gibbs energy change Vs temperature for reaction 1-4	74

4.21	Plot of micro-hardness as a function of distance across interface for the sample coated at 1573K	96
4.22	Profiles of Vicker's indentations at substrate and coating	96
4.23	Evolution of coefficient of friction with sliding distance	97
4.24	Variation of COF with Speed	97
4.25	Typical 3D profile of wear scar	98
4.26	(a) Variation in Wear rate of Al ₂ O ₃ Ball with speed (b) Variation in Wear rate of coating with Speed	99
4.27	SEM images of the worn surfaces (a) uncoated Mo-W alloy (b) Mo-W alloy coated at 1173K (c) Mo-W alloy coated at 1573K	99
4.28	Cross section of the coated sample after wear test	100
5.1	Phase diagram of Mo-Si and Mo-Cr-Si system	109
5.2	(a): Plot of sintered density vs temperature for fixed sintering time of 3h (b) The plot of sintered density vs time at 1873K	111
5.3	SEM images of hot pressed Mo-16Cr-4Si alloys sintered at 1873K and 10MPa load and the corresponding EDS sepctrum	112
5.4	BSE image of alloy sintered at 1673, 1773 and 1873K from left to right	113
5.5	Plot of growth of silicide phase with time. Inset shows the XRD pattern of sintered alloy hot pressed at 1873K	113
5.6	The phase diagram of CaO-SiO ₂	118
5.7	SEM image showing (a) Poor (b) Excellent slag metal separation	118
5.8	DTA/TG plot for mixture of MoO ₂ , Cr ₂ O ₃ and Si, showing the sharp peak near the melting temperature of Si is due to triggering of reduction reactions. Inset of Fig shows the DTA plot during cooling	120
5.9	Typical TG-DTA plot of reduction of MoO ₂ by Si taken in powder form. Inset shows a typical TG-DTA plot of reduction of MoO ₂ by Si taken in the pellet form	122
5.10	XRD of the product after reduction of (a) pelletized reactant and (b) powder reactant	123

5.11	Back scattered SEM image and the EDS analysis of the product after reduction	123
5.12	Exothermic peak locations for reduction of MoO ₂ to Mo at different temperatures and heating rates	126
5.13	Arrhenius Plot for the estimation of activation energy	127
5.14	SEM image taken in BSE mode of Mo-16Cr-4Si alloy (a) As reduced (b) Remelted and homogenized at 1873K for 10 hour	130
5.15	XRD pattern of remelted and homogenized Mo-16Cr-4Si alloy	131
5.16	(a) BSE image of homogenized Mo-16Cr-4Si alloy and (b), (c) and (d) are the elemental maps of Mo, Cr and Si respectively	132
5.17	SEM image taken in BSE mode of remelted + homogenized Mo-16Cr-4Si alloy	132
5.18	BSE image of remelted + homogenized Mo-16Cr-4Si alloy (left) and corresponding simulated image (right) produced by image analysis software based on difference of contrast in the microstructure	133
5.19	Plot of hardness for as-reduced and arc melted+homogenized alloy as a function of load	134
5.20	Profiles of a Vickers indentation at a load of 3 N, showing the variation of indentation size	135
5.21	Profiles of a Vickers indentation at a load of 3 N (a) at Phase A (b) at Phase B	135
5.22	Load displacement curve during bending test	136
5.23	SEM image of fractured surface after bend test	137
5.24	TG plot showing the oxidation behaviour of the sample with (red) and without coatings (black)	138
5.25	Specific weight gain vs. time plot of Mo-16Cr-4Si-.5Ti alloy at 1273, 1173 and 1273K in air.	139
5.26	SEM image of the oxidized surface at 1273K for 5hr and 50 hr of exposure.	140

	Inset shows the XRD pattern of oxides formed upon oxidation over alloy surface	
5.27	TG plots showing the oxidation behavior of alloy-1 and alloy-9	142
5.28	Specific weight change vs. time plot of alloy-1 and alloy-9 at 1273K in air. Insets show the SEM images of the oxidized surfaces	143
5.29	XRD pattern of oxidized surface formed upon oxidation over the surface of alloy-1 and 9	144
5.30	Effects of concentrations of the alloying elements on the oxidation behavior at 1273K for 1hr.	145
5.31	Plots of $\ln\{(dY/dt)/Y(1-Y)\}$ versus $\ln\{(1-Y)/Y\}$ for pure Mo. Variation of temperature with time is also shown on the right hand scale. Inset shows the Arrhenius plot of $\ln k(T)$ versus $1/T$ yielding activation energy for oxidation	149
5.32	BSE-SEM images of the two phase (a) Mo-16Cr-4Si and (b) Mo-16Cr-6Si alloys showing difference of contrast for different phase A (Mo rich) and B (Si rich)	150
5.33	TG plots showing the non-isothermal oxidation behaviour of Mo-16Cr-4Si and Mo-16Cr-6Si alloy	151
5.34	Plot of $\ln[(w_r-w_o)/(w_f-w_i)]$ vs $\ln(t-t_o)$	152
5.35	Plot of fractional oxidation function (Y) of Mo-16Cr-4Si alloy with time. Heating schedule is also shown in the plot	152
5.36	Plots of $\ln\{(dY/dt)/Y(1-Y)\}$ versus $\ln\{(1-Y)/Y\}$ for Mo-16Cr-4Si alloy. Inset shows the fractional oxidation rate as a function temperature	153
5.37	Arrhenius plot of $\ln k(T)$ versus $1/T$ yielding activation energy for oxidation of the alloy Mo-16Cr-xSi alloys having x= 4, 5, and 6 wt.%	154
5.38	SEM image of the oxidized surface for hot pressed (a) Mo-16Cr-4Si alloy (b) Mo-16Cr-6Si alloy. Insets show BSE-SEM images of corresponding alloys	155

5.39	XRD pattern of oxides formed upon oxidation over Mo-16Cr-4Si alloy surface	156
5.40	Load displacement curves of the alloy-1 and alloy-9 during bending test. Insets show the SEM images of fractured surfaces of the alloys after bend test	157
5.41	Line scan over the fracture surface of alloy-1, showing the variation of Mo, Cr and Si along two phase region	158
5.42	Effects of different concentrations of the alloying elements on the fracture toughness	159
5.43	Rate of weight change after oxidation and at 1273K and fracture toughness for the Mo-16Cr-4Si-xTi alloys, where x= 0.25, 0.5 and 1 wt. %	160
5.44	Load-displacement curves of Mo-16Cr-4Si-1Ti during bending test. Insets show the SEM images of fractured surfaces of the alloys after bend test	161
5.45	(a) Cross sectional SEM image of the Mo-16Cr-4Si-0.5Ti alloy sample oxidized at 1273K for 1 hr (b) corresponding EDS line scan	162
5.46	Elemental maps of the oxide region of the Mo-16Cr-4Si-0.5Ti alloy sample oxidized at 1273K for 5 hr	162
5.47	(a) Cross sectional SEM image of the Mo-16Cr-4Si-0.5Ti alloy sample oxidized at 1273K for 10 hr (b) corresponding EDS spectrum for the outermost layer	162
5.48	Cross-section of the coated samples using coating temperature at 1073K and 1373K	164
5.49	Isothermal section of Mo-Cr-Si ternary phase diagram at 1573K	165
5.50	Phase diagram of Cr-Si	166
5.51	Qualitative line profile in the coating area (Coating temperature =1573K), which shows that wherever Cr is more, Si is also more. Inset shows the same three dimensionally where the intensity is shows in arbitrary unit	166
5.52	Arrhenius plot of $\ln(T^{1/2} h)$ Vs $1/T$ for Mo-16Cr-4Si-0.5Ti alloy	169

	TG plot showing the oxidation behavior of the sample with and without coatings	
5.53	TG plot showing the oxidation behavior of the sample with and without coatings	170
5.54	Isothermal oxidation behaviour of the coated alloy for 50 h at 1273K	170
5.55	BSE image of cross section of the coated sample after oxidation and the qualitative line profile across the cross section	171

Table No.	Table Caption	Page No.
2.1	Property comparison of pure refractory metals	9
2.2	Composition and applications of different refractory metal alloys	10
2.3	Important and commonly used Mo based alloys and their recrystallisation temperature	21
2.4	Preferred compositional ranges suitable for use in high temperature oxidizing environment	28
2.5	The parabolic rate constants of three Mo-silicides formed by various experimental conditions at 1273K	37
4.1	Kinetic parameters for CRH sintering of Mo-30 wt% W alloy	81
4.2	Values of bD_B were calculated at various temperatures	81
4.3	Volume diffusion coefficients for Mo-30wt% W alloy evaluated through SID analysis	84
4.4	Kinetic analysis of SID shrinkage data of Mo-30 wt% W alloy green compacts according to Makipritti-Meng equation	85
4.5	Apparent activation energies evaluated from SID analysis	87
4.6	The results of the coating experiments over Mo-30W alloy	89
4.7	The exact compositions of the different layers at different coating temperatures	90
5.1	Average compositions of the different phases of the alloy	112
5.2	Results of silicothermy co-reduction experiments	115
5.3	Thermodynamic data used to calculate adiabatic temperature rise	117

5.4	Thermodynamic data for the different compounds (Where $j=4.185$)	124
5.5	Bulk composition of the alloy and analysis process	129
5.6	Details of microanalysis of alloy at different conditions	130
5.7	Different alloy compositions, hot pressing conditions, their theoretical and sintered densities and weight change upon oxidation	141
5.8	Kinetic parameters of SITG oxidation data of three alloys	154
5.9	The room temperature fracture toughness values of the nine alloys	157
5.10	Average compositions of the different contrasts regions within coating	165
5.11	Coating thickness and weight gain at different coating temperatures	168

List of Abbreviations

ADS	Accelerator Driven System
AHWR	Advanced Heavy Water Reactor
BCC	Body-Centered Cubic
BSE	Back Scattered Electron
CHTR	Compact High Temperature Reactor
COF	Co-efficient of Friction
CRH	Constant Rate of Heating
CTE	Co-efficient Thermal expansion
CVD	Chemical Vapor Deposition
DBTT	Ductile to Brittle Transition Temperature
DTA	Differential Thermal Analysis
EDS	Energy Dispersive Spectrometry
EBM	Electron Beam Melting
HAPC	Halide Activated Pack Cementation
HP	Hot Pressing
HIP	Hot Isostatic Pressing
HTR	High Temperature Reactor
ITER	International Thermonuclear Experimental Reactor
MA	Mechanical Alloying
PM	Powder Metallurgy
PVD	Physical Vapor Deposition
RCS	Rate Controlled Sintering
SID	Stepwise Isothermal Dilatometry
SITG	Stepwise Isothermal Thermogravimetry
SE	Secondary Electron
BSE	Back scattered electron
SEM	Scanning Electron Microscope
TD	Theoretical Density

TEC	Thermoionic Energy Convertor
TG	Thermogravimetry
TMA	Thermo Mechanical Analyzer
VAC	Vacuum Arc Casting
XRD	X-Ray Diffraction

List of Symbols

α	Extent of reaction
$f(\alpha)$	Kinetic model function
A	Pre exponential factor
β	Heating Rate
t	Time
k	Rate constant
n	Avrami Exponent
T	Absolute Temperature
K	Equilibrium constant
K_c	Fracture Toughness
σ_f	Flexural Strength
τ	average diameter of the crystallites
P	Equilibrium partial pressure
θ_B	Bragg angle
B_r	Resultant full width at half maxima
ρ	Density
x	Oxide film thickness
Y	Fractional Oxidation Function
$\Delta L/L_0$	Linear shrinkage
a	Particle radius
γ	Surface energy
D_v	Volume diffusion co-efficient
Q	Activation energy
R	Gas constant
k	Boltzman's constant
V	Volume
d	Density
Ω	Volume of vacancy

h	Coating thickness
m	Coating weight gain per unit surface area
M	Atomic weight
ΔG°	Standard free energy change
W_{Si}	Weight percent Si
W_{NH_4F}	Weight percent NH_4F

Chapter–1

1.1 Introduction

There is increasing demand of materials with high temperature and load-bearing capabilities for improved performance in energy, nuclear and aerospace industries [1,2]. A new generation of material systems with significant improvement in temperature capability beyond the operating limits of the conventional super alloys are required to meet this demand. Such materials require an appropriate combination of properties, such as low-temperature damage tolerance, high-temperature strength and creep resistance, in addition to superior oxidation resistance.

Refractory metals such as molybdenum, tungsten, niobium, tantalum, rhenium or their alloys possess excellent high-temperature strength coupled with fairly good ductility and toughness and therefore are candidate materials for high temperature applications [1]. Amongst these molybdenum is attractive and probably the most promising in terms of strength, density, melting temperatures, compatibility with molten metals, high thermal conductivity etc. [1]. However, Mo has to be alloyed suitably to overcome some of the inherent problems, which are: (a) decrease of strength rapidly at temperatures above $0.5 T_m$ (b) very susceptible to intergranular failure in the recrystallized state (c) catastrophic behaviour under oxidizing environments.

Solid solution strengthening is an approach to increase the recrystallization temperature as well as strength at temperature above $0.5 T_m$. Tungsten is the most suited alloying addition for solid solution strengthening of Mo matrix [3–7]. The addition of 30 wt.% W in Mo increases the capability of the alloy to retain strength at a temperature in excess of 1700°C [4].

To overcome the third problem mentioned above, attempts have been made to protect refractory metals from catastrophic oxidation either by alloying or application of oxidation resistant coatings. Application of coating over the known Mo based alloys looks to be a better and immediate solution as compared to exploring entirely new oxidation resistant alloy. However, coating is not a foolproof solution, because once the coating fails for any expected or unexpected reason, the component is likely to fail catastrophically. Therefore, the recent trend in design of high temperature system is that the substrate of the high temperature components should have sufficient levels of oxidation resistance to avoid catastrophic damage in case the coating fails. Since, none of the existing commercially available single phase Mo based alloys have adequate levels of oxidation resistance to prohibit them from

catastrophic failure. Therefore, an approach leading to development of composites is being explored, where brittle but oxidation resistant intermetallic matrix is toughened with metallic reinforcements [8–25]. Ductile reinforcement with solid solution of Mo and Cr, $(\text{Mo}, \text{Cr})_{\text{ss}}$ has been utilized in this study to improve the fracture toughness of the brittle matrix of $(\text{Mo}, \text{Cr})_3\text{Si}$ in dual phase Mo–Cr–Si composite alloys.

The preparation of Mo–30W alloy and Mo–Cr–Si composites is a highly challenging task and limited information exists in the open literature on the processing of these alloys. Preparation of these alloys by the conventional melt–casting process (arc or electron beam melting) is a highly energy intensive process. The reasons can be attributed to the following facts. Firstly, very high melting points and a large difference in the specific gravity of the alloying components results in a number of melting runs required for thorough homogenization. Secondly, a very high level of vacuum has to be maintained during melting as the alloying components can be oxidized even with the trace amount of air present. Thirdly, a large difference in the vapour pressure of the alloying components results in an excessive loss of metals and difficulties in achieving targeted chemical composition. On the other hand, mechanical alloying/powder metallurgy has emerged as an alternative route for preparation of advance materials [26]. Preparation of alloys through this route not only provides microstructural refinement but also imparts very high degree of homogeneity in the final product [27]. Powder metallurgy consolidated material generally is directly worked mechanically (rolling, forging etc.) into the final desired shape [28]. On the other hand, melt–cast alloys prepared by arc or electron beam require extrusion before they may be processed further during shaping.

In the present study, Mo–30W and Mo–Cr–Si alloys have been prepared by powder metallurgical route. Detailed sintering and its kinetics studies have been carried out. Different aspects of improving sinterability of the Mo–30W alloy powder were also studied.

An alternative self sustaining synthesis route for preparation of high temperature material is “Co–reduction route”, where metal oxides are reduced simultaneously by a reductant, which could be anyone or a combination of Al, Si, Ca, B, Mg etc. and the reactions which when triggered goes to completion because of their own exothermic heat [2, 29–30]. In the present study, attempts have been made to prepare Mo–Cr–Si alloys by silicothermic co–reduction technique using Si as reductant. The charge composition consisting of reductant, Si and oxides of Mo and Cr has been judiciously adjusted to achieve maximum alloy yield by

utilizing the heat of the chemical reactions effectively. The corresponding aspects of thermodynamic and reaction sequences have been studied in detail.

Prepared alloys have been characterized for composition, phases, microstructure, hardness, room temperature fracture toughness and oxidation behavior. Since oxidation is a thermally activated process, its activation energy is important to be known. Various equations have been suggested to calculate the activation energy. Preferably a minimum of four experiments are required at four different heating rates or different isothermal temperatures, for calculating activation energy for any thermally activated process by constant rate of heating (CRH) method or isothermal heating [31]. In the present work, attempt has been made to postulate a new methodology for determining oxidation kinetics parameters in order to reduce the number of experiments. This method will be especially useful in designing new alloys, by reducing the number of experiments required for performance evaluation, where limitation of material availability, experimental efforts and cost is of concern. The proposed method has been validated with known system and then utilized to study the oxidation of different Mo–Cr–Si alloys. Unlike the conventional methods that require multiple thermogravimetric experiments, this novel method gives the activation energy from the mass change data obtained from a single thermogravimetric experiment.

Further, development of silicide based protective coating on the prepared Mo–30W and Mo–Cr–Si alloys by halide activated pack cementation technique has been studied to overcome the problem of high temperature oxidation and to extend the life of the alloys at service temperature. Effect of different pack chemistries and coating temperatures on the evolution of phases, microstructures, coating thickness and surface morphology have been studied in detail.

1.2 Roadmap of the thesis

The organization of the thesis is as follows. Detailed literature review on refractory metals alloys with special emphasis on Mo alloy is presented in chapter 2. The potential applications of Mo based alloys, bottlenecks in widespread applications and need for a high performance composite alloy is emphasized in chapter–2. The effect of different alloying additions on different properties has also been discussed. Chapter 3 presents the experimental procedures for the preparation, characterization and performance evaluation tests of different Mo based alloys. Chapter 4 deals with different aspects of preparation of Mo–30W alloy powder, detailed sintering studies and subsequent development of oxidation resistant coating.

Whereas, Chapter 5 deals with the studies on preparation of Mo–Cr–Si composite alloy and to arrive at suitable composition, which would have superior oxidation resistance coupled with comparable fracture toughness. Major findings of the present thesis and scope for the future work are summarized in chapter 6. The references are included after the summary of the each chapter. List of publications from the present thesis are attached at the end of the thesis.

References

1. S. Majumdar. Processing of molybdenum and TZM alloy for advanced nuclear reactor systems, PhD Thesis. 2009, IIT , Mumbai, India.
2. I.G. Sharma, S.P. Chakraborty, and A.K. Suri. Preparation of TZM alloy by aluminothermic smelting and its characterization. *Journal of Alloys and Compounds* 393 (2005) 122–128.
3. H. L. Brown, C. P. Kempter. Elastic properties of thoriated W–Mo and W–Mo–Re alloys. *J. less-comm. met.* 12 (1967) 166–168.
4. Refractory metals and their industrial applications: a symposium, Issue 849, edited by R. E. Smallwood, ASTM International, 1984 – Technology & Engineering, p.p. 14–17.
5. V. T. Ababkov, N. N. Morgunova, B. D. Belyasov, V. N. Goldovskii. Alloys of the Mo–W System, *Metal Science and Heat Treatment.* 17(1975)907–910.
6. S. Majumdar G.B. Kale, I.G. Sharma. A study on preparation of Mo–30W alloy by aluminothermic co–reduction of mixed oxides. *J Alloys and Comp* 394(2005)168–175
7. D.B. Lee, G. Simkovich. Oxidation of molybdenum–tungsten–chromium–silicon alloys. *Oxid. Met.* 31 (1989) 265–274.
8. C.M. Ward–Closea, R. Minorb, P.J. Doorbarb. Intermetallic–matrix composites—a review. 4 (1996) 217–229.
9. D.M. Berczik. Method for enhancing the oxidation resistance of a molybdenum alloy and a method of making molybdenum Alloy. US Patent 5,595,616 (1997).
10. D.M. Berczik. Oxidation resistant Molybdenum Alloy. US Patent 5,693,156 (1997).
11. P.R. Subramanian, M.G. Mendiratta, D.M. Dimiduk. High temperature melting molybdenum–chromium–silicon alloys. US Patent 5,683,524 (1997).
12. R. Mitra, A.K. Srivastava, N. Eswara Prasad, S. Kumari. Microstructure and mechanical behaviour of reaction hot pressed multiphase Mo–Si–B and Mo–Si–B–Al intermetallic alloys. *Intermetallics* 14 (2006) 1461–1471
13. S. Paswan, R. Mitra, and S.K. Roy. Isothermal oxidation behaviour of Mo–Si–B and Mo–Si–B–Al alloys in the temperature range of 400–800 °C, *Mater. Sci. Engg. A* 424 (2006) 251–265.
14. R. Sakidja, J. S. Park, J. Hamann, and J. H. Perepezko. Synthesis of oxidation resistant silicide coatings on Mo–Si–B alloys. *Scripta Materialia* 53 (2005) 723–728
15. R. Sakidja, F. Rioult, J. Wernerb, J.H. Perepezko. Aluminum pack cementation of Mo–Si–B alloys. *Scr Mater* 55 (2006) 903–906.

16. J.H. Schneibel, R.O. Ritchie, J.J. Kruzic, P.R. Tortorelli. Optimization of Mo–Si–B Intermetallic Alloys. *Metall. Mater. Trans. A* 36 (2005) 525–531.
17. M.K. Meyer, M.J. Kramer, M. Akinc. Compressive creep behavior of Mo₅Si₃ with the addition of boron. *Intermetallics* 4 (1996) 273–281.
18. T.A. Parthasarathy, M.G. Mendiratta, D.M. Dimiduk. Oxidation mechanisms in Mo–reinforced Mo₅SiB₂ (T2)–Mo₃Si alloys. *Acta Mater.* 50 (2002) 1857–1868.
19. P. Jehanno, M. Heilmaier, H Saage, H. Heyse, M. Boning, H. Kestler, J.H. Schneibel. Superplasticity of a multiphase refractory Mo–Si–B alloy. *Scr. Mater.* 55 (2006) 525–528.
20. D. Sturm, M. Heilmaier, J.H. Schneibel, P. Jéhanno, B. Skrotzki, H. Saage. The influence of silicon on the strength and fracture toughness of molybdenum. *Mater. Sci. Eng. A* 463 (2007) 107–114.
21. K. Yoshimi, S. Nakatani, S. Hanada, H. Ko, Y.H. Park. Synthesis and high temperature oxidation of Mo–Si–B–O pseudo in situ composites. *Sci. Technol. Adv. Mater.* 3 (2002) 181–192.
22. A.P. Alur, N. Chollacoop, K.S. Kumar. High–temperature compression behavior of Mo–Si–B alloys. *Acta Mater.* 52 (2004) 5571–5587.
23. S. Burk, B. Gorr, H.J. Christ. High temperature oxidation of Mo–Si–B alloys: Effect of low and very low oxygen partial pressures. *Acta Mater.* 58 (2010) 6154–6165.
24. I.M. Gunter, J.H. Schneibel, J.J. Kruzic. Ductility and fracture toughness of molybdenum with MgAl₂O₄ additions. *Mater. Sci. Eng. A* 458 (2007) 275–280.
25. J. Das, R. Mitra, S.K. Roy. Oxidation behaviour of Mo–Si–B–(Al, Ce) ultrafine–eutectic dendrite composites in the temperature range of 500–700°C. *Intermetallics* 19 (2011) 1–8.
26. R.B. Schwarz, C.C. Koch. Formation of amorphous alloys by the mechanical alloying. *Appl. phy. Lett.* 49 (1986) 146–148.
27. Bose, G. Jerman and R.M. German. Properties of Swaged and Aged Molybdenum Doped Heavy Alloys. *Powder Metall. Intl.* 21 (1989) 9–13.
28. R. I. Jaffee, D. J. Maykuth, and V. D. Barth. Fabrication of tungsten for solid–propellant rocket nozzles, Defence metals information center, battelle memorial institute, Columbus 1, ohio, 1961.
29. I.G. Sharma, S.P. Chakraborty, A.K. Suri. Preparation of TZM alloy by aluminothermic smelting and its characterization. *J. Alloy Comp.*, 393 (2005) 122–128.

30. S.P. Chakraborty, S. Banerjee, I.G. Sharma, Bhaskar Paul, A.K. Suri. Studies on the synthesis and characterization of a molybdenum-based alloy. *J. Alloy Comp.* 477 (2009) 256–261.
31. J. Wang, R. Raj. Activation Energy for the Sintering of Two-Phase Alumina/Zirconia Ceramics. *J. Am. Ceram. Soc.*, 74 (1991) 1959–1963.

Literature review

2.1 Introduction

Detailed literature review on refractory metals alloys with special emphasis on Mo alloy is presented in this chapter. The potential applications of Mo based alloys, their bottlenecks in widespread applications and need for a high performance composite alloy coupled with oxidation resistant coatings is emphasized. The chapter deals with the survey of important properties of the commercially available or under investigated Mo based alloys, their limitations and the methodologies to overcome the limitations. An attempt has been made to highlight the lacunae in the field of processing, performance evaluations of Mo alloys and oxidation resistant coatings.

2.2 Refractory Metals and Alloys

The metallic elements niobium (Nb) and tantalum (Ta) of group VA, molybdenum (Mo) and tungsten (W) of group VIA are designated as refractory metals based on the arbitrary criteria of body centered cubic (bcc) crystal structure, minimum melting point of 2200K and the ratio of melting temperature of oxide to metal be less than unity [1]. In this special category of metals, the latest to find its entry is metal rhenium (Re) because of its high melting point next to tungsten. Of the five (Nb, Ta, Mo, W and Re) refractory metals Re possesses many unique features. Its crystallographic structure is hexagonal close packed, does not form carbides, possesses highest strain hardening coefficient, does not have ductile to brittle transition temperature and above all it imparts its good qualities to other elements when used as an alloying element. The excellent combination of the metallurgical properties of the refractory metals paved the way for their application in diverse field. Except Re, their common areas of application are steel industry and sintered carbide tools in the form of respective ferroalloys and carbides, respectively. Specific application such as that of niobium in the field of metallic superconductor and nuclear reactor, tantalum as miniature capacitor and tungsten as incandescent filament, molybdenum as heating element and cathode support and rhenium as alloy softener bestowed them prominent recognition. A property comparison of Nb, Ta, Mo, W and Re is presented in Table 2.1. Refractory metals and their alloys are capable of meeting an aggressive environment with respect to radiation, temperature, corrosion (gaseous and liquid metal) and stress for prolonged periods. Such materials are therefore, being considered as high temperature structural materials, for new generation reactors like accelerator driven system (ADS), compact high temperature reactor (CHTR), advanced heavy water reactor (AHWR), fusion devices [2,3] and space shuttles [4].

Prominent refractory metal alloys are presented in Table 2.2. There is an increasing demand for materials that can maintain reliability under ever-increasing temperature conditions. Conventional super-alloys having nickel, cobalt or iron-nickel as the major constituents, meet restricted high temperature applications and fail to qualify the benchmark of aerospace and nuclear industries. Generally, iron-nickel alloys (316 stainless steel) can be used up to a temperature of 923K whereas most of the nickel and cobalt based super-alloys can be used up to an operating temperature of about 1273K. Steel and nickel alloys though possess adequate strength at room temperature, have poor high temperature strength and low thermal diffusivity.

Table 2.1: Property comparison of pure refractory metals

Property	Niobium	Tantalum	Molybdenum	Tungsten	Rhenium
Crystal Structure	bcc	bcc	bcc	bcc	hcp
Density, g/cc	8.6	16.6	10.2	19.3	21.0
Melting Point, K	2711	3269	2883	3683	3453
Vapor Pressure at 2500K, (torr)	4×10^{-5}	8×10^{-7}	6×10^{-4}	7×10^{-8}	1.3×10^{-6}
Thermal Expansion, (ppm/K)	7.3	6.3	4.8	4.5	6.2
Thermal Conductivity, (W/m-K)					
At 293K	52.7	54.4	142	155	71
At 773K	63.2	66.6	123	130	...
Electrical Resistivity, ($\mu\text{ohm-cm}$)	14.4	13.1	5.4	5.3	18.5
Tensile Strength,(GPa)					
At 293K	0.4-0.7	0.2-0.5	0.7-1.4	0.7-3.5	0.7-2.0
At 773K	0.3-0.5	0.2-0.3	0.2-0.5	0.5-1.4
At 1273K	0.04-0.1	0.1	0.1-0.2	0.3-0.5	0.4-0.7
Young's Modulus, (GPa)					
At 293K	130	185	330	410	450
At 773K	125	180	320	390	415
At 1273K	110	170	280	365	360
Ductile to Brittle Transition Temperature (DBTT), K	<147	<25	250	...

Beyond 1200K, the refractory metal alloys are the only candidate materials for structural purposes. Fig. 2.1 shows the candidate materials with increasing operating temperatures, shifting the selection of the structural material of stainless steel, at or below 923K, to super alloys, Nb alloys, and Mo alloys above 923K, 1200K, and 1450K, respectively [5].

Table–2.2: Composition and applications of different refractory metal alloys

Alloy Designation	Nominal Composition (wt.%)	Applications
C–103 Nb–1Zr PWC–11 WC–3009 FS–85	Nb–10Hf–1Ti Nb–1Zr Nb–1Zr–0.1C Nb–30Hf–9W Nb–28Ta–10W–1Zr	Thrust chambers & radiation skirts for rocket and aircraft engines, piping for liquid alkali metal containment, sodium vapour lamp electrodes. Liquid metal container and piping.
Ta–2.5W Ta–10W T–111	Ta–2.5W Ta–10W Ta–8W–2Hf	Heat exchangers, linings for towers, valves and tubings. Hot gas valves, rocket engine skirts, corrosion resistant valves in the chemical industry.
Mo–TZM TZC Mo–30W MHC	Mo–(0.5–0.8)Ti–(0.1–0.2)Zr–(0.013–0.02)C Mo–1Ti–0.3Zr–0.03C Mo–30W Mo–1.5Hf–0.05C	Tooling materials in the isothermal forging of superalloys, structural materials for HTR, container material for molten zinc.
W–3Re W–5Re W–25Re	W–3Re W–5Re W–25Re	High temperature thermo–couples, Heaters etc.

Fig. 2.2 compares the yield strengths of Mo, Nb–1Zr, PWC–11, C–103, Mo–TZM, Mo–14Re, Mo–44.5Re, and T–111. The yield strength, although not an indicator of the creep properties of the materials, is a good measure to rank the materials in term of their strength at the operating temperatures of interest. Of note are the particularly high strengths of the molybdenum alloys Mo–14Re, Mo–44.5Re, Mo–30W and Mo–TZM, and of the tantalum

alloy T-111 [5]. Above 1000K, the strengths of the niobium alloys Nb-1Zr, PWC-11, and C-103 and of pure molybdenum are all comparable, but much lower than those of the Mo and Ta alloys.

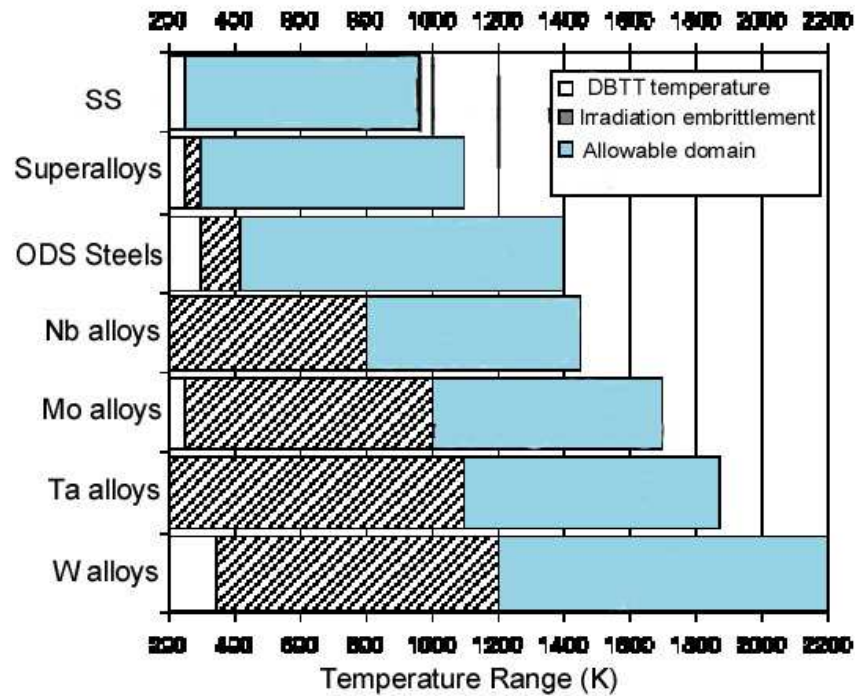


Fig. 2.1. Recommended operating temperature range of structural materials in space nuclear power systems [5].

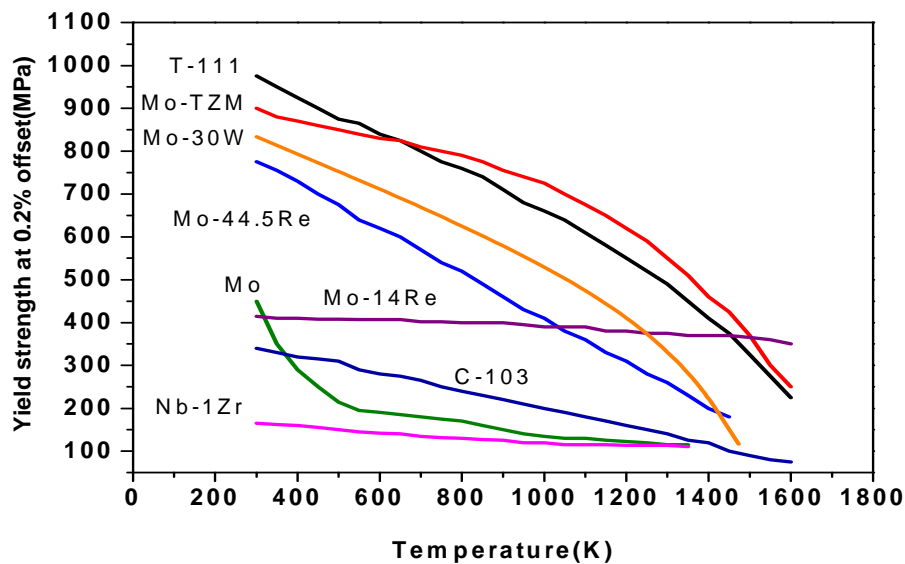


Fig. 2.2. Comparison of yield strengths of refractory metals and alloys [5].

In general, refractory alloys have high creep strength at high temperatures and excellent compatibility with alkali liquid metals as long as oxygen, nitrogen, carbon, and silicon impurities are kept below appropriate limits, typically in the range of a few to 10's ppm.

The major barrier to the use of refractory metals and alloys for high-temperature applications is their poor behaviour under oxidizing environments. The oxidation problem of refractory metals falls into two different categories. The first category consists of Nb and Ta which have very high oxygen solubility. Due to its high solubility of O₂ internal oxidation at low O₂ pressure without the formation of an external scale and affecting room temperature ductility and increase in strength. The second category includes Mo and W which have relatively low oxygen solubility but forms volatile oxides at high temperature. Therefore, choice for selection of refractory metals and alloys should be based on the operating environment especially with respect to the partial pressure of O₂. Taking into the design consideration of density, among the refractory metals, Nb followed by Mo are suitable candidates for structural applications from the above mentioned categories. The volatility of MoO₃ represents a significant degradation mechanism, but it is not as insidious as the oxygen embrittlement problem of Nb based alloys at low partial pressure of oxygen. In vacuum molybdenum has a virtually unlimited life at high temperature. In outer space, for example, the oxidation rate of molybdenum is insignificant.

2.2.1 Mo and Mo based alloys

Molybdenum is the most readily available, least expensive and highest consumption annually among the refractory metals. Most of it, however, is used as an alloying element in irons, steels and superalloys. Mo-based mill products occupy roughly 5% of the market [6].

2.2.1.1 Extraction of Mo

Almost all molybdenum is recovered from low-grade deposits of the mineral molybdenite. Deposits mined primarily for molybdenum constitute about 33% of world output. The remainder is obtained mainly as a by-product from mining of large, low-grade copper porphyry deposits. There is no known occurrence of primary molybdenite, which is presently being mined in India. The annual requirement of molybdenum is met by imports.

Molybdenum ore is beneficiated by froth flotation method, which yields a high grade concentrate containing about 90 to 95% MoS₂. The concentrate is roasted to drive off sulfur and a technical grade molybdic trioxide (MoO₃) is obtained. Molybdic oxide is the major form of molybdenum used by industry and the base material for the production of

ferromolybdenum, chemicals and molybdenum metal powder. The technical grade oxide is produced by roasting molybdenite concentrate in the multiple – hearth furnace at temperatures of up to 650°C. Molybdenum metal powder is produced by reducing pure molybdic oxide or ammonium molybdate with hydrogen. The purest metal powder (99.95% molybdenum minimum) is produced from ammonium molybdate. Ammonium molybdate is produced by reacting pure molybdic oxide with ammonium hydroxide and crystallizing out the pure molybdate [7, 8].

2.2.1.2 Properties vis-à-vis Applications

Molybdenum is a silver–white metallic element with an atomic number of 42, atomic weight of 95.95 and a density of 10200 kg/m³. The chemistry of molybdenum is complex since molybdenum exhibits oxidation states from – 2 to 6, coordination numbers from 4 to 8 and forms compounds with most inorganic and organic liquids. It has a melting point of about 2,610°C. Among the metallic elements, only osmium, rhenium, tantalum and tungsten have higher melting points. Other significant physical properties of molybdenum metal are good thermal conductivity (about one half that of copper), lower coefficient of thermal expansion of the pure metals, high strength at elevated temperatures, resistance to corrosion in a variety of mediums etc. Molybdenum is a strong carbide forming element and much of its alloying effect in steel is imparted through the formation of carbides. Mo has a high specific elastic modulus (i.e. E/ρ) and good strength at high temperatures. Mo and its alloys are attractive for applications requiring both high stiffness and low weight at temperatures beyond melting point of Ni based alloys.

Thermal conductivity of Mo is approximately 50% higher than that of steel, iron or nickel alloys. High thermal conductivity and good electrical and chemical properties led to application of Mo alloys in glass and zinc making industries and heat sinks. Its high thermal conductivity, low specific heat and low coefficient of thermal expansion, makes Mo resistant to thermal shock and fatigue, which is very important for its application in microelectronics. Therefore, Mo is widely used in electronics, solid–state devices, X–ray tubes, crystal growing, heat pipes, photo etched masks, etc. Mo exhibit good polishing ability to optical finish surfaces, necessary for high energy output, high surface temperature laser mirror components.

Mo and Mo–based alloys are commercially used for principally high temperature applications in hot equipment and hot working tools. TZM is the most studied, commercial high strength, high temperature material, which is widely used in hot–work tool application

such as die casting (even ferrous metals), hot extrusion (non-ferrous and ferrous metals), hot piercing stainless steel tubes, isothermal forging tools, isothermal shape rolling, hot gas valves and seals, hot turbine components etc.

Although poor oxidation resistance is observed in air at temperatures $> 500^{\circ}\text{C}$, molybdenum can be used for long term exposures in a controlled atmosphere. When considering the use of molybdenum for structural applications, limitations can be imposed by a ductile to brittle transition temperature (DBTT). Metals that have a body-centered cubic (bcc) structure typically exhibit generous levels of ductility and toughness at a homologous temperature $(T/T_m \text{ (K)}) \geq 0.3$, but brittle behavior is generally observed at a homologous temperature of 0.1, which is near room-temperature for molybdenum [9]. Application areas of Mo based alloys can be listed as:

1. In advanced nuclear power plants, new structural materials which are superior in the mechanical and corrosion properties to the conventional materials are desired strongly for raising thermal efficiency and also for securing the safety of the plant system during a long term service at high temperatures.
2. Turbine blades
3. High-temperature forging dies.
4. Future thermionic energy converters (TEC) are expected to operate at temperatures above 1900 K for several years. The creep resistance of the emitter material is thus important for the space power applications. Mo and Molybdenum alloys are considered as a potential material for TEC applications due to its good thermionic properties.
5. In ITER, optical components, such as mirrors mounted close to the plasma, will experience higher levels of radiation due to the neutron, gamma ray and particle irradiation than in present devices. It has been confirmed that metallic mirrors, such as molybdenum and tungsten, have a strong resistance to neutron and gamma ray irradiation.

Refractory high Z metals such as Mo and W have received great attention as the most promising materials for plasma facing components (divertor and limiter) of advanced fusion devices.

6. High temperature furnaces
7. Glass melting and processing equipment

2.2.1.3 Categories/ Types of Mo based alloys

2.2.1.3.1 Carbide strengthened alloys

This strengthening mechanism relies on the formation and dispersion of fine reactive metal carbides (HfC, TiC, ZrC etc.) in the matrix to strengthen and increase the recrystallization temperature. TZM (0.5%Ti, 0.08%Zr, rest Mo) is the most common and popular example of such methodology, where the formation of TiC and ZrC at grain boundaries, inhibit the grain growth and grain boundary failures. Other examples of carbide strengthened alloys are shown in Table 2.3.

In TZM, molybdenum is alloyed with small amounts of titanium, zirconium and carbon to produce a coarse distribution of carbides with some titanium and zirconium in solid solution [10]. An isothermal section at 873°K of Mo–Ti–Zr ternary phase diagram [11] has been presented in Fig. 2.3. It shows that Ti and Zr form solid solution with Mo up to a maximum limit of 1 wt.%. There is a strong tendency of brittle Mo_2Zr intermetallic phase formation at a higher percentage of Ti and Zr.

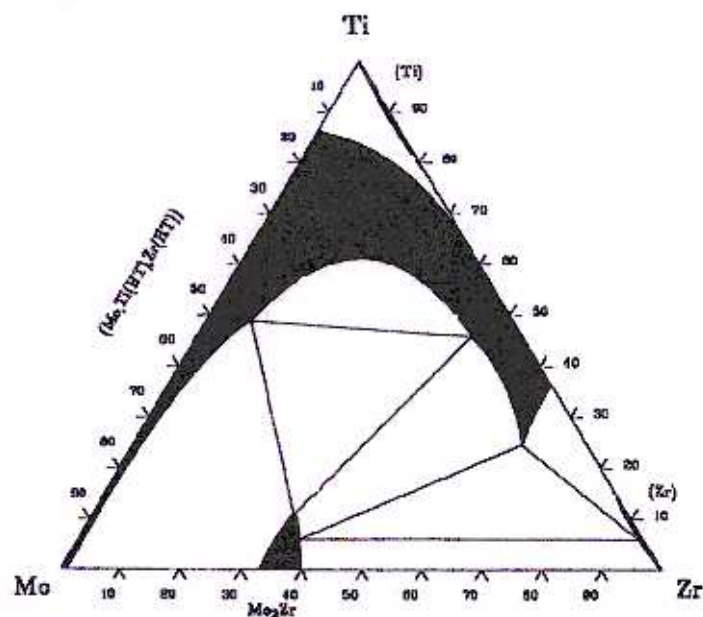


Fig. 2.3. Ternary phase diagram of Mo–Ti–Zr system, isothermal section at 873K [11].

TZM possesses a high melting point and hence, powder metallurgy is an alternate economical route of fabrication. Many products and devices are being manufactured through powder metallurgy route, because of many associated advantages. However, sintered material exhibits mechanical properties, which are not well suited for most applications. Thus, the

desired strength and ductility has to be achieved by several thermomechanical treatments after sintering. Hot isostatic pressing at 1873K of TZM powder prepared by plasma rotating electrode process and mechanical alloying has been reported earlier [1, 12, 13]. Sharma et al. [14] reported the studies carried out in preparation of the TZM alloy by aluminothermic co-reduction of mixed oxides.

High amounts of tensile ductility are typically observed in molybdenum–base alloys at low temperatures only when the grain size is fine, the oxygen content is low, and the ratio of carbon to oxygen is high [15]. Additions of carbon in unalloyed molybdenum have been shown to decrease the overall oxygen content in the alloy, prevent segregation of oxygen to the grain boundaries to minimize embrittlement, and result in the formation of carbides that strengthen grain boundaries. The presence of coarse (Ti, Zr) – rich carbides together with titanium and zirconium in solution inhibits grain growth and recrystallization at high temperature and results in higher creep resistance and strength for Mo–TZM at high temperatures.

The highest fracture toughness value for all molybdenum alloys are generally observed at temperatures between 473 and 673K and a slight decrease in toughness observed in 1073–1273K [16, 17].

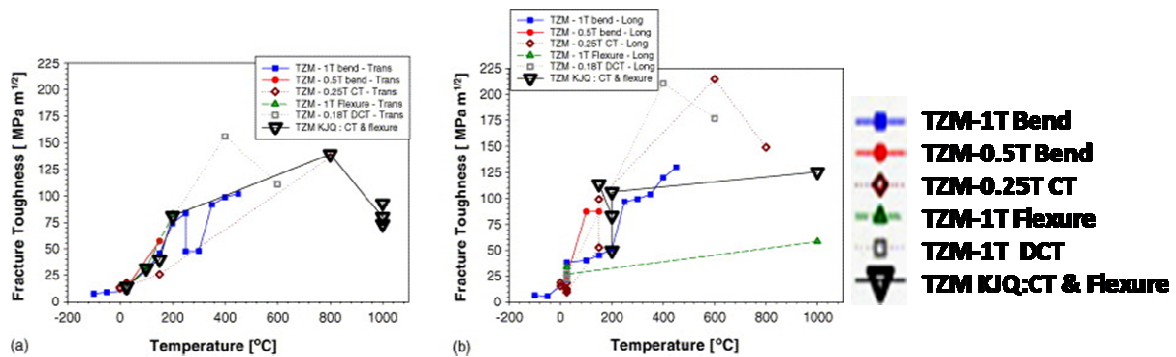


Fig. 2.4. Plot of fracture toughness results as a function of temperature for TZM obtained using the J–integral method: (a) transverse (T–L) orientation and (b) longitudinal (L–T) orientation. Each symbol represents the results of a single test, and the lines connect the points for each data set [17].

Despite a general trend for slightly lower fracture toughness values at 1073–1273K (Fig. 2.4) is observed for the molybdenum alloys, which is consistent with the trend of results observed for other metals at higher temperatures, no real temperature dependence for fracture toughness values can be resolved within the data scatter at temperatures between the DBTT and 1273K. The scatter in fracture toughness values can result in creep effects at high

temperatures, use of K_{J-max} and K_{JC} methods, and use of alternative specimen types, but variation in the degree of ductile laminate fracture mechanism from specimen to specimen is likely the most significant factor.

The excellent high temperature strength and thermal conductivity of molybdenum–base alloys provide attractive features for components in advanced reactors. However, refractory metal–base alloys react readily with oxygen and other gases, and molybdenum alloys are susceptible to losses from highly volatile molybdenum trioxide (MoO_3) species. Transport of radioactivity by the volatilization, migration and re–deposition of MoO_3 during a potential accident involving a loss of vacuum or inert environment represents a safety issue. Studies [18] on molybdenum at lower temperatures in high levels of oxygen report: (1) parabolic rate law at 523–723K; (2) linear behaviour above 673K; (3) the role of MoO_2 and other oxides (MoO_Z), where $2 < Z < 3$, between 723K and 923K; (4) high vaporization of MoO_3 , mass loss and oxidation rates above 923K.

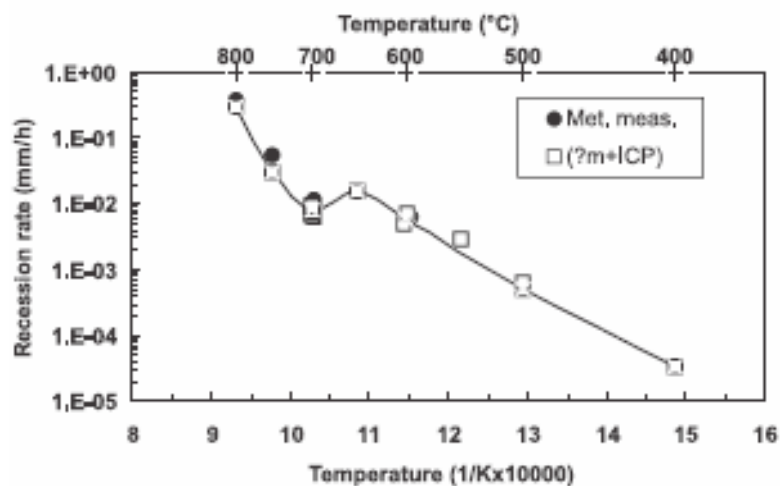


Fig. 2.5 Recession rates of TZM when oxidized in air [16].

Smolik et al. [18] experimentally measured the oxidation, volatilization and re–deposition of molybdenum from TZM in flowing air between 673K and 1073K. They plotted the recession rates, fractions of ‘reacted metal’ volatilized and mass flux rates with respect to reciprocal temperature. The plot for the recession rates is shown in Fig. 2.5. The plot shows a maximum at 923K (the rate at 923K is 2–3 times higher than at 873K and 973K) and then sharply increasing rates from 973 to 1073K. The oxidation rate as indicated by recession, showed an increasing trend to 923K, then a slight decrease, and then sharply higher rates due to high volatilization.

This trend in oxidation rate is very similar to those observed for the other refractory metals of niobium and tantalum. The irregularities are attributed to various non-stoichiometric phases other than Nb_2O_5 or Ta_2O_5 . A thin MoO_2 layer or an external MoO_3 layer with a thin sub-layer of MoO_2 or other oxides during the oxidation of molybdenum with air between 723K and 1043K was observed. The other oxides were reported as being non-stoichiometric, i.e., MoO_Z with 'Z' varying between 2 and 3. The similar characteristics of the refractory metals and the observations above suggest that the maximum at 923K in Fig. 2.5 is real and is likely to be caused by different types of oxides.

The plot of the calculating fraction of 'oxidized' molybdenum volatilized in Fig. 2.6 shows a marked increase above 923K. The amount of the oxide volatilized at 973K was generally 20–33%. Tests under exposure to high temperature helium containing oxygen resulted in embrittlement of both molybdenum and TZM alloy due to the grain boundary weakening by the oxygen contamination [19, 20].

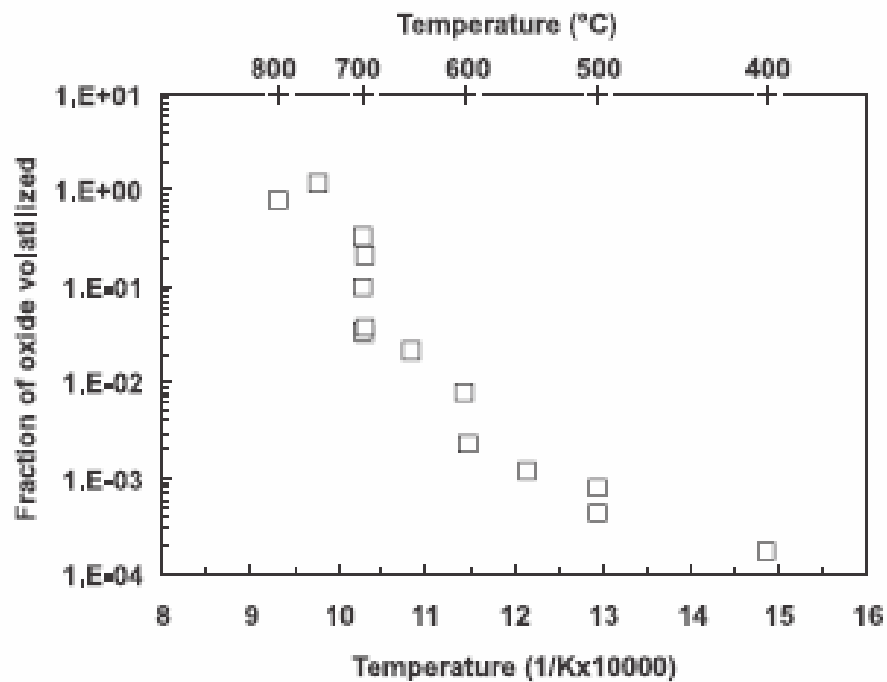


Fig. 2.6 Fraction of oxidized molybdenum that volatilizes [18].

Alur and Kumar [21] analyzed the weight changes of TZM resulting from isothermal oxidation for 24 h at different temperatures. The weight gain exhibited by TZM is of the order of 0.001% and 27% of the initial weight of the samples and at 573 and 873K respectively. Sharma et. al.[14] have studied the oxidation behavior of TZM in air and oxygen atmosphere. Thermal plots showing the oxidation pattern of TZM alloy under the atmospheres of air and oxygen are shown in Fig. 2.7. The plots exhibit gradual and slow

weight gain up to 673K due to the formation of dark brown MoO_2 at a sluggish rate on the specimen surface. At 673K and onwards, there was a sharp increase in the weight gain till 1023K due to the formation of greenish yellow MoO_3 layers at a rapid rate on the specimen surface. The cumulative weight gain was 70–80% which can be attributed to the formation of above oxide layers on the specimen surface. However, at 1023K onwards, there was a sharp decrease in the weight due to the volatilization of MoO_3 . The cumulative weight loss was recorded to be 40–50%. It is observed that the cumulative effect of weight change was much higher under the atmosphere of oxygen than in air. However, there was neither any weight gain nor any weight loss when the TZM specimen was heated under vacuum or argon.

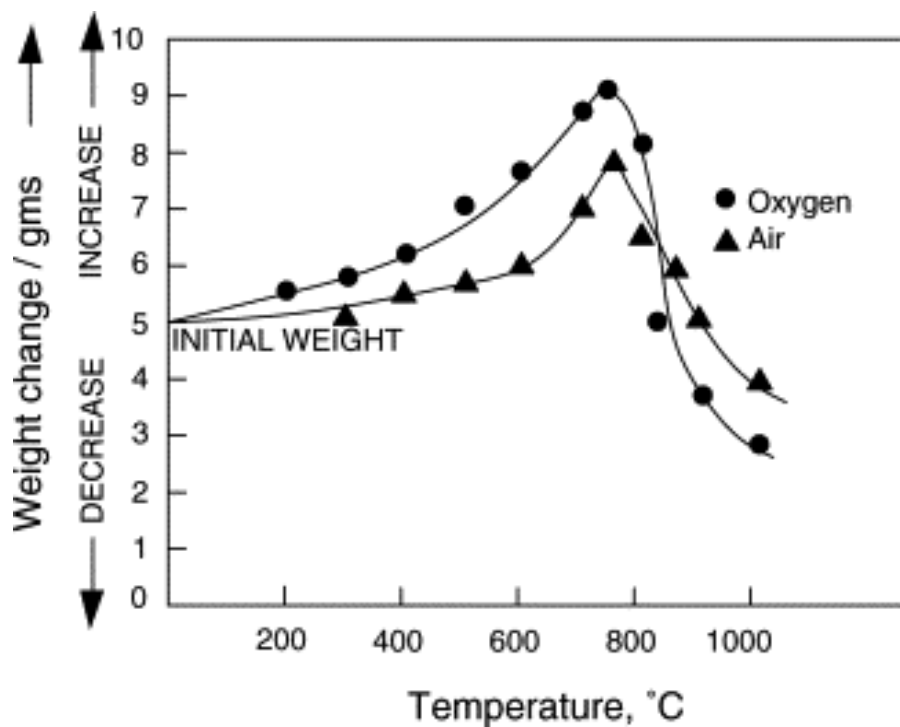


Fig. 2.7 Oxidation pattern of uncoated TZM alloy. [14].

Liquid metals are proposed to be used as coolant for high temperature reactors operating in the range of 1073–1273K. Lead (Pb) and lead–bismuth eutectic (44.5Pb–55.5Bi) have been the two leading candidate materials for spallation target and coolant because of their high atomic numbers, low melting points and low parasitic neutron capture [22]. One of the key requirements of the structural material for this kind of high temperature applications is the capability to withstand corrosion under liquid metal for prolonged duration. Temperature–gradient mass transfer will be the most damaging type of all material degradation phenomena in liquid metal because of large temperature gradient in the systems. The behaviour of the container material in the liquid metal is a function of temperature. After

a period of operation, solubility limits are reached, and the temperature–dependent solubility results in the transfer of the container material from the hottest location to the coldest location in the flowing loop. Cathcart and Manly [23] studied the relative resistance of 24 metals and alloys to mass transfer in liquid lead with a temperature gradient of 573K (773–1073K). The results indicated that only niobium and molybdenum showed no mass transfer, whereas the other materials showed little to heavy mass transfer. Suzuki et al. [24] compared corrosion test results for stainless steel and TZM in liquid mercury. No corrosion of TZM at 873K for 2000hrs was observed. In case of stainless steel selective dissolution of Ni, Cr was observed. Grain boundaries were attacked more compared to grain interiors. Fig. 2.8 shows the difference in solubility for the elements line Ni, Fe, Cr and Mo in mercury with increasing temperature. Molybdenum shows the lowest values amongst these elements. Mo and its alloys also are known to be corrosion resistant against liquid metals such as Pb, Li, Na apart from Hg.

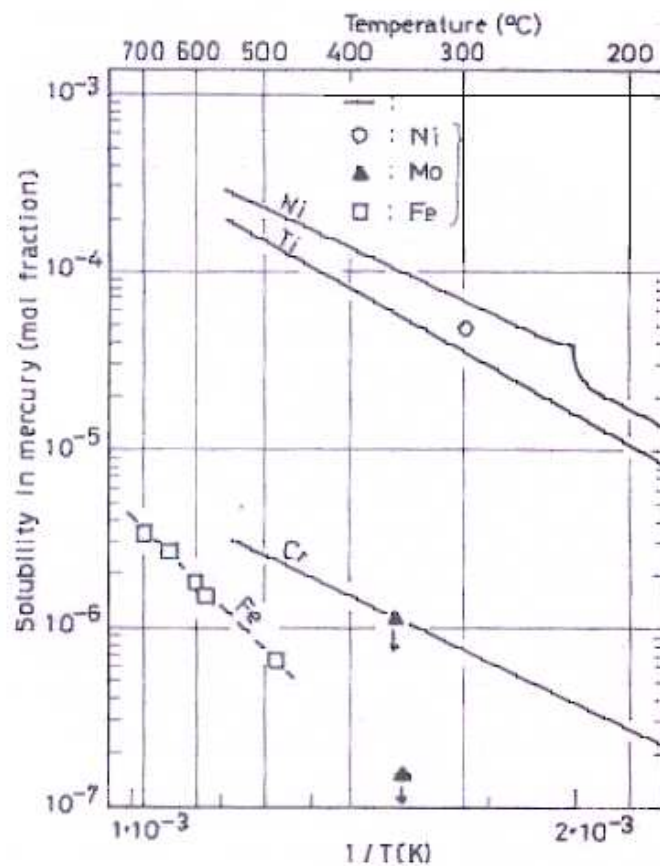


Fig. 2.8 Solubility of the elements in mercury at different temperatures [24].

Table –2.3: Important and commonly used Mo based alloys and their recrystallisation temperature

Alloy	Nominal Composition, Wt%	T _{Recrys.}
K		
Pure Mo	100 Mo	1373
Carbide–Strengthened		
TZM	0.5 Ti, 0.08 Zr, 0.03C	1673
TZC	1.2 Ti, 0.3 Zr, 0.1C	1823
MHC	1.2 Hf, 0.05 C	1823
ZHM	0.4 Zr, 1.2 Hf, 0.12C	1823
HWM–25	25 W, 1 Hf, 0.07 C	1923
Substitutional		
25 W	25 W	1473
30 W	30 W	1473
5 Re	5 Re	1473
41 Re	41 Re	1573
50 Re	47.5Re	1573
Dispersed–Phase		
PSZ 1523	0.5vol%ZrO ₂	
MH	150ppm K, 300 ppm Si	2073
KW 2073	200 ppm K, 300 ppm Si, 100ppmAl	
MLR 2073	0.7 La ₂ O ₃	
MY0.55 1573	Yttrium mixed oxide	

2.2.1.3.2 Solid solution strengthened alloys

The solid solution approach is the other route to increase the high temperature strength and recrystallization temperature. It relies on addition of solid solution elements to inhibit diffusion. W and Re are the most promising solid solution additive for enhancing the high temperature strength of Mo.

Among solid solution strengthened alloys, Mo–30W (wt. %) is the most widely used in various applications. This alloy is of commercial importance for its high melting temperature

of 3103K and its chemical inertness against corrosive molten zinc. Yield strength of Mo–30W with varying temperatures along with comparison with other alloys is presented in Fig. 2.2. Fig. 2.9 shows the phase diagram of Mo–W system [25], which shows that molybdenum and tungsten exhibit complete liquid solubility in all proportions. Mo–30W exhibits better formability and lower density as compared to W, while it exhibits higher strength, higher re-crystallization temperature and better corrosion resistance against liquid metal, as compared to Mo [26, 27].

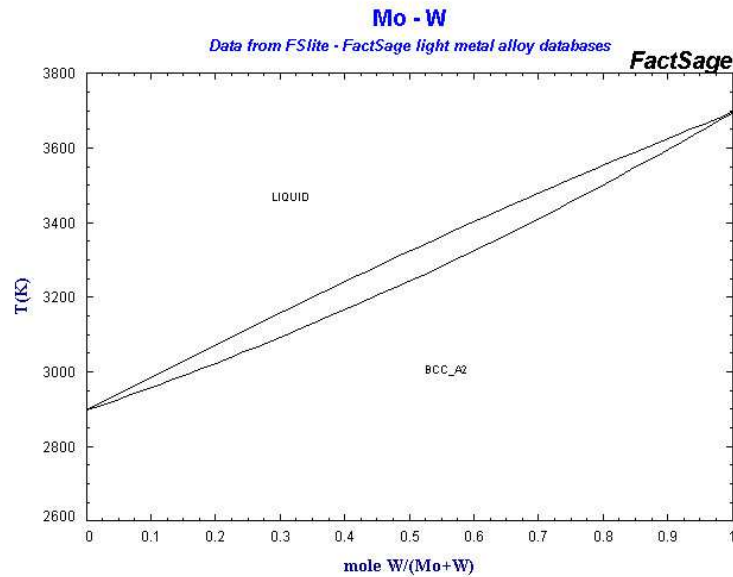


Fig 2.9 Phase diagram of Mo–W system [25]

Mo–30W has gained prominence because of higher melting temperature sought for missile aerospace and high temperature nuclear reactor applications. The Mo–30W solid–solution alloy was developed to withstand erosion or incipient melting of rocket nozzles at higher propellant combustion temperature. The 3105K melting point of Mo–30W, 477K higher than Mo, satisfied this criterion in several applications. However, the most significant markets developed afterward because of the alloy’s physical and chemical properties and adequate fabricability features [28].

It is low cost, lightweight alternatives to W–based alloys. Although metallic tungsten also provides outstanding resistance to chemical attack by molten zinc, the Mo–30W alloy is readily machinable and capable of manufacture into a variety of wrought shape including round bars, tubes, sheet, and plate, as well as simple assemblies [28, 29].

The earliest and most widespread use of Mo–30W in zinc industry was for pump equipment, used to transfer or agitate molten metal with some control. Critical Mo–30W pump elements are employed in various type liquid–metal pumps with outstanding service

records; in fact, the earliest known pump components have seen a decade of dependable pumping service in high purity molten zinc. Centrifugal impeller-type pumps are widely employed for molten metal pumping, and the impeller shaft has proven the most crucial pump component in molten zinc service [29].

Although the Mo–30 alloy is used in various applications, but very limited technical studies have been carried out for its synthesis and property evaluation. Majumdar et al. [30] have studied the feasibility of synthesis of the Mo–30W alloy by co-reduction route of mixed oxides of Mo and W. Because of high vapour pressure of Mo and W, substantial loss of metal takes place during the reduction process resulting poor yield. Mo–30W possesses a high melting point and hence, powder metallurgy is an alternate economical route of fabrication. However, very few technical literatures are available related to Mo–30W alloy with respect to its synthesis via powder processing route. It is necessary to understand each unit step of powder metallurgical route for synthesis of the alloy.

Mo–30W alloy cannot be used in oxygen containing atmosphere because of its poor oxidation resistance at high temperature. Its oxidation behaviour is only slightly better than Mo. For utilizing its high temperature properties effectively, it has to be prevented from high temperature oxidation by a suitable coating. Majumdar et al. [30] have studied some of the aspects of development of oxidation resistant silicide and aluminide coating over Mo–30W alloy by pack cementation technique. Although these coatings have been found useful for enhancing the oxidation resistance of refractory metal alloys, these seem to be not the final equilibrium and there exists a possibility of the dissolution of the coating into the substrate over a period of time. The role of inter-diffusion on the stability of silicide coatings needs to be studied, when the coated component is subjected to prolonged exposure. Other issues related to coatings shall be discussed in detail in the subsequent sub-section of coating.

2.2.1.3.3 Dispersion-strengthening – It rely on second phase particles introduced or produced during powder processing, to increase the resistance for recrystallization and stabilize the recrystallized structure [31, 32]. These alloys have enhanced high temperature strength. The examples of dispersion strengthened alloys are listed in Table 2.3.

2.2.1.4 Processing

Although Mo based alloys posses excellent high temperature properties along with favorable physical properties, the key challenge associated with the application is to establish

large-scale production capabilities, irradiation effects, expertise in fabricability and welding apart from the problem of oxidation and development of suitable coatings.

Mo based alloys display ductile to brittle transitions (DBTT), which lie above room temperature. Therefore they are typically brittle at room temperature unless special efforts are taken during processing. Mo based alloys are consolidated into products by the powder metallurgy process and by the consumable electrode vacuum-arc casting process. The powders are consolidated into finished products or mill shapes and ingots for further processing such as rolled into sheet and rod, drawn into wire and tubing. Because of their high melting points and ease of oxidation, refractory metals are usually worked in powder form. The science of modern powder metallurgy (P/M) actually started in the early 1900's when incandescent lamp filaments were made from tungsten powders. Another early P/M product was cemented tungsten carbide used in the manufacture of cutting tools. Powder metallurgy has grown as one of the most versatile methods of metal part fabrication because of manufacturing productivity advantages, materials conservation, wide range of engineering properties, design flexibility, near net shape fabricability, energy savings etc.

Complicated shapes are produced by isostatic pressing in collapsible containers, followed by sintering in high-temperature furnaces or induction heating. However, there is a limitation to the component size, which may be iso-statically pressed to uniform cold pressed densities. Thereafter a more difficult problem is that of the sintering of the pressed material. Most of the sintering furnaces have a temperature limitation of about 2473K, along with limitation of the hot zone. Sintered density of about 90% of theoretical is generally considered to be the minimum acceptable for satisfactory workability in the subsequent fabrication of the billet. There are serious furnace problems in achieving this density in large billets, for example the disproportionately long sintering time necessary at available lower temperatures.

Hot pressing is a potent method of consolidating refractory metal and alloys [33–41]. But very few literatures are available on the synthesis of Mo based alloys by hot pressing primarily because of limitation of inadequate mould materials. Graphite is the only feasible material, and excessive carburization has been anticipated during hot pressing in graphite. Therefore, a suitable technology and systematic study should be carried out to see the feasibility of preparation of Mo based alloys by hot pressing with the aim of minimizing carburization and lowering sintering temperature by application of simultaneous pressure.

The arc-casting process was developed for molybdenum. Large molybdenum ingots have been melted, extruded, and fabricated. Because of the large grain size of such ingots and the accompanying hot shortness, it has been a universal practice to extrude prior to other types of working. Extrusion breaks up and refines the as cast structure. A major advantage of the arc-casting process is that there is no apparent limit other than electrical power on the size of the ingot that can be produced. Furnaces as large as 100 inches in diameter are feasible. Therefore, for refractory metals the arc-casting process offers the best possibilities, if very large ingot sizes are required. But the arc casting of the Mo-30W alloy is a challenging task because of their large difference in density and vapor pressure. Vacuum arc casting can lead to loss of Mo and achieving chemical composition is tough. Thus component melting of Mo and W is technologically difficult and also there are no technical literatures available.

Electron-beam melting is an even newer process. Electron-beam melting process gained fame due to the extremely low interstitial content of the product melted, which results because of the melting in ultrahigh vacuum required for the process. However, the electron beam process results in extremely large grain size, larger even than in arc-cast ingots. The development of electron-beam furnaces is proceeding quite rapidly, and megawatt furnaces capable of melting as long as 20-inch ingots are being produced. Powder metallurgy consolidated material generally is directly worked into the final desired shape. On the other, arc-cast or electron beam melted ingots require extrusion before they may be worked further. Alternate synthesis route should be explored for synthesizing Mo based alloys, owing to the limitation of high temperature processing facilities.

2.2.1.5 Limitations w.r.t. Application and remedies

Molybdenum is attractive and probably the most promising in terms of strength, density, melting temperatures, compatibility with molten Pb-Bi eutectic, higher thermal conductivity etc. However, Molybdenum is very susceptible to intergranular failure in the recrystallized state (recrystallization embrittlement) and in the neutron irradiated state (irradiation embrittlement), which are major problems in their applications. The important and commonly used Mo based alloys and their recrystallisation temperature are listed in Table 2.3.

The main limitation of Mo based alloys can be listed as:

1. The strength of Mo decreases rapidly at temperatures above $0.5 T_m$. As a result, the use of pure molybdenum has been severely limited.
2. Molybdenum is very susceptible to intergranular failure in the recrystallized state (recrystallization embrittlement) and in the neutron irradiated state (irradiation embrittlement), which are major problems in their applications.
3. The major barrier to the use of molybdenum alloys for high-temperature applications is their catastrophic behaviour under oxidizing environments.

To overcome the first two problems mentioned above, carbide strengthening, solid solution strengthening and dispersion-strengthening are generally adopted. To overcome the third problem mentioned above, attempts have been made to protect refractory metals from catastrophic oxidation in high-temperature oxidizing environments either by alloying or application of oxidation resistant coatings. Application of coating over the known Mo based alloys looks to be a better and immediate remedy as compared to investigate newer oxidation resistant alloy, for taking care of the high temperature oxidation problem. However, coating is not a foolproof solution, because once the coating fails for any expected or unexpected reason, the component would fail catastrophically. Therefore, the recent trend in design of high temperature system is that the substrate of the high temperature components should have sufficient levels of oxidation resistance to avoid catastrophic damage in case the coating fails.

2.2.1.5.1 Mo based oxidation resistant alloys

The major barrier to the use of molybdenum alloys for high-temperature applications is their catastrophic behaviour under oxidizing environments. So, application of oxidation resistant coating is essential over the Mo based alloys. Coatings rich in aluminum and/or silicon (aluminide and silicide coatings) have been developed, which, when present on the surface of the refractory metal, oxidize and form protective Al_2O_3 and/or SiO_2 scales. However, diffusion of aluminum or silicon from the coatings into the substrate often occurs and this eventually has adverse effects on the mechanical properties of the substrate, as well as depleting the protective coating. Although extensive research has been done in the past to optimize coating compositions and to develop barrier layers to minimize the effects of interdiffusion, the latter objective has never been properly realized. Another major disadvantage of these coatings is that even pinholes in the coating can lead to rapid destruction of the substrate being protected.

Attempts have been made in the past to improve the oxidation resistance of Mo by alloying. Two approaches namely—“*reservoir phase approach*” and “*composite approach*”, have been studied extensively to enhance the oxidation resistance.

2.2.1.5.1.1 Reservoir phases approach

This approach requires the selection of reservoir phases, which are thermodynamically stable in the alloy, but are unstable in the presence of oxygen, so that the desired element can take part in the scale-forming process [42]. In that respect design of high-temperature alloys which would form protective SiO_2 and Al_2O_3 scales on exposure to high temperature, oxidizing environments are promising. One way to promote the growth of such scales is to incorporate sufficient amounts of Si or Al in the alloy substrate; typically, additions of approximately 35–45 wt.% (all alloy compositions are given in wt.%) of Si or Al would be required to form the respective scales, in the absence of additional protective scale forming elements.

One example of such alloy composition contain the matrix of Mo, dispersed second phase of titanium nitride and a third phase additive of aluminum and titanium. The second phase additive must be present in an amount effective to produce a protective scale, while not significantly degrading the mechanical properties or decreasing the melting point of the refractory metal. The third phase must be present in an amount effective to suppress the solubility of nitrogen in the refractory metal and enhance the stability of the second phase, while not significantly degrading the mechanical properties. A typical trend of weight change during oxidation testing of the mentioned Mo alloy is shown in Fig. 2.10. The other possible alloy system utilizing the same concept is tabulated in Table 2.4.

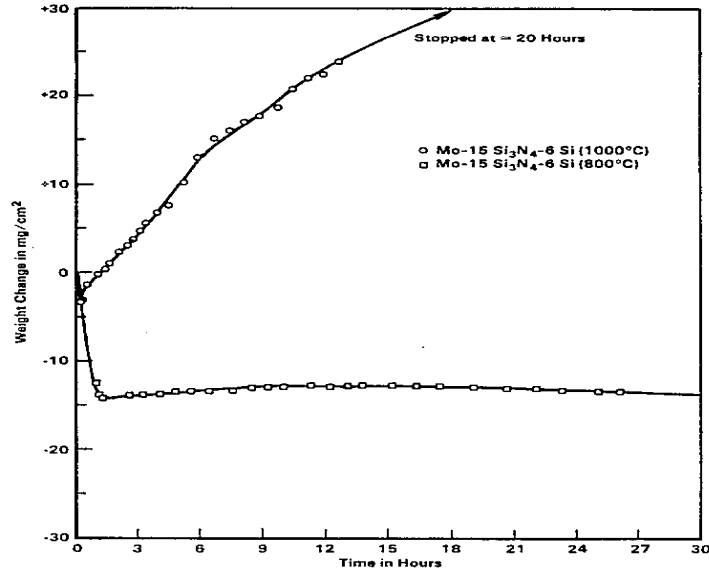


Fig. 2.10: The weight change during oxidation for two Mo-15Si₃N₄-6Si, oxidized for 50 hours at 1073K and 20 hours at 1273K

Table 2.4: Preferred compositional ranges suitable for use in high temperature oxidizing environment

System No.	Refractory Metal	Second Phase	Third Phase	Protective Oxide Scale
1	Mo (79-98%)	Si ₃ N ₄ (1-15%)	Si (1-6%)	SiO ₂
2	W (79-98%)	Si ₃ N ₄ (1-15%)	Si (1-6%)	SiO ₂
3	Mo (70-85%)	Cr ₂ N* (14-22%)	Cr* (1-8%)	Cr ₂ O ₃
4	W (70-85%)	Cr ₂ N* (14-22%)	Cr* (1-8%)	Cr ₂ O ₃
5	Mo (72-97%)	TiN (1-18%)	Al or Ti (1-9%)**	Outer TiO ₂ /Al ₂ O ₃ inner
6	W (72-97%)	TiN (1-18%)	Al or Ti (1-9%)**	Outer TiO ₂ /Al ₂ O ₃ inner
7	Nb (72-97%)	TiN (1-18%)	Al or Ti (1-9%)**	Outer TiO ₂ /Al ₂ O ₃ inner
8	Ta (72-97%)	TiN (1-18%)	Al or Ti (1-9%)**	Outer TiO ₂ /Al ₂ O ₃ inner

All % are in weight percent.

* The total combined % of Cr from Cr₂N and the free elemental Cr is at least 20%

** The total % of the elemental Al plus elemental Ti mixture cannot exceed 10% as the third phase

2.2.1.5.1.2 Composite approach (Ductile phase toughening)

Inverse composites or ductile phase toughened composites are a completely different class of materials, which utilize a ductile reinforcement, usually metallic, to improve the fracture resistance of a brittle matrix. Some reports have shown that the fracture toughness of alloys was enhanced by incorporating a ductile Mo phase to molybdenum silicides [43, 44]. The most studied alloy systems using a composite approach are three-phase Mo–Si–B alloys pioneered by Berczik [45, 46]. The alloy consists of a Mo (Si) solid solution (“ α -Mo”) and the intermetallic phases Mo_3Si and Mo_5SiB_2 (T2). These alloys have shown potential as oxidation-resistant structural materials for ultra high temperature applications. It is widely accepted that the ideal microstructure of these alloys would possess a continuous α -Mo matrix with embedded, homogeneously distributed intermetallic particles. While a continuous α -Mo matrix is favourable for room temperature toughening (due to crack trapping), the intermetallic particles should improve the oxidation resistance by facilitating the formation of a dense, protective boro-silicate glass layer on the material surface at high temperatures. Clearly, the key to achieving high fracture resistance in these materials is in making more effective use of the relatively ductile molybdenum phase, not unlike nickel-base superalloys where high toughnesses are obtained with a similarly high fraction of intermetallic precipitates.

The microstructures of Mo–Si–B alloys are characterized by three parameters. **First**, the morphology is important, *i.e.*, whether the α -Mo phase occurs in the form of discontinuous particles in a continuous Mo_3Si – Mo_5SiB_2 matrix, or whether particles of Mo_3Si – Mo_5SiB_2 are distributed in a continuous matrix of α -Mo. **Second**, the volume fraction of the toughening α -Mo phase is of key importance. **Third**, the size scale of the α -Mo phase is significant [47]. Fig. 2.11 (a) shows the microstructure of cast and annealed Mo–12Si–8.5B. The α -Mo (the bright phase) is distributed in the form of large primary and small secondary particles in a matrix consisting of Mo_3Si and Mo_5SiB_2 .

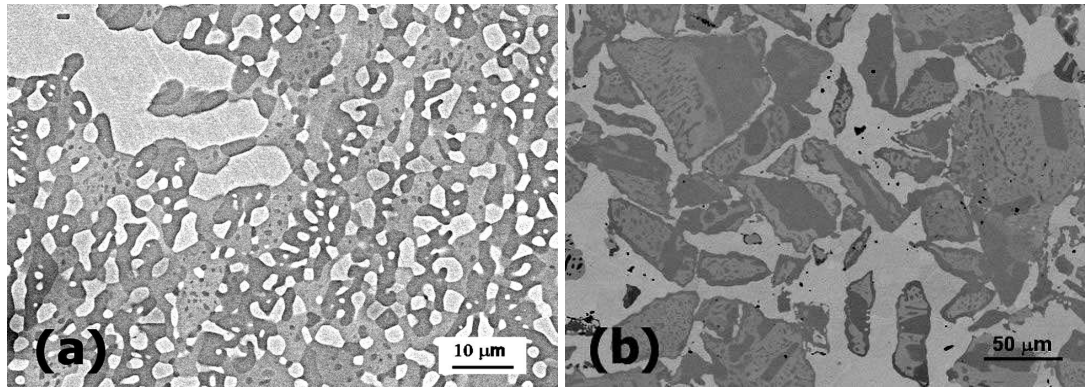


Fig. 2.11—SEM micrographs of (a) Mo–12Si–8.5B, arc-cast followed by annealing for 24 h at 1600 °C; and (b) Mo–Si–B consolidated from vacuum annealed Mo–20Si–10B powders by hipping for 4 h at 1873K and 207 MPa (30 ksi). The α -Mo volume fractions (bright phase) are 42 and 34 vol.% respectively [47].

A common feature of the oxidation behavior of these alloys is an initial region of fast mass loss followed by a region of much slower mass change. The initial mass loss is due to the rapid evaporation of Mo as MoO_3 . Once a sufficient quantity of MoO_3 has evaporated, the Si and B concentration on the surface becomes high enough to form a protective borosilicate film. Fig. 2.12 illustrates the fast initial weight loss for two Mo–Si–B alloys with different α -Mo volume fractions. As expected, the rate of the mass loss increases as the α -Mo volume fraction increases. A major difference of Mo– Mo_3Si – Mo_5SiB_2 intermetallics, as compared to typical structural ceramics, is the presence of the ductile α -Mo phase [47, 48].

Fig. 2.13 illustrates the pronounced increase in the room-temperature fracture toughness as the α -Mo volume fraction increases. When considering the suitability of Mo–Si–B-based materials for high-temperature structural applications, several property tradeoffs must be considered.

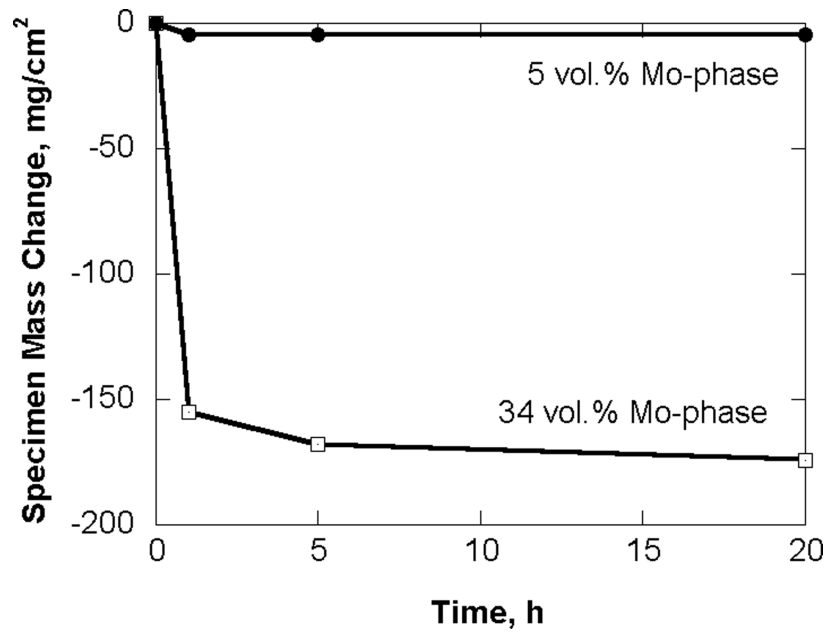


Fig. 2.12—Cyclic oxidation of Mo–Si–B alloys with different α -Mo volume fractions, at a temperature of 1473K and for 1-h cycles. The alloys were hipped Mo–20Si–10B powders (45 to 90 μm) that were vacuum annealed for different times to produce different α -Mo volume fractions [47].

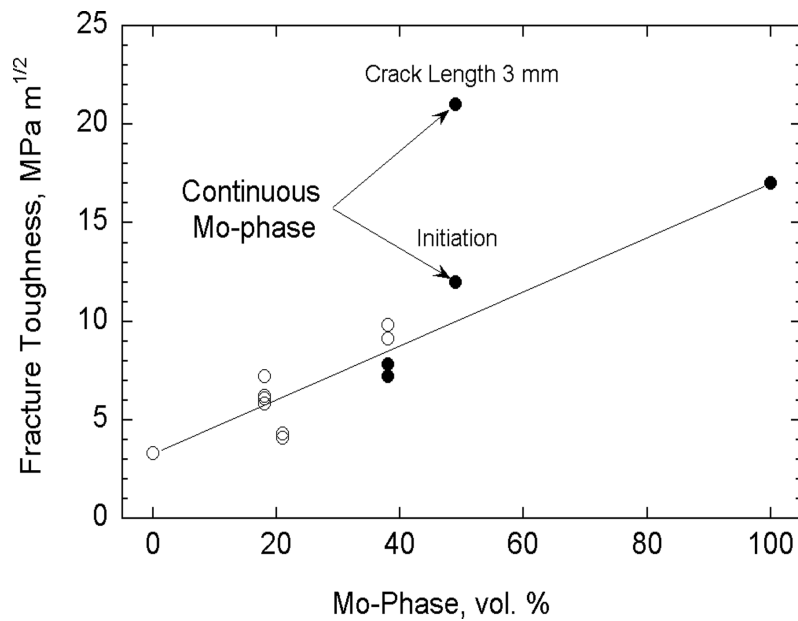


Fig. 2.13—Room-temperature fracture toughness as a function of the α -Mo volume fraction. Full and open symbols denote standard and nonstandard tests, respectively [47].

Although Mo–Si–B alloy system has emerged as a potential candidate for high temperature applications as an oxidation resistant alloy [49–58], but its application will be restricted in nuclear field where there will be a concern of neutron economy. As boron is a

neutron absorber, its use is prohibited in such application. Therefore alternate alloy systems need to be studied, emulating the concept of development of Mo–Si–B alloy. In this respect Mo–Cr–Si based alloys are important because it contains Cr and Si which is known to form oxidation resistant scale [59, 60].

2.2.1.5.2 Oxidation resistant coating

The major drawback of the Mo base alloys is their low oxidation resistance at high temperatures. The lack of oxidation resistance is due to the formation of non-protective molybdenum trioxide. Therefore, a protective coating is necessary for high-temperature applications of these Mo based alloys in oxidizing environments. A large number of coating techniques are available like cladding, physical vapor deposition (PVD), chemical vapour deposition (CVD), pack cementation, thermal spray coating, hot dipping, vacuum plasma coating, laser surface alloying etc. [61–80]. Each of these techniques presents various advantages and disadvantages depending upon the component to be coated and the end-use application. Although, many of these methods are in practice, however, they are not free from limitations

For high temperature oxidation resistance, a coating should exhibit following properties:

- ❖ Oxygen and metal ion diffusion should be restricted by coating
- ❖ The coating should have a low vapor pressure at the operating temperature,
- ❖ The melting point of the coating should be above the operating temperature,
- ❖ The coating should have low reactivity with the substrate, and
- ❖ It should have low reactivity with the high temperature environment

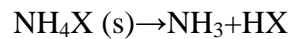
The most promising coating technique for protecting molybdenum base alloys is one in which the coating is formed in place, i.e., one in which the coating is metallurgically bonded to the substrate during the coating process and becomes an integral part of the base material. Such coating exhibits most of the properties listed above, which can be most successfully accomplished by the pack cementation process.

Pack cementation is a widely applicable in-situ coating technique, which produces a uniform and adherent coatings even on complex shaped structures. The coating layers and the substrates are found to be compatible with respect to adhesion, thermal expansion etc. This method is widely used to confer oxidation resistance on ferrous alloys as well as non ferrous especially for super alloys and refractory metal alloys. Usually relatively expensive aluminum or binary alloys grade reagent is used during the pack process with aluminum as a

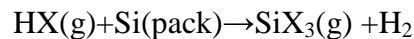
source. Pack cementation processes include aluminizing, chromizing, and siliconizing. Components are packed in metal powders in sealed heat-resistant retorts and heated in a furnace to precisely controlled temperature-time profiles. The schematic illustration of aluminide coating obtained by pack cementation is shown in Fig. 2.14. In the aluminizing process, a source of Al reacts with a chemical activator on heating to form a gaseous compound (e.g., pure Al with NaF to form AlF). This gas is the transfer medium that carries aluminum to the component surface. The gas decomposes at the substrate surface depositing Al and releasing the halogen activator. The halogen activator returns to the pack and reacts with the Al again. Thus, the transfer process continues until all of the aluminum in the pack is used or until the process is stopped by cooling. The coating forms at temperatures ranging from 973 to 1673K over a period of several hours [81–99].

An aluminizing pack cementation process is practiced commercially for various steels and for the growth of NiAl on Ni-base superalloys for use in turbine engines, chromizing is used on the surfaces of water wall panels in fossil fuel power plants, while silicide coating gives best oxidation resistance to refractory metal and alloys. The different steps for a silicide coating using halides and schematic illustration of the coated sample are shown below:

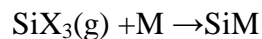
Decomposition



Formation of volatile aluminium halide



Deposition on the substrate



Where X is halide, generally Cl or F and M correspond to metal. The HAPC (Halide activated pack cementation) process is a diffusion coating process that involves embedding the substrate into a sealed or vented refractory container with a powder mixture called the pack, which is then heated at 1073–1473K in an inert atmosphere for 8–36 hrs.

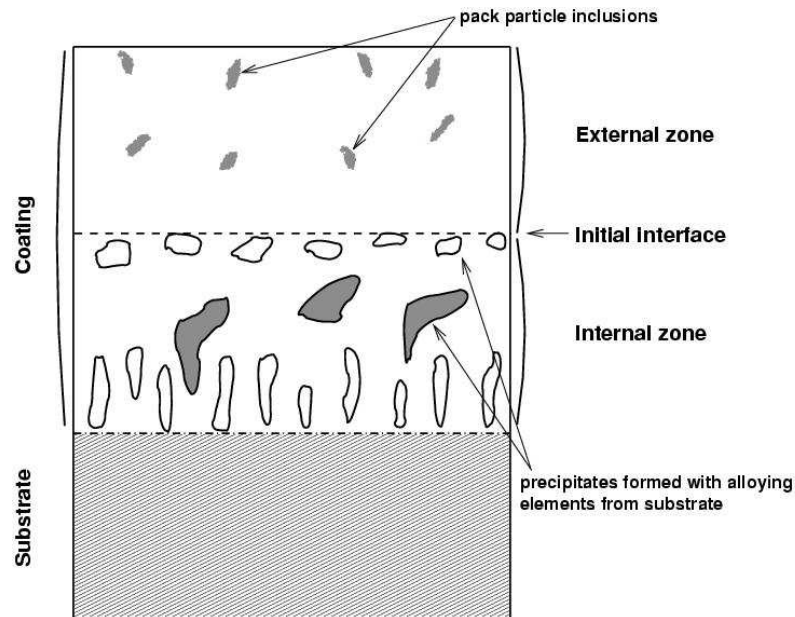


Fig. 2.14: Schematic illustration of aluminide coating obtained by pack cementation [39]

The powder pack is composed of a master alloy or pure element powder to be enriched at the substrate surface, a halide salt activator and inert filler. The HAPC technique is a form of in situ chemical vapour deposition because the halide activator decomposes at high temperature to produce volatile halide vapours of the elements. The chemical potential gradient drives the gas phase diffusion of the metallic halides to result in surface deposition.

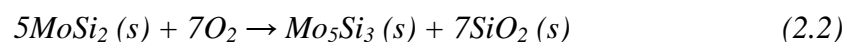
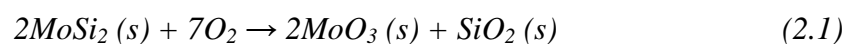
Silicides coatings are known to be the best oxidation resistant coating system for refractory metals and alloys, which exhibit most of the requirements for high temperature applications. The beneficial effects of silicides coatings on high temperature oxidation resistance are twofold. First, with sufficient concentration, Si can form a continuous vitreous silica layer between the metal and scale interface. This silica layer has a low concentration of defects, allowing it to become a good diffusion barrier and provide excellent oxidation resistance. Second, the preferentially formed silica acts as the nucleation site for the subsequent formation of chromia, which provides further oxidation protection for Mo based alloys containing Cr, such as Mo–Cr–Si alloys. Numerous researches have been carried out to develop silicide coatings over Mo based alloys such as TZM [100], Mo–30W [101], Mo–Si–B alloys [102–105] etc.

These protective metallic coatings are basically diffusion coatings. The coating process involves the reduction, deposition, ion interchange, diffusion, and the formation of new compounds. The coatings, then, are solid solutions, or intermetallic compounds, or both, and are composed of alloys of the coating materials and the substrate. They are an integral

part of the base metal and so bonding strength is excellent. The properties of these kinds of coatings can be controlled by a careful choice of the elements in the system and by proper control of the thermodynamics and kinetics of the reaction.

In the Mo–Si system, there are three stoichiometries compounds, i.e. C11b structured MoSi₂ (tetragonal), D8m structured Mo₅Si₃ (tetragonal), and A15–structured Mo₃Si (cubic) [106]. Among these, Molybdenum disilicide (MoSi₂) is most oxidation resistant because other two silicides lack Si content to cover the full surface by forming SiO₂. MoSi₂ is a promising candidate material for high temperature structural applications. It is a high–melting–point (2030 °C) material with excellent oxidation resistance and a moderate density (6.24 g/cm³). MoSi₂–based heating–elements have been used extensively in high–temperature furnaces. The low electrical resistance of silicides in combination with high thermal stability, electron–migration resistance, and excellent diffusion–barrier characteristics is important for various applications. Although silicide and alumunide coatings have been found useful for enhancing the oxidation resistance of Mo based alloys, these seem to be not the final equilibrium and there exists a possibility of the dissolution of the coating into the substrate over a period of time [107–109]. The role of inter–diffusion on the stability of silicide coatings needs to be studied, when the coated component is subjected to prolonged exposure. The major problems associated with MoSi₂ based silicide coatings are– problem of *pestring*, mismatch of coefficient of thermal expansion (CTE) with substrate and oxide layer, transformation of di–silicides to lower silicides such as Mo₅Si₃ or Mo₃Si etc. The details of the associated problems will be discussed one by one.

One major obstacle for MoSi₂ applications is structural disintegration during low temperature oxidation, which is known as the "*pest*" effect [110–114]. MoSi₂ disintegrates to a powder when subjected to oxidizing environments at 673–873K. This phenomenon was discovered in 1955 and has been referred to as MoSi₂ *pestring*. It has been suggested that the cause is grain boundary embrittlement produced by short–circuit diffusion of O₂ and subsequent dissolution into the grain–boundary areas. However, the exact nature of the pest effect is not clearly understood. There are two possible oxidation reactions for MoSi₂.



Both reactions are thermodynamically feasible, but the reaction (1) is favored, which results in pasting between 673–873K. It is known that MoSi₂–based coatings are prone to fail at temperatures less than 1368K, as defects in the coating such as pinholes or at geometrical

irregularities such as protrusions or sharp corners. Thus, if MoSi₂-based coatings are to be considered for the protection of Mo based alloys, coating evaluations are needed at lower temperatures.

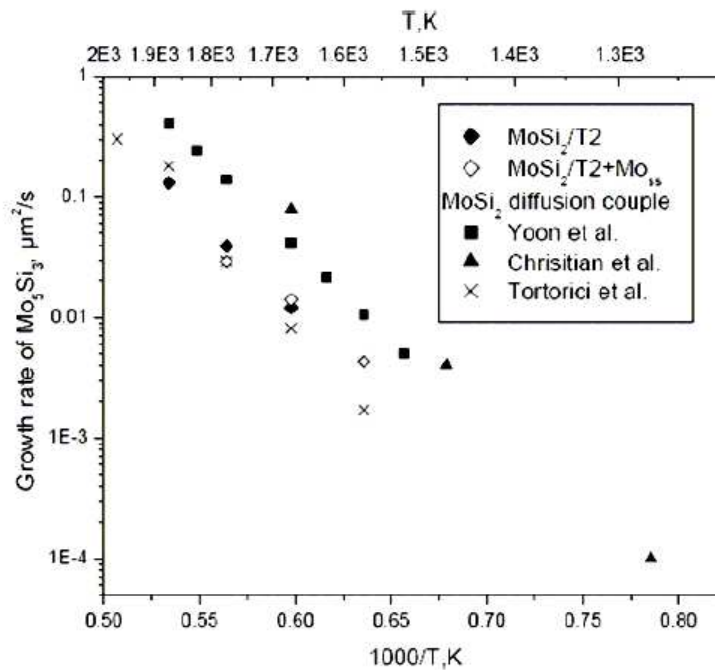
Coating efficiency depends on the structure of diffusive layer. As applied to molybdenum, the protective coating on it represents in general the disilicide phase. However, high-temperature operation of the refractory metal-silicide coating system leads to structural transformations of the diffusive layer caused by reactions on interface boundaries. That is, the highest silicides turn into the lowest, which are less effective in forming protective oxide films. Processes occurring in the silicide coatings are diffusive in character, and their quantitative description needs reliable data on silicon diffusivities in intermediate silicide phases (in this case, Mo₅Si₃ and Mo₃Si) at high temperatures. There are abundant researches devoted to silicon diffusion in the Mo₅Si₃ silicide [115–117]. However the vast majority of them are related to temperatures lower than melting point of silicon. For higher temperatures only solitary data are available in which the values either parabolic constants for Mo₅Si₃ layer growth or/and silicon diffusion coefficient were determined. On the other hand, in a number of researches [118, 120] molybdenum and silicon were used as initial reagents (Mo/Si diffusion couple) and parabolic constants for Mo₅Si₃ layer were determined for simultaneous growth of MoSi₂ and Mo₅Si₃ layers. Based on several researches, the parabolic rate constants of three Mo-silicides formed by various experimental conditions at 1273K are summarized in Table-2.5 and presented graphically in Fig. 2.15 (a) and (b). After determining the parabolic rate constant, a lifetime of MoSi₂ based coatings on three phases (Mo_{ss}+Mo₃Si+T2) alloy has been estimated and graphically presented in Fig. 2.16 [121].

Table–2.5: The parabolic rate constants of three Mo–silicides formed by various experimental conditions at 1273K

Diffusion couples	Process	Temperature range (°C)	Parabolic growth rate constant (cm ² /s)		
			MoSi ₂ (<i>k</i> ' ₃)	Mo ₅ Si ₃ (<i>k</i> ' ₂)	Mo ₃ Si (<i>k</i> ' ₁)
Si/Mo	Dipping of Mo into In–Si melts	1000–1200	2.90 × 10 ⁻¹⁰	5.69 × 10 ⁻¹⁴	– ^b
	Pack siliconizing	855–1100	5.50 × 10 ⁻¹⁰	– ^b	–
	CVD of Si on Mo from SiHCl ₃ –H ₂	1200–1700	3.90 × 10 ^{-10a}	–	–
	Diffusion annealing	900–1350	1.81 × 10 ⁻¹⁰	4.63 × 10 ⁻¹⁴	–
MoSi ₂ /Mo	Diffusion annealing	1200–1700	– ^b	9.18 × 10 ^{-13a}	–
		1000–1400	–	1.76 × 10 ⁻¹²	–
		1360–1600	–	1.25 × 10 ^{-11a}	–
Mo ₅ Si ₃ /Mo	Diffusion annealing	1500–1715	–	–	1.40 × 10 ^{-14a}

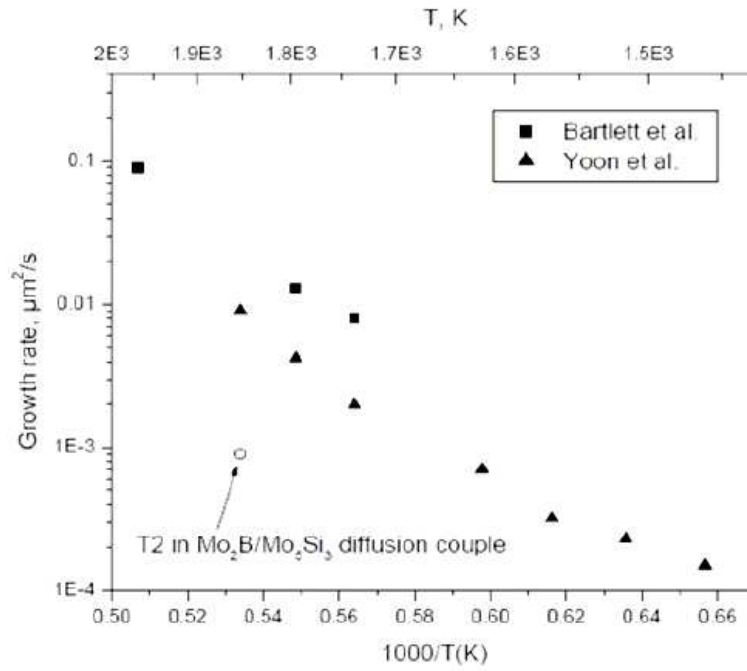
^a Signifies a value calculated from a reported temperature dependence.

^b Signifies the absence of corresponding Mo–silicide phase.



(a)

Fig. 2.15 (a): Arrhenius plot of parabolic growth rate as a function of the reciprocal temperature for Mo₅Si₃



(b)

Fig. 2.15 (b): Arrhenius plot of parabolic growth rate as a function of the reciprocal temperature for Mo_3Si

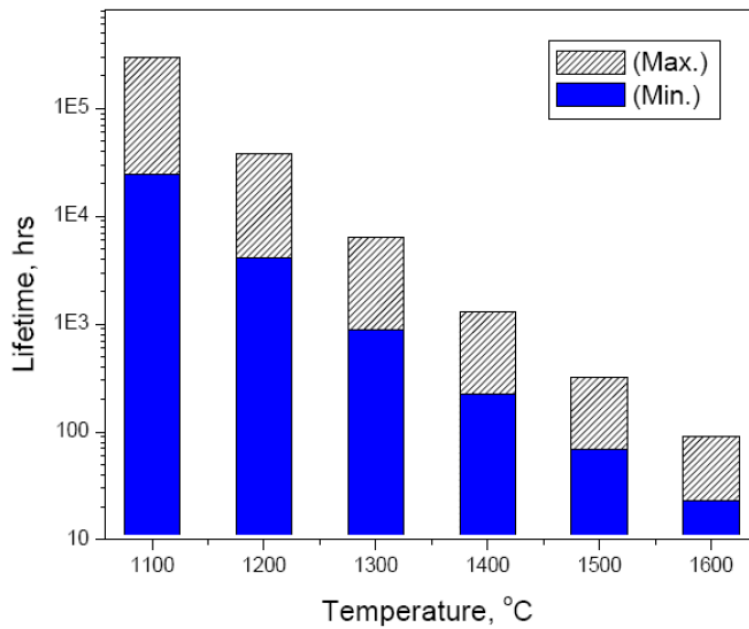


Fig. 2.16: Estimated lifetime of MoSi_2 based coatings on three phases ($\text{Mo}_{ss} + \text{Mo}_3\text{Si} + \text{T}_2$) alloy.

Another basic problem with MoSi₂ based coatings arises from the difference between the thermal expansion coefficients of MoSi₂ and molybdenum. During deposition at temperatures in the range 1273 – 1323K, the coating and substrate are unstressed. However, the difference between the thermal expansion coefficient for MoSi₂ ($8.56 \times 10^{-6} \text{ K}^{-1}$) [122] and that for molybdenum ($5.6 \times 10^{-6} \text{ K}^{-1}$) [122] (as measured from 0 to 1473K) creates tensile stresses in the coating on cooling because the MoSi₂ contracts more than the molybdenum substrate. The stresses are normally large enough to fracture the coating because MoSi₂ has a negligible ductility below 1073K [123, 124]. Although the cracks may heal on reheating to or above the application temperature, they will not reseal in the temperature range 923 – 1273K. Thus, a coating is needed that either has a lower application temperature or forms oxides that will seal the cracks on reheating.

Many cracks within the oxide scale may also be induced by the large volume expansion inherent to oxidation of MoSi₂ coating. Another mechanism of crack formation is the thermal stress from a CTE mismatch between the oxide scale and the MoSi₂ coating during cooling. It is also seen that many defects such as pores and cracks in the oxide scale were formed in the isothermal oxidation temperature.

In order to overcome these problems, the new coating design strategy needs to be considered to minimize interdiffusion reactions or maximize the high temperature stability of the coating, minimize mismatch in CTE of coating layer to the substrate and oxide layer etc. These can be achieved by suitably alloying the coating. One attractive feature of MoSi₂ is that it can be metallurgically alloyed with other silicides to improve its properties. Tungsten disilicide (WSi₂), which is also tetragonal C11b, forms a complete solid solution with MoSi₂ at all compositions. The addition of refractory alloying elements such as W can slow down the growth rate of (Mo,W)₅Si₃ [121, 125]. The recent Kanthal Super 1900 heating elements can operate at an element temperature of 2173K in the air and oxidizing environments. These Super 1900 elements are actually a solid solution alloy of MoSi₂ and WSi₂. The material used is a homogenous material with the chemical formula Mo_xW_ySi₂. In the chemical formula, the molybdenum and tungsten are isomorphous and can thus replace one another in the same structure. The material does not consist of a mixture of the materials MoSi₂ and WSi₂.

Suitable alloying additions also have to be searched to increase the spallation resistance, self healing properties and adhesion of oxide layer formed by mostly decreasing the viscosity of the SiO₂ oxide layer.

2.3 Summary

Beyond 1400K, the refractory metal alloys are the only candidate materials for structural purposes. Refractory metal alloys are of significant interest for ultra high temperature applications, because of its high melting point, high temperature tensile strength, superior creep properties and above all, excellent corrosion compatibility with alkali liquid metals.

The choice for selection of refractory metals and alloys should be based on the operating environment especially with respect to partial pressure of O₂. Taking into the design consideration of density, among the refractory metals, Nb followed by Mo are suitable candidates for structural applications. The volatility of MoO₃ represents a significant degradation mechanism, but it is not as insidious as the oxygen embrittlement problem of Nb based alloys at low partial pressure of oxygen. In vacuum molybdenum has a virtually unlimited life at high temperature. In outer space, for example, the oxidation rate of molybdenum is insignificant.

Molybdenum is the most readily available, least expensive and highest consumption annually among refractory metals.

Alternate synthesis route should be explored for synthesizing Mo based alloys, owing to the limitation of high temperature processing facilities, inherent problems such as high vapour pressure of Mo, high melting point, density difference between alloying elements etc.

Due to high melting point of Mo–30W, powder metallurgical route is the most effective synthesis route. However, very few technical literatures are available related to Mo–30W alloy with respect to its synthesis via powder processing route. It is necessary to understand each unit steps of powder metallurgical route for synthesis of the alloy such as powder preparation, mechanical alloying, compaction, sintering etc.

Mo–30W alloy cannot be used in oxygen containing atmosphere because of its poor oxidation resistance at high temperature. Its oxidation behaviour is only slightly better than Mo. For utilizing its real high temperature properties effectively, it has to be prevented from high temperature oxidation by a suitable coating.

Alternate boron free composite alloys such as Mo–Cr–Si need to be studied, emulating the concept of oxidation resistant Mo–Si–B alloy.

New coating design strategy needs to be considered to minimize interdiffusion reactions or maximize the high temperature stability of the coating, minimize mismatch in CTE of coating layer to substrate and oxide layer etc.

References

1. S. Majumdar. Processing of molybdenum and TZM alloy for advanced nuclear reactor systems, PhD Thesis. 2009, IIT , Mumbai, India.
2. Y. Kubota, S. Masuzaki, T. Morisaki, K. Tokunaga, and N. Noda. Design and thermal performance of an improved mechanically attached module for divertor plate of LHD, *Fusion Engineering and Design* 75–79 (2005) 297–301.
3. D. G. Cefruga, E. Menapace, G. Cambi, S. Ciattaglia, L. Petrizzi, G. Cavallone, M. Costa, and U. Broccoli. Activation of TZM and stainless steel divertor materials in the NET fusion machine. *Journal of Nuclear Materials* 212–215 (1994) 644–648.
4. S. A. Beske, Y. Arikawa, R. N. Andrews, and W. Lundbald. Chemical compatibility studies of GaAs and CdZnTe with the alloys WC–103 and TZM. *Journal of Crystal Growth* 137 (1994) 102–106.
5. M. S. El-Genk, and J. M. Tournier, “A review of refractory metal alloys and mechanically alloyed-oxide dispersion strengthened steels for space nuclear power systems”, *Journal of Nuclear Materials* 340 (2005) 93–112.
6. http://bama.ua.edu/~mweaver/courses/MTE585/Refractory%20Metals_2012.pdf
7. Flow studies for recycling metal commodities in the United States. Edited by Scott F. Sibley, 2004 “Mo recycling in the United States, by John W Blossom”, pp. L1–9
8. http://www.portal.gsi.gov.in/gsiDoc/pub/DID_Mo_WM.pdf
9. C. Gandhi and M.F. Asby. Overview no. 5: Fracture–mechanism maps for materials which cleave: FCC, BCC and HCP metals and ceramics. *Acta metallurgica* 27 (1979) 1565–1602.
10. Standard Specification for Molybdenum and Molybdenum Alloy Plate, Sheet, Strip, and Foil, ASTM B386–95, American Society for Testing and Materials, Philadelphia, PA, 1997.
11. P. Villars, A. Prince, and H. Okamoto. Handbook of ternary alloy phase diagram 10 (1995) 12670.
12. S. Majumdar, S. Raveendra, I. Samajdar, P. Bhargava, I.G. Sharma. Densification and grain growth during isothermal sintering of Mo and mechanically alloyed Mo–TZM. *Acta Materialia*, 57 (2009) 4158–4168.

13. D. R. Ervin, D. L. Bourell, C. Persad, and L. Rabenberg. Structure and properties of high energy, high rate consolidated molybdenum alloy TZM. *Materials Science and Engineering A102* (1988) 25–30.
14. I.G. Sharma, S.P. Chakraborty, and A.K. Suri. Preparation of TZM alloy by aluminothermic smelting and its characterization. *Journal of Alloys and Compounds* 393 (2005) 122–128.
15. B.V. Cockeram, R.W. Smith, and L.L. Snead. The influence of fast neutron irradiation and irradiation temperature on the tensile properties of wrought LCAC and TZM molybdenum. *Journal of Nuclear Materials* 346 (2005) 145–164.
16. B. V. Cockeram. The fracture toughness and toughening mechanisms of wrought low carbon arc cast, oxide dispersion strengthened, and molybdenum–0.5 pct titanium–0.1 pct zirconium molybdenum plate stock. *Metallurgical and Materials Transactions A* 36 (2005) 1777–1791.
17. B.V. Cockeram. The mechanical properties and fracture mechanisms of wrought low carbon arc cast (LCAC), molybdenum–0.5pct titanium–0.1pct zirconium (TZM), and oxide dispersion strengthened (ODS) molybdenum flat products. *Materials Science and Engineering A* 418 (2006) 120–136.
18. G.R. Smolik, D.A. Petti, and S.T. Schuetz. Oxidation and volatilization of TZM alloy in air. *Journal of Nuclear Materials* 283–287 (2000) 1458–1462.
19. T. Noda, M. Okada, and R. Watanabe. Effects of exposure to high–temperature helium containing oxygen on the mechanical properties of molybdenum and TZM–Mo alloy at room temperature. *Journal of Nuclear Materials* 91 (1980) 103–116.
20. T. Noda, M. Okada, and R. Watanabe. AES analysis of embrittled molybdenum and TZM–Mo alloy in an oxidizing atmosphere. *Journal of Nuclear Materials* 101 (1981) 354–358.
21. A.P. Alur, and K.S. Kumar. Monotonic and cyclic crack growth response of a Mo–Si–B alloy. *Acta Materialia* 54 (2006) 385–400.
22. J. J. Park, D. P. Butt, and C. A. Beard. Review of liquid metal corrosion issues for potential containment materials for liquid lead and lead–bismuth eutectic spallation targets as a neutron source. *Nuclear Engineering and Design* 196 (2000) 315–325.
23. J. V. Cathcart, and W. D. Manly. The mass transfer properties of various metals and alloys in liquid lead. *Corrosion* 12 (1956) 43–47.

24. T. Suzuki, and I. Mutoh. Corrosion of a Type 304 stainless steel and a molybdenum–base TZM alloy in refluxing mercury with a small amount of potassium. *Journal of Nuclear Materials* 184 (1991) 81–87.
25. <http://resource.npl.co.uk/mtdata/phdiagrams/mow.htm>
26. H. L. Brown, C. P. Kempter. Elastic properties of thoriated W–Mo and W–Mo–Re alloys. *J. less–comm. met.* 12 (1967) 166–168.
27. D.B. Lee, G. Simkovich. Oxidation of molybdenum–tungsten–chromium–silicon alloys. *Oxid. Met.* 31 (1989) 265–274.
28. V. T. Ababkov, N. N. Morgunova, B. D. Belyasov, V. N. Goldovskii. Alloys of the Mo–W System, *Metal Science and Heat Treatment.* 17(1975)907–910.
29. Refractory metals and their industrial applications: a symposium, Issue 849, edited by R. E. Smallwood, ASTM International, 1984 – Technology & Engineering, p.p. 14–17.
30. S. Majumdar G.B. Kale, I.G. Sharma. A study on preparation of Mo–30W alloy by aluminothermic co–reduction of mixed oxides. *J Alloys and Comp* 394(2005)168–175.
31. R.B. Ellis. Dispersion strengthening of metals. *American Scientist* 52(1964) 476–487.
32. J. R. Groza and J. C. Gibeling. Principles of particle selection for dispersion–strengthened copper, *Material Science and Engineering, A* 71(1993) 115–125.
33. Z. Li, L.M. Peng. Ultra–high temperature Mo–Si–B alloys Synthesis, microstructural and mechanical characterization. *Materials Letters* 62 (2008) 2229–2232.
34. S.C. Tjong, K.F. Tam, S.Q. Wu. Thermal cycling characteristics of in–situ Al–based composites prepared by reactive hot pressing. *Composites Science and Technology* 63 (2003) 89–97.
35. M. R. Farhang , A. R. Kamali, M. N.Samani. Effects of mechanical alloying on the characteristics of a nanocrystalline Ti–50 at.%Al during hot pressing consolidation. *Materials Science and Engineering: B* 168 (2010)136–141
36. R. Mitra, A.K. Srivastava, N. Eswara Prasad, S. Kumari. Microstructure and mechanical behaviour of reaction hot pressed multiphase Mo–Si–B and Mo–Si–B–Al intermetallic alloys. *Intermetallics* 14 (2006) 1461–1471
37. L.M. Peng J.H. Wang , H. Li, M. Gong. Processing and mechanical properties of multiphase composites based on Mo–Si–Al–C system. *Journal of Alloys and Compounds* 420 (2006) 77–82.

38. H. Saage, K. Kruger, D. Sturm, M. Heilmaier, J. H. Schneibel, E. George, L. Heatherly, C. Somsen, G. Eggeler, Y. Yang. Ductilization of Mo–Si solid solutions manufactured by powder metallurgy. *Acta Mater* 57 (2009) 3895–3901.
39. D. M. Shah. MoSi₂ and other silicides as high temperature structural materials. Edited by S.D. Antolovich, R.W. Stusrud, R.A. MacKay, D.L. Anton, T. Khan, R.D. Kissinger,
40. R. Mitra, Rohit Khanna, V.V. Rama Rao. Microstructure, mechanical properties and oxidation behavior of a multiphase (Mo,Cr)(Si,Al)₂ intermetallic alloy–SiC composite processed by reaction hot pressing. *Materials Science and Engineering A* 382 (2004) 150–161.
41. R. Gibala, A. K. Ghosh, D. 13. Van Aken, D. J. Srolovitz, A. Basu, H. Chang, D. P. Mason and W. Yang. Mechanical behavior and interface design of MoSi₂–based alloys and composites. *Materials Science and Engineering, A* 155 (1992) 147–158.
42. V. Nagarajan, I.G.Wright. Reservoir phase approach. US Patent No.4,762,557; 1988.
43. M. Akinc, M.K. Meyer, M.J. Kramer, A.J. Thom, J.J. Huebsch, and B. Cook. Boron–doped molybdenum silicides for structural applications. *Mater. Sci. Eng. A*, A261 (1999) 16–23.
44. M. K. Meyer, M. J. Kramer, M. Akinca. Compressive Creep Behavior of Mo₅Si₃ with the Addition of Boron. *Intermetallics*, 4 (1996) 273–281.
45. D. M. Berczik: U.S. Patent No. 5,595,616, United Technologies Corp., East Hartford, CT, 1997.
46. D.M. Berczik: U.S. Patent No. 5,693,156, United Technologies Corp., East Hartford, CT, 1997.
47. J.H. Schneibel, R.O. Ritchie, J.J. Kruzic, and P.F. Tortorelli. Optimizaton of Mo–Si–B Intermetallic Alloys. *Metallurgical And Materials Transactions A* 36 (2005) 525–531.
48. H, Choe, J. H. Schneibel, and R. O. Ritchie. On the fracture and fatigue properties of Mo–Mo₃Si–Mo₅SiB₂ refractory intermetallic alloys at ambient to elevated temperatures (25 °C to 1300 °C). *Metall. Trans. A*, 34 (2003) 225–239.
49. V. Supatarawanich , D. R. Johnson, C.T. Liu. Effects of microstructure on the oxidation behavior of multiphase Mo–Si–B alloys. *Mater. Sci. Engg. A*, 344 (2003) 328–339.
50. T. A. Parthasarathy, M. G. Mendiratta, D. M. Dimiduk. Oxidation mechanisms in Mo–Reinforced Mo₅SiB(T₂)–Mo₃Si alloys. *Acta Mater.* 50 (2002) 1857–1868.

51. J. H. Schneibel, C. T. Liu, L. Heatherly L, M. J. Kramer. Assessment of Processing Routes and Strength of a 3-Phase Molybdenum Boron Silicide ($\text{Mo}_5\text{Si}_3\text{-Mo}_5\text{SiB}_2\text{-Mo}_3\text{Si}$). *Scr. Mater.*, 38 (1998) 1169–1176.
52. Y. Yang, H. Bei, S. Chen, E. P. George, J. Tiley, Y. A. Chang. Effects of Ti, Zr, and Hf on the phase stability of $\text{Mo}_5\text{Si}_3\text{-Mo}_5\text{SiB}_2$ alloys at 1600°C. *Acta Mater.*, 58 (2010) 541–548.
53. Y. Yang, Y. A. Chang, L. Tan, W. Cao. Multiphase equilibria in the metal-rich region of the Mo–Ti–Si–B system: thermodynamic prediction and experimental validation. *Acta Mater.*, 53 (2005) 1711–1172.
54. S. Burk, B. Gorr, H. J. Christ. High temperature oxidation of Mo–Si–B alloys: effect of low and very low oxygen partial pressures. *Acta Mater.*, 58 (2010) 6154–6165.
55. H. Choe, J. H. Schneibel, R. O. Ritchie. On the fracture and fatigue properties of Mo– Mo_3Si – Mo_5SiB_2 refractory intermetallic alloys at ambient to elevated temperatures (25°C to 1300 °C). *Metallurgical and Materials Transactions A Volume 34* (2003) 225–239.
56. J. A. Lemberg and R. O. Ritchie. Mo–Si–B Alloys for Ultrahigh-Temperature Structural Applications. *Advanced Materials*, 24 (2012) 3445–3480.
57. P. Jain, K.S. Kumar. Tensile creep of Mo–Si–B alloys. *Acta Materialia* 58 (2010) 2124–2142.
58. R. Mitra, A.K. Srivastava, N. Eswara Prasad, S. Kumari. Microstructure and mechanical behaviour of reaction hot pressed multiphase Mo–Si–B and Mo–Si–B–Al intermetallic alloys. *Intermetallics* 14 (2006) 1461–1471.
59. D.B. Lee and G. Simkovich. Oxidation of Molybdenum–Chromium–Palladium Alloys *Oxidation of Metals*, 34 (1990) 13–22.
60. P.R. Subramanian, M.G. Mendiratta, and D.M. Dimiduk: Patent 623 US 5 683 524, 1997.
61. A. S. Khanna, and A. K. Pattanaik. Recent trends in coatings for high temperature applications. *Trans Metal Finishers' Association of India* 3, 1997, 187–205.
62. D. Chatterji, R. C. Devries and G. Romeo. Protection of superalloys for turbine application, in *Advances in corrosion science and technology* (eds) M G Fontana and R W Staehle (New York: Plenum Press) Vol. 6, 1976, 1–87.
63. K. K. Biswas, S Datta, S. K. Das, M. C. Ghose, A. Mazumdar and N. Roy. High temperature resistance coatings for gas turbine. *Trans. Ind. Ceram. Soc.* 1986, 4543–55.

64. S. Datta. Handbook of ceramics (ed.) S Kumar (Calcutta: Kumar & Associates) Vol. II, 1995, 289–299.
65. S. Datta. High temperature resistant coatings for aeronautical application. Bull. Mater. Sci. 21 (1998) 421–434.
66. J.E. Mahan. Physical Vapor Deposition of Thin Films. New York: John Wiley & Sons, 2000. ISBN 0471330019.
67. H.K. Pulker (Ed.), Verschleiss-Schutzschichten unter Anwendung der CVD/PVD Verfahren, Expert, Sindelfingen, Germany (1985).
68. B. Blushan, B.K. Gupta. Hard coatings; Handbook of Tribology, McGraw Hill, New York (1991), 14.1–14.148.
69. B. Navinšek. Improvement of cutting tools with TiN PVD hard coatings. Mater. Manuf. Processes (USA), 7 (1992) 363–382
70. I. Milosev, B. Navinsek. A corrosion study of TiN (Physically vapour deposition) hard coatings deposited on various substrates Surf. Coat.Technol. 63 (1994) 173–180.
71. A.S .Khanna, A. Gasser, K. Wissenbach, Ming Li, V.H.Desai and W.J. Quadackers. Journal of Material Science 30 (1995) 4684–4694.
72. H. Chen, Y. Gang, C. Wenbin, L. Kaijun, L. Feng. Simulation of the organic thin film thickness distribution for multi–source thermal evaporation process. Vacuum, 85 (2010) 448–451.
73. S. Vincent. Trends in sputtering. Progress in Surface Science, 64 (2000) 1–58.
74. B. Lux, C. Colomblor, H. Altena, K. Stjernberg. Preparatlon of alumina coatings by chemical vapour deposition Thin Solid Films 138 (1986) 49–64.
75. M. Halvarsson, S. Vuorinen. Microstructure and performance of CVD x–Al₂O₃ multi layers. Mater Sci Eng A 209 (1996) 337–44.
76. C. Duret and R.Pichoir. Coatings for high temeparture applications. E.Lang (editor), applied sci. publ. 1983, 33–40.
77. C.W. Draper, C.A. Ewlng. Review Laser surface alloying: a bibliography, J. Mater. Sc. 19 (1984) 3815–22.
78. A.S. Khanna,W.J.Quadackers, H Schuster, A.Gasser, K.Wissenbach and E.W.Kreutz. Structure and Reactivity of Surface. C. Morterra, A. Zecchina and G. Costa, (eds) Elsevier, publ., (1989) 535–545.

79. Z. Qiao Yan, X. Xiong , P. Xiao, F. Chen, H. B. Zhang, B.Y. Huang. Si–Mo–SiO₂ oxidation protective coatings prepared by slurry painting for C/C–SiC composites. *Surface & Coatings Technology* 202, 2008, 4734–4740.
80. A. Juul Rasmussen, A. Agüero, M. Gutierrez, M. Jose, L. Qstergard. Microstructures of thin and thick slurry aluminide coatings on Inconel 690. *Surface Coating & Technology* 202 (2008) 1479–1485.
81. S. R. Levine, and R. M. Caves. Thermodynamics and kinetics of pack aluminide coating formation on IN – 100. *Journal of Electrochemical Society* 121 (1974) 1051–1064.
82. R. Bianco, M. A. Harper and R.A. Rapp. Ceria–Based High–Temperature Coatings for Oxidation Prevention. *JOM*, 43 (1991) 20–25.
83. I. R. Pichoir. High Temperature Alloys for Gas Turbines, D. Coutouradis et al., eds. (Appl. Sci. Pub., London, 1978), 191–195.
84. C. Rosado, M. Schütze. Development of Coatings for Environments with high sulphur. *Mater. Corros.* 54 (2003) 831–839.
85. A.B. Smith, A. Kempster, J. Smith. Vapour aluminide coating of internal cooling channels, in turbine blades and vanes. 120–121 (1999) 112–117.
86. Shankar, A.L.E. Terrance, S. Venkadesan. The effect of diffusion barrier formation on the kinetics of aluminizing in Inconel–718. *Mater. Sci.* 29 (1994) 5424–5430.
87. W.F. Gale, J.E. King. Microstructural development in aluminide diffusion coatings on nickel– base superalloy single crystals. *Surf. Coat. Technol.* 54–55 (1992), 8–12.
88. B.M. Warnes, D.C. Punola. Clean diffusion coating by CVD. *Surf. Coat. Technol.* 4–95 (1997) 1–11.
89. D.S. Rickerby, M.R. WInstone. Coatings for gas turbines. *Mater. Manuf. Process.* 7 (1992) 495–502.
90. E. Glenney, and J. E. Restall. Evaluation of the properties of protected molybdenum and 0.45% titanium–molybdenum alloy. *Journal of the Less–Common Metals* 9 (1965) 367–387.
91. M. G. Mendiratta, T. A. Parthasarathy, and D. M. Dimiduk. Oxidation behavior of α Mo–Mo₃Si–Mo₅SiB₂ (T2) three phase system. *Intermetallics* 10 (2002) 225–232.
92. G. L. Miller, and F. G Cox. Development of oxidation resistance of some refractory metals. *Journal of the Less–Common Metals* 2 (1960) 207–222.

93. O. Kyrylov, R. Cremer, and D. Neuschütz. Deposition of alumina hard coatings by bipolar pulsed PECVD. *Surface and Coatings Technology* 163 (2003) 203–207.
94. Z. D. Xiang, and P. K. Datta. Relationship between pack chemistry and aluminide coating formation for low temperature aluminisation of alloy steels. *Acta Materialia* 54 (2006) 4453–4463.
95. S. Majumdar, I. G. Sharma, I. Samajdar, P.J. Bhargava. Relationship between pack chemistry and growth of silicide coatings on Mo–TZM alloy. *Journal of Electrochemical Society*. 155 (2008) 734–740.
96. A. Mueller, G. Wang, R. A. Rapp, E. L. Courtright, and T. A. Kircher. Oxidation behavior of tungsten and germanium–alloyed molybdenum disilicide coatings. *Materials Science and Engineering A* 155 (1992) 199–207.
97. Z. D. Xiang, S. R. Rose, and P. K. Datta. Vapor phase codeposition of Al and Si to form diffusion coatings on γ -TiAl. *Materials Science and Engineering A* 356 (2003) 181–189.
98. Z. D. Xiang, S. R. Rose, and P. K. Datta. Codeposition of Al and Si to form oxidation–resistant coatings on γ -TiAl by pack cementation process. *Material Chemistry and Physics* 80 (2003) 482–489.
99. S. Majumdar, P. Sengupta, G.B. Kale, and I.G. Sharma. Development of multi layer oxidation resistance coating on Niobium and Tantalum. *Surface and Coatings Technology* 200 (2006) 3713–3718.
100. S. Majumdar, I.G. Sharma, S. Raveendra, I. Samajdar, P. Bhargava. In situ chemical vapour co–deposition of Al and Si to form diffusion coatings on TZM. *Materials Science and Engineering: A*, 492 (2008) 211–217.
101. S. Majumdar, I.G. Sharma, A.K. Suri. Development of oxidation resistant coatings on Mo-30W alloy. *International Journal of Refractory Metals and Hard Materials* 26 (2008) 549–554
102. R. Sakidja, J. S. Park, J. Hamann, and J. H. Perepezko. Synthesis of oxidation resistant silicide coatings on Mo–Si–B alloys. *Scripta Materialia* 53 (2005) 723–728
103. R. Sakidja, F. Rioult, J. Werner, J.H. Perepezko. Aluminum pack cementation of Mo–Si–B alloys. *Scr Mater* 55 (2006) 903–906.

104. Z. Tang, A. J. Thom, M.J. Kramer, M. Akinc. Characterization and oxidation behavior of silicide coating on multiphase Mo–Si–B alloy. *Intermetallics*, 16 (2008) 1125–1133
105. R. Sakidja, J.H. Perepezko. Coating designs for oxidation control of Mo–Si–B alloys *Scripta Materialia*, 46 (2002)765–770
106. A. B Gokhale, G. J Abbaschian. The Mo–Si (Molybdenum–Silicon) system. *Journal of Phase Equilibria* 12(1991)493–498
107. E. A. Brandes and G. B. Brook, *Smithells Metals Reference Book*, 7th Ed., 1992, p. 11–376.
108. W. J. Boettinger, J. H. Perepezko, and P. S. Frankwicz. Application of Ternary Diagrams to the Development of MoSi₂–Based Materials. *Materials Science and Engineering*, A155 (1992) 33–44.
109. K. S. Kumar and C. T. Liu. Ordered Intermetallic Alloys, Part II: Silicides, Tri–aluminides, and Others, *JOM*, 45 (1993) 28–34.
110. T. C. Chou and T. G. Nieh. Pesting of the High–Temperature Intermetallic MoSi₂, *JOM*, 1993, 15–22.
111. B. V. Cockeram, G. Wang and R. A. Rapp. Growth kinetics and pesting resistance of MoSi₂ and germanium–doped MoSi₂ diffusion coatings grown by the pack cementation method. *Materials and Corrosion* 46 (1995) 207–217.
112. C. G. McKamey, P. F. Tortorelli, J. H. DeVan, and C. A. Carmichael. A study of pest oxidation in polycrystalline MoSi₂. *J. Mater. Res.*, 7 (1992) 2747–2755
113. T. C. Choua. Kinetics of MoSi₂ pest during low–temperature oxidation. *J. Mater. Res.*, 8 (1993) 1605–1610.
114. K. Yanagihara, K Przybylski, T Maruyama. The role of microstructure on pesting during oxidation of MoSi₂ and Mo(Si,Al)₂ at 773 K. *Oxidation of Metals* 47 (1997) 277–293.
115. J. K. Yoon, J.K. Lee, K.H. Lee, J.Y. Byun, G.H. Kim, K. Thong. Microstructure growth kinetics of the Mo₅Si₃ and Mo₃Si layers in MoSi₂/Mo diffusion couple. *Intermetallics* 11 (2003) 687.
116. J.K. Yoon, G.H. Kim, J.Y. Byun, J.SKim, C.S. Choi. Simultaneous growth mechanism of intermediate silicides in MoSi₂/Mo system. *Surface and Coatings Technology* 118 (2001) 129.

117. A.N. Christensen. Preparation and characterization of molybdenum silicides (Mo_3Si and Mo_5Si_3). *Acta Chemica Scandinavica, Series A: Physical and Inorganic Chemistry* A37 (1983) 519.
118. P.C. Tortorici, M.A. Dayananda. Growth of silicides and interdiffusion in the Mo–Si system. *Metall. Mater. Trans A*, 30 (1999) 545–550.
119. H.L. Zhao, M.J. Kramer, M. Akinc. Thermal expansion behavior of intermetallic compounds in the Mo–Si–B system. *Intermetallics* 12 (2004) 493
120. F. Chu, D.J. Thoma, K.J. McClellan, P. Peralta, Mo_5Si_3 single crystals: physical properties and mechanical behavior. *Materials Science & Engineering, A: Structural, Materials: Properties, Microstructure and Processing* A261 (1999) 44.
121. Z. Tang. M_5Si_3 (M=Ti, Nb, Mo) based transition–metal silicides for high temperature applications. PhD Thesis, 2007. Iowa State University, Ames, Iowa
122. J.F. Shackelford and W. Alexander. *Thermal Properties of Materials. Materials Science and Engineering. Handbook* Ed. Boca Raton: CRC Press LLC, 2001.
123. T.A. Kircher, E.L. Courtright. Engineering limitation of MoSi_2 coating. *Materials Science & Engineering, A: Structural Materials: Properties, Microstructure and Processing* 155 (1992) 67.
124. P.I. Glushko, V.I. Zmii, N.A. Semenov, B.M. Shirokov. Stability and heat resistance of silicide coatings on refractory metals. Part 3. Stability of silicide coatings on niobium heated in air at 1500–1800 °C. *Powder Metallurgy and Metal Ceramics (Translation of Poroshkovaya Metallurgiya (Kiev))* 42 (2003) 154.
125. J. K. Yoon, J. Y. Byun, J. S. Kim and C. S. Choi, *Taehan Kumsok Hakhoechi.*, 36, 2143 (1998).

Chapter–3

Experimental Procedure

3. Experimental Procedure

3.1 Introduction

Two categories of Mo based alloys were studied in the present work. First category belongs to solid solution strengthened Mo–30W alloy, while the second category belongs to Mo–Cr–Si–Ti composite alloy. The different methods used for the preparation of alloys are – powder metallurgical route, silicothermic co–reduction and hot pressing. The products were characterized and compared for different key properties. Based on the results, the most suitable processing technique for respective alloys was identified. In this chapter, experimental details for the preparation of different Mo based alloys by different techniques, characterization techniques and performance evaluation tests are described.

3.2 Equipment and Instruments

The major equipments used in the present study can be broadly classified into two categories: (i) processing equipments and (ii) characterization instruments.

a) Processing equipments

- i) Planetary ball mill
- ii) Hydraulic press – for making green pellets
- i) Arc furnace
- ii) Vacuum hot press
- iii) Controlled atmosphere furnace

b) Characterization Instruments

- ii) XRD
- iii) SEM
- iv) XRF/EDS
- v) TG–DTA
- vi) Hardness tester
- vii) Flexural strength (UTM)
- viii) Dilatometer

Before describing the processing techniques in detail, small introduction and working principle of various *processing equipments* used in the course of the study is presented in a chronological order.

Planetary ball mill

The alloying process can be carried out using different apparatus, namely, attritor, planetary mill or a horizontal ball mill. However, the principles of these operations are same for all the techniques. Since the powders are cold welded and fractured during mechanical alloying, it is critical to establish a balance between the two processes in order to alloy successfully. Planetary ball mill is a most frequently used system. The ball mill system consists of one turn disc (turn table) and two or four bowls. The turn disc rotates in one direction while the bowls rotate in the opposite direction. The centrifugal forces, created by the rotation of the bowl around its own axis together with the rotation of the turn disc, are applied to the powder mixture and milling balls in the bowl. The powder mixture is fractured and cold welded under high energy impact [1].

The Fig. 3.1(a) below shows the motions of the balls and the powder. Since the rotation directions of the bowl and turn disc are opposite, the centrifugal forces are alternatively synchronized. The impact energy of the milling balls in the normal direction attains a value of up to 40 times higher than that due to gravitational acceleration. Hence, the planetary ball mill can be used for high-speed milling.

For all nanocrystalline materials prepared by high-energy ball milling synthesis route, surface and interface contamination is a major concern. In particular, mechanical contamination introduced by the milling media (Fe or WC) as well as the ambient gas (trace impurities such as O₂, N₂ in rare gases) can be problems for high-energy ball milling. However, using optimized milling speed and milling time may effectively reduce the level of contamination. Moreover, ductile materials can form a thin coating layer on the milling media that reduces contamination tremendously. Atmospheric contamination can be minimized or eliminated by sealing the vial with a flexible “O” ring after the powder has been loaded in an inert gas glove box. Small experimental ball mills can also be completely enclosed in an inert gas glove box. Besides the contamination, long processing time, no control on particle morphology, agglomerates, and residual strain in the crystallized phase are the other disadvantages of high-energy ball milling process.

Fig.3.1 (a) is a schematic diagram of showing process of milling and 3.1(b) the actual photograph of the equipment. Mixing is achieved by the high energy impact of balls; the energy levels of balls are as high as 12 times the gravitational acceleration. Rotation of base plate provides the centrifugal force to the grinding balls and independent rotation of bowls to

make the balls hit the inner wall of the bowls. Since the bowls are rotating in alternate (one forward cycle and one reverse cycle) directions a considerable part of grinding will take place in addition to homogenous mixing. Bowls inner walls are lined with WC and balls are made up of WC.

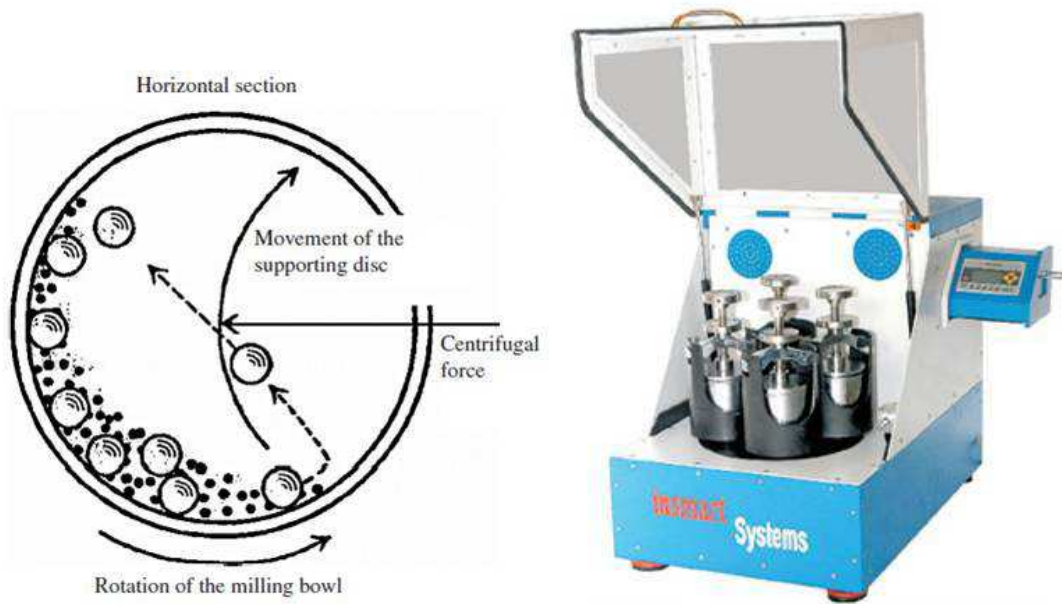


Fig. 3.1: (a) Schematic view of the motion of the ball and powder mixture (b) Actual photograph of the planetary ball mill used

Hydraulic press

Fig. 3.2 is the actual photograph hydraulic press used. This equipment is used to make the green compacts to increase the physical contact between the particles. This will enhance the solid state reaction among the reactants. In the press, a hydraulic power pack is provided to give desired pressure and directional control to the hydraulic cylinder. The powder is loaded in a die set and desired force is applied through the bottom plunger for a predetermined time. After releasing the force, the green pellet is ejected from the die. Die set and plungers are made up of WC.



Fig. 3.2 Hydraulic Press

Arc Furnace

An electric arc furnace (EAF) transfers electrical energy to thermal energy in the form of an electric arc to melt the charged materials. The arc is established between an electrode and the melting bath and is characterized by a low voltage and a high current. Arc furnaces differ from induction furnaces in that the charge material is directly exposed to an electric arc, and the current in the furnace terminals passes through the charged material.

William Siemens took out patents for an electric arc furnace in 1878 – 79 while the first electric arc furnaces were developed by Paul Héroult, with a commercial plant established in the United States in 1907 [2,3]. Direct arc electric furnaces are very popular for the melting of alloy in the range from a few kilograms, for laboratory units, to in excess of 100 tonnes per batch. Typically units found in foundries are in the range of 1 to 10 tonnes.

Arc furnace can be categorized into two categories– consumable and non–consumable. In the consumable arc furnace, the charge material which is to be melted itself acts as an electrode. Non–consumable arc furnace equipped with tungsten or graphite

electrode for melting the material. Non-consumable arc furnace having tungsten electrode has been used in the present study to prepare the alloys. The present arc melting furnace consists of a water-cooled stainless steel bell jar hinged to a fixed base plate. The electrode (stinger) shaft penetrates the top of the bell jar. The stinger is sealed at the top of the bell jar by means of a ball joint and stainless steel bellows. The hearth is water-cooled copper with interchangeable top surface. Various cavity configurations can be provided in the hearth top surface. Light and window ports facilitate inside observation. Clamps are provided for operation at a slight positive pressure. Provision is made for attachment to a vacuum pump for evacuation prior to backfilling with inert gas. Fig. 3.3 shows the schematic image of an arc melting furnace used.

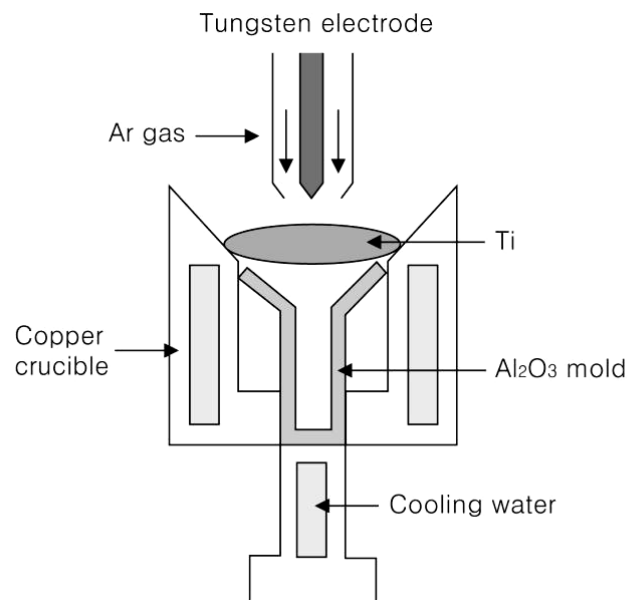


Fig. 3.3 Schematic of an arc melting furnace

Vacuum Hot press

Fig 3.4 (a) is a schematic diagram of a hot press and (b) the actual photograph along with vacuum system. Hot pressing is a high-pressure, low-strain-rate powder metallurgy process for forming a powder or powder compact at a temperature high enough to induce sintering and creep processes. This is achieved by the simultaneous application of heat and pressure. Hot pressing is mainly used to fabricate hard and brittle materials. One large use is in the consolidation of diamond-metal composite cutting tools and advanced ceramics. The

densification works through particle rearrangement and plastic flow at the particle contacts. The loose powder or the pre-compacted part is in most of the cases filled to a graphite mould that allows induction or resistance heating up to temperatures of about 2673 K under a pressure of up to 50 MPa.

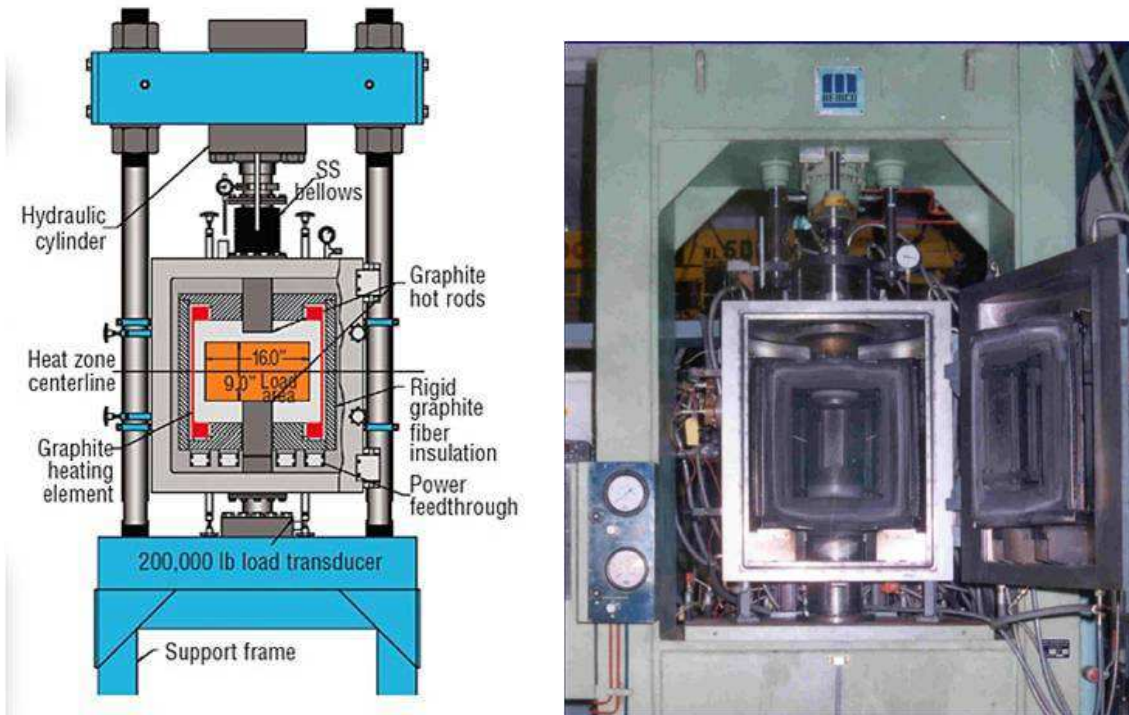


Fig. 3.4 (a) Schematic of hot press and (b) Actual photograph of the equipment

Controlled atmosphere furnace

Tubular furnaces were used to carry out sintering and coating experiments in controlled atmosphere. Fig. 3.5 is the schematic of the controlled atmosphere furnace. These furnaces are essentially a resistance furnace with silicon carbide and Mo-silicide heating elements, which are placed outside re-crystallized alumina tube. A maximum temperature of 1873K and 2073K could be obtained in silicon carbide and Mo-silicide heating element furnaces respectively. The furnace has a built-in PID temperature-controller, which enables accurate control of the rates of heating or cooling. The temperature is measured using Pt-6%Rh/Pt-30%Rh thermocouple. The furnace has gas inlet and outlet port. Argon was used to create an inert atmosphere while He+4% H_2 was used to create reducing atmosphere. There is a limitation of maximum heating rate of (5 K/min) for alumina tubular furnace. Therefore an Inconel tube furnace was used for experiments, in which fast heating and cooling was required. Nichrome wire is wound around the outside of the inconel work tube making it an integral part of the tube furnace.

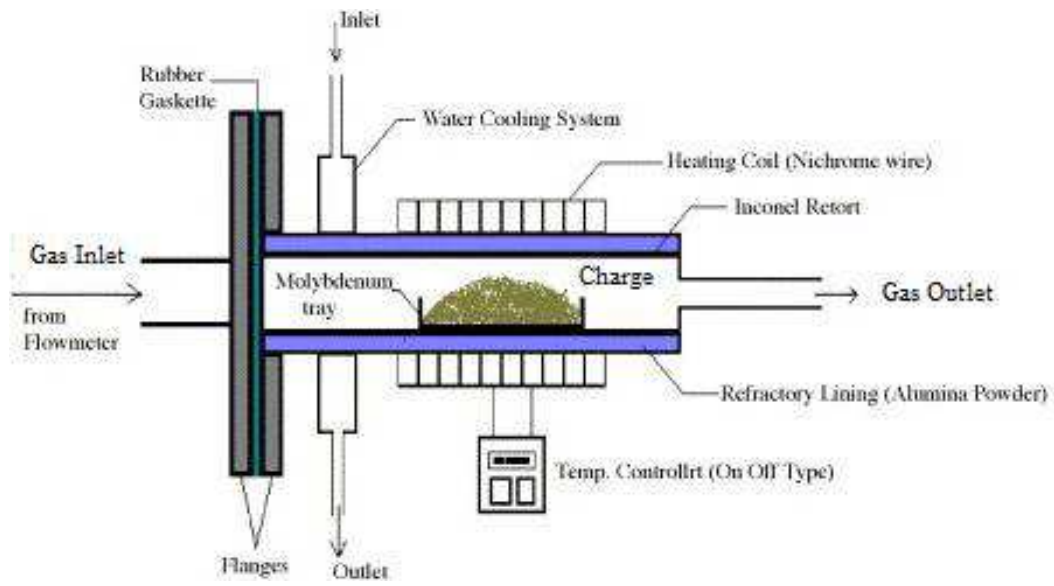


Fig. 3.5 Schematic of controlled atmosphere furnace

3.3 Preparation of solid solution strengthened Mo–30W alloy

3.3.1 Mechanical Alloying

Elemental powders of Mo and W with a purity of 99.9% and an average agglomerate size of 5 and 6 microns, respectively were mixed in the desired composition ratio of Mo–30 wt.% W and subjected to mechanical alloying in a high energy planetary ball mill for different durations from 5 h to a maximum of 25 h. The speed of the planetary ball mill was fixed to 300 rpm. The small amounts of samples were taken out at the interval of 5h for characterization.

3.3.2 Sintering studies

The mechanically alloyed and co-reduced powders were subsequently cold pressed into green compacts of 6 mm diameter and 5–6 mm length at a pressure of 300 MPa. Green densities of the samples were measured using the geometrical dimensions. The green density of the cold pressed specimens was around 65 % theoretical densities (TD). Sintering was done in furnace having MoSi₂ heating element in reducing atmosphere created by He–4%H₂ mixture gas. Green pellets were sintered at different temperatures range from 1673 to 2073 K (1673 to 2073K) (heating rate of 15 K/minute) for several hours (2 to 4 hours). After completion, the samples were cooled down to room temperature and then removed from the furnace for further characterization.

The green compacts were also subjected to dilatometry to measure the dynamic changes in sample length during sintering for different heating schedules. All dilatometric measurements were carried out in a vertical type thermo mechanical analyzer (TMA) [Setsys Evolution TMA 1600, M/s SETARAM, France] with a minimum load (1g) condition in reducing atmosphere (Ar–4% H₂, 20 ml/min). Shrinkage profiles were recorded by heating the green compacts at a heating rate of 20 K/min. up to the programmed temperature followed by cooling (30 K/min.) to ambient. One sample, already sintered up to 1573 K with an isothermal hold period of 1 h at the maximum temperature (under the same reducing conditions) was measured for its expansion behavior separately up to the same temperature with the same heating cycle in order to evaluate the linear thermal expansion behavior of this alloy. This expansion was subtracted from the as measured shrinkage data of green compacts to determine the net shrinkage.

A special sintering schedule was employed for recording the shrinkage behavior using stepwise isothermal dilatometry (SID) method. In this experiment, shrinkage was

continuously measured while heating the green pellet from 298 to 973 K at a heating rate of 20 K/min. and then onwards up to 1523 K with the same rate of heating and an isothermal hold of 30 minutes at each 50 K interval (step). The program was chosen in a manner so that shrinkage during the non-isothermal part can be minimized as far as possible. The densities of the sintered samples were measured both dimensionally as well as by Archimedes principle using water as the immersion liquid. Microstructures of samples sintered at different temperatures were studied using scanning electron microscopy.

3.4 Preparation of Mo–Cr–Si–Ti composite alloys

3.4.1 Hot pressing route

Elemental powder of Mo, Cr, Si and Ti having an average particle size of 5, 8, 6 and 4 microns, respectively, were mixed in the desired composition of Mo–16Cr–4Si–0.5Ti (wt.%), using a turbo–mixer (MXM 2, Insmart, India make) unit. The mixed powders were pressed uni–axially into compacts by applying a pressure of 200 MPa. The compacts were then pressed in a graphite die of 25 mm diameter at different temperatures from 1573K to 1923K under 10 MPa pressure for 0.5 h to 3 h in vacuum. The hot pressed pellets were grinded from all sides to remove the graphite (C) layer.

The cleaned pellets were weighed and density measured by using Archimedes’s principle in distilled water. (Balance model AT 261 Delta Ra; supplier: Mettler Toledo). Density was calculated by taking the ratio of weight in air to the volume of displaced water. Samples were then cut into different sizes using diamond wafer blades. Cut samples were hot mounted and polished with diamond slurry of 15, 1 and 0.25 μm to obtain mirror finish. Polished samples were used for characterization studies such as – phase identification, hardness measurement, microscopy etc.

3.4.2 Silicothermic co–reduction route

MoO₂ (purity >99.9%, mesh size #300), Cr₂O₃ (99.5% purity, mesh size # 200) and Si (99.5% purity, ~10 μm) were used as starting materials. The co–reduction campaign of MoO₂, Cr₂O₃ has been carried out in a specially designed two end open cylindrical shaped mild steel reactor with length 0.25 m and ID 0.1 m. The reactor was internally lined with dead burnt paste of magnesia powder, binder (Na₂SiO₃) and water. During lining, a slight tapering was provided at the bottom of the reactor to facilitate deposition of the molten alloy at the bottom. The lined reactor was then air dried for overnight and fired at 473K to make it completely moisture free. The charge composed of MoO₂, Cr₂O₃, flux CaO, heat booster and Si reductant as well as alloying addition in requisite amount, were thoroughly mixed in turbo mixer and poured into the reactor cavity. The reactant mixture was then rammed mildly to improve particle–to–particle contact. A small amount of trigger mixture (containing potassium chlorate and aluminum taken in the ratio of 2:1 by weight) was kept over the charge at the center.

The schematic of the experimental setup is shown in Fig. 3.6 [4]. The reaction was initiated by bringing a fresh pickled burning magnesium ribbon in contact with the trigger mixture. The reaction was quite vigorous, however well controlled. It was brought to

completion very rapidly. After adequate cooling the alloy button formed at the bottom of the charge was collected by breaking the top slag layer. The co-reduction process was also investigated by DTA/TG (setsys evolution 24, Setaram Instrumentation, France).

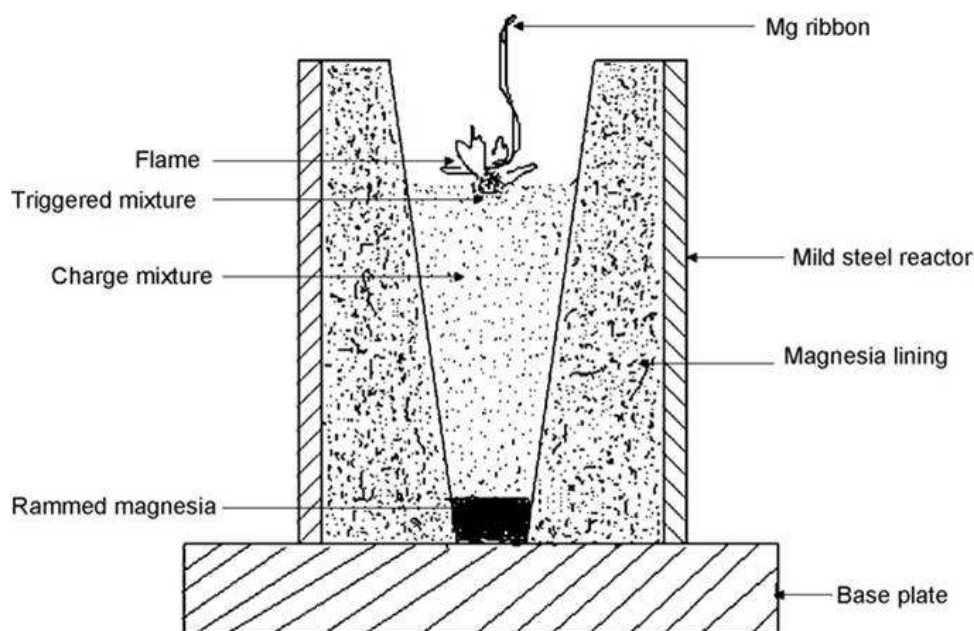


Fig. 3.6 Schematic of experimental set-up for conducting co-reduction experiments

As-reduced alloy samples which were obtained with reasonable good consolidation and separation from slag were further re-melted in an arc melting furnace under an argon atmosphere using non-consumable tungsten electrode in water cooled copper hearth. The re-melted samples were homogenized in inert (high pure Ar) atmosphere at 1873K for 10 hrs.

Thermal analyses of silicothermic reduction of individual oxides (Mo and Cr oxide) were carried out in TG-DTA. The charges were taken in powder as well as pellet form. Thermal analysis studies were carried out at different heating rates to estimate the activation energy.

3.5 Pack cementation coating process

Small specimens of dimensions 5 mm × 3 mm × 2 mm were cut from the synthesized alloy. The specimens were polished and cleaned before conducting coating experiments. The cleaned samples were weighed and subsequently placed in the pack. The pack powder mixtures were prepared by weighing out and mixing appropriate amounts of powders of Si, Al₂O₃ and NH₄F (as activator). The pack comprising of 20Si–2.5NH₄F–77.5Al₂O₃ (wt.%) was used for this study. The packs were prepared by filling the pack powders around the substrates in a cylindrical alumina crucible of 36 mm diameter and 48 mm length. The crucible was then sealed with an alumina lid using high temperature cement. The cement sealing was dried for 24 hrs at room temperature followed by controlled heating inside a tubular furnace under argon flow. The schematic of the experimental setup is shown in Fig. 3.7. Initial curing treatment was given at 423K for 2 hrs followed by heating at 523K for 2 hrs to facilitate further curing of the cement and to remove any moisture from the pack. Subsequently the temperature of the furnace was raised to set temperature (1073K to 1573K) at a heating of 4K min⁻¹ and held for different durations. The furnace was then cooled to room temperature at a slow rate. The coated samples were washed in water jet to remove any residual powder from the surface. Weight gain and thickness measurements of the coated specimens were conducted. The coated samples were cut normal to the coating surface and metallographically polished to 1μm diamond finish. The as-coated surfaces and the cross sections were examined for their morphology, thickness, microstructure and composition using SEM and EDS (Oxford, X–Max 80).

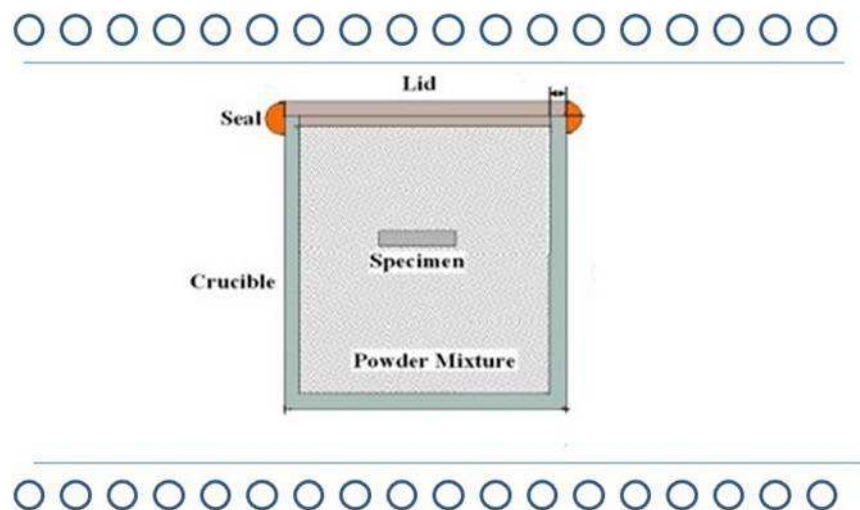


Fig. 3.7 Schematic of experimental set-up for conducting pack cementation experiment

3.6 Characterization of the prepared alloys

3.6.1. Compositional, phase and microstructural characterization

The bulk quantitative estimations of products were carried out by the chemical analysis using different analytical methods such as spectrophotometry, gravimetry and volumetry for different elements. The chips from alloy button from different locations were drilled out and dissolved in aqua-regia. Analyses of the samples were done using the dissolved aqua-regia solution and the averages of compositions of different locations were determined. The bulk chemical composition of the alloys were also determined by XRF, while the quantitative Microanalysis was carried out by EDS for evaluating compositional variation by observing microstructure of respective alloys.

Synthesized alloys were characterized for their phases at room temperature by powder X-ray diffraction method. The chemical composition of the synthesized alloy was also confirmed by conventional chemical analysis. X-ray diffraction pattern of the powders was recorded on a powder diffractometer (model-PW 1820, Philips) with Ni filtered Cu K α radiation, operating at 30 kV and 20 mA. All diffraction patterns were recorded in the 2θ range from 20 to 65°, with a slow scanning rate of step size 0.5°/s.

The morphology of the synthesized powders was observed with a scanning electron microscope (Model MV2300CT/100, Camscan, UK). The crystallite size of synthesized powders was determined using X-ray line broadening of primary peak of the alloy and calculated using the Scherrer equation [5]. Si single crystal was used as an external standard for calibration as well as deduction of instrumental broadening.

$$\tau = \frac{0.9\lambda}{\beta \cos \theta} \quad (3.1)$$

$$\beta^2 = \beta_m^2 - \beta_s^2 \quad (3.2)$$

Where τ is the average diameter of the crystallites in Å. β_m and β_s are the measured full width at half the maximum intensity (FWHM) of the (110) reflection line from the sample and 28.45° line of the Si standard, respectively, 2θ is the diffraction angle corresponding to the peak maximum, and λ is the Cu K α weighted wavelength ($\lambda = 1.5406$ Å).

The specimens were cut and polished following standard metallographic techniques to reveal the respective microstructures. The polished samples were then etched using a chemical mixture (Murakami's reagent) containing K₃Fe(CN)₆, KOH and H₂O in the ratio of

1:1:10 by volume. The microstructures of etched and unetched alloys were examined using optical and scanning electron microscope (Model MV2300CT/100, Camscan, UK).

3.6.2 Mechanical Testing

Hardness test

The hardness of alloys were measured in an automatic micro hardness tester machine on the mirror polished samples at several locations using a load of 1–5 N for 10s. At least 5 readings were taken at a fixed load and averages of all were considered.

Room temperature fracture toughness test

Single edge notched bend (SENB) specimens were fabricated from the alloy samples following the ASTM E399 specifications using an electro–discharge machine. The specimens were grinded and polished to the final dimensions of 4 mm (W) × 3 mm (B) × 24 mm (L). Where, W= width, B = thickness of the specimens.

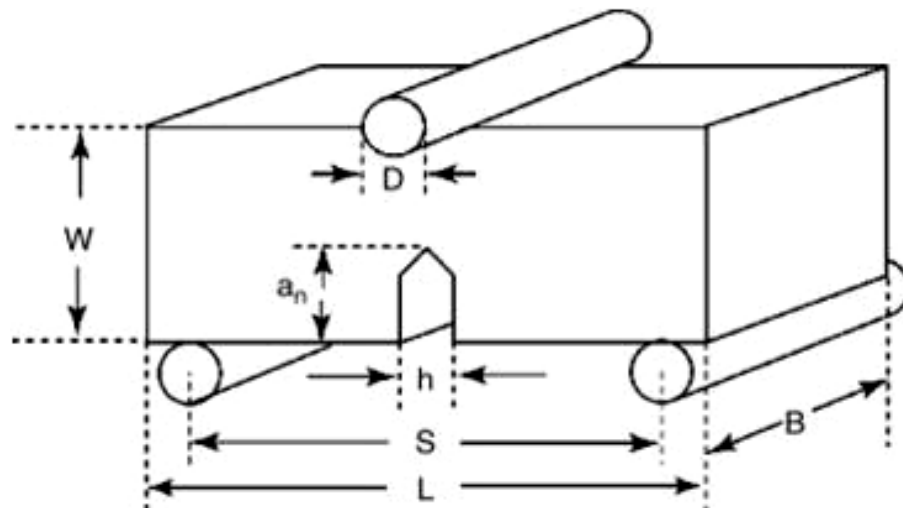


Fig. 3.8 Schematic of 3–point single edge notched bend (SENB) sample geometry

Both the flexural strength and the fracture toughness measurements were carried out on a MTS machine, using a three–point bending test with a loading span of 18 mm and a cross–head speed of 0.5 mm/min. The schematic of the three point bend test is shown in Fig. 3.8. The peak load in the load–displacement curve was used to determine the flexural strength (σ_f) and the fracture toughness (K_C) of the samples using the respective standard equations following ASTM 399 [6] ,

$$\sigma_f = 3P * S/WB^2 \quad (3.3)$$

$$K_C = [P S f(a/W)]/(B * W^{3/2}) \quad (3.4)$$

$$f\left(\frac{a}{W}\right) = 3 \sqrt{\frac{a}{W}} \cdot \frac{1.99 - \left(\frac{a}{W}\right) \left(1 - \frac{a}{W}\right) \left[2.15 - 3.93 \frac{a}{W} + 2.7 \left(\frac{a}{W}\right)^2\right]}{2 \left(1 + 2 \frac{a}{W}\right) \left(1 - \frac{a}{W}\right)^{3/2}} \quad (3.5)$$

Where “a” is notch depth (0.8-1mm), P is the peak load, B is the thickness of the specimens, S is span and $f(a/W)$ is a geometrical factor. Equation-3 for “a/W” is considered to be accurate ~ 1 % over the range $0.2 < a/W < 1$ [6]. The tests were conducted in triplicate for checking the repeatability. The fractured samples were observed under SEM in secondary electron imaging mode to reveal type of failure.

3.6.3 Oxidation Studies

Oxidation studies using conventional approach

Small specimens were cut from the synthesized alloys, followed by polishing and cleaning ultrasonically in acetone. TG (thermogravimetry) analyses were carried out for evaluating the oxidation behavior of the bare and coated alloys, under non-isothermal heating conditions in 1 atmospheric oxygen pressure with a flow rate of 20ml/min. The weight change profile was recorded up to 1273K at a heating rate of 10K /min.

The thermal stabilities were also evaluated by heating them under isothermal heating conditions at different temperatures and different durations. In the isothermal oxidation studies, the specimens with the dimensions of $10 \times 5 \times 5$ mm were introduced into a furnace, when the temperature of the furnace reached the set value. Each sample was carefully weighed before and after exposure. Reaction products formed were identified by XRD. The morphology and the nature of the oxide layers were examined by SEM and EDS. Oxidation tested samples were further evaluated by visual observation, elemental mapping of oxidized surface and cross sectional microscopy.

Oxidation kinetic studies by stepwise isothermal study

Oxidation tests were also carried out using a novel stepwise isothermal method in thermobalance to determine the oxidation kinetics in a single experiment. Specimens were cut from the synthesized alloys and grinded to known surface area followed by polishing and ultrasonically cleaning in acetone. Oxidation tests were carried out at 1 atmosphere oxygen pressure in a thermobalance and weight change profiles were recorded at a heating rate of 20

K/min up to the 773 K then onwards up to 1073 K with the same rate of heating and an isothermal hold of 60 minutes at each 100 K interval. Phases present on the surface of the oxidized samples were characterized by X-ray diffraction (XRD) in an Inel-make unit (model MPD) with Cr-K_α radiation at 25 mA 35 kV. The morphology and natures of oxides layers were analyzed by observing the surface and the cross-section in scanning electron microscopy (SEM, Camscan MV2300CT/100, UK), equipped with energy dispersive spectrometry (EDS, Oxford, X-Max 80).

3.6.3 Wear Test

The reciprocating sliding wear and friction experiment was performed using a computer controlled reciprocating sliding machine (PLINT TE-77) that produces a linear relative oscillating motion with a ball-on-flat configuration. A spring loaded Al₂O₃ ball (of diameter 3/8") sample is made to oscillate with a relative linear displacement of a constant stroke and frequency against a fixed flat sample of the coated and uncoated alloys. The variation in tangential force is recorded and the corresponding coefficient of friction (COF) is calculated online, with the help of a computer-based data acquisition system. According to the commercial supplier's data, the Al₂O₃ balls have a surface roughness of Ra ~0.02 μm, a hardness of ~18 GPa, and a fracture toughness of ~5 MPa . m^{1/2}. Before the wear tests, all the samples and the balls were ultrasonically cleaned with acetone. The reciprocating sliding experiments were performed at a constant load of 7 N and 1.0 mm linear stroke, for duration of 100,000 cycles. The influence of varying sliding speed by varying oscillating frequency (10, 15, 20 Hz) on the friction and wear response was investigated. All the experiments were conducted in an ambient atmosphere at room temperature (30 ± 2 °C) with a relative humidity (RH) of 40 ± 5%.

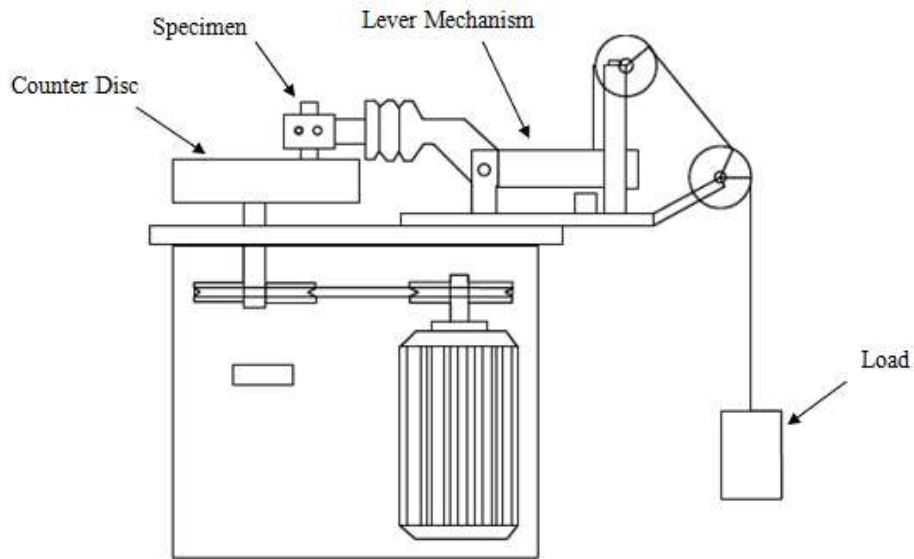


Fig. 3.9 Schematic of the wear test set-up [7]

Subsequent to the sliding wear test, the wear scar on each of the flat samples was measured using a computer-controlled 3D Optical Profiler (CCI-MP Taylor Hobson). 2-D depth profiles at different locations over the sliding distance were extracted and integrated to calculate wear volume. From the measured wear volume, the specific wear rates [wear volume / (load. Distance)] was calculated. A detailed characterization of the worn surfaces of the coated samples and counter-body balls were performed using SEM and optical microscope respectively.

References

- [1] <http://www.understandingnano.com/nanomaterial-synthesis-ball-milling.html>
- [2] <http://www.crucibleservice.com/history.aspx?c=20>
- [3] http://en.wikipedia.org/wiki/Electric_arc_furnace
- [4] S.P. Chakraborty, S. Banerjee, I.G. Sharma, Bhaskar Paul, A.K. Suri. Studies on the synthesis and characterization of a molybdenum–based alloy. *J. Alloy Comp.* 477 (2009) 256–261.
- [5] B.D Cullity, *Elements of X-ray Diffraction*, Addison-Welsey, Reading, MA, 1969.
- [6] ASTM Standard E399 – 09, “Standard Test Method for Linear-Elastic Plane-Strain Fracture Toughness K_{Ic} of Metallic Materials”
- [7] <http://www.leonardocentre.co.uk/contents/item/display/122>

Chapter-4

**(Preparation of Mo-30W alloy and
development of oxidation resistant coatings)**

4.1 Introduction

Mo–30 wt.% W alloy is of interest as a high temperature nuclear structural material because of its better formability, high temperature strength and improved oxidation resistance as compared to other Mo based alloys [1, 2]. It is extensively used as components for zinc processing, e.g. pump components, nozzles, thermocouple sheaths, stirrers for the glass industry, sputter targets for coating technology etc. Therefore, it is a potential candidate material for the applications where extensive liquid metal handling is required.

Preparation of Mo–30 wt.% W alloy by the conventional melt–casting process is a highly energy intensive process. The reasons can be attributed to the following facts. Firstly, very high melting points (2893 K and 3653 K for Mo and W, respectively) and a large difference in the specific gravity (10.2 g/cc and 19.32 g/cc for Mo and W, respectively) of the alloying components results in a number of melting runs required for thorough homogenization at very high temperatures nearly 3300 K. Secondly, a very high level of vacuum has to be maintained during melting as the alloying components can be oxidized even with the trace amount of air present in the reaction vessel. Thirdly, because of high vapour pressure of Mo at the melting point of W, substantial loss of Mo takes place during the melting under vacuum. Fig. 4.1 shows the variations of vapour pressure of Mo and W with temperature, indicating a big difference of vapour pressure at a given temperature.

Mo–30W possesses very high melting point and therefore, powder metallurgy is an alternate economical route of fabrication. Powder metallurgy is the most promising production route for commercial Mo, W and their alloys. More than 97% of Mo products are processed by powder metallurgical route and the remainder is processed by electron–beam melting (EBM) and vacuum arc casting (VAC).

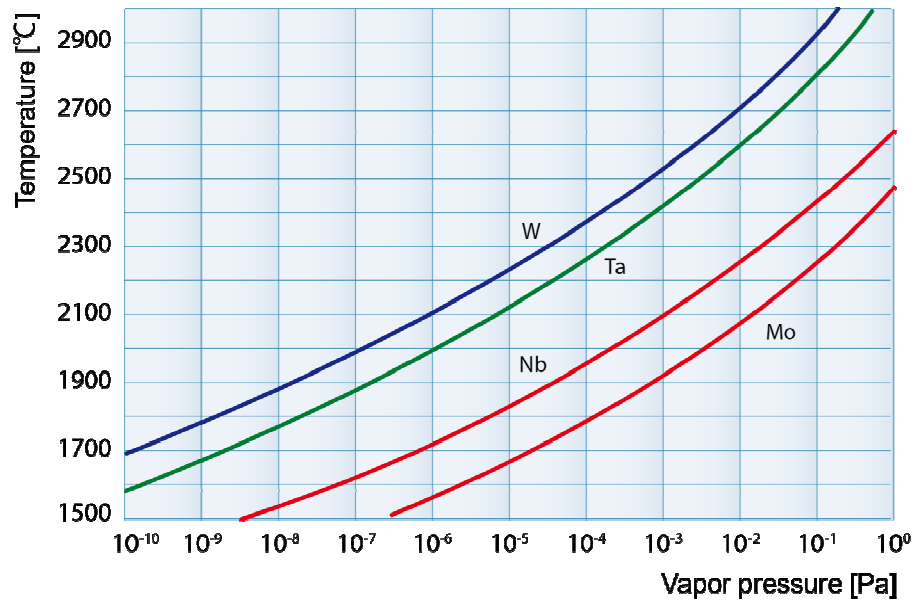


Fig. 4.1: Variation of vapour pressures of refractory metals with temperature [10]

The finer grain structure of powder metallurgical products is advantageous for both the secondary processing and the mechanical properties of the finished products. However, very few technical literatures are available related to Mo–30W alloy with respect to its preparation via powder processing route. It is necessary to understand each unit steps of powder metallurgical route. The major unit operations of powder metallurgical route are powder preparation, compaction and sintering.

Mechanical alloying has emerged as an alternative route in the recent past that has drawn wide attention for preparation of advance materials after its discovery by Schwarz and Koch [3]. Preparation of alloy powder through this route not only provides microstructural refinement but also imparts very high homogeneity of the final product [4, 5]. Apart from this, a significantly less energy requirement for the alloy preparation, as compared to the conventional melt–casting technique makes this method economically attractive.

Once a homogeneous alloy powder is prepared, the next important task is to convert it to desired shapes with appropriate mechanical and physical properties. Sintering of these powders therefore becomes utmost important during shaping. As pointed out earlier that, most of the molybdenum based products are produced by adopting powder metallurgical processing sequences including pressing and sintering followed by mechanical working in order to achieve near theoretical density and desired microstructure of the final product. Understanding the sintering mechanism of these powders therefore becomes very essential from both applied as well as research point of view. In this regard, a prior knowledge of the initial stage of sintering is very important to understand its exact mechanism. Considerable

efforts have been made in the past to understand the kinetics and mechanisms involved during the initial stage of sintering [6–8]. Few studies on sintering of molybdenum [9–12] and tungsten [13–15] have also been reported earlier. Gospodinov et al. [16] studied the activated sintering of a mixture of tungsten and molybdenum powders in presence of Ni. However, the details of exact sintering kinetics of Mo–W alloy powder are not available in the open literature. In the present study, attempt has been made to evaluate the kinetics of sintering from both, the non–isothermal i.e. constant rate of heating (CRH) method as well as the stepwise isothermal dilatometry method.

Although, Mo–30W alloy exhibits most of the properties required for high temperature applications, it cannot be used in oxygen containing atmosphere because of the poor oxidation resistance at high temperature. Its oxidation behaviour is only marginally better than Mo. For utilizing its high temperature properties effectively, it has to be prevented from high temperature oxidation by a suitable coating. Pack cementation is a widely applicable in–situ coating technique, which produces uniform and adherent coatings even on complex shaped structures [17–23]. In the present chapter, results on the development of *silicide* based protective coating on Mo–30W alloy by halide activated pack cementation technique using different pack mixtures have been presented. Effect of pack chemistry and temperature on evolution of phases, microstructures, coating thickness and surface morphology has been discussed. Performance evaluation tests were carried out for the coated alloy with respect to oxidation and wear.

The first part of the chapter deals with the results on the preparation of Mo–30W powder, sintering and sintering kinetics. The second part deals with the results on the development of oxidation resistant coating over Mo–30W alloy.

4.2 Studies on preparation of Mo–30W alloy powder

4.2.1 Mechanical alloying

Fig. 4.2 shows the room temperature X–ray diffraction pattern of the Mo–30 wt.% W powder prepared by mechanical alloying for 15 h. The alloyed powder has been found to have the single phase cubic molybdenum structure as revealed by a perfect match with the literature data (PCPDF–421120).

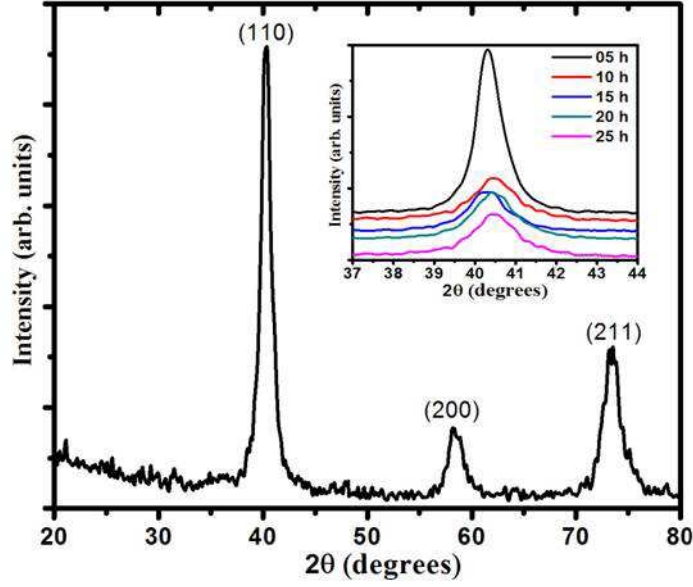


Fig. 4.2 XRD pattern of Mo–30 wt.% W powder prepared by mechanical alloying for 15 h. Inset shows the variation of Mo (110) peak as a function of milling duration

The inset in Fig. 4.2 shows the enlarged view of the diffraction patterns corresponding to the principle (110) peak for powders prepared with different milling duration. The crystallite size of these powders was determined using X–ray line broadening of (110) peak of the alloy and calculated using the Scherrer formula [24]. Si single crystal was used as an external standard for calibration as well as deduction of instrumental broadening.

$$\tau = \frac{0.9\lambda}{\beta \cos \theta} \quad (4.1)$$

$$\beta^2 = \beta_m^2 - \beta_s^2 \quad (4.2)$$

Where τ is the average diameter of the crystallites in Å. β_m and β_s are the measured full width at half the maximum intensity (FWHM) of the (110) reflection line from the sample and 28.45° line of the Si standard, respectively, 2θ is the diffraction angle corresponding to the peak maximum, and λ is the Cu K α weighted wavelength ($\lambda = 1.5406$ Å).

Gradual peak broadening and decreasing peak intensity can be clearly observed with increasing milling time. This can be attributed to (a) decreasing crystallite size from 12.5 nm for 5 h milled powder to about 7.6 nm for 25 h milled powder as revealed by crystallite size evaluation using peak broadening and (b) due to gradually increasing strain in the system with increasing milling time. Fig. 4.3 shows the SEM image of Mo–30 wt.% W powder prepared by mechanical alloying for 25 hours, which reveals an agglomerated form of the

powder. The agglomerate size as measured from the SEM images is $15 (\pm 3) \mu\text{m}$. This agglomeration is mainly due to very small crystallites with very high surface energy being formed during mechanical alloying. This is further evident from the inset of Fig. 4.3, which clearly reveals the nanocrystalline nature of the as prepared powder. Fig. 4.4 shows the EDS spectra of the same powder confirming the targeted chemical composition without any notable contamination during the alloying process. Fig. 4.5 presents the X-ray diffraction patterns corresponding to the principal (110) peak for as compressed green pellet and pellets sintered to different temperatures. A shift of this reflection peak towards higher angles (from 40.32° for powder milled for 5 h to 40.58° for the compact sintered at 1100°C) is observed. This indicates a reduction in the lattice parameter of the sintered alloy and can be attributed to the (a) atomic radius mismatch between Mo & W and (b) distortion of the molybdenum lattice due to tungsten diffusion in it. A similar result of lattice distortion of Mo is reported by Gospodinov et al. for Mo–W system [16] due to the formation of W–Mo solid solution.

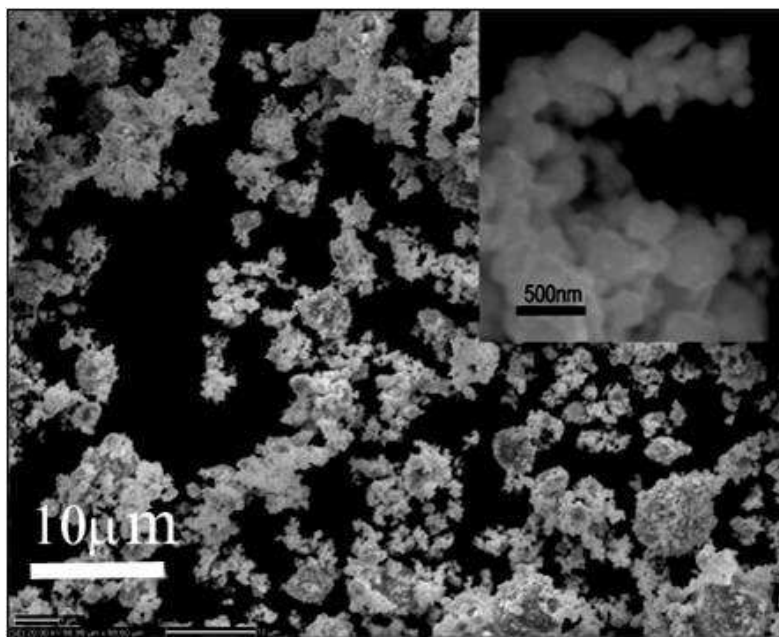


Fig. 4.3 SEM image of Mo–30 wt.% W powder prepared through mechanical alloying (25 h milling). Inset shows the higher magnification image of agglomerated particles to show the sub–micron nature of the powder.

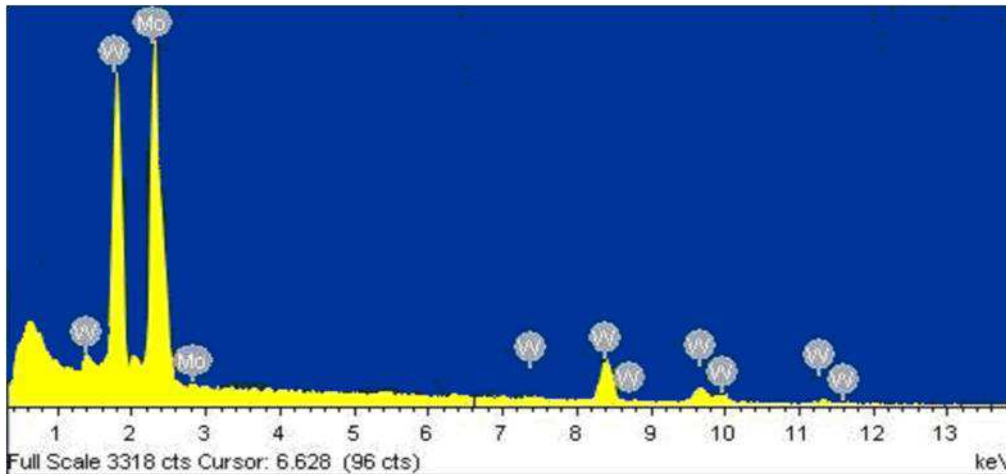


Fig. 4.4 EDS Spectra of mechanically alloyed Mo–30 wt.% W powder.

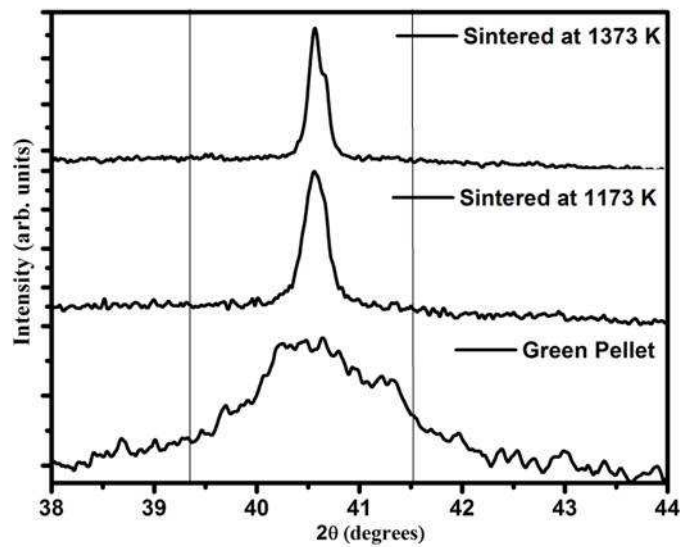


Fig. 4.5 XRD patterns of Mo (110) peak for (a) Mo–30 wt.% W green compact, (b) sample sintered up to 1173 K and (c) sample sintered up to 1373 K.

4.3 Sintering Studies

Fig. 4.6 shows the relationship between sintering temperature and relative density of the sintered Mo–30W alloy compacts made from the powder prepared by mechanical alloying route. The sintering time was kept constant of 2h. The theoretical density of the alloy was calculated, using the classical rule of mixture [25] to yield a value of 1197 kg/m^3 . Initially the density of compacts made from both the powder increased quickly, with increasing

sintering temperature. Later on, above 1300°C, the density increases slowly, indicating a change in the sintering mechanism.

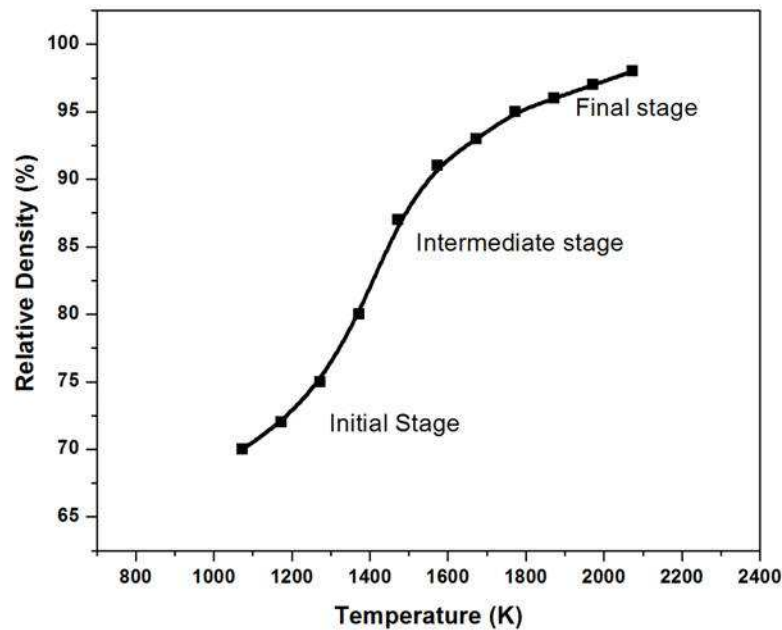


Fig. 4.6 Plot of sintered density with respect to sintering temperature for fixed sintering time of 3h for green compacts prepared from mechanically alloyed powder and co-precipitated cum reduced powder.

Sintering kinetics is important to be known for optimization of the processing of powder metallurgical parts with different properties. Selection of optimum sintering temperature and time, heating and cooling rates generally require number of experiments. On the basis of the sintering plot (Fig. 4.6), three different stages of sintering can be assumed where different sintering mechanisms are dominant at different sintering stages. Out of the three stages, determination of sintering kinetics of first stage of sintering is relatively simple because of the occurrence of more than one possible operating mechanism at intermediate and final stages of sintering makes them complex. Therefore studies have been extended to determine sintering kinetics in the initial stage for the mechanically alloyed powder. In the present study, we have attempted to evaluate the kinetics of sintering from both, the non-isothermal i.e. constant rate of heating (CRH) method as well as the stepwise isothermal dilatometry method. Model sintering equations suggested by Young and Cutler [26], originally developed by Johnson and co-workers [27] were used to analyze the shrinkage data generated during non-isothermal constant rate of heating (CRH) sintering schedule.

Stepwise Isothermal Dilatometry (SID) is a relatively new approach as compared to conventional sintering studies and has proven its usefulness in analyzing the sintering mechanism of fine ceramic powders [28–31]. In our earlier work [32], we have shown the utility of this approach for studying the sintering kinetics of submicron sized Co metal powders. With this approach, it is possible to evaluate both, the sintering mechanism and the apparent activation energies using a single shrinkage data obtained from dilatometry. The same approach has been used to determine the possible mechanism of sintering in the present work. Observed results from SID have been analyzed by a model given by Makipirtti–Meng. It has been found that the model fits equally well to explain the sintering kinetics of alloys systems prepared through mechanical alloying.

4.3.1 Sintering kinetics using constant rate of heating (CRH) method

Model sintering equations suggested by Young and Cutler [26], originally developed by Johnson and co-workers [27] were used to analyze the shrinkage data generated during non-isothermal constant rate of heating (CRH) sintering schedule.

Johnson [27] suggested the basic sintering equations individually for volume and grain boundary diffusion as

$$y_{Vol}^2 = \left(\frac{5.26\gamma\Omega D_V t}{kTa^3} \right) \quad (4.3)$$

$$y_{gb}^3 = \left(\frac{2.63\gamma\Omega b D_B t}{kTa^4} \right) \quad (4.4)$$

where y is the net linear shrinkage ($\Delta l/l_0$); Ω , the volume of vacancy (m^3); γ , the surface energy (J/m^2); D_V , the volume diffusion coefficient given by $D_V = D_V^0 \exp(-Q_V/RT)$ (m^2/s); bD_B , the product of grain boundary thickness ‘ b ’ and grain boundary diffusion coefficient ‘ D_B ’ given by $bD_B = bD_B^0 \exp(-Q_{bDB}/RT)$ (m^3/s); k , the Boltzmann constant (J/K); T , the temperature (K); a , the particle radius (m) and t is time (s), Q_V and Q_{bDB} are the activation energy for volume diffusion and grain boundary diffusion respectively.

Sintering kinetics utilizing the constant rate of heating (‘CRH’ i.e. $c = T/t = dT/dt$) technique for the initial stage of densification ($\sim 5\%$), using different models has been reported by different researchers. For submicron size powder systems, sintering begins even before the steady state of isothermal part is reached. To account for that, sintering has been studied by CRH method. Above equations, originally suggested by Johnson have undergone further modification by different research groups. Out of the several modifications, the one proposed by Young and Cutler [26] however, is mostly used. The modified equations

individually developed for volume and grain boundary diffusion, as suggested by them are given as equation (3) and (4), respectively.

$$\ln\left(yT \frac{dy}{dT}\right) = \ln\left(\frac{2.63\gamma\Omega D_V^0}{ka^3c}\right) - \left(\frac{Q_V}{RT}\right) \quad (4.5)$$

$$\ln\left(y^2T \frac{dy}{dT}\right) = \ln\left(\frac{0.71\gamma\Omega bD_B^0}{ka^4c}\right) - \left(\frac{Q_{bD_B}}{RT}\right) \quad (4.6)$$

From above equations, it is clear that the activation energies for volume diffusion and grain boundary diffusion are obtained from the slopes of the plots between $\ln(yT dy/dT)$ versus $1/T$ and $\ln(y^2T dy/dT)$ versus $1/T$, respectively.

Fig. 4.7 shows the linear shrinkage profiles of Mo–30 wt.% W alloy powder compacts sintered at different temperatures with constant rate of heating schedule (CRH) keeping the rate of heating to be 20 K/min. It can be seen that the maximum shrinkage is achieved for sample heated up to 1573 K yielding nearly 91% (sintered density ~ 10.9 g/cc) theoretical density of Mo–30 wt.% W alloy. It can be visibly seen that instead of an initial expansion, normally expected due to usual thermal expansion of any material before the actual sintering commences, a small amount of shrinkage was observed while sintering these compacts under reducing atmosphere.

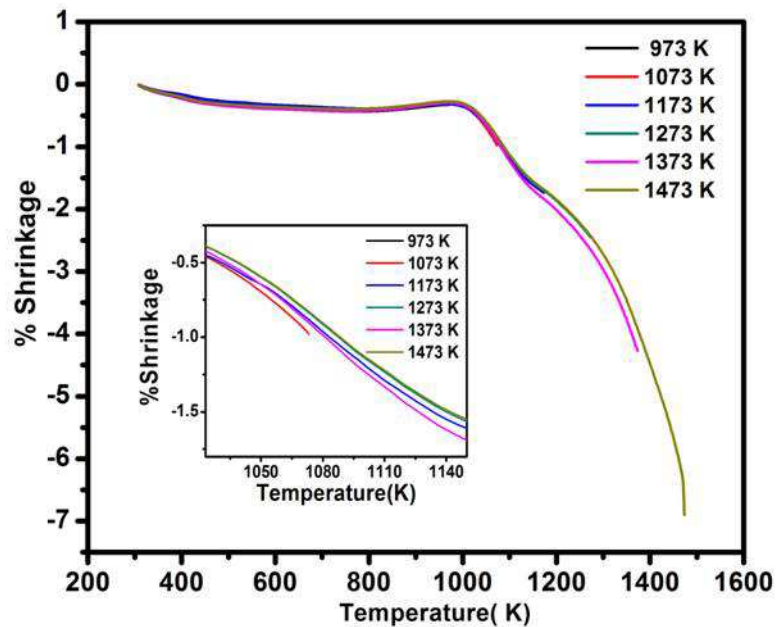


Fig.4.7 Shrinkage profiles of Mo–30%W alloy powder compacts sintered at different temperatures with constant rate of heating (20 K/min). Inset shows the variation in shrinkage profile in different experiment (magnified).

The initial shrinkage observed at temperatures below 1023 K before the onset of actual sintering can be explained as due to (i) reduction of surface contamination (oxides) layers to metal and thus reducing the volume and (ii) very high surface energy and highly deformed nature of the sub-micron sized powders that facilitate their aggregation at relatively lower temperatures and hence exhibiting shrinkage. This phenomenon has been illustrated in detail in the previous study [32]. Since the individual curves represent the shrinkage obtained at the same heating rate (20 K/min), ideally all these should represent a single curve. Therefore an average of all the shrinkage values at given temperatures was obtained and was used for subsequent analysis. Further, as the model equations applicable to the initial stage of sintering were used for analysis of sintering kinetics, the shrinkage data was limited to 1473 K (i.e. up to ~ 5% of shrinkage). As explained earlier, the plots of $\ln(yT \cdot dy/dT)$ versus $1/T$ and $\ln(y^2T \cdot dy/dT)$ versus $1/T$, that are shown in Fig. 4.8 together, allow the calculation of activation energy and the frequency factor for volume diffusion and grain boundary diffusion, respectively as presented in Table-4.1.

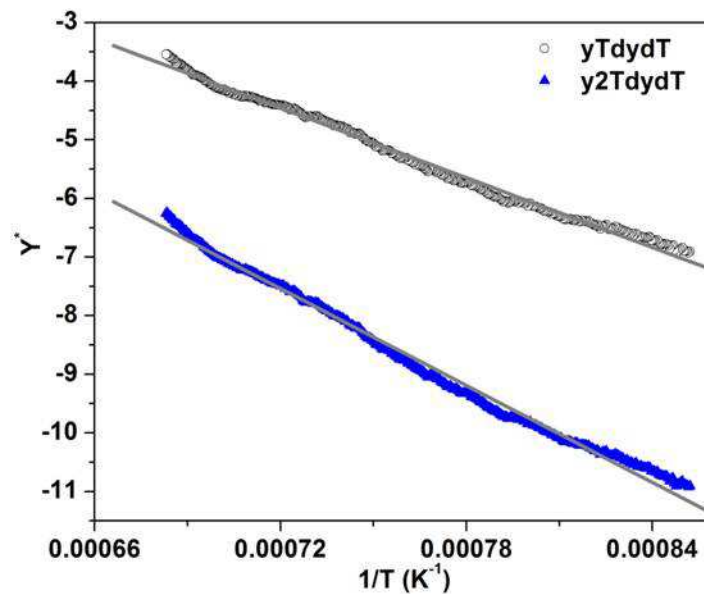


Fig.4.8 Plot of $\ln(yT \cdot dy/dT)$ and $\ln(y^2T \cdot dy/dT)$ versus $1/T$. Grey line curve shows the least-squares linear fit of the evaluated data.

The similarity in the two Arrhenius plots shown in Fig. 4.8 suggests that the mechanism for sintering here could be either volume diffusion or grain boundary diffusion or simultaneous occurrence of both [33]. Actually, the diffusion rate is determined by temperature, powder characteristics and the specific structure of material. Further, the diffusion rate determines the paths of diffusion, through the volume or the boundaries of crystals, dislocations, or the surfaces. Volume diffusion in crystals is the most difficult

material transport mechanism with the highest activation energy barrier associated with it. The path then becomes easier for diffusion through dislocations, boundaries and surfaces [34]. However, in the present system, the calculated activation energy for volume diffusion (190 kJ/ mole) seems to be erroneous (towards a lower side) since the reported activation energy value for pure Mo is much higher (~400 KJ/mole) [35]. Although Davade et al. [33] have also reported lower activation energy for lattice diffusion than grain boundary diffusion, they substantiated the observation by the term called ‘enhanced boundary diffusion’.

Table – 4.1: Kinetic parameters for CRH sintering of Mo–30 wt% W alloy

Q_{GB} (kJ / mol)	Q_V (kJ / mol)	bD_B^0 (m ³ /s)
230	190	7.44X10 ⁻⁹

While it was initially thought that volume diffusion was the dominant sintering mechanism in the densification of pure molybdenum or Mo based alloys, studies on activated sintering showed that the grain boundary mobility retarded the densification process, thus causing the apparent activation energy to be driven up to the values that appeared more in line with volume diffusion [36]. The consensus among the researchers however is that grain boundary diffusion is considered to be the dominant densification mechanism for most of the Mo based alloys [36]. Our results also match with the same line of thought. Thus the model employed here does give an idea about the dominant mechanism during the initial stage of sintering, which is grain boundary diffusion with an activation energy of ~230 kJ/ mol. Using the expression $bD_B = bD_B^0 e^{(-Q_{bD_B}/RT)}$, the values of bD_B were calculated at various temperatures and are presented in Table – 4.2. The values fall well in line with the expected trend of increasing grain boundary diffusion coefficients with increasing temperatures.

Table – 4.2 Values of bD_B were calculated at various temperatures

Temperature (K)	bD_B (m ³ /s)
973	3.1x10 ⁻²¹
1023	1.3x10 ⁻²⁰
1073	4.5x10 ⁻²⁰
1123	1.4x10 ⁻¹⁹

4.3.2 Sintering kinetics using Stepwise Isothermal Dilatometry (SID)

Rate-controlled sintering (RCS) of green compacts has been developed and studied widely for optimized densification and grain size control [37, 38]. The prime feature of RCS is the control of the sintering process according to a specific shrinkage rate profile. It aims to eliminate the pores in an efficient way by controlling the diffusion kinetics of the material. Similar to this, Stepwise Isothermal Dilatometry (SID) is one more approach to understand sintering kinetics. Makipirtti and Meng [28–32] proposed a model to analyze the SID shrinkage data. According to this model, the fractional densification function Y , for an isotropic sintering behaviour is expressed as

$$Y = \frac{V_o - V_t}{V_o - V_f} = \frac{L_o^3 - L_t^3}{L_o^3 - L_f^3} \quad (4.7)$$

Where $V_o (L_o)$, $V_t (L_t)$, and $V_f (L_f)$ are the initial volume (length), volume (length) at time t , and volume (length) of the finally densified specimen, respectively. A normalized rate equation as suggested by Makipirtti–Meng method is given as

$$\frac{dY}{dt} = nk(T)Y(1-Y)\left(\frac{1-Y}{Y}\right)^{1/n} \quad (4.8)$$

$$k(T) = k_o \exp(-Q/RT) \quad (4.9)$$

Here $k(T)$ is specific rate constant, k_o , the frequency factor Q , the energy of activation R , the universal gas constant and n is a parameter related to the sintering mechanism.

Fig. 4.9 shows the shrinkage profile and shrinkage rate of the green compact subjected to SID sintering schedule. It also shows the variation of shrinkage rate occurring at each isothermal step during sintering. The experimental shrinkage curve obtained by dilatometry is generally in the form of [27, 39]:

$$y = [k(T)t]^m \quad (4.10)$$

If volume diffusion is the only operative mechanism, then the shrinkage rate is given by

$$dy/dt = n(5.34)\Omega D_v / kTa^3)^m t^{(m-1)} \quad (4.11)$$

Similarly, if the grain boundary diffusion is operative solely, then the shrinkage rate is given as

$$dy/dt = n(2.14\gamma\Omega bD_B/kTa^4)^m t^{(m-1)} \quad (4.12)$$

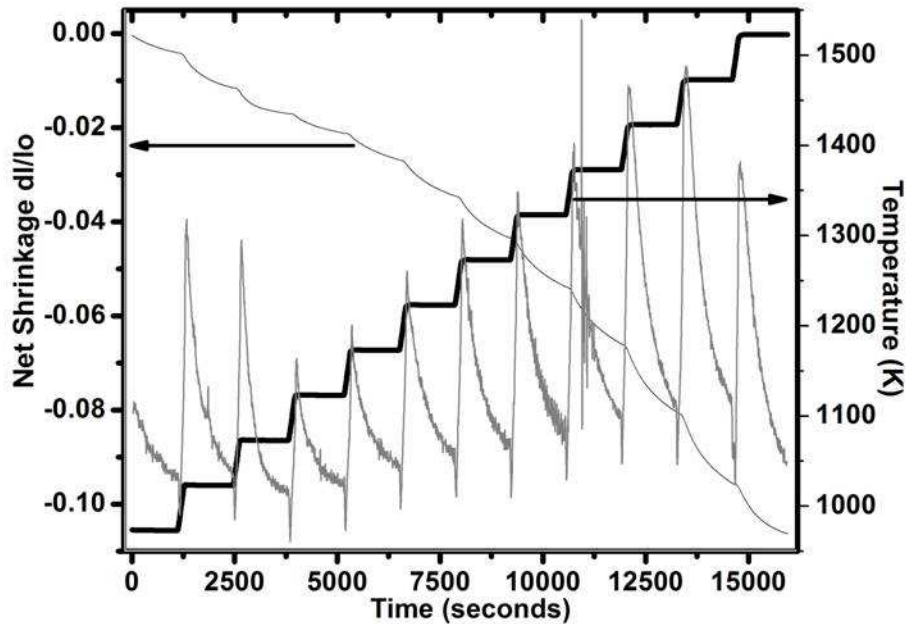


Fig. 4.9 SID shrinkage profile of Mo-30 wt.% W alloy green compact along with the temperature program followed for the SID experiment. The Curve in grey colour show the shrinkage rate $\{d(l/l_0)/dt\}$ as a function of time

Fig. 4.10 shows the plot between $\log (dy/dt)$ and $\log t$ for different isothermal steps. From the slope of the plots, the sintering exponents 'm' has been determined for each isothermal step. The value of 'm' varies from $\sim (0.2$ to $0.3)$ up to 1073 K to 0.5 up to 1473 K. It is therefore evident that for temperature up to 1073 K, grain boundary diffusion (GB) is the rate controlling mechanism. However, from the next step, volume diffusion takes over as the rate controlling mechanism of sintering. From the values of intercepts, the diffusion coefficients at different temperatures have been evaluated and presented in the Table – 4.3.

Table – 4.3 Volume diffusion coefficients for Mo–30wt% W alloy evaluated through SID analysis

Temperature (K)	D_V (m^2/s)
900	1.5×10^{-19}
1000	4.9×10^{-18}
1100	1.4×10^{-16}
1200	2.3×10^{-15}

The coefficients evaluated here are very close to the reported diffusion coefficients for pure molybdenum ($1.6 \times 10^{-15} m^2/s$) and tungsten ($1.3 \times 10^{-15} m^2/s$) at 1773 K evaluated by high temperature tracer determinations [40]. This is very close to the values obtained in this study.

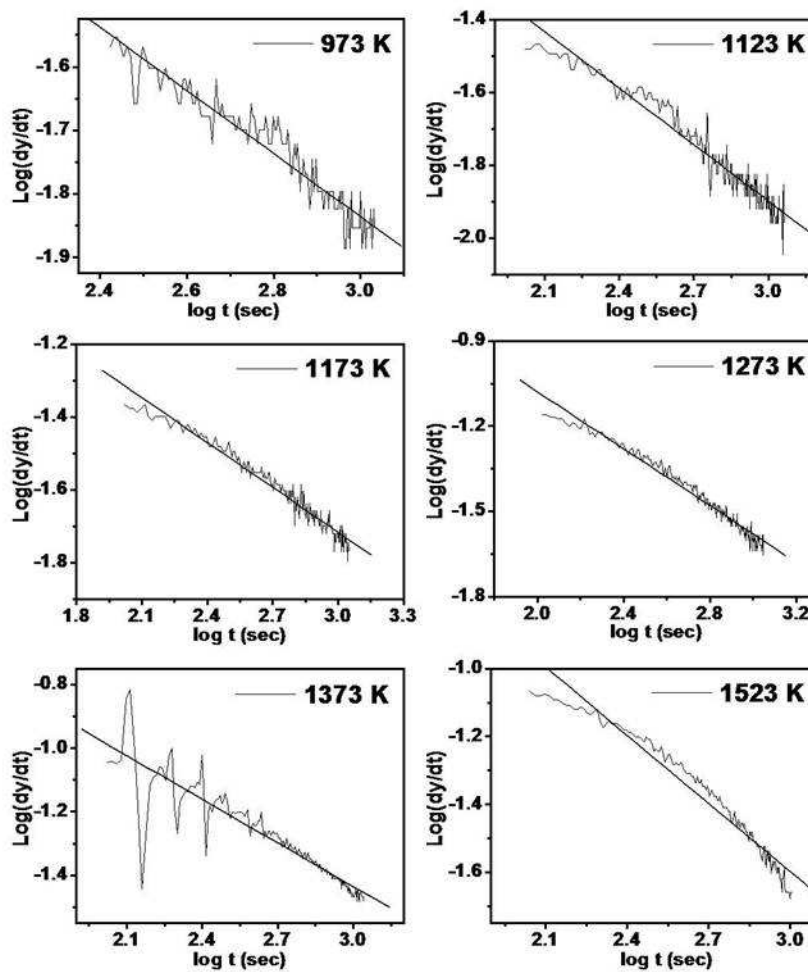


Fig.4.10 Plot of $\log(dy/dt)$ vs $\log t$ at different isothermal steps

Using Makipirtti–Meng model, as described earlier, the shrinkage data, after fitting into equation–4.8 is plotted in Fig. 4.11 as $\ln \{(dY/dt)/Y/(1-Y)\}$ vs $\ln[(1-Y)/Y]$. A near straight line behavior for each isothermal zone indicates the validity of the model with present shrinkage data of Mo–30 wt% W alloy. The Values of slope ‘ $1/n$ ’ and intercept ‘ $\ln nk(T)$ ’, evaluated by least–squares linear fitting for each straight line segment of the curve, are presented in Table – 4.4. Parameter ‘ n ’, that relates to the sintering mechanism takes nearly two different average values in the measured temperature range as $1/n \sim 0.2$ (1373 – 1473 K) and ~ 0.13 – 0.18 (1073–1323 K). These values suggest that there are two different sintering mechanisms, operative as the dominant processes over the above temperature intervals.

Table–4.4 Kinetic analysis of SID shrinkage data of Mo–30 wt% W alloy green compacts according to Makipirtti–Meng equation

Temperature (K)	1/n	n	ln k(T)	Regression
973	0.588	1.69	–20.20	0.994
1023	0.304	3.29	–19.37	0.995
1073	0.149	6.67	–17.23	0.994
1123	0.134	7.41	–16.12	0.991
1173	0.182	5.48	–15.84	0.992
1223	0.170	5.87	–14.48	0.988
1273	0.164	6.07	–12.82	0.992
1323	0.176	5.65	–10.85	0.991
1373	0.202	4.94	–9.05	0.994
1423	0.218	4.58	–7.29	0.996
1473	0.259	3.85	–6.07	0.993

Fig. 4.12 shows the Arrhenius plot between $\ln k(T)$ and $1/T$ for the SID shrinkage data. The curve can be best fitted into two linear segments in the temperature ranges from 973–1173 K and 1173–1523 K.

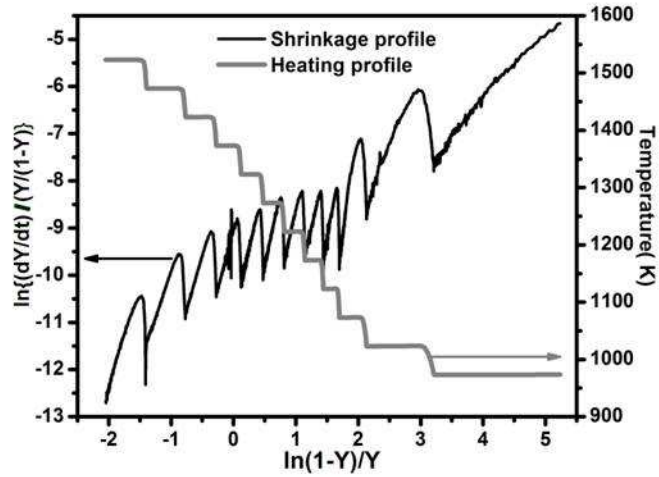


Fig. 4.11 Plots of $\ln\{(dY/dt)/Y/(1-Y)\}$ versus $\ln\{(1-Y)/Y\}$ according to Mecipritti–Meng equation. Variation of temperature with time is also shown on the right hand scale

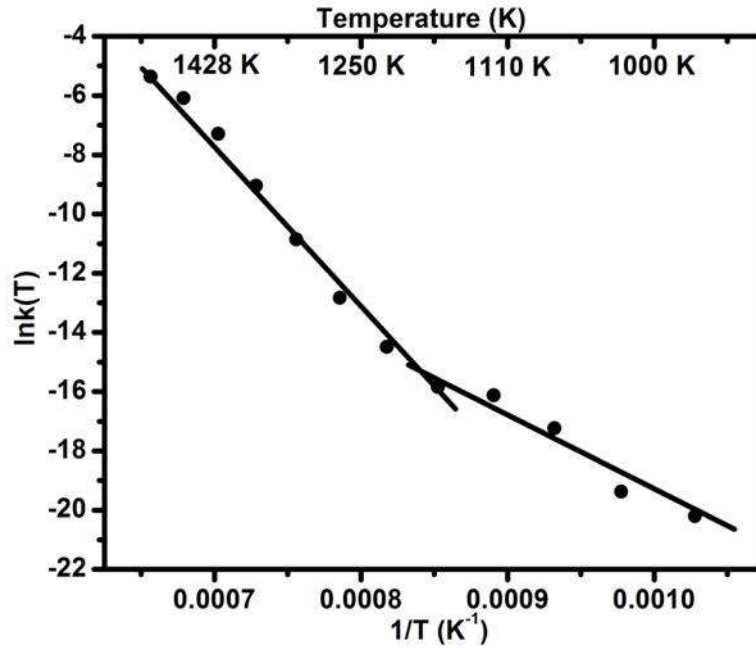


Fig.4.12 Arrhenius plot of $\ln k(T)$ versus $1/T$ based on the data in Table 4

The apparent activation energy ‘ Q ’ was calculated from the slopes of each segment and compared with that of various sintering mechanisms reported in the literature [5, 7]. The values are presented in Table–4.5. It is evident that the initial stage of sintering of Mo–30 wt.% W powder compacts can be divided into two main stages. The first stage (973–1173 K) relates to sintering within the aggregates, formed upon coalescence of the individual crystallites and leading to neck formation through grain boundary diffusion. This is further

supported by the SEM image recorded on 1173 K sintered sample that shows initial stage of neck formation (Fig. 4.13a). The activation energy value calculated from the least square regression analysis of data between 973–1173 K comes out to be 230 kJ /mole. A higher value of activation energy (480 kJ /mole) for temperature range 1173–1523 K is an indicative of lattice diffusion as the dominant process for mass transport. The micrograph recorded on sample sintered at 1373 K (Fig. 4.13c) clearly reveals the same.

Table–4.5 Apparent activation energies evaluated from SID analysis

Temperature range	Activation energy	Dominant mechanism
973–1173 K	230 kJ/mol	Grain Boundary Diffusion
1173–1523 K	480 kJ/mol	Lattice Diffusion

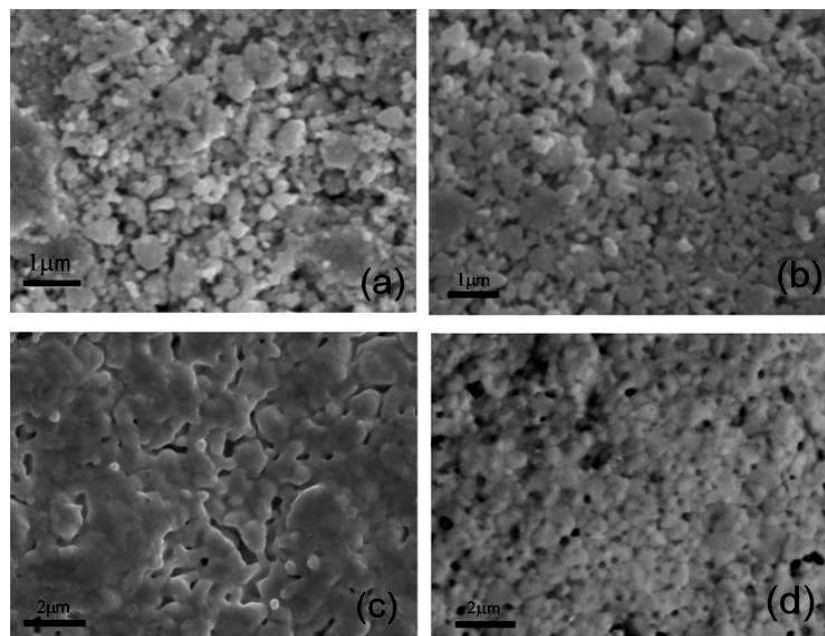


Fig. 4.13 SEM micrographs of Mo–30 wt% W alloys sintered at temperatures (a) 1173K (b) 1273K (c) 1373K (d) 1523K

It is seen from the Fig.4.9 that initially there is distinct shrinkage rate in the isothermal stage of 1023 and 1073 K and thereafter the shrinkage rate increases gradually with temperature. The maximum net shrinkage during an isothermal soak period occurs at 1373 K with the maximum rate of shrinkage. The shrinkage rate then decreases with further temperature increase. The gradual increase in shrinkage rate with increasing temperature is due to enhanced thermally activated diffusion. The maxima in the shrinkage rate clearly accounts for all possible mass transport mechanisms operating in tandem. A further decrease

in the rate of shrinkage is mainly due to grain growth related phenomena. With progressive grain growth, the effective area offered by the grain boundaries decreases in the system. Since the grain boundaries act as vacancy sink for mass transport from the bulk, a reduction in it lead to events that decrease the mass transport rate and hence a reduction in the observed shrinkage rate. Grain growth can occur only after a certain degree of shrinkage because the neck curvatures are initially very large and pin the grain boundaries [41]. In case of Mo–30 wt.% W, visible grain growth can be seen only beyond 1373 K as seen in the SEM image (Fig. 4.13d).

From the above discussion, it is therefore quite clear that the SID approach is a very useful tool to evaluate the sintering kinetics of metallic systems and gives fairly reliable values of the activation energies associated with different mechanism of mass transport using the dilatometry data of a single experiment. The model results are found to be consistent with the micro structural evolution, as revealed by SEM analysis (Fig. 4.13).

4.4 Pack siliconisation

The results of the coating experiments have been summarized in Table–4.6. First, second and third rows show the effect of concentration of activator, whereas second, fourth and fifth rows show the effect of temperature on the thickness, composition and nature of the coating. From the results it is seen that the activator has no significant role on the coating thickness and formation of multilayer coatings. However, the effect of activator was seen on the surface morphology of the coating.

Table–4.6: The results of the coating experiments over Mo–30W alloy

Acivator (wt. %)	Temperature (°C)	Thickness/Remark (µm)	Coating Composition (at. %)
1	900	25, Single porous layer	Si–65.1, Mo–28.9, W–5.7
2.5	900	30, Single smooth layer	Si–65.5, Mo–29.0, W–5.5
10	900	32, Single curvy layer	Si–66.4, Mo–28.5, W–5.1
2.5	1100	50, Single smooth layer	Si–65.4, Mo–29.7, W–4.9
2.5	1300	60, Double layer	Si–65.9, Mo–29.5, W–4.6

4.4.1 Evolution of microstructure, phase and interface

Fig. 4.14a and 4.14b show the SEM images captured in back scattered electron mode of the cross-sections of the coated specimen, heat treated at 1173K and 1573K for 6h with 2.5% activator as a representative. Cross-sectional SEM image of the sample coated using higher content of activator (10%) showed non-uniform (wavy) interface, while uniform interface was seen for the coated sample using 2.5% activator. At least 10 measurements were taken and the average thicknesses of the coating layers were determined. The coating thicknesses obtained at coating temperatures of 1173 and 1573K were 25 and 60 μ m respectively. No cracks were observed in the coating layer. Single layer and double layer coatings were observed in the microstructure of the coating for the sample coated at 1173K and 1573K respectively. The quantitative microanalyses in the different layers, shows the concentration of Si as 66 at. % in the coating region for sample coated at 1173K and at the outer layer of sample coated at 1573K. Whereas, concentration of Si was found to be 37 at.% of the inner layer of sample coated at 1573K. 66 at.% Si corresponds to (Mo, W)Si₂ and 37 at. % corresponds to (Mo, W)₅Si₃ layer. The exact compositions of the different layers at different conditions are given in Table-4.7.

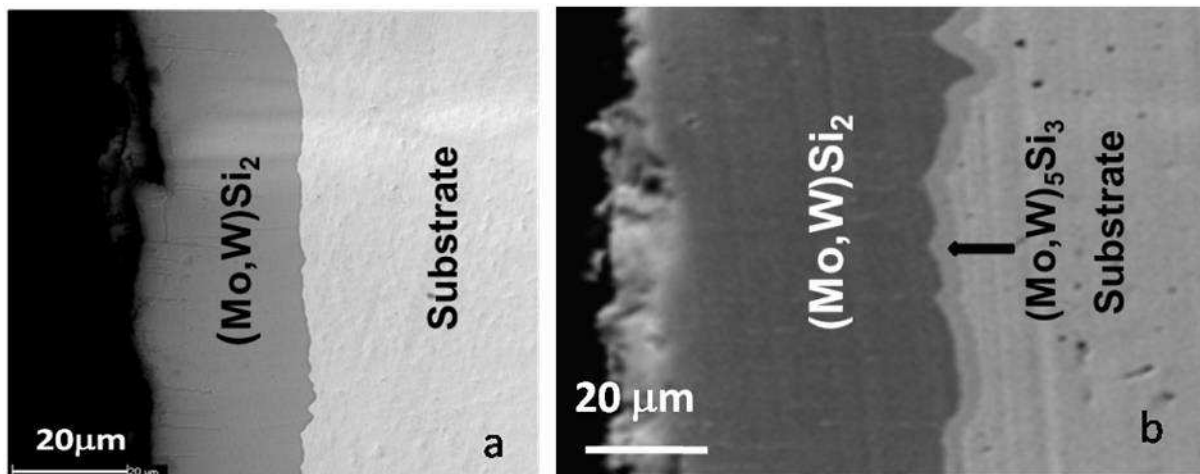


Fig. 4.14a and 4.14b BSE images of the cross-sections of the coated specimen, heat treated at 1173K and 1573K.

Table: 4.7: The exact compositions of the different layers at different coating temperatures

Coating Temperature	Average composition (At. %)		Ratio of Mo to W	
	Outer layer	Inner layer	Outer layer	Inner layer
900°C	Si-65.5, Mo-29.0, W-5.5	—	5.27	—
1300°C	Si-65.9, Mo-29.5, W-4.6	Si-36.04, Mo-49.7, W-13.9	6.41	3.7

Fig. 4.15 shows the BSE image and corresponding EDS line scan over the interface of sample coated at 1573K. From the line scans it is clearly seen that the concentration of W is higher in the coating region as compared to the substrate. However, the average composition of the coating layer does not show an increase in the concentration of W. To understand this anomaly, point analysis was carried out along the interface at several locations at fixed gap. Fig. 4.16 and Fig. 4.17 show the concentration profile along the interface determined from point analysis of the sample coated at 1173K and 1573K respectively. From the profile it is seen that concentration of both Mo and W decreased in the coating region while the concentration of Si increased. Therefore, the result of EDS line scan shown in Fig. 4.15 was found to be erroneous. The line scan carried out in this study is basically a qualitative technique, where the abundance of particular X-ray energy, rather than its intensity is plotted with distance along a line. It cannot differentiate between two elements having very close characteristic X-ray energy. Fig. 4.18 shows the spectrum of coating region that shows that the Si K_{α} line (1.7398 keV) and the W M_{α} line (1.7744 keV) are very close and merged. Therefore, the individual concentration profile of W and Si shown in Fig. 4.15 is actually for the combined profile of W and Si.

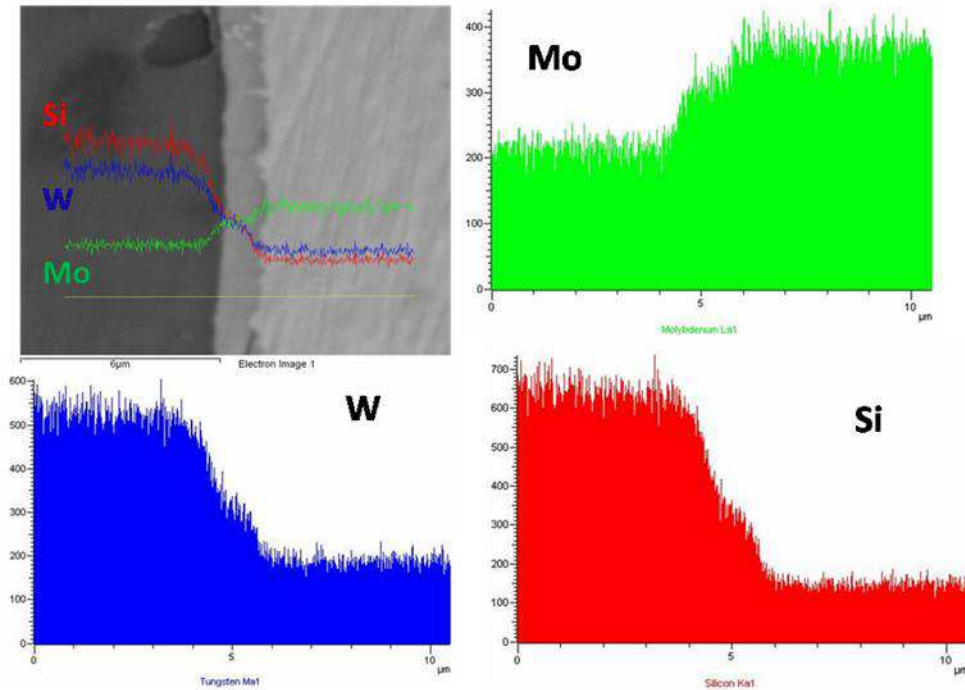


Fig. 4.15: BSE image and corresponding EDS line scan over the interface of sample coated at 1573K, which shows the formation of double layer of $(\text{Mo,W})_2\text{Si}$ coating

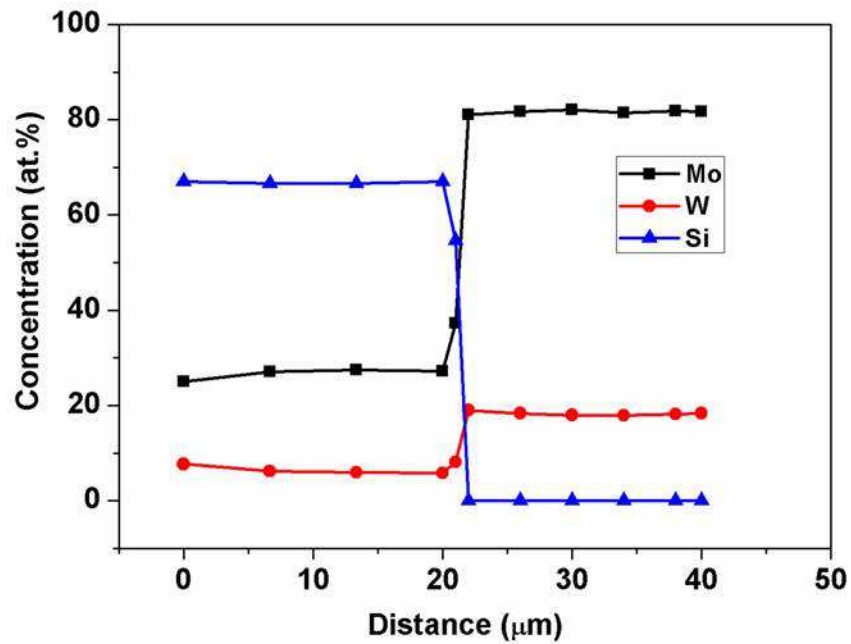


Fig. 4.16 Concentration profile along the interface determined from point analysis for the sample coated at 1173K

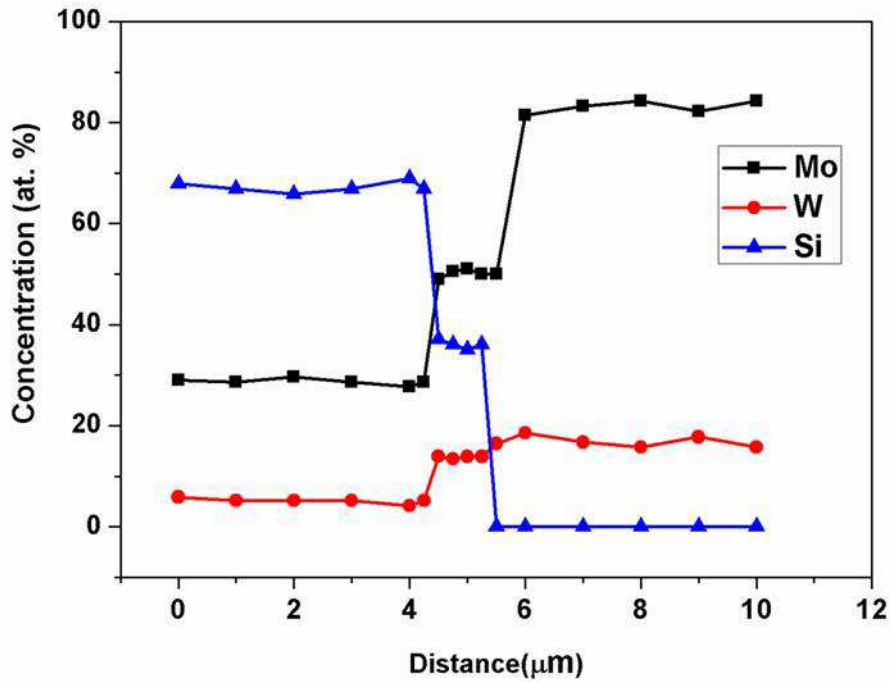


Fig. 4.17 Concentration profile along the interface determined from point analysis for the sample coated at 1573K

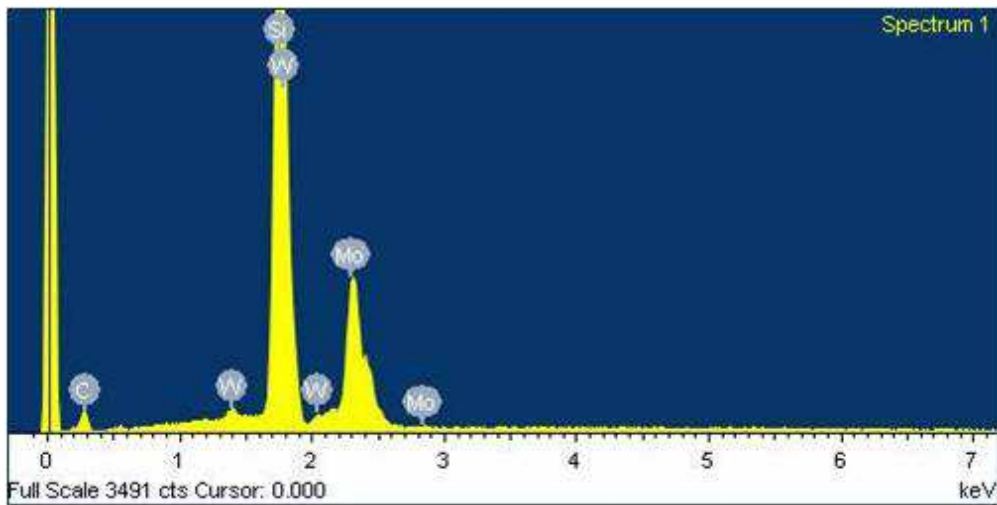
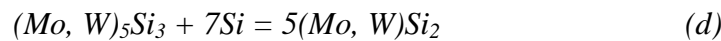
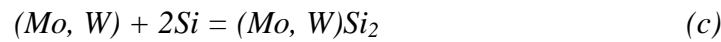
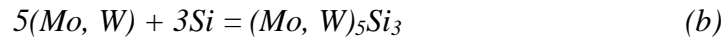


Fig. 4.18 Spectrum of coating region

The mechanism of pack cementation coating is known to be governed by the inward diffusion of Si flux into the substrate. However, if this were to be true, the Mo to W ratio in the substrate and coating (silicide) should be same. In contrast, the ratio of Mo to W was found to have increased in the coating region as compared to substrate as shown in the Table–4.8. Further, the ratio of Mo to W in the coating increased with increase in coating temperature. A higher ratio of Mo to W in the coating region indicates that the coating was

formed not only because of the inward diffusion of Si but there is also a role of outward diffusion of Mo. To understand the exact mechanism, the process needs to be studied from the formation of the very first layer. In the pack cementation technique, the primary driving force for diffusion of the halide vapors from the surroundings to the metal surface is the chemical potential gradient. First of all, activator, NH_4F dissociates into NH_3 and HF at about 573K and subsequent reactions between HF and Si results to the formation of the vapors of SiF_4 , SiF_3 , SiF_2 and SiF . The coating process is primarily dictated by the formation, migration and finally dissociation of Si– fluorides. Actually, first of all, a monolayer of any of the three silicide is formed due to the dissociation of silicon fluoride (either of SiF_4 , SiF_3 , SiF_2 or SiF) to Si. The Formation of three different types of silicides can be shown as [42]:



Immediately after the formation of first layer of silicide, the silicon layer and (Mo, W) are separated by the silicide layer. For the reaction to proceed further, either (Mo, W) or Si must diffuse through the silicide layer.

Silicon is the dominant diffusing specie in the disilicides such as – TiSi_2 , VSi_2 , NbSi_2 and TaSi_2 [43, 44]. Since these disilicides and $(\text{Mo}, \text{W})\text{Si}_2$ have similar structures, Si is expected to be the dominating diffusing species in $(\text{Mo}, \text{W})\text{Si}_2$ also. The crystal structure of these disilicides is shown in Fig. 4.19. MoSi_2 phase has a body centered tetragonal, C11b structure with 6 atoms per unit cell [45]. The typical unit cell consists of different layers of Mo and Si; each Mo layer followed by two layers of Si. A Mo atom is surrounded by 10 Si atoms, while a Si atom is surrounded by 5 Si and 5 Mo atoms. The silicon atoms have only silicon as nearest neighbours, therefore the silicon diffusion could take place through a silicon vacancy mechanism. While the metal atoms cannot diffuse by a single vacancy mechanism, since the metal atoms have only silicon atoms as nearest neighbours [43, 44]. Mo should be practically immobile unless it diffuses because of the concentration of different kinds of defects. Therefore, if the first layer formed is disilicide, coating should be governed by inward diffusion of Si flux into the substrate.

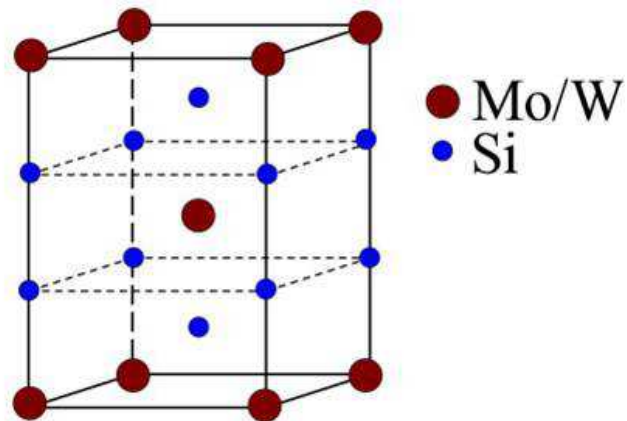


Fig. 4.19: Crystal structure of disilicides

On the other hand Mo_5Si_3 has a body centered tetragonal (BCT) structure with 32 atoms per unit cell. Since there are only 2 Si–Si bonds compared to 8 Mo–Mo bonds in the structure, higher diffusion rate of Mo would be expected for equal concentration of vacancies in the structure. Therefore, if the second layer is metal rich silicides, such as $(\text{Mo,W})_5\text{Si}_3$, one would expect higher diffusion rate of Mo. Although, the calculation of tracer diffusion coefficients indicates that on an average Si is almost 103 times faster than Mo, but Mo would not be immobile as in the case of disilicide [45].

Since the ratio of Mo to W in the coating region is found to increase in the coating region, $(\text{Mo,W})_5\text{Si}_3$ is expected to be the first layer formed at metal–silicon interface. Since, the diffusion of Mo is higher than the diffusion of W at a given temperature; Mo would diffuse outwardly rather than W to enhance coating in the silicide–Si interface. This is important to mention here that, in the absence of W in the alloy, the role of outward diffusion of Mo in coating formation could not have been realized. The prediction of formation of $(\text{Mo,W})_5\text{Si}_3$ at the first instance is also corroborated through the thermodynamic data. Since Mo is the major constituent, thermodynamic data on Molybdenum silicides should be well applicable for (Mo, W)–silicides as well. All these reactions shown through equation–(1) to (4) are feasible for Mo and can take place spontaneously. However, the generation of Mo_5Si_3 is the easiest, with the lowest Gibbs energy change shown in Fig. 4.20 [42].

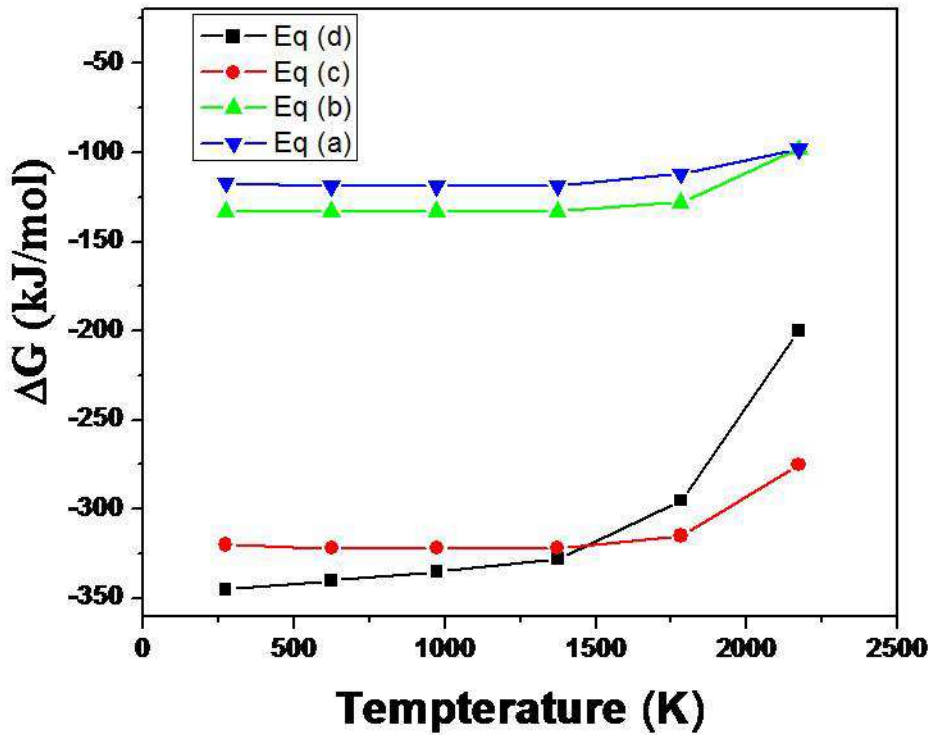


Fig. 4.20: Gibbs energy change Vs temperature for reaction 1–4

4.5 Hardness studies

Fig. 4.21 shows the plot of micro-hardness as a function of the distance across interface for the sample coated at 1300 °C. The Vickers micro-hardness values of the (Mo,W)Si₂ phase found to be 1250 ± 30 Hv for both the samples, while the hardness value for (Mo, W)₅Si₃ phase ranged between 726 ± 20 Hv. Fig. 4.22 shows the profiles of Vicker's indentations at a load of 25gm, which shows the variation of indentation size at coating and substrate. It is clear that the diagonals of indentations at substrate are longer than the diagonal of indentation at coating, yielding lower hardness at the same load.

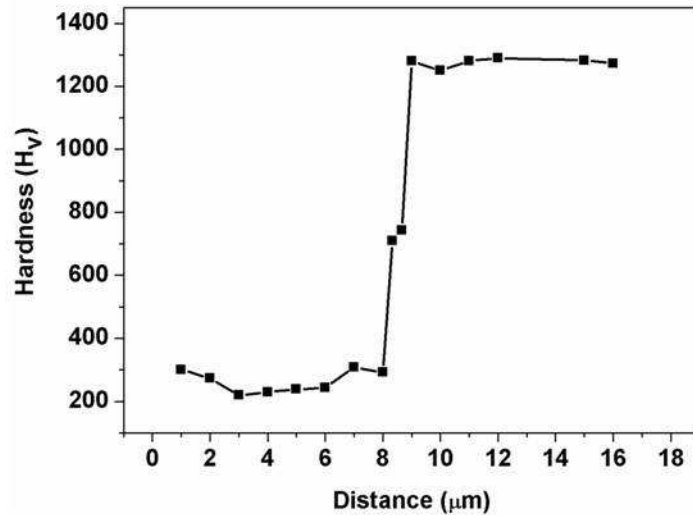


Fig. 4.21 Plot of micro-hardness as a function of distance across interface for the sample coated at 1573K

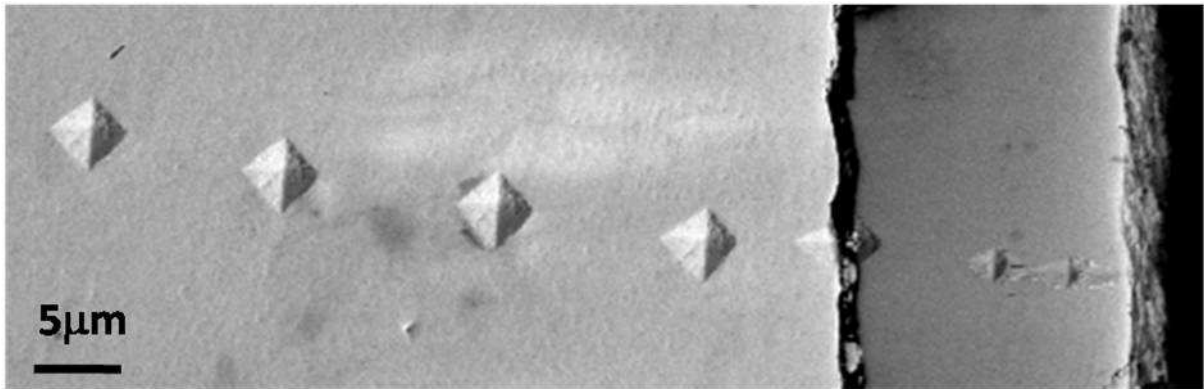


Fig. 4.22 Profiles of Vicker's indentations at substrate and coating

4.6 Friction and Wear Behavior

The frictional behavior of the coated (at 1173K and 1573K) and uncoated samples were investigated during reciprocating sliding against a alumina (Al_2O_3) ball (3/8" Dia) at sliding frequency varied from 10 Hz to 30 Hz, keeping other variables (100 000 cycles, 1 mm amplitude, and 7 N load) constant. The evolution of coefficient of friction (COF) against the sliding distance for all three samples are shown in Fig. 4.23, while Fig. 4.24 presents variation of average COF with sliding frequency. Regular fluctuations in frictional curve of Mo-W alloy were observed, which are more prominent during initial sliding. Such fluctuations in COF can be attributed to the wear debris formation and stick slip behavior during sliding. For MoSi_2 coated samples frictional curve are much stable indicating smooth sliding. However average COF in both the coated samples were in narrow range of 0.47–0.42. As sliding frequency is increased this band had further narrowed. General tendency of

reduction in average COF with increased sliding frequency was noted in all the samples. Single layered coating has shown reduced friction coefficient as compared to double layered coating. It is generally realized that relative motion of ceramic/ceramic wear debris can reduce friction by accommodating sliding and absorbing the deformation energy. Such contact also leads to lower real contact area as compared to ceramic/metal contacts.

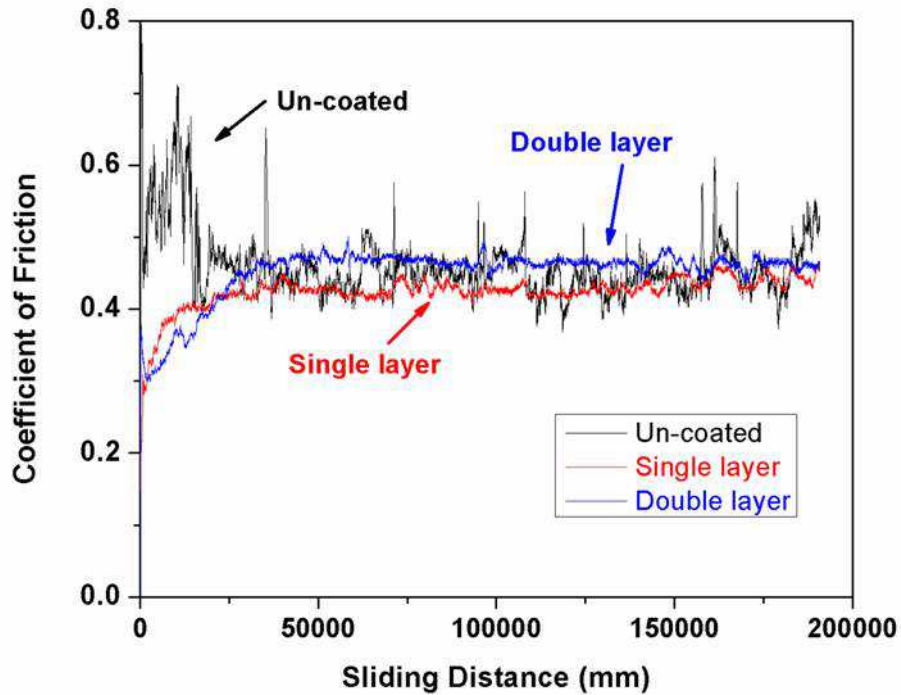


Fig. 4.23 Evolution of coefficient of friction with sliding distance

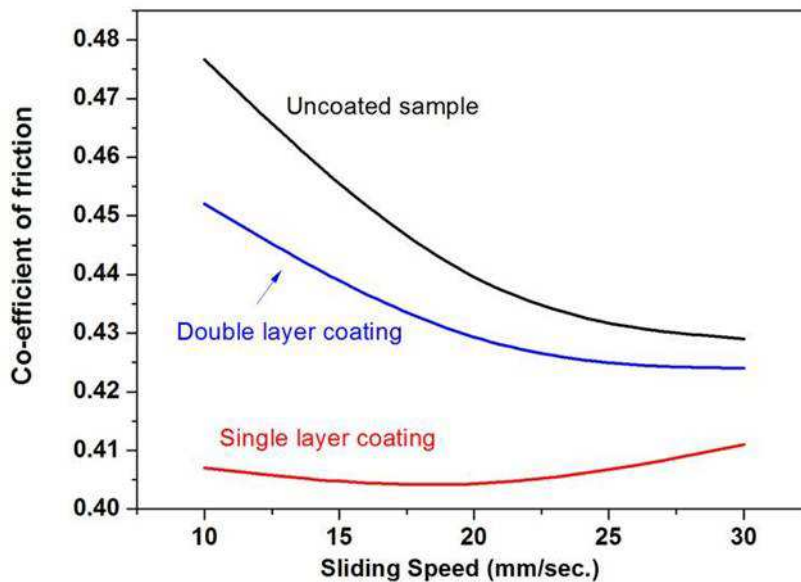


Fig. 4.24 Variation of COF with Speed

A typical 3D depth profile of the wear scar of Mo–W alloy is presented in Fig. 4.25. Variation of wear rate of alumina ball and flat sample with change in sliding frequency are presented in Fig. 4.26(a) and Fig. 4.26(b) respectively. It can be noted that the wear rate of the uncoated Mo–W alloy is significantly higher at all sliding speed as compared to coated samples. It was also observed that the wear rate of uncoated Mo–W alloy reduced with increase of sliding speed, whereas the wear rate of coated samples increased with sliding speed. The wear rates of both the coated samples were found almost equal at all test conditions.

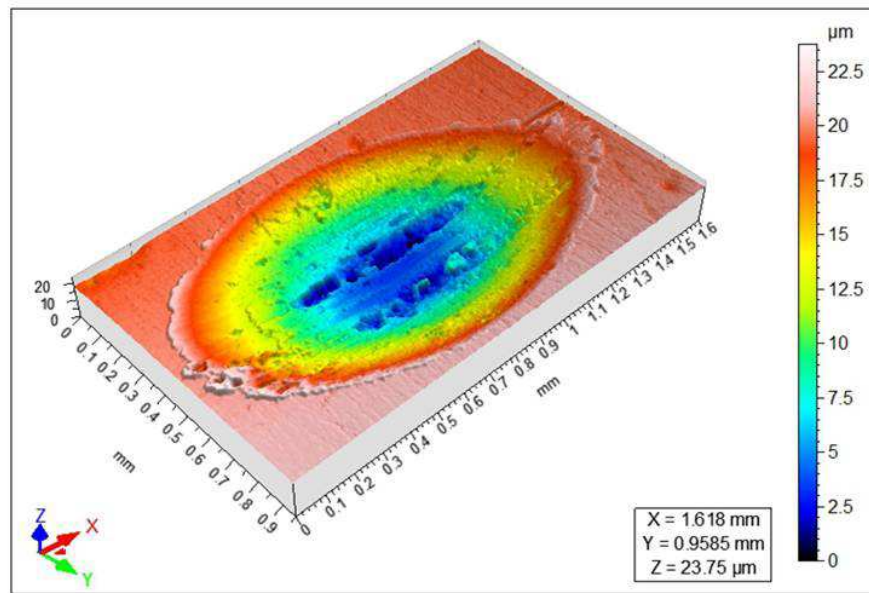


Fig. 4.25 Typical 3D profile of wear scar

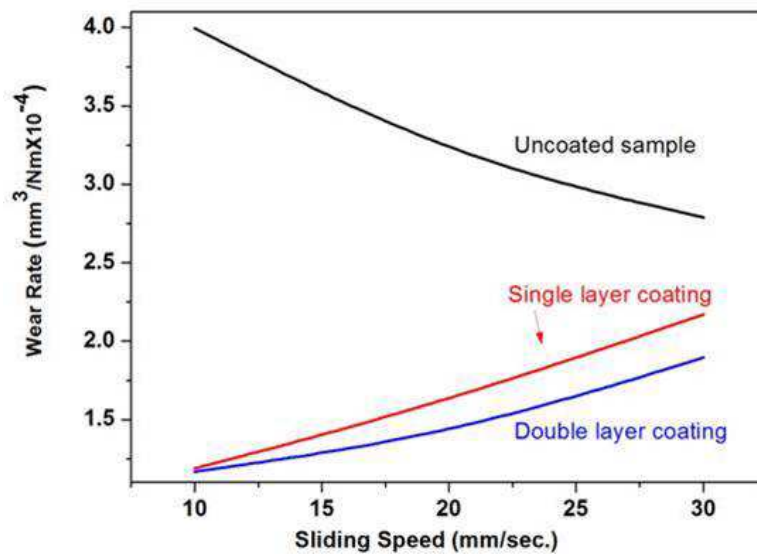


Fig. 4.26(a) : Variation in Wear rate of Al₂O₃ Ball with speed

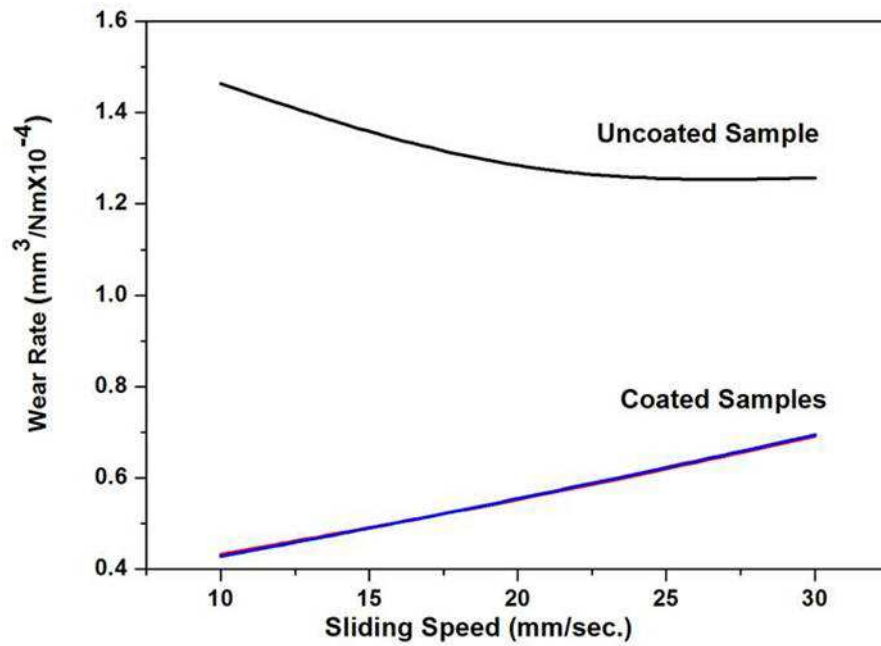


Fig. 4.26(b) Variation in Wear rate of coating with Speed

In order to understand the wear mechanisms, the topographical observations of the worn surfaces were made using SEM (Fig. 4.27a to 15C). Fig. 4.27 (a) indicates microcracks and large region of spalling along the sliding direction on un-coated Mo–W alloy sample. The wear debris particles were located around the wear scar, and some amount of compacted debris could be found on the worn surface. Representative worn surfaces of the coated samples show mild abrasive grooves (Fig. 4.27 (b) and Fig. 4.27 (c)). The presence of crack networks and mild abrasion is noticeable on the worn surface shown in Fig. 4.27 (b). There was no evidence of any transfer of material from the counter body to the samples.

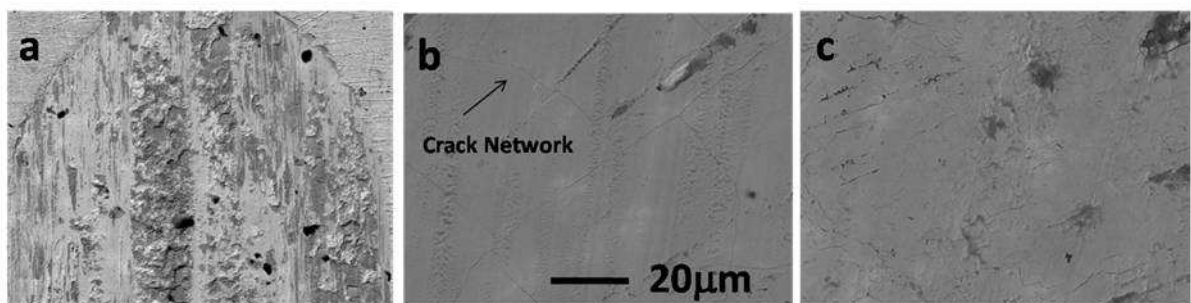


Fig. 4.27 SEM images of the worn surfaces (a) uncoated Mo–W alloy (b) Mo–W alloy coated at 1173K (c) Mo–W alloy coated at 1573K

Sample coated at 1573K shows less surface cracks and surface de-lamination as compared to sample coated at 1173K. Apart from crack network, SEM image of sample coated at 1573K also indicates material pullout along the sliding direction. Therefore, coated sample having a double layer (coated at 1573K) is more crack resistant and less prone to de-lamination as compared to single layer coated sample. There were no evidences found for de-lamination between inner and outer layer, when examined the cross sections of the coated samples. Fig. 28a and 28b shows the cross section of the coated sample after wear test. The double layer coated sample clearly shows the role of the inner layer in resisting cracking propagation. On the other hand, crack propagated/penetrated to the substrate in case of single layered coated sample. The $(\text{Mo,W})_5\text{Si}_3$ inner layer contains more metallic concentration [Mo and W] (as compared to $(\text{Mo,W})\text{Si}_2$) and therefore expected to have better fracture resistance in comparison to $(\text{Mo,W})\text{Si}_2$.

Besides, the coated sample having a double layer is expected to be less prone to delamination during thermal cycling because of minimization of mismatch of co-efficient of thermal expansion of substrate and coatings. Thermal stress resulting from the mismatch in co-efficient of thermal expansion (CTE) between the coating and substrate can cause cracks in the coating, if they reach or exceed a critical value (the strength of silicides).

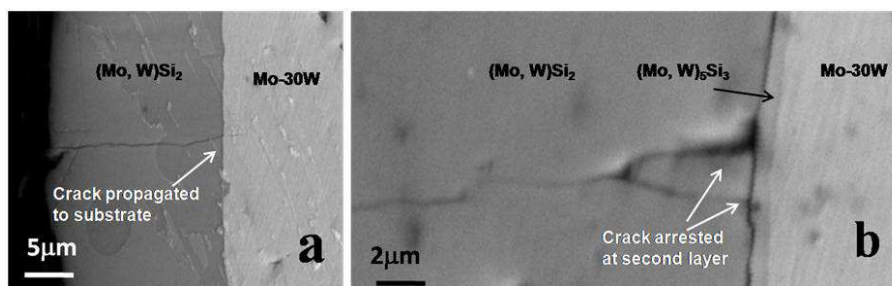


Fig. 4.28a and 4.28b Cross section of the coated sample after wear test

4.7 Oxidation test

Cyclic oxidation tests were carried out for coated samples at 1273K in flowing air for 50h. The samples were kept for 10 h at each cycle. There was no chipping or peeling-off of the coating material from the coated surface at the end of the heating cycle. Maximum weight gain ($4 \times 10^{-5} \text{ kg/m}^2$) was observed for the sample which was coated at 1173K using 2.5% activator, suggesting the excellent protectiveness of the coating against oxidation.

4.8 Summary

1. Sintering kinetics of sub micron sized Mo-30 wt.% W alloy powder prepared through mechanical alloying was studied by both, constant rate of heating (CRH) and stepwise isothermal dilatometry (SID) technique.
2. Sintering in this alloy occurs through two dominant mechanisms with average activation energies of 230 and 480 kJ/ mole corresponding to grain boundary diffusion and lattice diffusion, respectively. The results are found to be consistent with the microstructural evaluation as studied by SEM analysis.
3. Furthermore, the diffusivities calculated in this study agree well with previous reported values by high temperature tracer determinations.
4. To protect the Mo-30W alloy under oxidizing atmosphere, silicide based oxidation resistant coating were formed. Double layer coating consisting of $(\text{Mo,W})_5\text{Si}_3$ and $(\text{Mo,W})\text{Si}_2$ was formed at coating temperature of 1573K, whereas single layer coating consisting of $(\text{Mo,W})\text{Si}_2$ was formed at coating temperature below 1573K.
5. The hardness values of the $(\text{Mo,W})\text{Si}_2$ phase ranged between 1250 ± 30 Hv for both the samples coated at 900°C and 1300°C , while the hardness value for $(\text{Mo, W})_5\text{Si}_3$ phase ranged between $726 \pm 20\text{Hv}$.
6. The wear rate of un-coated Mo-W alloy is significantly higher at all sliding speed as compared to $(\text{Mo, W})\text{Si}_2$ coated samples. Although wear rate of both coated samples is almost equal at all test conditions, double layer coating formed at 1300°C showed improved crack resistance.
7. Double layered coated alloy showed excellent oxidation resistant under cyclic oxidation test at 1273K for 50h.

References

- [1] H. L. Brown, C. P. Kempter. Elastic properties of thoriated W–Mo and W–Mo–Re alloys. *J. less–comm. met.* 12 (1967) 166–168.
- [2] D.B. Lee, G. Simkovich. Oxidation of molybdenum–tungsten–chromium–silicon alloys. *Oxid. Met.* 31 (1989) 265–274.
- [3] R.B. Schwarz, C.C. Koch. Formation of amorphous alloys by the mechanical alloying. *Appl. phy. Lett.* 49 (1986) 146–148.
- [4] H.G. Tang, X.F. Ma, W. Zhao, S.G. Cai, B. Zhao, Z.H. Qiao. The mechanical properties of magnesium matrix composites reinforced with 10 wt.% W14Al86 alloy particles. *J. Alloys Compd.* 430 (2007) 77–80.
- [5] A. Bose, G. Jerman and R.M. German. Properties of Swaged and Aged Molybdenum Doped Heavy Alloys. *Powder Metall. Intl.* 21 (1989) 9–13.
- [6] W.D. Kingery, M. Berg. Study of the initial stages of sintering. *J. Appl. Phys.* 26 (1955) 1205–1212.
- [7] J.G.R. Rockland. On the rate equation for sintering by surface diffusion. *Acta Metall.* 14 (1966) 1273–1279.
- [8] R.L. Coble. Initial Sintering of Alumina and Hematite. *J. Am. Ceram. Soc.* 41(1958) 55–62.
- [9] D.J. Jones. Practical aspects of sintering tungsten and molybdenum. *J. less–comm. met.* 2 (1960) 76–85.
- [10] <http://www.plansee.com/>
- [11] R. M. German, Z.A. Munir. Heterodiffusion model for the activated sintering of molybdenum. *J. less–comm. met.* 58 (1978) 61–74.
- [12] D.C. Blaine, J. D. Gurosik, S.J. Park, R. M. German, D. F. Heaney. Master Sintering Curve Concepts as Applied to the Sintering of Molybdenum. *Metall. Mater. Trans. A* 37A (2006) 715–720.
- [13] N.C. Kothari. Sintering kinetics in tungsten powder. *J. less–comm. met.* 5 (1963) 140–150.
- [14] J.A.M Van Liempt, *Rec. Trav. Chim.* 64 (1945) 239–245.
- [15] X F. Ashby. A first Report on Sintering Diagrams. *Acta Metallurgica* 22(1974) 275–289.

- [16] G.A.Gospodinov, V.K.Pangarova, D.K.Lambiev. Activated sintering of a mixture of tungsten and molybdenum powders. *Sov. Powder Metall. Met. Ceram.*, 15 (1976) 159–161.
- [17] R. Sakidja, F. Rioult, J. Werner, J.H. Perepezko. Aluminum pack cementation of Mo–Si–B alloys. *Scr Mater* 55 (2006) 903–906.
- [18] R. Sakidja, J.S. Park, J. Hamann and J.H. Perepezko. Synthesis of Oxidation Resistant Silicide Coatings on Mo–Si–B Alloys. *Scr. Mater.*, 53, (2005) 723–728.
- [19] S. Majumdar, I. G. Sharma, S. Raveendra, I. Samajdar and P. Bhargava. In situ chemical vapour co–deposition of Al and Si to form diffusion coatings on TZM. *Mater. Sci. Eng.*, 492, 211–217 (2008).
- [20] S. Majumdar, I. G. Sharma, I. Samajdar, P.J. Bhargava. Relationship between pack chemistry and growth of silicide coatings on Mo–TZM alloy. *Journal of Electrochemical Society*. 155 (2008) 734–740.
- [21] S. Majumdar and I. G. Sharma. Oxidation behavior of MoSi₂ and Mo(Si, Al)₂ coated Mo–0.5Ti–0.1Zr–0.02C alloy. *Intermetallics.*, 19, 541–545 (2011).
- [22] J. S.Park, R. Sakidja and J. H. Perepezko. Coating Designs for Oxidation Control of Mo–Si–B Alloys. *Scr. Mater.*, 46, 765–770 (2002).
- [23] B. Paul, S. Majumdar and A. K. Suri. Microstructure and mechanical properties of hot pressed Mo–Cr–Si–Ti in–situ composite, and oxidation behavior with silicide coatings. *Int. J. Refractory Metals and Hard Mater.*, 38 (2013) 26–34.
- [24] B.D Cullity, *Elements of X–ray Diffraction*, Addison–Welsey, Reading, MA, 1969.
- [25] B.C. Rathore, P. Bharati. Theoretical optimisation of constitution of alloys by decoding their densities. *Mater Lett* 2007;61:2956–2960.
- [26] W.S. Young, I.B. Cutler. Initial sintering with constant rate of heating. *J. Am. Ceram. Soc.* 53 (1970) 659–663.
- [27] D.L. Johnson. New method of obtaining volume, grain–boundary, and surface diffusion coefficients from sintering data. *J. Appl. Phys.* 40 (1969) 192–200.
- [28] R. Yan, F. Chu, Q. Ma, X. Liu, G. Meng. Sintering kinetics of samarium doped ceria with addition of cobalt oxide. *Mater. Lett.* 60 (2006) 3605–3609.
- [29] G. Y. Meng, O. T. Sorensen, Y. Han (Ed.), *Advanced Structural Materials*, vol. 2 Elsevier Science Publishers B.V., Amsterdam, Netherlands, 1991 369–374.

- [30] H. T. Wang, X. Q. Liu, F. L. Chen, G. Y. Meng. Fabrication of silicon-based ceramic J. Am. Ceram. Soc. 81 (1998) 781–784.
- [31] Y. F. Liu, X. Q. Liu, S. W. Tao, G. Y. Meng, O. Toft. Sorensen, Ceram. int. 28 (2002) 479–486.
- [32] B. Paul, D. Jain, A.C. Bidaye, I.G. Sharma, C.G.S. Pillai. Sintering kinetics of submicron sized Cobalt powder. Thermochim. Acta, 488 (2009) 54–59.
- [33] V.V. Dabhade, T.R. Rama Mohan, P. Ramakrishnan. Sintering behavior of titanium–titanium nitride nanocomposite powders. Mater. Sci. Eng. A 452–453 (2007) 386–394.
- [34] V. S. Bakunov, A. V. Belyakov. Production of transparent ceramic. Glass Ceram., 50 (1993) 287–[291](#).
- [35] S. Majumdar, S. Raveendra, I. Samajdar, P. Bhargava, I.G. Sharma. Densification and grain growth during isothermal sintering of Mo and mechanically alloyed Mo–TZM. Acta Materialia 57 (2009) 4158–4168.
- [36] R.M. German, Sintering Theory and Practice, John Wiley and Sons, New York, 1996.
- [37] M.L. Huckabee, H. Palmour III. controlled sintering of fine grained Al₂O₃. Am. Ceram. Soc. Bull. 51 (1972) 574–576.
- [38] M. Kramer. Rate-controlled sintering of Si₃N₄ densification kinetics and microstructure development J. Mater. Sci. Lett. 14 (1995) 778–782.
- [39] D. Lahiri, S.V. Ramana Rao, G.V.S. Hemantha Rao, R.K. Srivastava. Study on sintering kinetics and activation energy of UO₂ pellets using three different methods J. Nucl. Mater. 357 (2006) 88–96.
- [40] D. F. Kalinovich, I. I. Kovenskii, and M. D. Smolin, Sov. Powder Metall. Met. Ceram., 4 (1965) 324–326.
- [41] P. E. Zovas and R. M. German. Activated and Liquid Phase Sintering– Progress and Problems, Journal of Metals, 35 (1983) 28–38.
- [42] H. Qiaodan, L. Peng, Q. Da, Y. Youwei. Self-propagation high-temperature synthesis and casting of Cu–MoSi₂ composite. J Alloys and Comp. 2008;464;157–161.
- [43] F.M. d'Heurle.. Material properties of silicides and device technology implications. In VLSI Science and Technology/ 1982, ed. C. J. Dell'Oca and W. M. Bullis, pp. 194–209. Pennington, NJ: Electrochem. Society.

- [44] C. M. Doland. Molybdenum silicide formation on single crystal, polycrystalline and amorphous silicon: growth, structure and electrical properties Thesis, University of Houston–University Park.
- [45] S. Prasad, A. Paul. Growth mechanism of phases by inter–diffusion and atomic mechanism of diffusion in the molybdenum–silicon system. *Intermetallics* 19 (2011) 1191–1200.

Chapter–5

(Preparation of Mo–Cr–Si composite alloy and development of oxidation resistant coatings)

5.1 Introduction

Design of high temperature material having properties such as high temperature oxidation resistance, strength, creep resistance on one hand and room temperature fracture toughness on the other is a challenging task in material science. Maximum operating temperature capability of superalloys has risen significantly, but eventually it faces melting point limitation of major alloying element e.g. Co, Ni. The next choice is refractory metals and alloys, because of their high melting points and their high temperature strength. The major barrier to the use of molybdenum based alloys for high-temperature applications is their catastrophic behaviour under oxidizing environments. The oxidation problem of refractory metals falls into two different categories. The first category consists of Nb and Ta which have very high oxygen solubility. Due to its high solubility of O_2 , internal oxidation occurs at low O_2 pressure without the formation of an external scale and affecting room temperature ductility and increase in strength. The second category includes Mo and W that have relatively low oxygen solubility but form volatile oxides at high temperature. Therefore, choice for selection of refractory metals and alloys should be based on the operating environment especially with respect to partial pressure of O_2 . Taking into the design consideration of density, among the refractory metals, Nb followed by Mo are suitable candidates for structural applications from the above mentioned categories. The volatility of MoO_3 represents a significant degradation mechanism, but it is not as insidious as the oxygen embrittlement problem exhibited by Nb based alloys at low partial pressure of oxygen.

To improve the alloy oxidation resistance, additions of Al, Si, Cr or their combinations are required because they form stable and protective oxide scales – Al_2O_3 , SiO_2 , or Cr_2O_3 respectively. Alloying with Cr, Al, Si has not been very successful because of the need for a high level of addition of alloying elements to form external protective scale that allow brittle intermetallic phase such as aluminides and silicides to form. However, recent success with multiphase system, especially Mo–Si–B alloy, has paved the path for the future research in this direction. The multiphase approach has led to the study of the systems that provide a high level of freedom in selecting compositions of the constituent phases in order to obtain a more favorable balance of high temperature strength, creep, good oxidation resistance and at the same time damage tolerance ability particularly at lower temperatures. This class of alloys are also known as refractory metal intermetallic composite (RMIC). In this category, Mo–Si–B alloy system has been studied extensively, in which the more ductile Mo_{ss} phase is reinforced with Mo_3Si (A15) and Mo_5SiB_2 (T2) phases [1–17]. Efforts have

also been made to enhance further the room temperature ductility, fracture toughness [18], phase stability [19] and high temperature oxidation resistance [20, 21] of these materials with alloying additions of Ti, Zr, Al, Ce, Hf etc. Multi-phase structure gives the extra degree of freedom of variation for achieving desired properties. For Mo, Si is the most important alloying element which results in various combination of desirable multiphase system. Less than 10 wt % of Si concentration in Mo, form a two-phase structure of Mo +Mo₃Si. The concentration of Si needed for establishment of a self-healing and protective layer, can be reduced significantly by the addition of a third element such as Cr. Cr forms a solid solution with Mo and increases the oxidation resistance [22]. So, Mo–Cr–Si ternary alloy system emerged as a promising candidate possessing good properties for high temperature applications [23]. However, a very little information is available in the literature on the processing and the properties of Mo–Cr–Si alloys.

Once the alloying elements are selected, the second unknown design parameter is alloy composition. The ratios of the volume ratio of the two constitutive phases (Matrix Mo and silicides) change according to alloy compositions, which are the deciding factor for oxidation resistance and fracture toughness of the alloys. Hence, it is not possible to choose a single alloy composition that exhibits both good oxidation resistances at high temperature as well as fracture toughness at room temperature. Therefore, optimization of the composition is necessary for achieving targeted properties. Based on the experience of Mo–Si–B alloys, the consensus is that about 30% of volume ratio of second phase is required for adequate room temperature fracture toughness along with high temperature oxidation resistance of the RMICs. Therefore, the composition of the Mo–16Cr–4Si was chosen from the ternary phase diagram which has 30% of volume percentage Mo_{ss}. Fig.5.1 shows the phase diagram of Mo–Si and ternary Mo–Cr–Si.

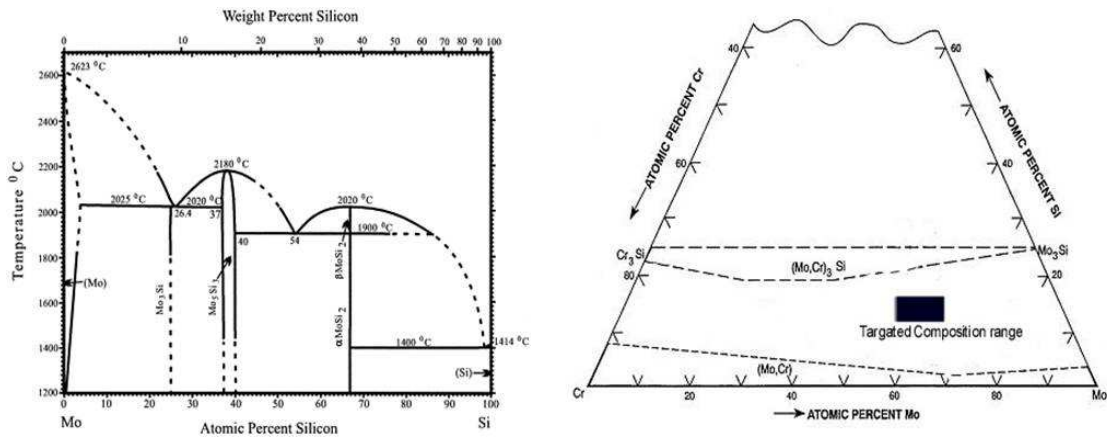


Fig. 5.1: Phase diagram of Mo–Si and Mo–Cr–Si system

The RMICs are synthesized using both the in–situ and the ex–situ processes. The materials produced by the in–situ method show superior characteristics; for instance, better adhesion between the intermetallic phase and the matrix phase, formation of more stable intermetallic phase, improved fatigue and creep resistance, uniform size distribution of the dispersed phase particles etc. [24]. The evolution of the microstructure, which consists of a matrix and the reinforced precipitates, depends directly on the processing route used for synthesis of the in–situ composite. Several processing techniques, which include spark plasma sintering [25], self–propagating high–temperature synthesis [26], hot isostatic pressing [27, 28], arc–melting [29] etc. have been successfully used to prepare the silicide–based composites.

Arc melting and powder metallurgy routes are the conventional techniques adopted to synthesize molybdenum based multiphase alloys. However, it is difficult to achieve good consolidation with homogeneity in alloy composition by arc melting technique due to high melting temperatures of alloying components. Self propagating high temperature synthesis (SHS) route has also been used frequently for the synthesis of different intermetallics (Mo_5Si_3 , MoSi_2) but mixtures of Mo and Si powders in the proportion corresponding to Mo_3Si (~9 wt % Si) could not be ignited for SHS reaction to proceed, even after preheating the charge [30]. Another alternative self sustaining synthesis route for synthesis of high temperature material is “Co–reduction synthesis route” also known as “Thermite smelting”. In this process, metal oxides are co–reduced simultaneously by a reductant which could be anyone or a combination of Al, Si, Ca, B, Mg etc. and the reactions which when triggered goes to completion because of their own exothermic heat [31–33]. Thermite process has many distinct advantages over other melting processes such as relatively high proportion of metallic products, low processing cost, fast process rate, high energy may or may not require

external heating from high-temperature furnace, flexibility of batch size etc. Therefore, an attractive and affordable alternative can be provided by thermit smelting as compared to the conventional methods for producing ceramic composites and intermetallic compounds. The essential feature of “Co-reduction synthesis route” like SHS process is a single step process and the heat required to drive the chemical reaction is supplied from the reacting constituents themselves. Once ignited, extremely high temperature (adiabatic temperature) can be achieved due to the highly exothermic reaction proceeding in a short time. This technique has been successfully utilized for making commercially important molybdenum based alloys such as TZM and TZC [32–33].

Hot pressing is another possible route to synthesize composites in-situ [34]. It utilizes high-pressure, and low-strain-rate for forming a powder compact at a temperature high enough to induce sintering and creep processes.

Since the ratio of volume ratio of the two constitutive phases (Mo_{ss} and silicide) is the deciding factor for the oxidation resistance and the fracture toughness of these alloys. No alloy composition would have good oxidation resistance at high temperature as well as good fracture toughness at room temperature. One approach to nullify the oxidation response of the different alloy compositions is through the application of coating [35, 36]. Pack cementation is a widely used in-situ coating technique, which produces uniform and adherent coatings even on complex shaped structures. The substrates and the coating layers formed by this method are compatible with respect to adhesion, thermal expansion etc. due to the formation of the in situ metallurgical bond [37–40].

This chapter covers the different aspects of synthesis of Mo–16Cr–4Si alloy by reaction hot pressing and co-reduction smelting technique using Si as reductant. Further study has been extended to examine the effect of varying concentrations of different alloying additions on the key properties such as oxidation resistance and the room temperature fracture toughness. Detailed characterization studies with respect to evolution of microstructure, fractography and oxidation behavior have also been carried out. Evolution of phases, microstructures after hot pressing and silicothermic reaction were studied by means of XRD, SEM and EDS. Besides, MoSi_2 based coatings were developed over the optimized alloy substrate, using the halide activated pack cementation technique. Oxidation behaviour of the alloys was studied with and without the protective coatings.

5.2 Studies on hot pressing

Fig.5.2 (a) shows the relationship between hot pressing temperature and relative density of the sintered Mo-16Cr-4Si alloy, for a constant sintering time of 3h. The theoretical density of the alloy was calculated, using the classical rule of mixture [41] to yield a value of $\sim 8470 \text{ kg/m}^3$. During the hot pressing at 10 MPa load, initially the density of sample increases quickly, with increasing hot pressing temperature. Later on, above 1800K, the density increases slowly, indicating a probable change in the sintering mechanism. Similarly, Fig.5.2 (b) shows the variation of relative density with respect to time at 1873K. There is no significant increase in density after 2 h of sintering time.

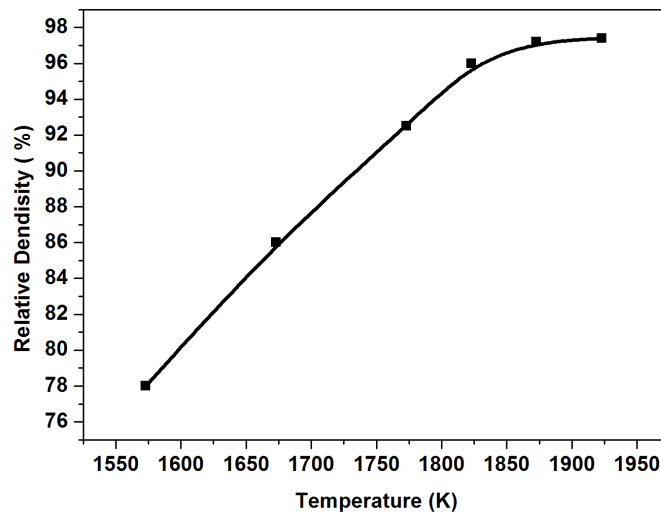


Fig. 5.2 (a): Plot of sintered density vs temperature for fixed sintering time of 3h.

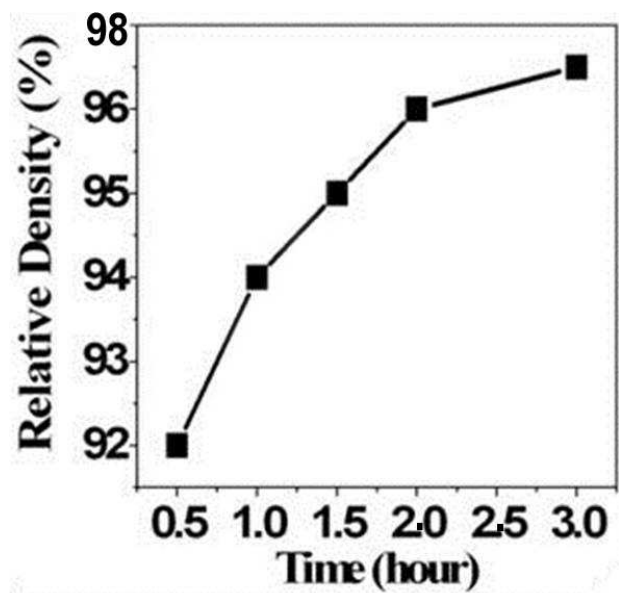


Fig. 5.2 (b) The plot of sintered density vs time at 1873K

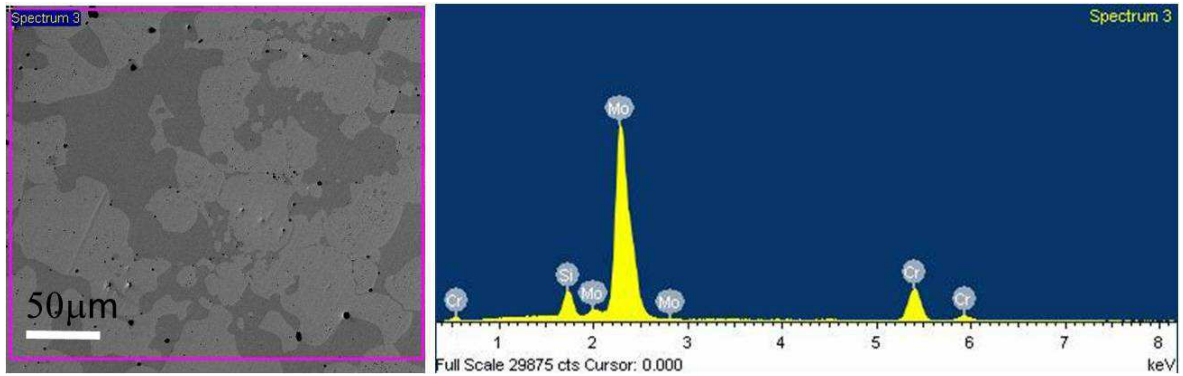


Fig.5.3: SEM images of hot pressed Mo-16Cr-4Si alloys sintered at 1873K and 10MPa load and the corresponding EDS spectrum

Fig.5.3 shows BSE image of Mo-16Cr-4Si alloy, sintered at 1873K and 10 MPa pressure and corresponding EDS spectrum. The microstructure of as sintered alloy consisted of two different contrast regions, namely white and dark due to different chemical compositions in these regions. The quantitative microanalysis in those regions was carried out by EDS for evaluating compositional variation. The detailed chemical compositions of these phases are shown in Table-5.1.

Table-5.1: Average compositions of the different phases of the alloy

Phase	Mo wt. %	Cr wt. %	Si wt. %
A	83.37	14.98	1.29
B	76.37	14.65	8.98

From the composition, it is seen that the first phase (phase-A) appearing light (white) is made up of a solid solution phase, basically of Mo and Cr with small amount of Si. The concentration of Si in the second (phase-B, appearing dark) is ~25 at.%, which indicates that the phase B is basically Mo_3Si type intermetallic phase, which was also confirmed by the XRD analysis. The XRD pattern of the sintered alloy is shown in the inset of Fig.5.5. The XRD result confirms the presence of peaks corresponding to elemental molybdenum and Mo_3Si . The slight shift of the Mo and Mo_3Si peaks are observed because of the lattice distortion caused by the formation of a solid solution of Mo with Cr and Si. The peaks corresponding to elemental Cr or Si (or their compounds) are not present.

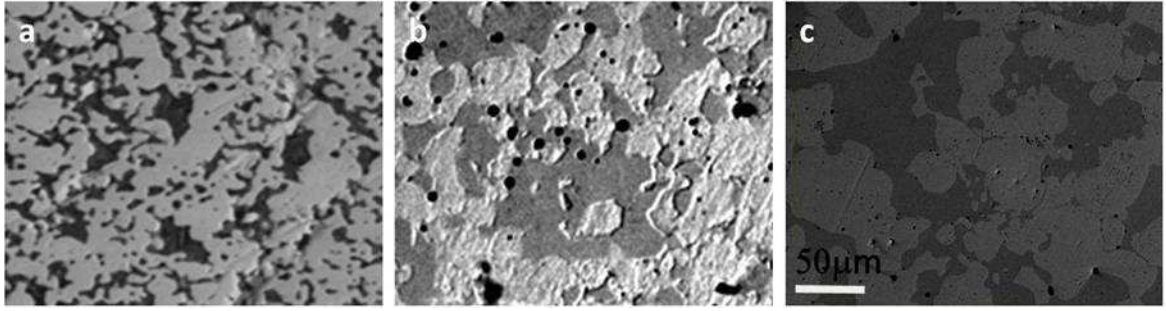


Fig.5.4: BSE image of alloy sintered at (a) 1673, (b) 1773 and (c) 1873K

Fig.5.4 shows the BSE images of the alloys sintered at 1673K, 1773K and 1873K, revealing the growth of the second phase and Fig.5.5 shows the influence of the hot pressing temperature on the average size of the silicide phase (phase-B), showing a sigmoidal growth behavior. When the temperature is lower than 1773K, the silicide phase grows slowly, and thereafter, it grows rapidly and then gradually until it finally reaches a constant size. The phase ratios (volume percentage) of the two constitutive phases were calculated using the ternary phase diagram of Mo–Cr–Si [23]. The volume percentage of phase–A was also determined using image analysis software as well as manually by intercept method, with the microstructures taken at different locations and at different magnifications. The average volume percentage of phase–A has been found to be around 28% for the sample hot pressed at 1873K, which is consistent with the value predicted by the ternary phase diagram of Mo–Cr–Si.

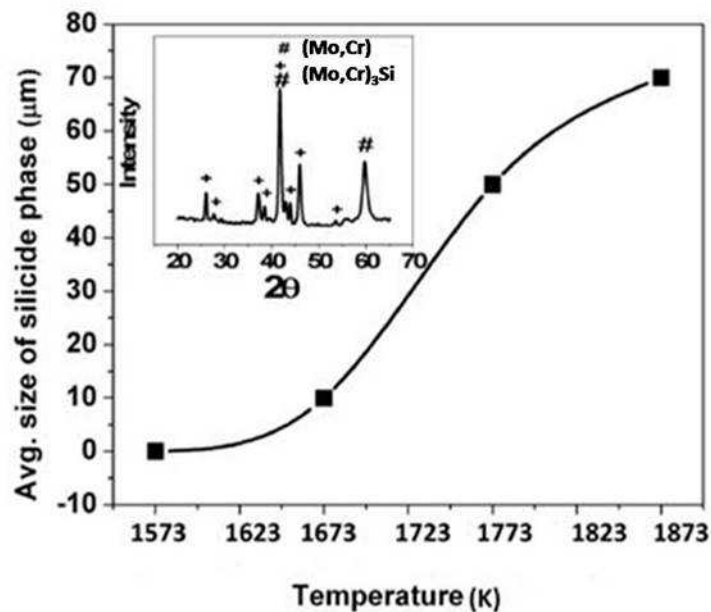


Fig.5.5: Plot of growth of silicide phase with time. Inset shows the XRD pattern of sintered alloy hot pressed at 1873K

Phase ratio (volume percentage) was calculated by means of the Lever rule utilizing the ternary phase diagram. The volume percentage of Mo rich areas (phase A) of the alloy was also determined by using image analysis software as well as manually by intercept method with microstructure taken at different location and at different magnification. The volume percentage of phase A was found out to be 28%, which is consistent with the phase diagram.

5.3 Studies on Silicothermic co-reduction

Numbers of thermite smelting experiments were conducted on 100g alloy scale with an aim to achieve targeted alloy composition with excellent slag-metal separation and higher yield. The basic thermite charge was composed of oxide intermediates of MoO₂, Cr₂O₃ and reductant Si taken in their appropriate ratio to prepare a molybdenum based alloy of composition, Mo-16Cr-4Si (wt.%). The results of the smelting campaign have been summarized in Table-5.2.

Table-5.2: Results of silicothermy co-reduction experiments

Exp no.	Charge composition (g)									Alloy composition (wt%)			Remark
	MoO ₂	Cr ₂ O ₃	Si	CaO	KClO ₃	Al	X	Q	Y	Mo	Cr	Si	
							(wt%)	(kcal/kg)	(wt%)				
1.	107	23.3	35	0.0	23	10	0.0	566	75	80.23	14.10	5.67	B
2.	107	23.3	37	5.0	25	11	5.0	560	78	80.22	13.98	5.80	A-B
3.	107	23.3	37	5.0	30	13	5.0	580	85	80.12	13.91	5.98	A
4.	100	24.0	35	5.0	25	11	2.0	560	70	80.15	14.50	5.35	B
5.	100	24.0	33	10.0	30	13	0.0	572	76	80.15	14.90	4.95	A-B
6.	100	25.0	30	10.0	36	16	0.0	595	85	80.18	15.70	4.12	A
7.	100	25.0	28	10.0	36	16	0.0	580	80	80.20	15.90	3.90	A

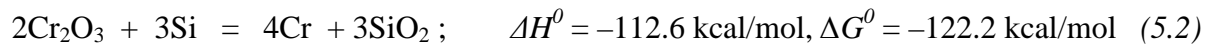
X- Excess Silicon taken over stoichiometric amount

Q- Specific heat of the charge

Y- Alloy yield, A- Good slag metal separation, B- Poor slag metal separation

In the context of thermite smelting, it is appropriate to mention here that the specific heat of the overall charge is critical to accomplish the smelting operation with good slag metal separation, as heat evolved from the chemical reactions of the reactants is utilized for melting as well as consolidation. Hence, the very first step in the feasibility of thermite smelting should be thermodynamic calculation for heat of the reaction and adiabatic temperature rise. From thermodynamic point of view, combination of fairly large negative value of free energy and enthalpy changes (ΔG° and ΔH°) are desirable for a chemical reaction to proceed autogenously. In this connection, the chemical reactions involved in the present

thermite smelting campaign and the corresponding thermodynamic data are indicated below for their thermal consideration.



It is evident from the above thermodynamic data that both the reactions are thermodynamically favourable. In a metallothermic reduction smelting, the chemical reaction, in order to proceed autogenously with efficient slag–metal separation and higher alloy yield, a large amount of thermal energy is required equivalent to 600–1000 kcal.kg⁻¹ as predicted by Hall and Dautzenberg [42–44]. In the present case, combined specific thermal energy of the above reactions was found to be around 500 kcal.kg⁻¹, that falls short from the recommended range. Hence heat booster in the form of a chemical mixture of KClO₃ and Al in the ratio of 2:1 by weight was added to the charge to improve the thermal yield of overall charge. Heat booster acted as per the following reaction.



An enormous amount of heat (specific heat = 1710 kcal/kg) was yielded by this reaction and proving to be an ideal choice as heat booster among other such as (NaNO₃, I₂ etc). The basic aim of adding heat booster is to raise the adiabatic temperature (T_{ad}) of the overall reaction. Thus the amount of heat booster to be added is decided by T_{ad} which is calculated by the following thermodynamic equation:

$$\Delta H_{298} = \sum n_i (\Delta H)_i \quad (5.4)$$

$$\Delta H = \int_{298}^{T_m} C_{ps} dT + \Delta H_m + \int_{T_m}^{T_B} C_{pl} dT + \Delta H_B + \int_{T_B}^{T_{ad}} C_{pb} dT \quad (5.5)$$

where ΔH_{298} is the heat of reaction of the system at 298K; ΔH and n_i are the molar heat of products formation and the mole coefficient of products; C_{ps} , C_{pl} and C_{pb} are the heat capacities of solid, liquid and gaseous state of products; T_m and ΔH_m the melting point and heat of melting of products; T_B and ΔH_B the boiling point and heat of boiling. The calculated T_{ad} for the thermite experiment without heat booster was found to be below 1273K which was insufficient for effective slag– metal separation and satisfactory yield. During thermite smelting for obtaining excellent slag metal separation, any two of following approach can be adopted:

- (a) Increase of the specific heat of the reactants so as to achieve higher T_{ad} to such an extent so that both metal/alloy (matrix) and slag melt with superheat of at least of

373K above the melting temperature. In this liquid state, due to the density difference of metal and oxides (oxides being lighter float over metallic phase) excellent slag metal separation is achieved.

- (b) Fluidity of the slag phase should be increased so that better separation of metal and slag is accomplished within a very short span of time in molten condition, as the time for whole mass to remain in liquid state is very short.

In the present case, the T_{ad} of the present batch size was raised to $\geq 2573\text{K}$ by the addition of 25 g KClO_3 along with required amount of Al, which is well above the melting temperature of both alloy and slag, SiO_2 . The thermodynamic data used in the calculation of T_{ad} are given in Table-5.3 [45].

Table-5.3: Thermodynamic data used to calculate adiabatic temperature rise

Element/Compound	Sp. Heat capacity, C_P (kJ/kg/K)	Heat of Fusion, H_m (kJ/mole)	Melting Point (K)
Mo	0.25	37.48	2617
Cr	0.46	21	1857
Si	0.70	50.2	1410
SiO_2	0.73	9.6	1728
Al_2O_3	0.88	25.5	2040
KCl	0.69	26.53	772
Al	0.90	10.7	660

It is worth mentioning here that, apart from the heat evolved from the main reduction reactions, other small exothermic reactions for the formation of molybdenum and chromium silicides further added heat to the total specific heat of the reaction. It is not known which silicides form and in what proportion, hence, for the sake of computing T_{ad} , it is assumed that the entire Si was consumed in the reduction process and in the formation of Mo_3Si phase.

In the present reduction smelting campaign, SiO_2 is the main slag phase having a high melting temperature of 1923K. For utilizing second approach for better slag metal separation, CaO (lime) was added to the reactants to form a low melting slag phase with SiO_2 . It is evident from the binary phase diagram of SiO_2 and CaO as shown in Fig.5.6, that a number of compounds are formed with the combination of SiO_2 and CaO at different temperature and composition. However, the slag phase corresponding to the composition $2\text{CaO} \cdot \text{SiO}_2$ has

lower melting temperature of 1673K. Hence, CaO was added accordingly to achieve the above slag composition.

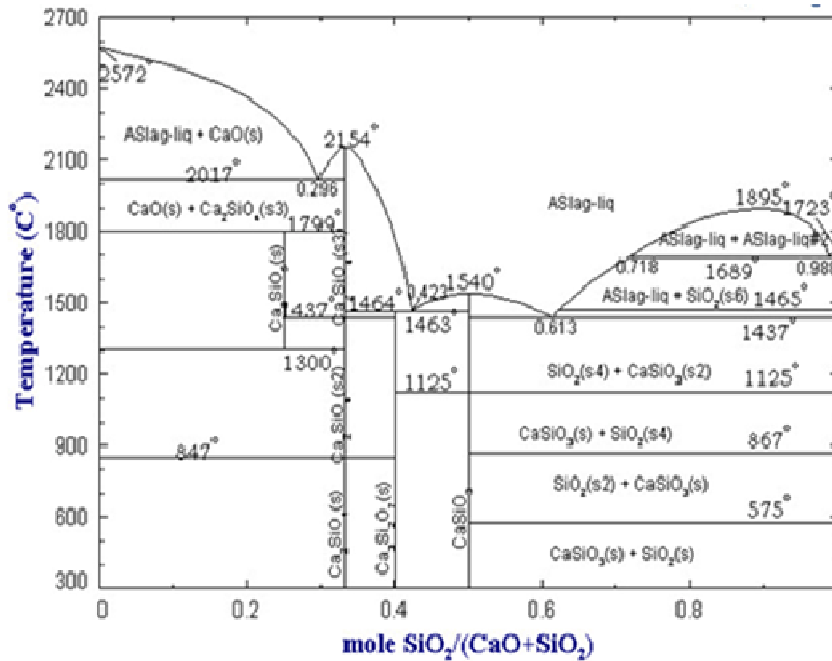


Fig.5.6 The phase diagram of CaO–SiO₂

The alloy yield of 75% was achieved in the first experiment as per the Table–I using only stoichiometric amount of MoO₂, Cr₂O₃ and reductant Si. It is clearly visible in the Fig. 5.7 that the traces of slag particles are embedded in the metal matrix indicating poor slag–metal separation.

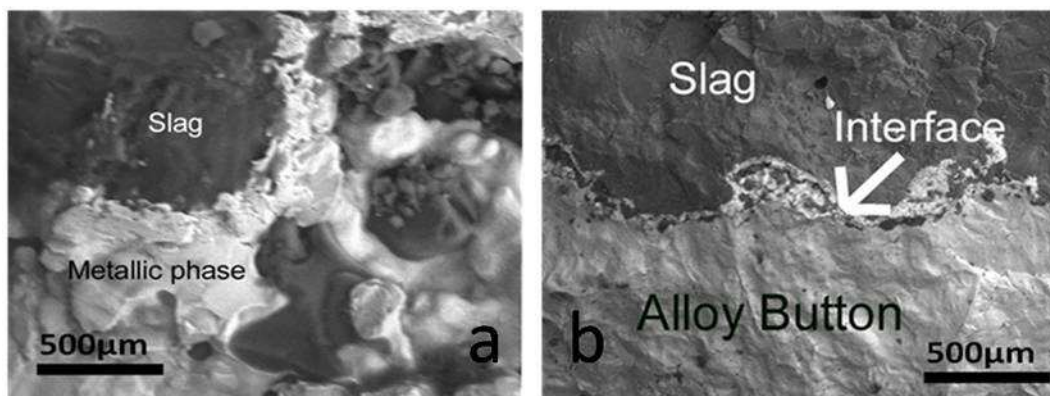


Fig.5.7 SEM image showing (a) Poor (b) Excellent slag metal separation

This is because of inadequate specific heat of the reacting mass thus resulting in lower T_{ad} . In metallothermy, it is customary to use excess reductant in the charge over stoichiometric amount to increase the yield of the product by leading the reaction to completion [32–33]. Therefore in the second experiment (Table–5.2), 5% excess Si over stoichiometric amount, 5g CaO were added along with the desired amount of heat booster to

keep the specific heat in the desired range. Although the yield increased marginally but the corresponding slag metal separation has been found to be only good. It was noticed in experiment No.3 onwards, that further increase in the heat booster in the charge improved overall specific heat and thus resulted in significant increase in the alloy yield with excellent slag–metal separation. The alloy composition corresponding to the stoichiometric amount of reactant with heat booster and CaO was evaluated by chemical analysis and the composition was found to be 80.12 Mo–13.91Cr–5.98Si (wt.%) with respect to the target composition of 80 Mo–16Cr–4Si (wt.%). Immediate formation of molybdenum and chromium silicides during smelting using free Si which is to be used as reductant, the Si content was found to be more in the synthesized alloy than the target amount. To get the desired composition further experiments were required. In the next set of experiments MoO₂ (↓), Cr₂O₃ (↑), CaO, Si and heat booster were added in required quantity. Finally an alloy composition 80 Mo–16Cr–4Si was achieved with more than 80% yield and excellent slag metal separation. A clear slag–metal demarcation and their regions of occupancy are clearly illustrated by the SEM image as shown in Fig.5.7b. It is appropriate to mention here that the final product is obtained without having any traces of Al. Al was added in the stoichiometric quantity as per reaction given in equation–5.3, which is highly thermodynamically favorable. Hence Al has very little chance to join the alloy phase. KCl is volatile which vaporizes at T_{ad} whereas there is strong tendency of Al₂O₃ to form a low melting phase with SiO₂.

The charge composition taken in experiment no.–6 was separately heated in TG–DTA as well as in a resistance heating furnace to determine the temperature required to trigger the exothermic reactions. The charge (composition as in exp. no. –1 in Table–5.2) was placed in an alumina crucible and heated up to 1773K with a heating rate of 15 K/min. At 673K the reaction ignited and in the short span, reaction went into completion. In contrast the mixture of stoichiometric amount of MoO₂, Cr₂O₃ and Si, in absence of heat booster needed 1673K to trigger the reaction. Fig.5.8 shows the DTA/TG plot for above reactant mixture, which shows a large exothermic peak at 1673K. As the melting point of Si is 1683K, which indicate that the triggering temperature may have coincided with the melting of Si. Inset of Fig.5.8 shows the DTA plot during cooling, which is almost flat corroborating the fact that the exothermic peak is due to non reversible reaction only, which may be either reduction of MoO₂ or Cr₂O₃ by Si as reductant.

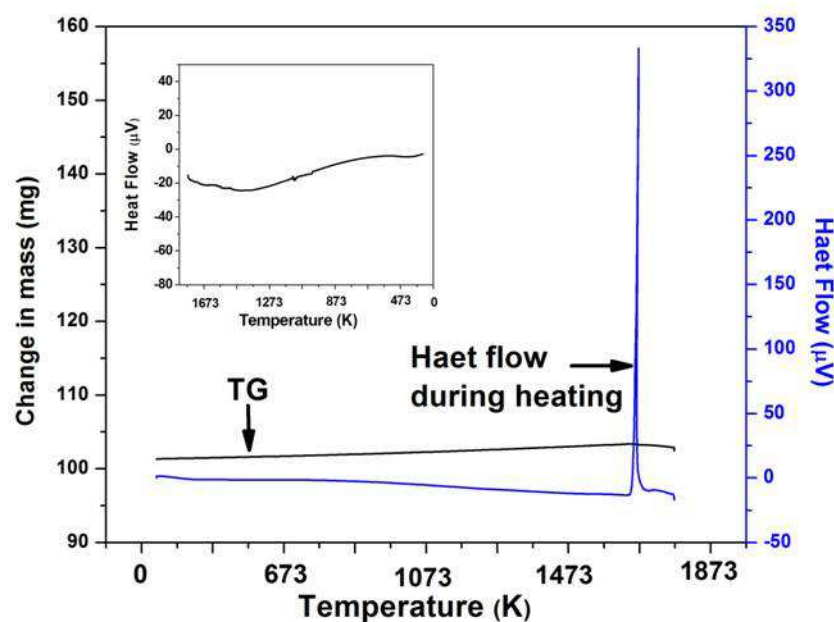


Fig.5.8 DTA/TG plot for mixture of MoO_2 , Cr_2O_3 and Si, showing the sharp peak near the melting temperature of Si is due to triggering of reduction reactions. Inset of Fig shows the DTA plot during cooling

As the free energy value, ΔG°_{1573} is -172.8 kcal/mole and -73.5 kcal/mole for Cr_2O_3 and MoO_2 respectively, Cr_2O_3 is more stable than MoO_2 . Thus the reaction $\text{MoO}_2 + \text{Si} = \text{Mo} + \text{SiO}_2$ (reaction-1) is the first to get triggered then reaction $2\text{Cr}_2\text{O}_3 + 3\text{Si} = 4\text{Cr} + 3\text{SiO}_2$ (reaction-2). Thereafter remaining Si melt is expected to react with Mo to give MoSi_3 . Fig.5.8 also shows the TG plot which reveals that there is no mass loss during the reaction which is expected, since there is no volatile species in the reaction involved as the TG-DTA experiment was done under inert atmosphere using high pure He gas. Although above co-reduction reactions (given in equation- 5.1 & 5.2) are thermodynamically favorable but the activation energies are very high. A high temperature is therefore required to trigger the reaction. Once ignited the reaction proceeds to completion in a very short span of time as the kinetics at that temperature is expected to be very fast. From thermodynamic calculation using equation-4 and 5, the T_{ad} of reaction given in equation-5.3 ($\text{KClO}_3 + \text{Al} = \text{KCl} + \text{Al}_2\text{O}_3$) reaches about 1773K with charge composition as given in experiment no.-6 in Table-5.2. Thus reaction shown in equation-5.3 is the first to take place which then raises the temperature of charge to desired temperature to trigger the next reaction i.e. reduction of MoO_2 and then Cr_2O_3 in series the same sequence.

5.3.1 Kinetics of silicothermic reduction

As the major constituent of these alloys are Mo, therefore the thermodynamic and kinetics study on the feasibility of reduction of molybdenum oxides by Si is utmost important. In the present study, the thermodynamic aspects of reduction of molybdenum oxide to molybdenum by metallothermy process have been described. The overall chemical reaction involved in the silicothermy reduction with corresponding free energy and enthalpy data are indicated below.



$$\Delta H_{298}^{\circ} = -323.4 \text{ kJ/mol}, \Delta G_{298}^{\circ} = -320.3 \text{ kJ/mol}$$

It is evident from the above thermodynamic data that the reaction (5.6) is thermodynamically favourable and exothermic in nature. The reduction process was investigated by DTA to determine the reduction initiation temperature and mechanism of silicothermic reduction.

Commercially available MoO₂ (purity >99.9%, mesh size #300) and Si (99.5% purity, average particle size ~10 μm) were used as starting materials. Thermogravimetric studies for investigating reduction process were conducted using TG–DTA equipment. The charge mixture consisting of MoO₂ and reductant Si (10% by wt. excess Si over stoichiometric amount) were thoroughly mixed and about 30 mg of blended powder were heated up to 1600 °C with different heating rates of 8, 12, 15 and 20 K/min in pure Ar atmosphere. Excess reductant (Si) was added to accomplish complete reduction of MoO₂ by compensating any loss of reductant (Si) due to its oxidation or volatilization. Helium was used as carrier gas and argon was used as protective gas for the furnace chamber. The chamber was evacuated up to 10⁻² mbar after charging the sample followed by filling up with required carrier gas. Charge components for silicothermic reduction experiments were used as loose powder moderately packed as well as in the pellet forms for conducting silicothermic reduction experiments. The pellets were prepared by hydraulic pressing using a pressure of 100 MPa. As-reduced products were characterized for their phases at room temperature by powder XRD, SEM and EDS.

Fig. 5.9 indicates TG–DTA plot showing results of reduction reaction between MoO₂ and Si carried out in inert atmosphere at a heating rate of 15 K/min.

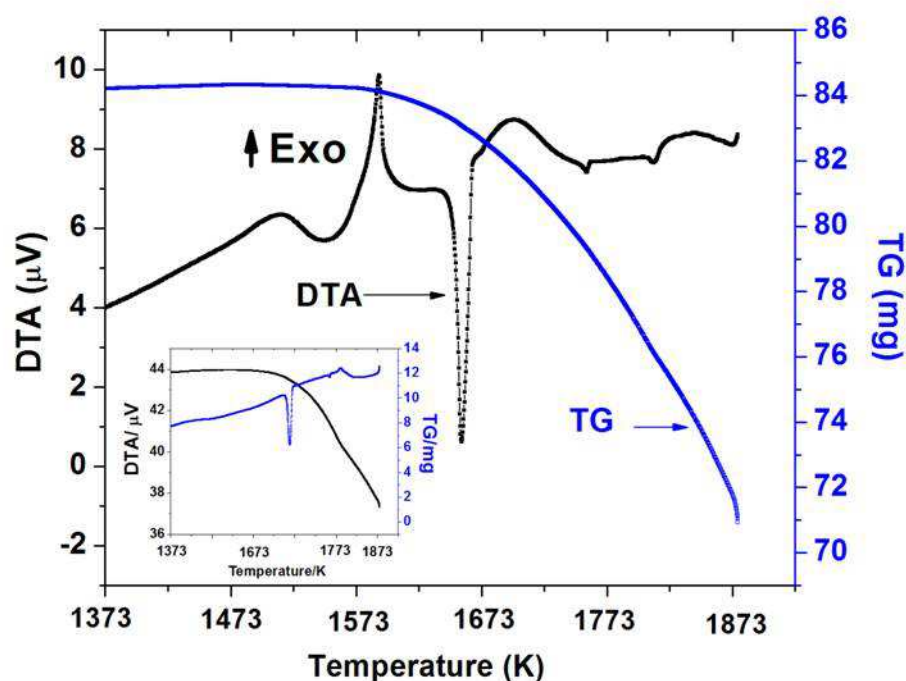


Fig.5.9 Typical TG–DTA plot of reduction of MoO_2 by Si taken in powder form. Inset shows a typical TG–DTA plot of reduction of MoO_2 by Si taken in the pellet form

The plot exhibits two peaks, one exothermic peak and other endothermic peak. The endothermic peak was formed as a result of melting of un–reacted Si, while formation of an exothermic peak at 1603K can be attributed to the reduction reaction between MoO_2 and Si. It is reported in the literature that any metallothermic kind of reduction, either aluminothermic or silicothermic or any other type of redox reaction, is usually triggered by the exothermic heat made available by oxidation of excess metal/reductant (Si, Al etc). It is also demonstrated by Sarangi et. al.[46] that no reaction took place for aluminothermic reduction in absence of O_2 or in argon atmosphere. It was because of absence of heat available by lack of oxidation of reductant (Si), which essentially needs O_2 . However, the reduction of MoO_2 to Mo by Si in inert atmosphere was confirmed by XRD shown in Fig.5.10. The XRD plot shows SiO_2 as the slag phase and Mo as the metallic phase. Fig.5.11 shows the back scattered SEM image and corresponding EDS analysis of the product after reduction which reveals basically oxygen rich region (slag phase) and oxygen depleted region (metal phase). Thus, the exothermic peak in the Fig.5.9 appears due to the reduction of

MoO₂. Since the reduction experiments were carried out in inert atmosphere, exchange of oxygen atoms from the contact points of MoO₂ and Si particles is the only way for oxidation of Si, which can promote the next reactions.

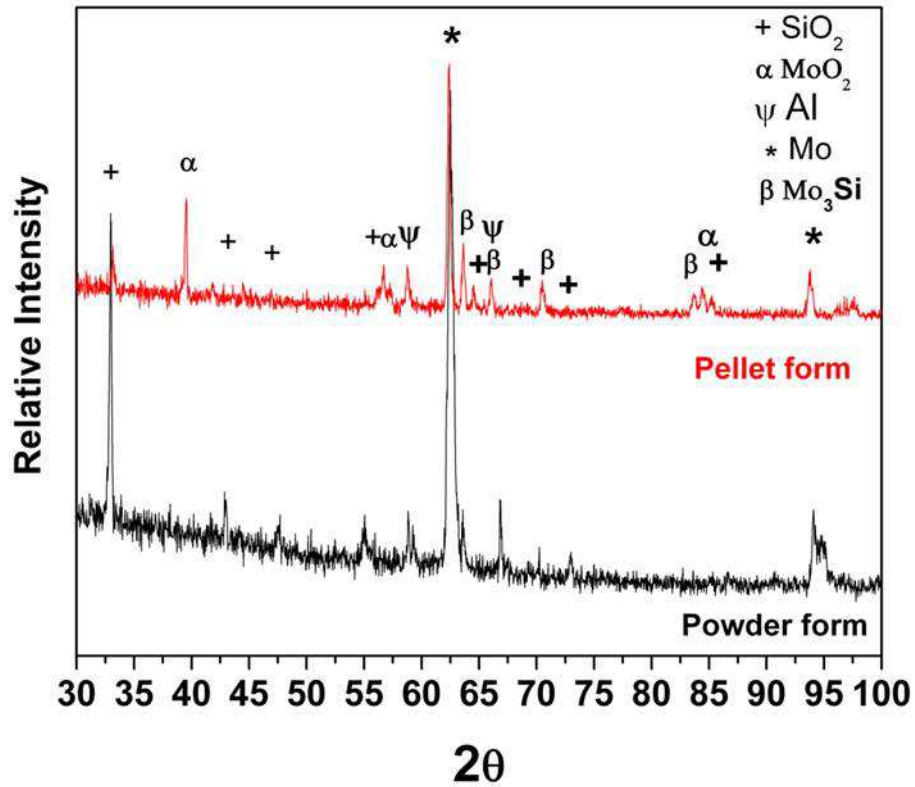


Fig.5.10 XRD of the product after reduction of (a) pelletized reactant and (b) powder reactant

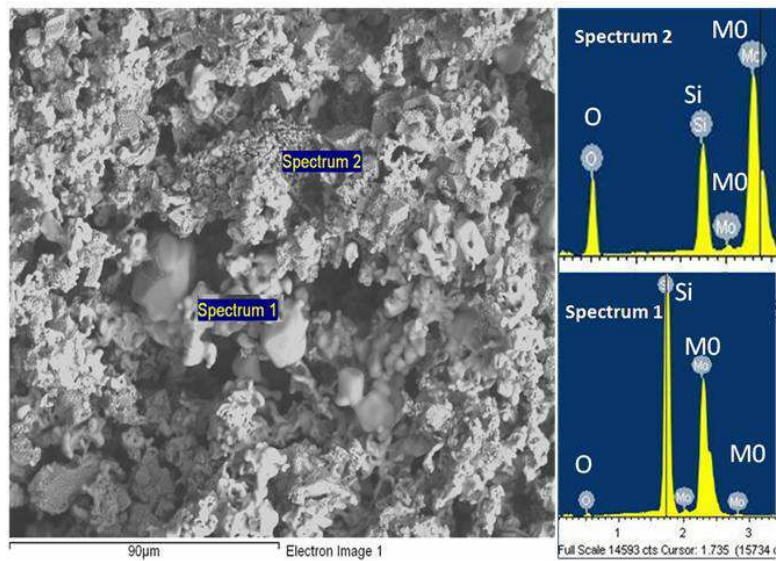


Fig.5.11 Back scattered SEM image and the EDS analysis of the product after reduction

Corresponding TG plot (Fig.5.9) demonstrates a continuous weight loss during reduction indicating formation of some gaseous phases. The only possible gaseous phase in this system could be the formation of volatile phase of SiO (Silicon mono-oxide) as per chemical equation (5.7) and (5.8) and due to its volatilization, the cumulative weight loss would be around 28%. By analyzing the TG plot it is noticed that the weight loss incurred is about 20%, which substantiates the fact of formation of SiO at contact points between particles. The balance weight loss equivalent to 8% can be attributed to the fact that some fraction of SiO formed is apparently used in reduction and balanced fraction of SiO vaporized to yield 20% weight loss during TG experiments. Thus the reduction goes into completion following a series of steps instead of single equation as shown in equation-(5.9) and the probable mechanism of reduction can be understood by following set of equations as mentioned below.



All the above reactions are thermodynamically feasible at 1533K as the free energy changes are negative. The free energy values used in the calculations are tabulated in Table-5.4.

Table-5.4: Thermodynamic data for the different compounds (Where j=4.185)

Compound	ΔG° (J/mole)	Temperature range (K)
MoO_{2-x}	$-138,547.43j + 40.622jT$ [48]	925–1533
MoO_2	$140500j + 4.6jT \log T - 56.8jT$ [47]	298–1533
SiO_2	$-216817j + 56.07jT - 4.37jT \log T$ [47]	700–1700
SiO	$-101592j + 22.43jT - 2.69jT \log T$ [49]	298–1685
SiO	$-25806.45j - 19.02jT$ [50]	298–1685

The role of gaseous phase in the process of reduction was corroborated by the fact that there was only partial reduction when the reactant mixtures were pelletized. Inset of Fig. 5.9 demonstrates the TG-DTA plot showing the results of reduction experiments conducted for a reactant mixture used in the form of pellet at a heating rate of 15K/min in Ar

atmosphere. The plot shows only a single endothermic peak, which was identified as melting of un-reacted Si. Although no exothermic peak was observed, however partial reduction of MoO_2 to Mo by Si was confirmed by XRD as shown in Fig. 5.10. The XRD plot shows peaks corresponding to SiO_2 , un-reacted MoO_2 and Mo_3Si phases. Since the sample quantity used was very small as compared to the size of the XRD aluminum sample holder, so the peak of Al was also detected. Excess reductant (Si) was added intentionally as stated earlier, however Si was not detected in the XRD plot. The excess Si may have been consumed during the formation of solid solution with Mo [51] or formation of Mo_3Si phase in case of loose powder reactant mixture and reactant mixture in the form of pellet respectively.

Basically present silicothermic reactions have gaseous, solid as well as liquid components involved in the entire redox process. However, charge mixture used in pellet form has very limited permeability available as compared to charge used as loose powder pack. Therefore, the reduction reaction was only confined at the surface level or at discrete locations at different time, and could not propagate through the charge properly making the reaction very sluggish. This has resulted the reaction step as shown in equation-5.9 to occur only partially. Therefore, the corresponding sharp exothermic peak was not detected. Partial reduction of MoO_2 to Mo by Si was also confirmed by XRD as shown in Fig. 5.10.

In addition, the exothermicity of the reaction given in equation-5.6 (along with 10% excess Si) is sufficient to promote the reaction autogenously, however to compensate the loss of Si in the form of SiO during reduction process, we had to add additional 10% excess Si. The excess Si acts as a heat sink and reduces the specific heat (total exothermic heat per unit mass) considerably. Therefore, overall reduction in this case (pellet form) is only partially successful. However, in case of loose charge powder, the reaction took place uniformly all over the surfaces including exterior as well as interior parts. Hence, in this case the reduction was comparatively much successful.

In the context of metallothermic smelting, it is appropriate to mention here that the specific heat of the overall charge is critical to accomplish the smelting operation. The specific heat of the charge used in the present experimental campaign is about 2071kJ/kg which is below the recommended range of specific heat value (2520–4000 kJ/kg) for reduction reaction along with good slag– metal separation [32–33].

Silicothermic reduction has also been carried out in air atmosphere, but due to formation of highly volatile species, MoO_3 followed by its rapid volatilization, resulted in

heavy loss of the reactant which limits the experiments to be done in thermo-balance. So, further studies have not been pursued.

Fig. 5.12 show the TG-DTA plots for reactant mixtures for the heating rates of 8, 12 and 15 K/min showing reduction temperatures at 1573, 1591 and 1603K respectively.

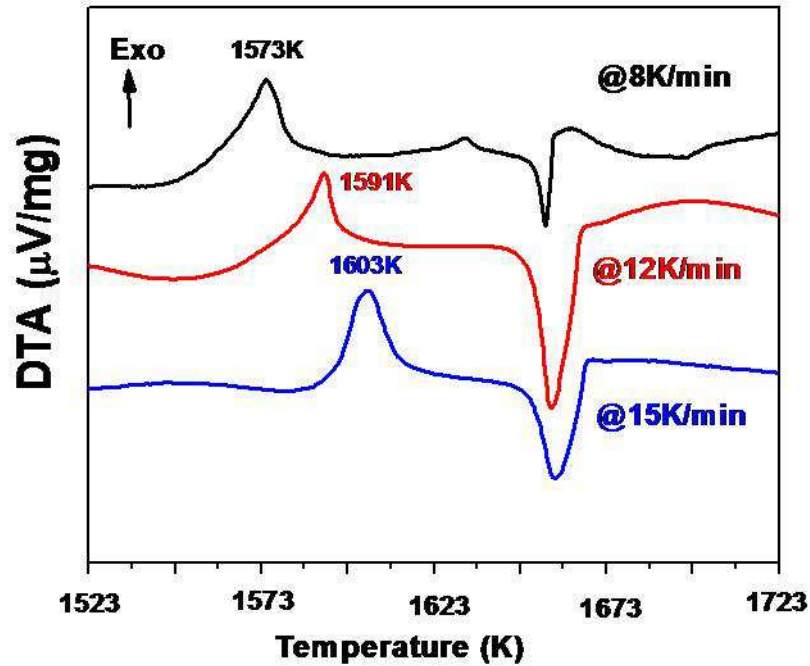


Fig. 5.12 Exothermic peak locations for reduction of MoO_2 to Mo at different temperatures and heating rates

Although reduction reaction indicated in equation-5.6 is thermodynamically favorable but the activation energy appears to be high due to solid state reaction. A high temperature is therefore required to initiate the reaction. Once triggered, the reaction proceeds to completion in a very short span of time as the kinetics at that temperature is very fast. Thus, the prior knowledge of activation energy is helpful in such reactions. For the kinetics of thermally stimulated solid-state reactions, the following formula has been widely accepted:

$$\frac{d\alpha}{dt} = A \exp\left(-\frac{Q}{RT}\right) f(\alpha) \quad (5.10)$$

where α is the extent of reaction, t , the time, R , the universal gas constant, T , the temperature, $f(\alpha)$, the kinetic model function, and A and Q are apparent pre-exponential factor and apparent activation energy, respectively.

In this study, model-free approaches were used in kinetic evaluation. Model-free methods allow evaluation of the Arrhenius parameters without choosing the reaction model $f(\alpha)$. The widely used approaches for thermally activated transformation processes in the solid state can be investigated by non-isothermal experiments if several measurements with different heating rates [52] are the isoconversional methods according to Friedman [53] and the integral isoconversional method according to Kissinger [54] and Ozawa [55]. For non-isothermal analysis at constant heating rate, mean activation energy, Q , can be derived using Kissinger equation, which depicts the relationship between heating rate and peak temperature [54, 56–59].

$$\ln\left(\frac{T_p^2}{\beta}\right) = \frac{Q}{RT_p} + c \quad (5.11)$$

Where, β = heating rate, T_p is the peak temperature, Q is the activation energy, A is pre-exponential factor and c is constant. From the slope of plot $\ln(T_p^2/\beta)$ vs $1/T_p$, activation energy can be estimated. In the present work, different heating rates (8, 12, 15 and 20 K/min) were used. The peak position is influenced significantly by the heating rates. The activation energy for the reduction of MoO_2 by silicon was derived from the slope of plot shown in Fig. 5.13.

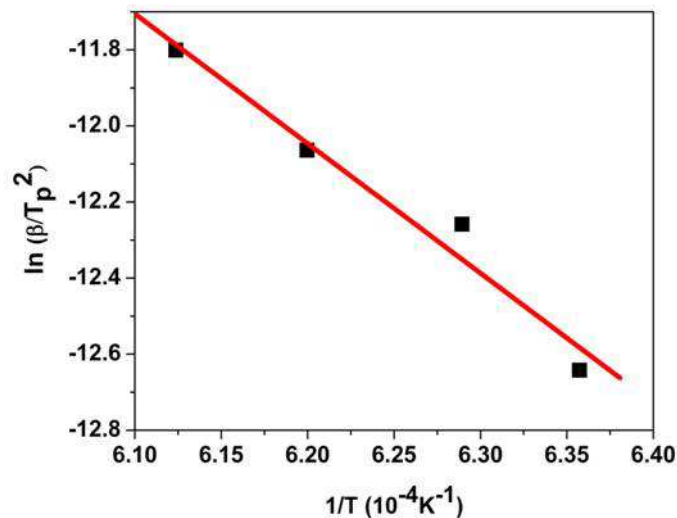


Fig. 5.13 Arrhenius Plot for the estimation of activation energy

The value of activation energy was found to be 309 kJ/mole. On the other hand the activation energy for reduction of MoO_2 to Mo by hydrogen has been reported to be 185

kJ/mole by Majumdar et al. [60] and 98.6 kJ/mole by Kennedy et al. [61]. The activation energy value for reduction of MoO_2 by Si, determined in this study is higher than the activation energy of reduction of MoO_2 by hydrogen, because in the later case reductant, hydrogen being in a gaseous phase can easily permeate through the pores and channels which facilitate easier reduction unlike the solid state reduction process such as metallothermy. Hence higher activation energy would be required for reduction of oxide powder with metal powder. The rate controlling step in this case may be either formation of SiO or its diffusion through the regime of Mo-oxide particles. The activation energy required for the oxygen diffusion into the Si substrate is estimated to be 155kJ/mole [62]. However, the activation energy calculated in the present study [309 kJ/mole] is much higher than the activation energy required for the oxygen diffusion into the Si substrate. Thus, the probable rate controlling step can be predicted as the diffusion of SiO in the Mo-oxide particles.

5.3.2 Composition and Microstructural characterisation

5.3.2.1 Bulk compositional analysis

The bulk quantitative estimations of as reduced as well as arc melted alloys were carried out by the chemical analysis using different analytical methods such as spectrophotometry, gravimetry and volumetry for different elements. The chips from different locations of the alloy button were drilled out and dissolved in aqua-regia. Analyses of the samples were done using the dissolved aqua-regia solution and the averages of compositions of different locations were determined. The results of analysis of the as-reduced alloys obtained under different experimental conditions are presented in Table-5.1. The final composition and analysis process of the remelted alloy has been tabulated in Table-5.5.

Table-5.5: Bulk composition of the alloy and analysis process

Element	Wt percentage	Analysis process
Mo	80.10	Spectrophotometry, Gravimetry
Cr	15.80	Gravimetry, Volumetry
Si	4.10	Gravimetry, Spectrophotometry
Al	Not detected	Spectrophotometry

5.3.2.2 Microstructure and Micro compositional analysis

Backscattered SEM micrographs of (a) as reduced and (b) remelted and homogenized alloy were shown in Fig. 5.14. The microstructure of as reduced alloy was consisted of three different contrast regions, namely, grey, white and black due to different chemical compositions acquired in those regions. The quantitative microanalysis in those regions was carried out by EDS for evaluating compositional variation with contrast and the corresponding analysis results were shown in Table-5.6. The black colored region was actually formed by Cr rich $(\text{Mo,Cr})_3\text{Si}$ phase where the average content of Cr was around 18%.

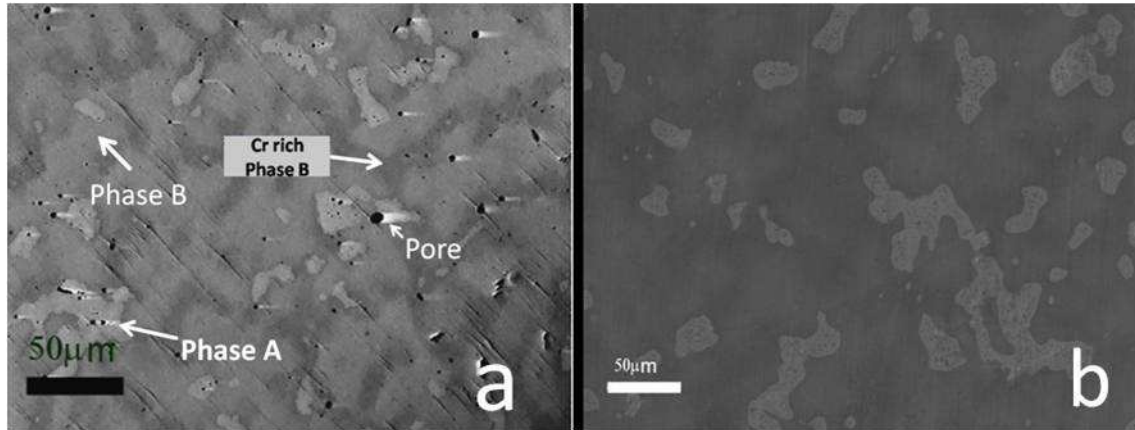


Fig. 5.14 SEM image taken in BSE mode of Mo–16Cr–4Si alloy (a) As reduced (b) Remelted and homogenized at 1873K for 10 hour

Table–5.6: Details of microanalysis of alloy at different conditions

Condition	Si(wt.%/at.%)	Cr (wt.%/at.%)	Mo (wt.%/at.%)	Volume percentage
As reduced–Phase A	1.89/5.77	8.98/14.78	89.12/79.46	55
As reduced–Phase B	7.96/21.52	8.45/12.34	83.59/66.14	27
As reduced–Black region	7.91/20.15	17.74/24.4	74.36/55.45	18
Heat treated1600–Phase A	1.24/3.84	8.12/13.74	90.58/82.42	28
Heat treated1600–Phase B	8.25/21.77	11.18/15.95	80.57/62.28	72
Grey region at Phase A	7.09/19.09	11.57/16.82	81.34/64.1	–
White region at Phase A	0.86/2.68	9.4/15.76	89.74/81.57	–

On subjecting homogenization treatment, the black region was found to disappear indicating redistribution of Cr uniformly throughout the matrix. As compared to as–reduced alloy, the microstructure of homogenized alloy was consisted of two phases as revealed by back scattered SEM image. The first phase (phase–A) appearing light (white) was made up of a solid solution phase basically by Mo and Cr containing around 1.8 at% Si. The second phase (phase–B), appearing dark (grey) was made up of (Mo,Cr)₃Si intermetallic phase. The XRD pattern of the remelted alloy obtained under optimum experimental condition has been indicated in Fig. 5.15. The well defined peaks as exhibited in the XRD plot conformed to

elemental molybdenum (with shifting of peaks) and the minor peaks matched with the phases of MoSi_3 . A shift of Mo reflection peak towards higher angle (from 40.51° for pure Mo to 41.77°) was observed. This was due to a reduction in the lattice parameter of the alloy which can be attributed to the atomic radius mismatch mainly between Mo & Cr and distortion of the molybdenum lattice by diffusion of Cr in it. The slight shifting of the Mo peak is due to the solid solution with Cr and presence of Si within the Mo rich region. However, peaks corresponding to elemental Cr, Si and Al (or its compounds) were not observed.

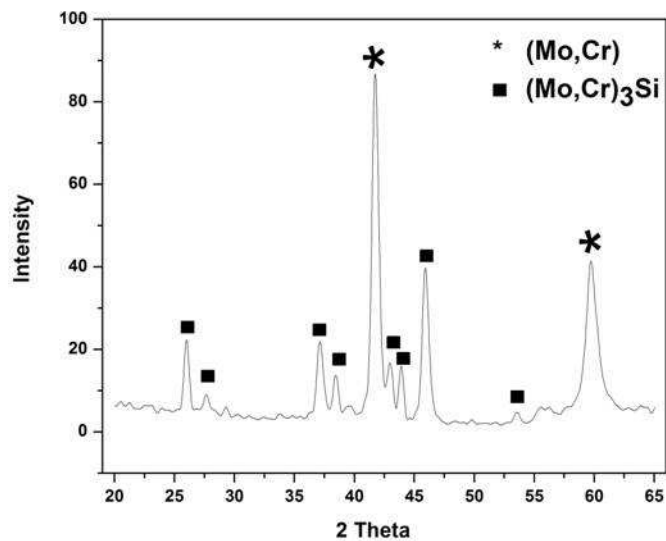


Fig. 5.15 XRD pattern of remelted and homogenized Mo-16Cr-4Si alloy

Elemental mappings of the remelted alloy of composition 80.18Mo-15.70Cr-4.12Si were depicted in Fig. 5.16. The maps consisted of basically Si rich area (appearing dark) and Si depleted area (appearing light). Cr is almost uniformly distributed in the matrix. The content of Si in the Si rich area was found to be 10 wt % (stoichiometric content of Si in of Mo_3Si) confirming the XRD result. The content of Si in Si depleted area was ~ 1.2 wt. %, which is basically Mo rich area. The overall Si content in the alloy was 4.12 wt. %. On further increase in magnification and corresponding microanalysis, it was seen that within Phase-A (Mo rich phase), traces of Si rich areas were present at random as shown in Fig. 5.17 (a). Qualitative elemental line scan indicating variation of composition of phase-A was shown in Fig- Fig. 5.17(b). Utilizing the ternary phase diagram in Fig. 5.1 (b), phase ratios (volume percentage) were calculated by means of the lever rule. The volume percentage of Mo rich area was also determined by using image analysis software as well as manually by intercept method with microstructure taken at different location and at different

magnification. The average volume percentage of Mo rich area was found to be around 28% for remelted and homogenized sample, which is consistent with the ternary phase diagram of Mo–Cr–Si. BSE image of alloy and corresponding simulated image produced by image analysis software based on difference of contrast in the microstructure yielded 28% of bright phase (shown in blue in Fig. 5.18). The phase ratio is an important parameter in designing RMIC as the oxidation resistance and creep strength, on one hand, and room–temperature fracture toughness, on the other, vary in mutually opposite way on the volume fraction of the Mo (ss) phase. In this regard several property tradeoffs must be considered.

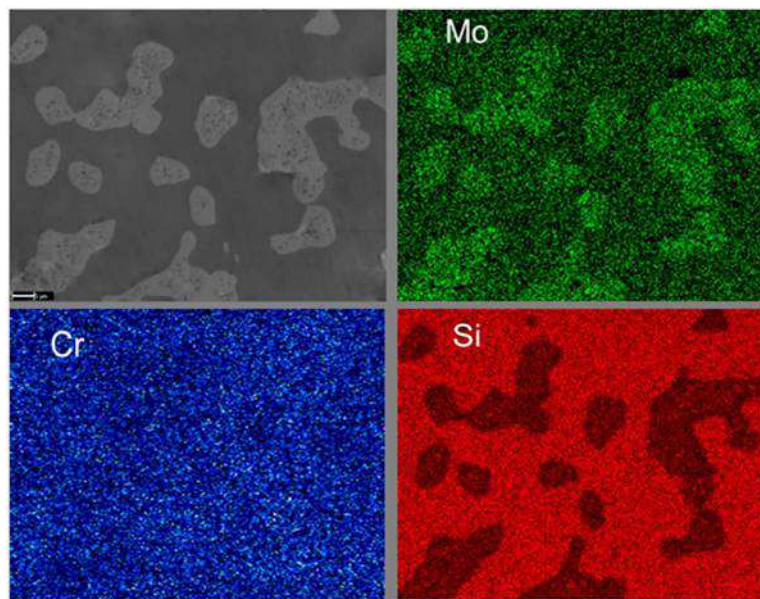


Fig. 5.16 (a) BSE image of homogenized Mo–16Cr–4Si alloy and (b), (c) and (d) are the elemental maps of Mo, Cr and Si respectively

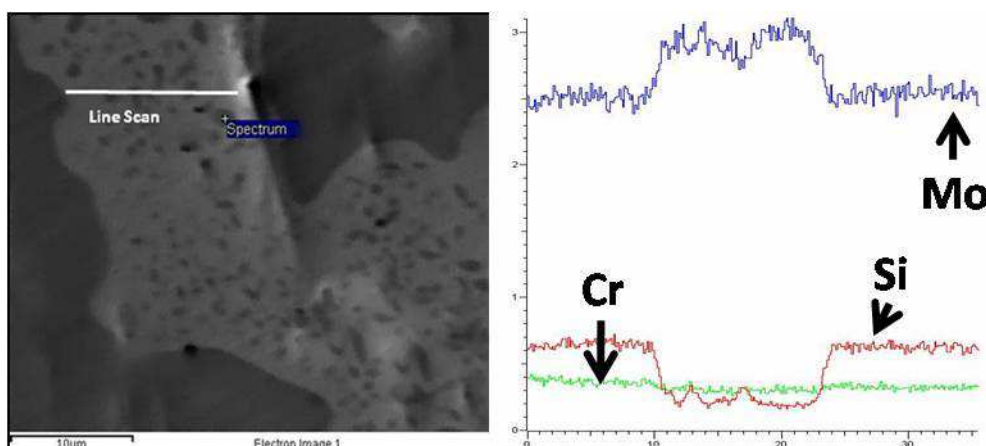


Fig. 5.17 SEM image taken in BSE mode of remelted + homogenized Mo–16Cr–4Si alloy showing Si rich areas (black) within phase A, Fig also shows the elemental variation across the line of phase A qualitatively

The composite density was calculated using the classical rule of mixture to yield a value of 8390 kg/m^3 . In a separate step the densities were measured according to Archimedes principle and were found to be 8240 and 8350 kg/m^3 for as reduced and remelted cum homogenized samples respectively. The density of as reduced sample was equivalent to around 98% of theoretical density, due to presence of pores (about 2%) generated during synthesis which was also seen in Fig-5a.

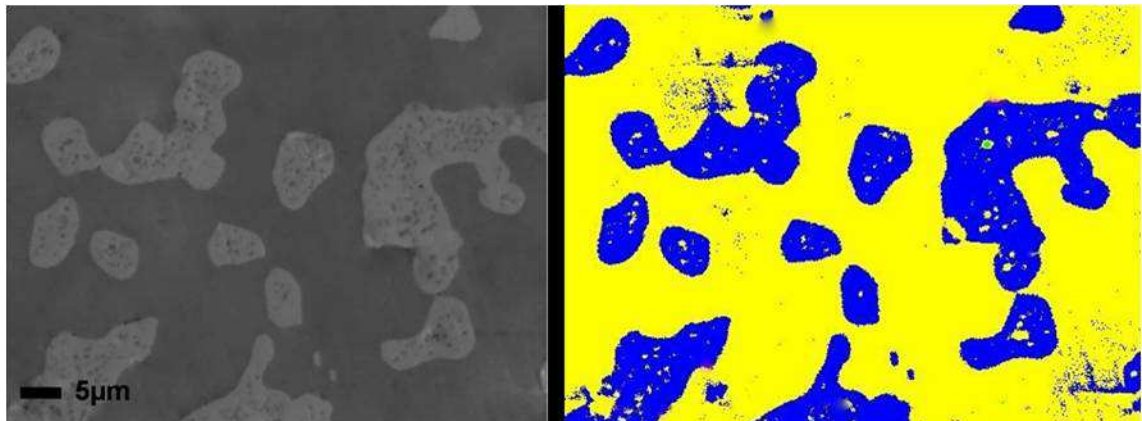


Fig. 5.18 BSE image of remelted + homogenized Mo-16Cr-4Si alloy (left) and corresponding simulated image (right) produced by image analysis software based on difference of contrast in the microstructure

5.4 Mechanical Properties

5.4.1 Hardness test

The average values of hardness of phase A and B for the hot pressed Mo–16Cr–4Si alloy at 3N load are 6800 ± 15 MPa and 11300 ± 10 MPa, respectively. Whereas, the variation of hardness of silicothermally reduced Mo–16Cr–4Si alloy with applied load has been shown in Fig. 5.19. Therefore, the hardness of hot pressed alloy is lower as compared to the alloy synthesized by silicothermic route. It is apparently because of presence of oxygen impurity as an interstitial in the product of silicothermic co–reduction route. It is noteworthy to mention here that the oxygen content was 0.8 % and 0.01% for the alloy prepared by silicothermic and hot pressing route respectively. The oxygen content was reduced to 0.3% after remelting of reduced alloy, so the hardness, as shown in Fig. 5.19. Since the hot pressing was done under vacuum ($\sim 10^{-5}$ mbar), there is a minimum chance of picking up oxygen. From the plot (Fig. 5.19) it is seen that, in both cases, hardness decreases with increasing load. In Fig. 5.19, all the data are for hardness of silicide phase. The profiles of Vicker indentations at a load of 3 N, showing the variation of indentation size at different phases were shown in Fig. 5.20. It is clear that diagonals of indentations at phase A (solid solution) is longer than the diagonal of indentation at phase B (silicides), yielding lower hardness at same load.

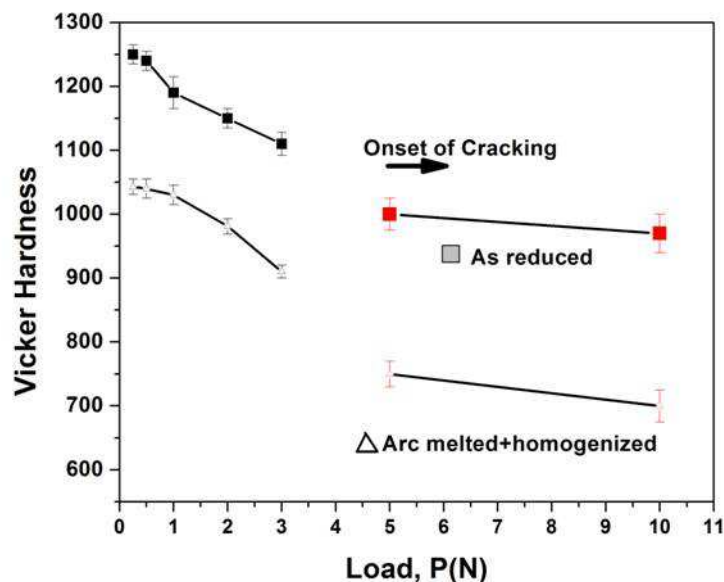


Fig. 5.19 Plot of hardness for as–reduced and arc melted+homogenized alloy as a function of load

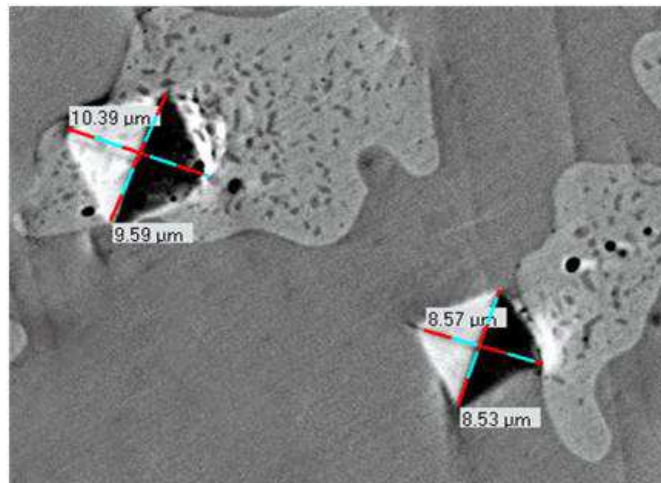


Fig. 5.20 Profiles of a Vickers indentation at a load of 3 N, showing the variation of indentation size

This phenomenon is observed also in ceramics [63] and bulk metallic glasses [64]. It is also seen that above a critical load, some cracking at the corners takes place. No cracking at faces have been observed. Cracking acts as a dissipative mechanism and thus lowers the value of hardness. For higher loads, above 3 N, cracks are always observed around the indentations, thus it is the “critical load for cracking”. For brittle materials (poor toughness), this critical load is of importance. Indeed the initiation of a crack is associated with the creation of a long crack and the failure of the structure (poor resistance to crack propagation). The profiles of Vickers indentation at a load of 3 N along the corners and the faces at both phases are shown in Fig. 5.21.

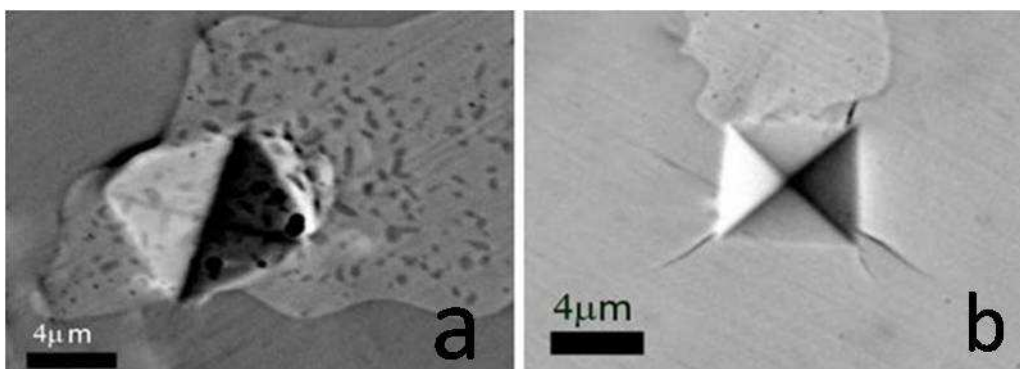


Fig. 5.21 Profiles of a Vickers indentation at a load of 3 N (a) at Phase A (b) at Phase B

No pile-up is observed around indentation at phase B while a clear ≥ 500 nm high pile-up is present along the faces of indentation at phase A. The pile up is due to the plastic flow of the material, showing the evidence of ductility of phase A. The fracture toughness increases due to the crack arresting capability of phase A, which is clearly seen in Fig. 5.21

(b). Crack intercepts by the primary Mo phase, hinder the catastrophic fracture through the formation of unbroken ductile–particle ligaments in the crack wake [65–68]. The fracture toughness of the system can be enhanced by the presence of the ductile phase; it is either by crack blunting, branching, deflection or combinations of these. Crack deflection or branching alters the loading mode (I to mode II) so crack propagation is hindered resulting in increase in fracture toughness. Due to the crack hindrance (Fig. 5.21b) and plastic deformation (Fig. 5.21a) of the Mo–phase, together with crack deflection and interfacial de–bonding the toughness of the alloy is expected to enhance.

5.4.2 Room temperature fracture toughness test

The SENB tests for determining fracture toughness were conducted in triplicate for checking the repeatability. The room temperature flexural strength and the fracture toughness of the hot pressed Mo–16Cr–4Si alloy determined are 615 ± 15 MPa and 10.7 ± 0.5 MPa.m^{1/2}, respectively.

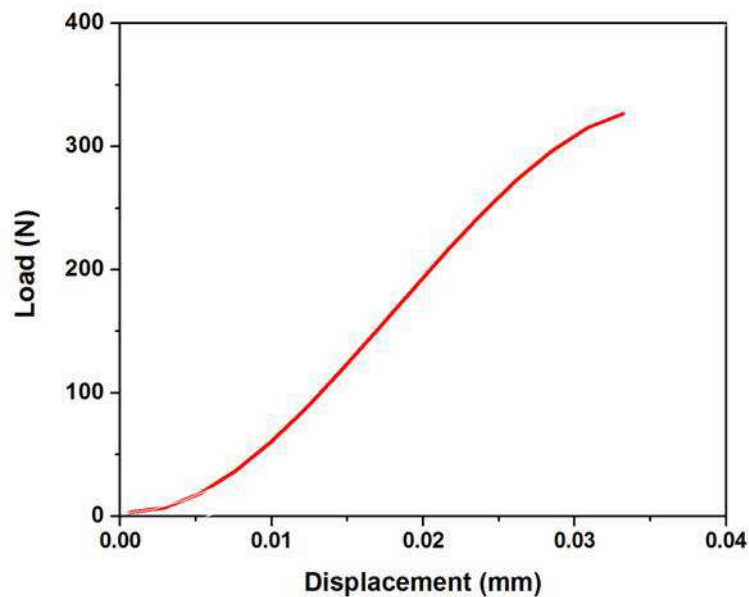


Fig. 5.22: Load displacement curve exhibited by Mo–16Cr–4Si alloy during bending test

The load displacement curve during the test is shown in Fig 5.22, which indicate some ductility beyond a strain of 0.032. Fig. 5.23 shows the fracture surfaces of the alloy after bending tests at room temperature. The predominant fracture mode for the alloy was transgranular cleavage consisting mainly quasi–cleavage where the fracture facets were not appeared as well defined planes. This fracture mode corresponds to the silicide (Mo, Cr)₃Si phase while (Mo,Cr)_{ss} phase exhibits a significant percentage of intergranular fracture.

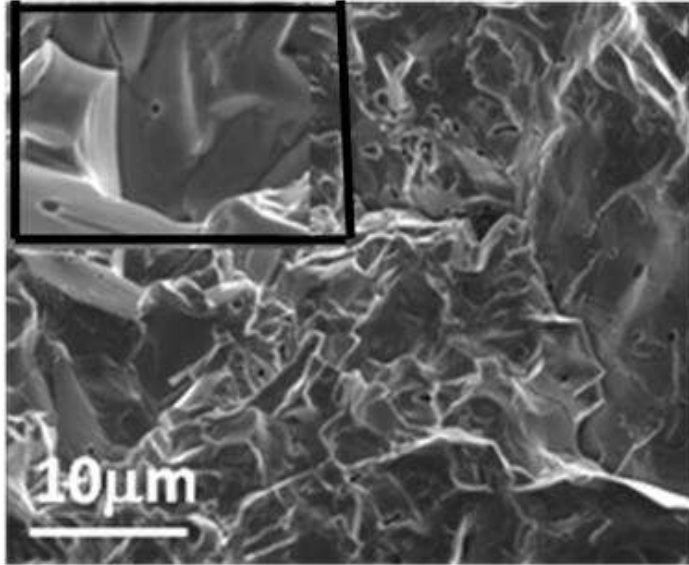


Fig. 5.23: SEM image of fractured surface of Mo-16Cr-4Si alloy after bending test

Fig. 5.23 also shows the presence of micro pores, which acts as site for blunting the propagating cracks, adding to enhancement of fracture toughness. Application of vacuum during hot pressing, help in escaping of chemisorbed gases, oxygen impurity causing further increase in density during sintering and reduce the segregation of silica along the grain boundaries during cooling. In-situ composite of Mo-Cr-Si, synthesized in this manner is expected to possess excellent mechanical properties due to the elimination of detrimental silica layer observed with pre-alloyed powders.

5.5 Oxidation studies

TGA plot for oxidation during continuous heating followed by isothermal holding at 1273K is given in Fig. 5.24, which shows initial stage of oxidation behaviour of the alloy in flowing air. Initial mass gain is mainly due to the formation of MoO_3 , SiO_2 , Cr_2O_3 and later mass loss is due to volatilization of MoO_3 . In the plot, the rate of change of weight loss tends to decrease with time, indicating some resistance offered by the alloy against oxidation. Longer soaking time is required to reflect the preventive nature of alloy against oxidation. So, Isothermal studies at different temperatures have been carried out in horizontal furnace in flowing air. The data of weight change per unit area with time, obtained during isothermal oxidation at different temperatures are presented in Fig. 5.25. It is seen that initially the rate of change of mass loss was high but with time the oxidation rate decreased substantially due to the formation of protective SiO_2 and Cr_2O_3 layer over alloy surface. Formation of SiO_2 and Cr_2O_3 phases has been confirmed by XRD analysis of surface oxide layer of the composites after 50 h, as shown in the inset of Fig. 5.26. This indicates that the sample surfaces are completely oxidized and covered with thick SiO_2 and Cr_2O_3 only. The EDS analysis of the oxide scale shows the presence of Si, Cr and O peaks, and these observations corroborate the XRD analysis.

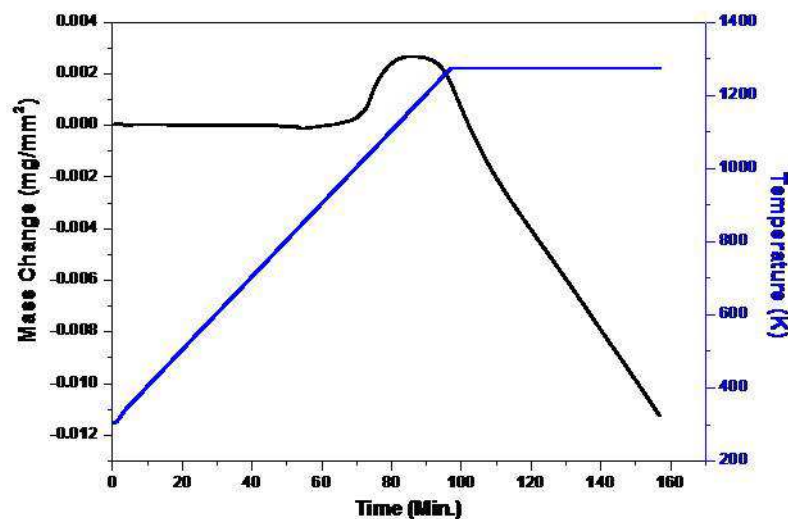


Fig. 5.24: TG plot showing the oxidation behaviour of the Mo-16Cr-4Si alloy sample

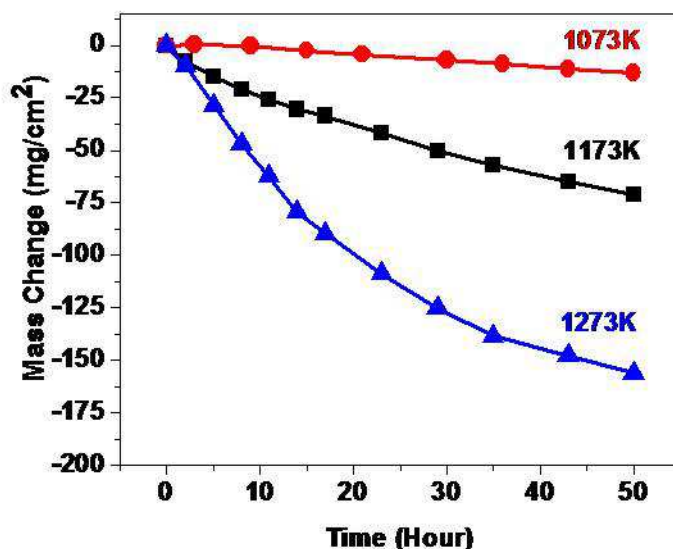


Fig. 5.25 Specific weight gain vs. time plot of Mo-16Cr-4Si-.5Ti alloy at 1073, 1173 and 1273K in air.

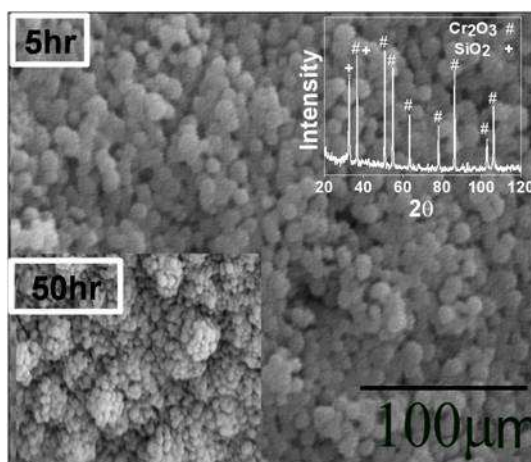


Fig. 5.26: SEM image of the oxidized surface at 1273K for 5hr and 50 hr of exposure. Inset shows the XRD pattern of oxides formed upon oxidation over alloy surface

Upon exposure to air at elevated temperature, at the first instance, the surface is covered with competitive oxide formation of Mo, Cr and Si. Simultaneously the oxide of Mo starts to vaporize from the oxide-gas interface, leaving behind the porous oxide layer. Supply of O₂ from the atmosphere through the flawed outer layer continues, due to increase in porosity. This causes inward diffusion of O₂ and precipitation of small Cr₂O₃ and SiO₂ particles behind the oxide scale while the external scale grows and accordingly the metal-oxide interface recedes. As the reaction proceeds, Cr₂O₃ and SiO₂ particles are linked and agglomerated by lateral growth to form a complete oxide layer of Cr and Si. Thus, once a

sufficient quantity of MoO_3 has evaporated, the Si and Cr concentration on the surface becomes high enough to form a protective layer against further oxidation. In the present case, the morphology of the oxide scale consists of mainly oxides particles. SEM of the surface after oxidation at 1273K for 5 and 50 h has been presented in Fig. 5.26. The surface was crack free but porous at 5h but with time coagulation/agglomeration of oxides takes place, which try to close the pores with time and makes the oxide layer more protective.

5.6 Effect of varying concentrations of alloying additions on different properties

5.6.1 Oxidation behaviour

To study the influence of concentrations of Cr and Si on the oxidation resistance of the Mo–Cr–Si alloys, different alloys with varying concentrations of Cr and Si were prepared by reactive hot pressing. The alloy compositions and hot pressing conditions are tabulated in Table–5.7. TG plots for oxidation of alloy 1 and 9 during continuous heating followed by isothermal holding at 1273K are shown in Fig. 5.27, which shows initial stage of oxidation behaviour of the alloys.

Table–5.7 Different alloy compositions, hot pressing conditions, their theoretical and sintered densities and weight change upon oxidation

Exp. No. (alloy)	Mo	Cr	Si	Hot pressing time At 1873K,10MPa	Theoretical density(g/cc)	Sintered density(g/cc)	K_Q (MPa*m ^{1/2})	$\Delta mg/mm^2/sec$ (x 10 ⁻⁴)
1	80	16	4	300 min	8.49	8.24	10.5	-1.620
2	79	16	5	240 min	8.24	8.03	9.8	-1.220
3	78	16	6	180 min	7.98	7.82	7.4	-1.160
4	76	20	4	270 min	8.35	8.14	8.4	-1.310
5	75	20	5	240 min	8.09	7.92	7.5	-1.398
6	74	20	6	180 min	7.93	7.81	5.5	-0.977
7	72	24	4	270 min	8.19	7.99	8.45	-1.392
8	71	24	5	240 min	8.04	7.87	5.2	-1.022
9	70	24	6	180 min	7.81	7.69	5.0	-0.950

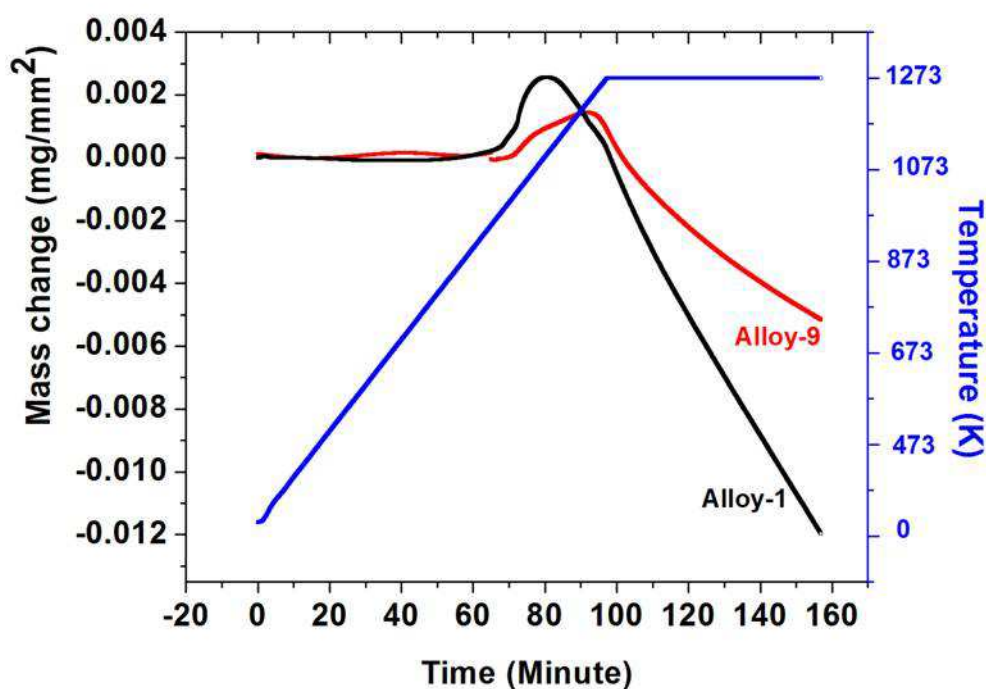


Fig. 5.27: TG plots showing the oxidation behavior of alloy-1 and alloy-9

A common feature of the oxidation behavior of all the alloys is an initial weight gain, which is mainly due to formation of oxides of Mo, Cr and Si, followed by mass loss due to volatilization of MoO_3 . Once a sufficient amount of MoO_3 evaporates from the surface, Si and Cr concentration on the surface become high enough to form a protective SiO_2 and Cr_2O_3 film. From the plot in Fig. 5.27, it is depicted that, the rate of change of weight loss tends to decrease with time, indicating some resistance offered by the alloy against oxidation. Longer soaking time is required to reflect the preventive nature of alloy against oxidation. Therefore, isothermal studies at different temperatures have been carried out in horizontal furnace in flowing air. The data of weight change per unit area against time, obtained during isothermal oxidation at 1273K for alloy-1 and alloy-9 is presented in Fig. 5.28.

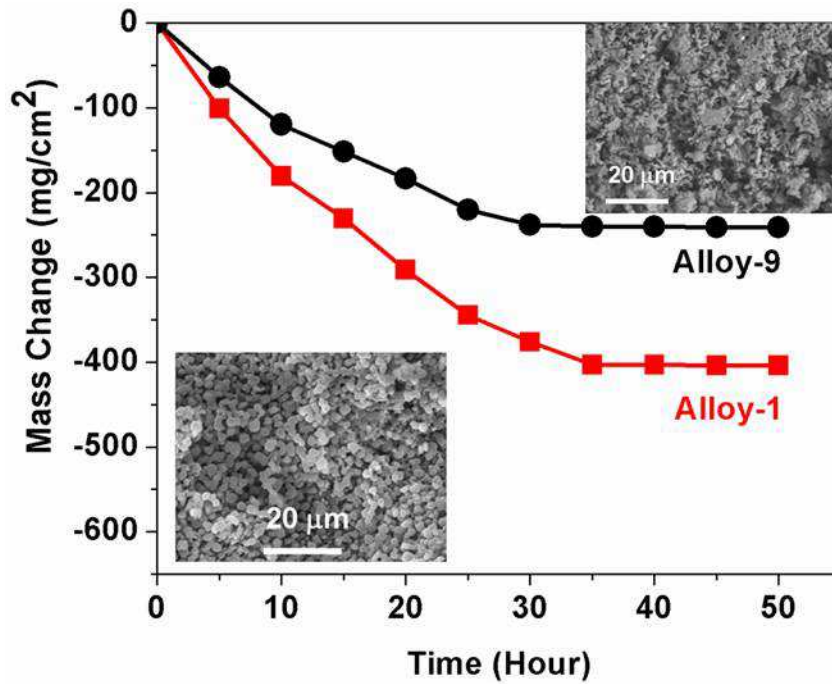


Fig. 5.28: Specific weight change vs. time plot of alloy-1 and alloy-9 at 1273K in air. Insets show the SEM images of the oxidized surfaces

It is seen that initially the rate of change of mass loss is high but with time the oxidation rate decreases substantially, due to the formation of SiO_2 and Cr_2O_3 layer over alloy surface. Upon exposure of the alloy to O_2 at elevated temperatures, at the first instance, the surface is covered with competitive oxide formation of Mo, Cr and Si. Above 903K, MoO_3 begins to grow over the scale surface at a faster rate, and growth continues up to 998K [71]. The vapor pressure of MoO_3 increases significantly at 998K, and MoO_3 begins to vaporize from the oxide-gas interface, leaving behind the porous oxide layer. Supply of O_2 from the atmosphere through the flawed outer layer continues due to increase in porosity, which leads to further oxidation of the substrate material. The Gibbs free energies of the formation are -523.5 and -678.3 KJ/mole O_2 for Cr_2O_3 and SiO_2 respectively at 1273K. Both oxides are thermodynamically stable and readily form by exposure of air or oxygen at higher temperatures. With time, Cr_2O_3 and SiO_2 precipitates are linked and agglomerated by lateral growth to form a complete oxide layer of Cr and Si. XRD pattern of surface oxide layer of the alloys after 50 h are shown in Fig. 5.29, where formation of cristobalite phase of SiO_2 and Cr_2O_3 were confirmed in both the alloys. Therefore the oxide scale consists of mixture of SiO_2 and Cr_2O_3 .

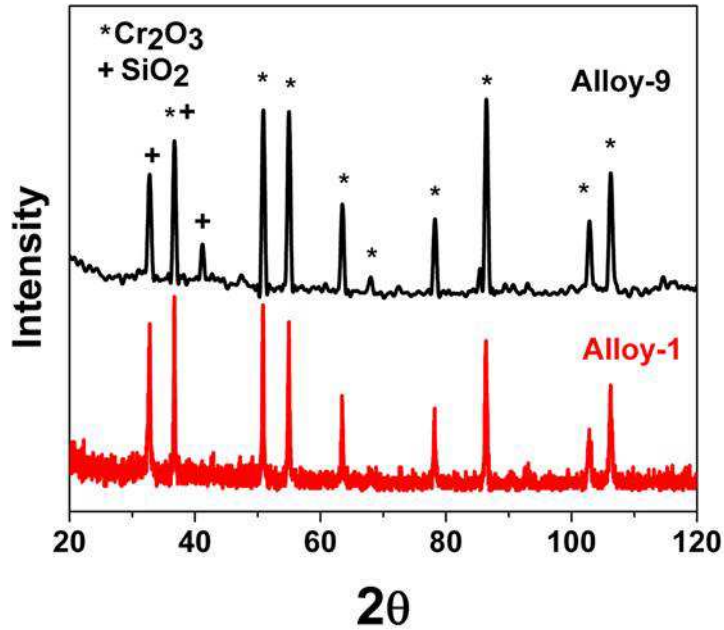


Fig. 5.29: XRD pattern of oxidized surface formed upon oxidation over the surface of alloy-1 and 9

Fig. 5.28 shows weight loss profile during isothermal oxidation at 1273K, for alloys having different $(\text{Mo,Cr})_{\text{ss}}$ volume fraction. The weight loss increases as the volume fraction of $(\text{Mo, Cr})_{\text{ss}}$ increases. Apart from the change in volume fraction of $(\text{Mo,Cr})_{\text{ss}}$, other factor such as porosity, relative concentration of Cr and Si in outer film, temperatures of exposures etc. affect the oxidation behavior. Therefore, it is difficult to identify the individual effect of alloying elements on oxidation behavior, but the data generated through this study will guide the research in proper direction with respect to range of alloying additions.

Fig. 5.30 shows graphically, the effects of different concentrations of the alloying elements on the oxidation behavior. The relative slopes of the linear graphs indicate significance of the concentrations of Cr and Si additions on the oxidation behavior of the alloys. From the slopes of the different segments of plots, it is seen that the weight change due to oxidation is more sensitive for the alloys having Cr content between 16–20 wt.% in comparison to 20–24 wt.% for all the three levels of Si.

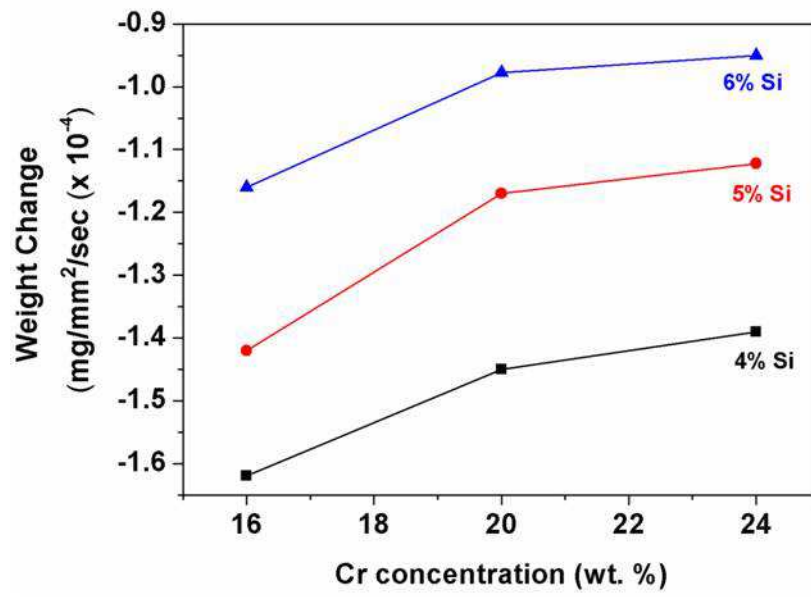


Fig. 5.30: Effects of concentrations of the alloying elements on the oxidation behavior at 1273K for 1hr.

5.6.1.1 Kinetics of oxidation

Thermal oxidation problem restrict the widespread use of molybdenum and its alloys as a structural material, although the high temperature mechanical properties are promising. Therefore understanding the kinetics of oxidation is of utmost importance. Considerable efforts have been made in the past to understand the kinetics and mechanisms involved in oxidation of Mo and its alloys [69–73]. Since oxidation is a thermally activated process, activation energy and the governing rate laws are important to be known. The activation energies for the oxidation of metals are related to their band gaps, heats of formation, electronic conductivity of the oxides formed [74] and their work functions [75, 76]. Band gap, electronic conductivity of the oxides, work function etc. of the metals can be altered by suitable alloying additions, which can increase the activation energy, resulting improvement of the oxidation resistance. Thus, determination of the activation energy for oxidation is important in correlating with the above physical properties and understanding the oxidation behavior of metals and alloys.

Various equations have been suggested to describe the oxidation kinetics and calculate the activation energy [77]. Preferably four experiments are required at four different heating rates or different isothermal temperatures, for calculating activation energy for any thermally activated process by constant rate of heating (CRH) method or isothermal heating [78, 79]. In this respect stepwise isothermal thermogravimetry (SITG) would have an advantage, because in the single experiment activation energy could be found out, using the analogies for evaluating sintering kinetics from stepwise isothermal dilatometry (SID). SID is a relatively new approach as compared to conventional sintering studies and has proven its usefulness in analyzing the sintering mechanism of ceramic [80–84], metal [85] and alloys [86].

In the present study, we have attempted to imbibe the methodologies of SID, for using SITG method to determine oxidation kinetics of molybdenum and proving the applicability of the novel method. Further, SITG has been used for evaluating the oxidation kinetics parameters for oxidation resistant Mo–16Cr–xSi alloys where x= 4, 5 and 6 wt.%. No such data of oxidation kinetics parameters of Mo–16Cr–xSi alloys are available in the open literatures.

Commercially available pure molybdenum strip of known area was cut from a sheet, and used for oxidation test at 1 atmosphere oxygen pressure in a thermobalance using alumina crucible. Samples were heated at a heating rate of 20 K/min. up to the 523 K then

onwards up to 673 K with the same rate of heating and an isothermal hold of 60 minutes at each 50 K interval (step). At higher temperatures (beyond 673 K) a quantitative estimation of oxidation rates of pure Mo is complicated because of the high vaporization rate of MoO₃. Therefore, oxidation study for Mo was limited up to 673 K to avoid any interference of weight gain with the vaporization of MoO₃.

5.6.1.1.1 Theory

In general a study of the oxidation behavior of any system begins with some measurement of the extent of conversion of the original system to oxide as a function of time *t* under selected condition of temperatures and oxygen pressure. Then the data are analyzed to yield a rate law. The conventional equation for oxidation kinetics is generally described as:

$$x^m = kt \quad (5.12)$$

Where ‘*x*’ is the oxide film thickness or the mass gain due to oxidation, which is proportional to the oxide film thickness, *t* is time at isothermal hold, *k* is the rate constant and ‘*m*’ is the exponent related to the oxidation mechanism. In wider application ‘*x*’ is a specific measurement which may be weight change, oxygen consumption, thickness of oxide layer, recession of the metallic system or some combination of these. The conventional kinetic laws stated above to characterize the oxidation kinetics is based on simple oxidation models. Practical oxidation problems usually involve much more complicated oxidation mechanisms than considered in these simple analyses.

In this study the specific measurement is weight change determined by thermo-gravimetry (TG). To analyze any type of stepwise isothermal data, “dynamic and relative” changes with respect to different steps of isothermal holding should be considered [80]. So, for SITG experiments, ‘*x*’ should correspond to dynamic relative weight change. An equation to describe “dynamic” relative specific weight change with time can be written as in equation–5.13, assuming that the total exposed specific area (*A*) of the sample remain constant during the process.

$$x = \frac{(w_t - w_o)}{(w_f - w_t)} = [k(T)(t - t_o)]^n \quad (5.13)$$

Where,

$$k(T) = k_o \exp(-Q/RT) \quad (5.14)$$

Where t_0 is the time at which the given isothermal step is started, w_o , w_t , and w_f are the initial weight, weight at particular time 't' and weight of the samples when oxidation is completed respectively. $k(T)$ is the specific rate constant which obeys the Arrhenius law, k_o , the frequency factor, Q , the apparent activation energy, R , the universal gas constant and 'n' is a parameter related to the oxidation mechanism. Equation-5.13 can further be modified to include fractional oxidation function (Y) as,

$$\frac{w_t - w_o}{w_f - w_o} = \frac{Y}{1-Y} = [k(T)(t - t_0)]^n \quad (5.15)$$

Where, the fractional oxidation function, Y can be defined as:

$$Y = \frac{(w_t - w_o)}{(w_f - w_o)} \quad (5.16)$$

The value of fractional oxidation function, Y varies from 0 to 1. Equation-5.15 is fairly reasonable for the initial stage of oxidation, as the change in a growing process (growth of oxides or weight change) should be proportional to $[k(T)t]^n$. A normalized rate equation can be written as equation-5.17, by taking derivative and eliminating $(t - t_0)$.

$$\frac{dY}{dt} = nk(T)Y(1-Y) \left(\frac{1-Y}{Y} \right)^{1/n} \quad (5.17)$$

Equation-5.18, become linear by taking log on both side of equation-5.17,

$$\ln \left\{ \frac{dY}{dt} / Y(1-Y) \right\} = \frac{1}{n} \ln \left[\frac{(1-Y)}{Y} \right] + \ln[nk(T)] \quad (5.18)$$

The plot of $\ln \{(dY/dt)/Y(1-Y)\}$ versus $\ln[(1-Y)/Y]$ where Y can be known from equation-5 as w_o , w_t , and w_f are all experimentally determined using SITG. The plot in the form of a straight lines during the isothermal steps, indicate the equation is well valid to the case under investigation.

5.6.1.1.2 Kinetic analysis of Mo by SITG measurement

Using the above model, the weight change data of Mo, after fitting into equation-5.18 is plotted in Fig.5.31 as $\ln \{(dY/dt)/Y(1-Y)\}$ vs $\ln[(1-Y)/Y]$. A near straight line behavior for each isothermal zone indicates the validity of the model for the oxidation data of Mo. The values of slopes ' $1/n$ ' were 0.94, 1.08, 0.81, 0.91 and intercepts ' $\ln nk(T)$ ' were -9.5, -9.2, -

7.8, -5.7 at isothermal sections of 523, 573, 623 and 673 K respectively, evaluated by least-squares linear fitting for each straight line segments of the curve with regression parameters better than 0.998. The inset of Fig-1 shows the Arrhenius plot of $\ln k(T)$. The apparent activation energy ' Q ' was calculated from the slopes of linear fit and found to be 135 ± 6 kJ/mole. The result obtained was in good agreement with the previously published results reported by Gulbransen et al. [71] and Vijn [74], where they reported the value of activation energy for oxidation of pure Mo to be 151 and 146 KJ/mol respectively, proving the effectiveness and validity of the model.

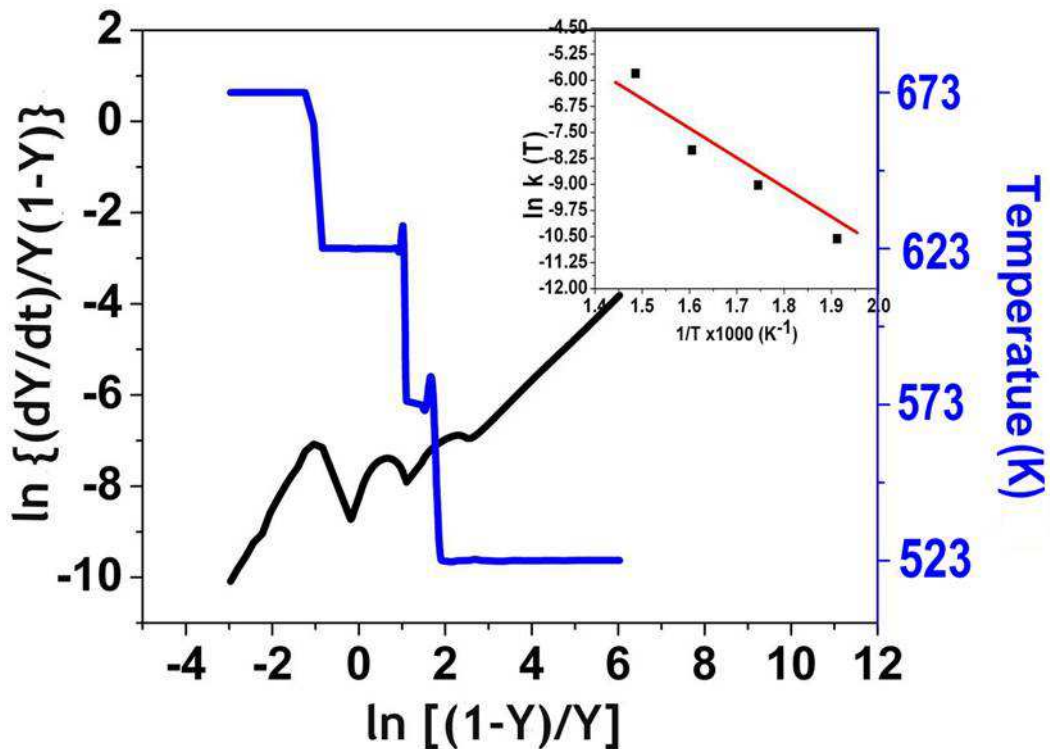


Fig.5.31: Plots of $\ln\{(dY/dt)/Y(1-Y)\}$ versus $\ln\{(1-Y)/Y\}$ for pure Mo. Variation of temperature with time is also shown on the right hand scale. Inset shows the Arrhenius plot of $\ln k(T)$ versus $1/T$ yielding activation energy for oxidation

5.6.1.1.3 Oxidation studies and kinetic analysis of Mo-16Cr-xSi alloys based on SITG measurement

Sintered densities of all the three hot pressed alloys were found to be $> 96\%$ of theoretical densities. Fig.5.32a and b show the SEM images taken in back scattered mode revealing the microstructures of sintered Mo-16Cr-4Si and Mo-16Cr-6Si alloys respectively. The microstructures consisted of two different contrast regions as white and black due to different chemical compositions acquired in those regions. The phase-A, appearing white was made up of a solid solution phase basically of Mo and Cr containing

small amount of Si. The phase-B, appearing black was made up of $(\text{Mo}, \text{Cr})_3\text{Si}$ intermetallic phase. The volume percentages of phase A are 28, 26 and 23% respectively for the alloy having 4, 5 and 6 wt% Si.

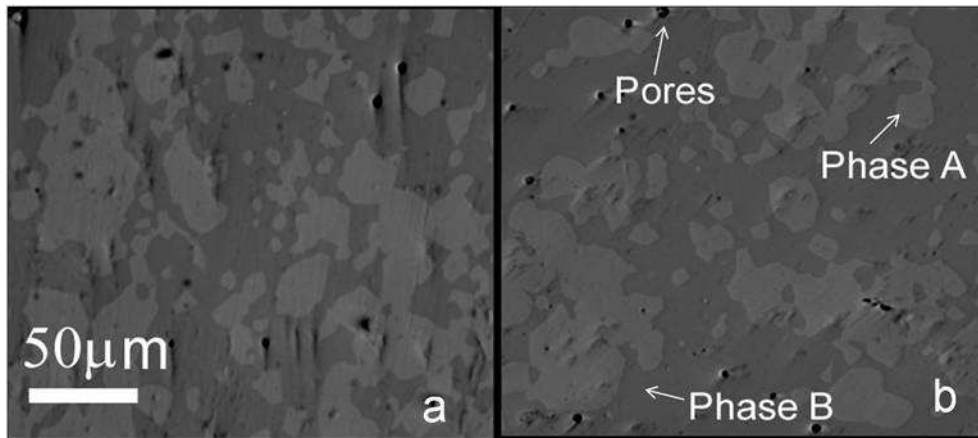


Fig.5.32: BSE-SEM images of the two phase (a) Mo-16Cr-4Si and (b) Mo-16Cr-6Si alloys showing difference of contrast for different phase A (Mo rich) and B (Si rich)

Non-isothermal TGA studies for oxidation have first been carried out to determine the onset of temperatures at which weight losses start taking place i.e. the temperatures at which volatilization of MoO_3 surpass the weight gains due to the formation of oxides constituents. TGA plots for oxidation during continuous (non-isothermal) heating up to 1273K are given in Fig. 5.33, which shows initial stage of oxidation behavior of the alloys in flowing O_2 . Initial mass gains are mainly due to formation of oxides of Mo, Cr and Si, whereas later mass losses are due to volatilization of MoO_3 .

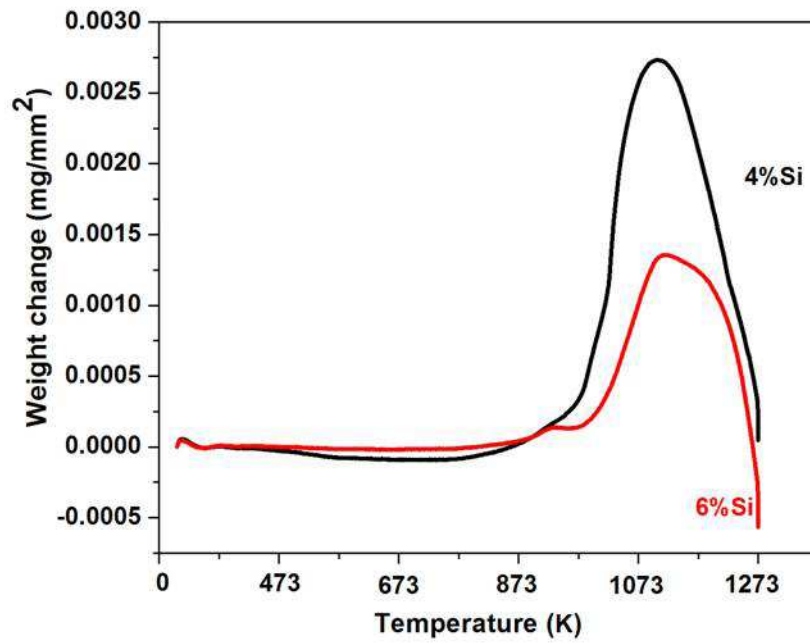


Fig. 5.33: TG plots showing the non-isothermal oxidation behaviour of Mo-16Cr-4Si and Mo-16Cr-6Si alloy

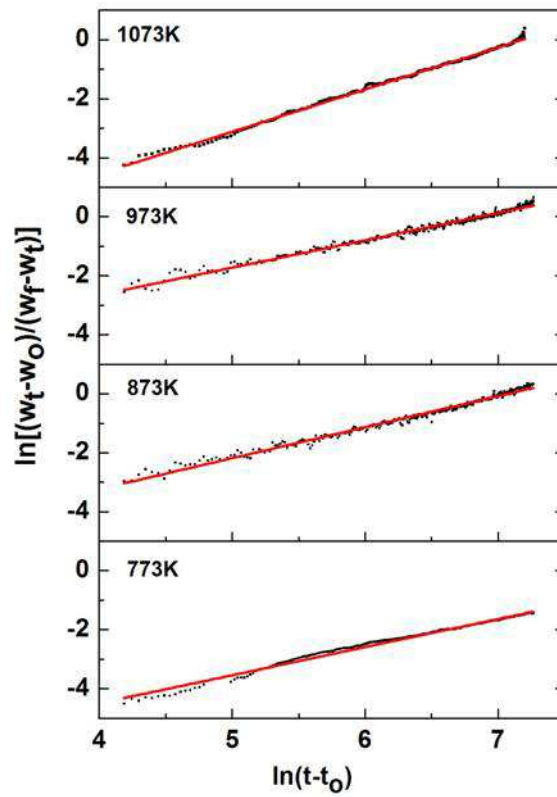


Fig. 5.34: Plot of $\ln[(w_t - w_o)/(w_f - w_i)]$ vs $\ln(t - t_o)$

Based on the findings, stepwise isothermal heating schedule has been selected. Fig. 5.34 shows the plot of $\ln[(w_f - w_o)/(w_f - w_i)]$ vs $\ln(t - t_o)$ using equation-5.13. The linearity at each isothermal steps shows the validity of the model proposed. Fig. 5.35 shows the plot of fractional oxidation function (Y) with time for Mo-16Cr-4Si alloy during the isothermal steps. It has been seen that the maximum weight gain was observed during the soaking at 700°C. Weight loss was observed during heating the sample beyond the heating schedule shown in Fig. 5.35. So, only weight gain data have been considered in the whole SITG analysis. The weight change data for Mo-16Cr-4Si alloys, after fitting into equation-5.18 is plotted in Fig. 5.36.

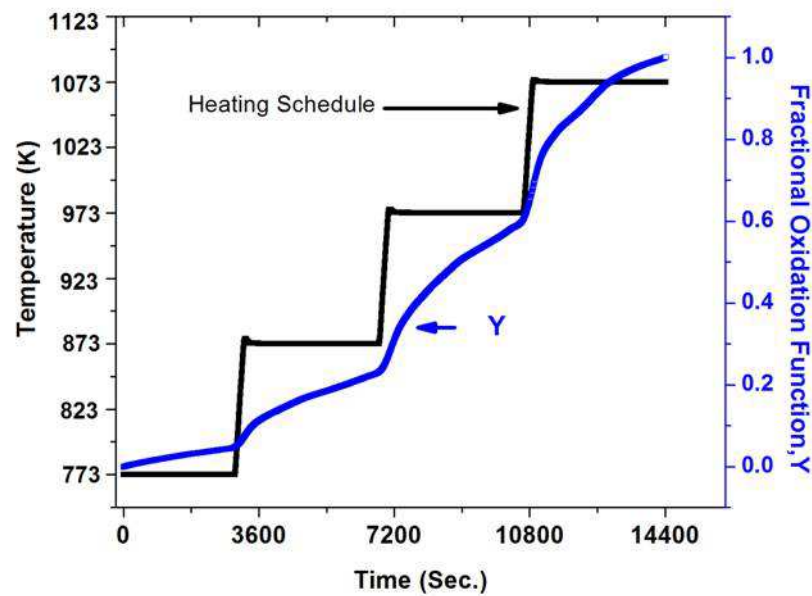


Fig. 5.35: Plot of fractional oxidation function (Y) of Mo-16Cr-4Si alloy with time. Heating schedule is also shown in the plot

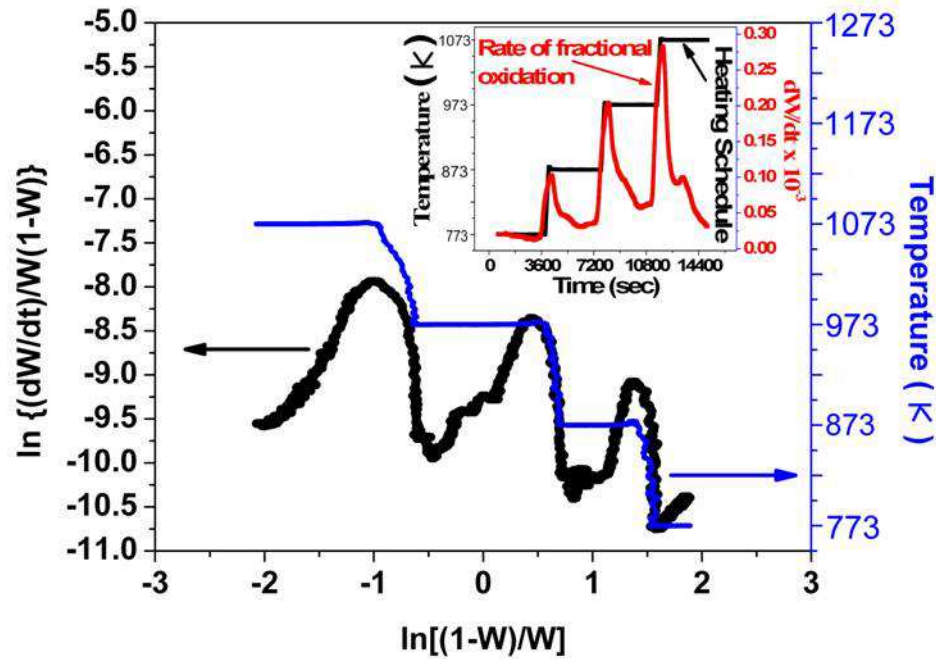


Fig. 5.36: Plots of $\ln\{(dY/dt)/Y(1-Y)\}$ versus $\ln\{(1-Y)/Y\}$ for Mo-16Cr-4Si alloy. Inset shows the fractional oxidation rate as a function temperature

A near straight line behavior have been seen for each isothermal section which indicates the weight change data is well fitted to present model. It is seen from the inset of Fig. 5.36 that there is increase in rate of fractional weight gain with increase in isothermal holding temperature gradually with time up to 973 K. The maximum net rate of weight gain was recorded during an isothermal soak period of 25 minute at 1073 K. The rate of weight change then decreases with further soaking period as seen in the inset of Fig. 5.36. The gradual increase in rate of change of weight with increasing temperature is due to enhanced thermally activated diffusion O_2 . The maxima in the oxidation rate accounts for all possible mass transport mechanisms operating in tandem. Afterward, decrease in the rate of weight change is mainly due to two reasons—firstly, the formation of protective oxide layer which inhibit diffusion of O_2 through oxide layers. The continued chemical reaction of oxide formation thus slows down and so the rate of change of weight. Secondly, due to simultaneous volatilization of MoO_3 , the net rate of weight change decreases.

The Values of slope ' $1/n$ ' and intercept ' $\ln nk(T)$ ', evaluated by least-squares linear fitting for each straight line segment of the curve for all three alloys have been presented in Table-5.8.

Table–5.8 Kinetic parameters of SITG oxidation data of three alloys

Temp. (K)	4% Si		5% Si		6% Si	
	1/n	ln nk(T)	1/n	ln nk(T)	1/n	ln nk(T)
773	0.95	-17.90	1.1	-14.35	1.33	-11.96
873	1.2	-14.61	1.21	-11.71	1.68	-9.67
973	1.1	-11.79	1.15	-8.98	1.16	-7.55
1073	1.45	-8.10	1.32	-6.27	1.71	-5.47

Arrhenius plots between $\ln k(T)$ and $1/T$ for the SITG data for the three alloys are shown in Fig. 5.37. The apparent activation energy ‘ Q ’ was calculated from the slopes of straight lines and found to be 167, 191 and 247 kJ/mole for the alloys having 4, 5 and 6 wt.% Si respectively in the temperature range of 773–1073 K. Thus, the activation energy for oxidation increases with increase in the concentration of Si in the Mo–Cr–Si alloys.

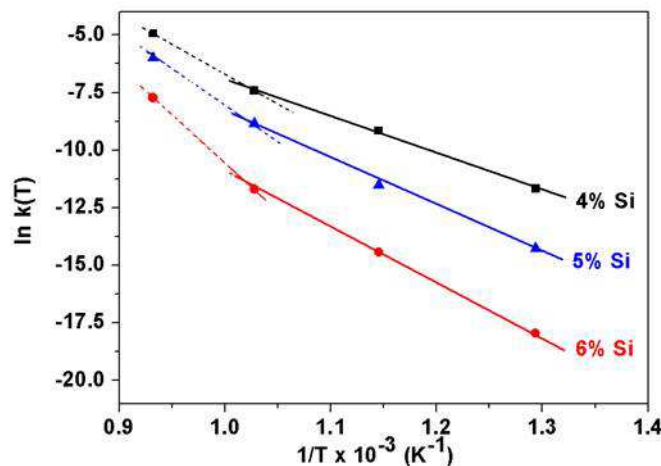


Fig. 5.37: Arrhenius plot of $\ln k(T)$ versus $1/T$ yielding activation energy for oxidation of the alloy Mo–16Cr–xSi alloys having x= 4, 5, and 6 wt. %

From the Table–5.8 it is seen that the parameter ‘ $1/n$ ’, which relates to the oxidation mechanism takes nearly same values in the measured temperature ranges for individual alloy, which shows the similarity of oxidation mechanism. Here it is worthy to mention that the ‘ $1/n$ ’ is different from the exponent ‘ m ’ described in equation–5.12. The slope ‘ $1/n$ ’ cannot predict the oxidation rate laws (parabolic, linear, cubic or other oxidation rate law) as possible by exponent ‘ m ’. However since the slope ‘ $1/n$ ’ is related to oxidation mechanism, it would take different values for different oxidation mechanism. The values of ‘ $1/n$ ’ has been

found higher for higher isothermal step and lower Si content which indicates that lower values of ' $1/n$ ' correspond to a relatively more complex oxidation phenomena.

SEM images of oxidized surfaces of the Mo–16Cr–4Si and Mo–16Cr–6Si alloys after stepwise oxidation schedule are presented in Fig. 5.38a and b respectively, while back scattered electron (BSE) image of the corresponding alloys before oxidation are also shown in the respective insets. The oxidized alloys exhibited a uniform and continuous oxide surface. XRD pattern of the surface oxide layer of the alloys confirmed the formation of SiO_2 and Cr_2O_3 phase. Fig. 5.39 shows the XRD pattern of the surface oxide layer of the Mo–16Cr–4Si alloy. The surfaces were crack free but porous and the morphology of the oxide scales consisted of mainly of particulates. The porous nature of the oxide layer is seen in SEM image in Fig. 5.38 (a), while dense oxide scale is seen in SEM image in Fig. 5.38 (b) revealing better oxidation resistance of the Mo–16Cr–6Si alloy. Since, Mo–16Cr–4Si alloy consists of 28% Mo_{ss} phase against 23% for Mo–16Cr–6Si alloy, the oxidation resistance is inferior. Thus, volume percentage of Mo_{ss} phase plays the decisive role in providing oxidation resistance of the alloys.

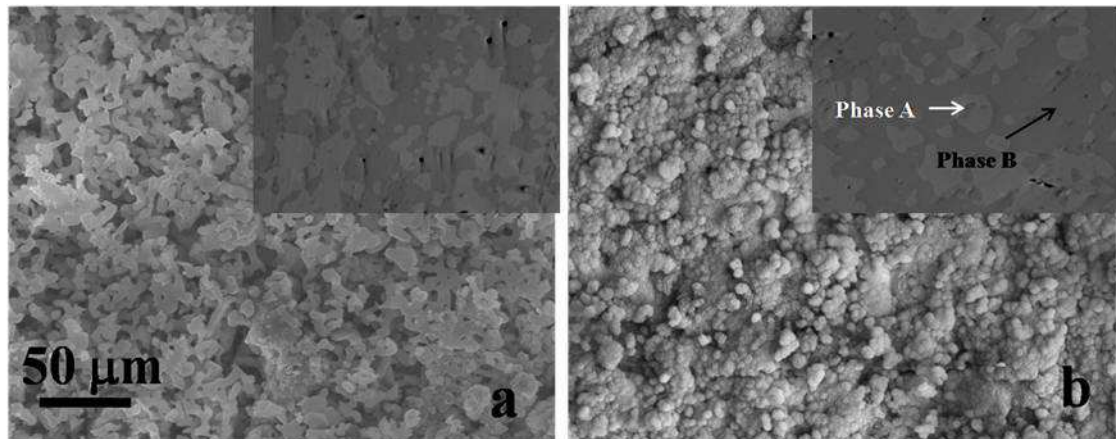


Fig. 5.38: SEM image of the oxidized surface for hot pressed (a) Mo–16Cr–4Si alloy (b) Mo–16Cr–6Si alloy. Insets show BSE–SEM images of corresponding alloys

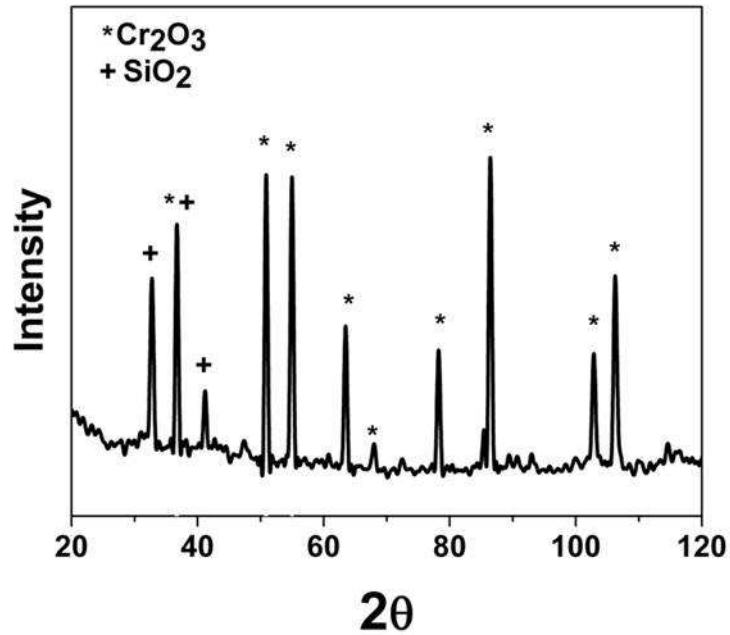


Fig. 5.39: XRD pattern of oxides formed upon oxidation over Mo-16Cr-4Si alloy surface

In summary, oxidation kinetics of Mo and Mo-16Cr-xSi alloys were studied by SITG technique. The model was found to fit well with the weight change data of both Mo and Mo-16Cr-xSi alloys and hence validated its usefulness for oxidation studies of metal and alloys to evaluate the oxidation kinetics and gives fairly reliable values of the activation energies using the thermogravimetry data of a single experiment. Effect of Si on the oxidation resistance was evaluated. The activation energy was found to be 167, 191 and 247 kJ/mole for the three alloys having Si 4, 5 and 6 wt.% respectively.

5.6 Effect of varying concentrations of alloying additions on

5.6.2 Fracture toughness

Different alloys with varying concentrations of Cr and Si were prepared by reactive hot pressing, to study the influence of concentrations of Cr and Si on the room temperature fracture toughness of the Mo–Cr–Si alloys. The alloy compositions and hot pressing conditions are tabulated in Table–5.7. The room temperature fracture toughness values of the nine alloys are presented in Table–5.9.

Table–5.9 The room temperature fracture toughness values of the nine alloys

Alloy	Mo	Cr	Si	K_Q (MPa.m ^{1/2})
1	80	16	4	10.5
2	79	16	5	9.8
3	78	16	6	7.4
4	76	20	4	8.4
5	75	20	5	7.5
6	74	20	6	5.5
7	72	24	4	8.45
8	71	24	5	5.2
9	70	24	6	5.0

The maximum and minimum flexural strengths are found to be 650 MPa and 375 MPa for alloy–1 and alloy–9 respectively. The load displacement curves of the alloy–1 and alloy–9 during the tests are shown in Fig. 5.40. Insets show the SEM images of fractured surfaces of both the alloys after bend test at room temperature. The predominant fracture mode for both the alloys was transgranular cleavage consisting mainly of quasi–cleavage. This fracture mode corresponds to the silicide (Mo,Cr)₃Si phase, while (Mo,Cr)_{ss} phase exhibits a significant percentage of intergranular fracture. Fig. 5.41 shows qualitative elemental line scan over the fracture surface of alloy–1, indicating variation of composition as well as fracture mode. The scan actually encompasses two–phase region, which are “Si rich” and “Mo rich”. The content of Si in the Si rich area was found to be 10 wt % (stoichiometric content of Si in of Mo₃Si while the content of Si in Si depleted area was ~ 1.2 wt. %, which is basically Mo rich area. The differences in the fracture modes of the two phases are clearly visible in the SEM image of the fracture surface shown in Fig. 5.41. The

fracture toughness of the system can be enhanced by the presence of the ductile phase; either by crack blunting, branching, deflection, creating extra surfaces by tearing or combinations of these. Crack deflection or branching alters the mode of loading (mode I to mode II), therefore crack propagation is hindered resulting in increase in fracture toughness. Due to the crack hindrance and plastic deformation of the Mo rich phase, together with crack deflection and interfacial de-bonding the toughness of the alloy was enhanced.

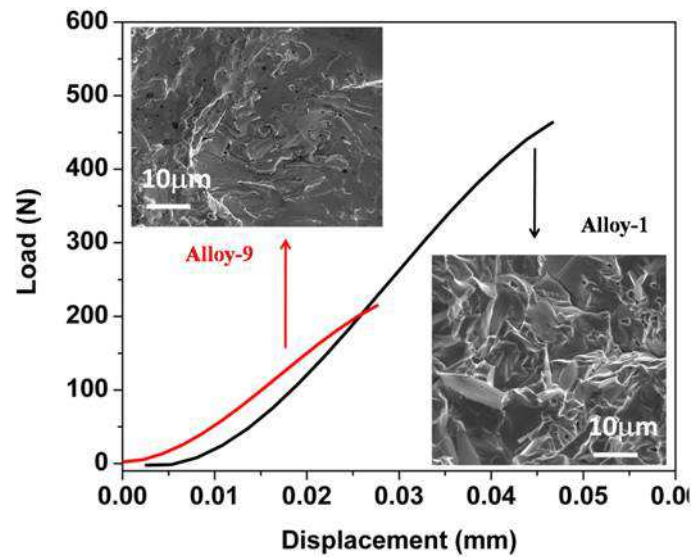


Fig. 5.40: Load displacement curves of the alloy-1 and alloy-9 during bending test. Insets show the SEM images of fractured surfaces of the alloys after bend test

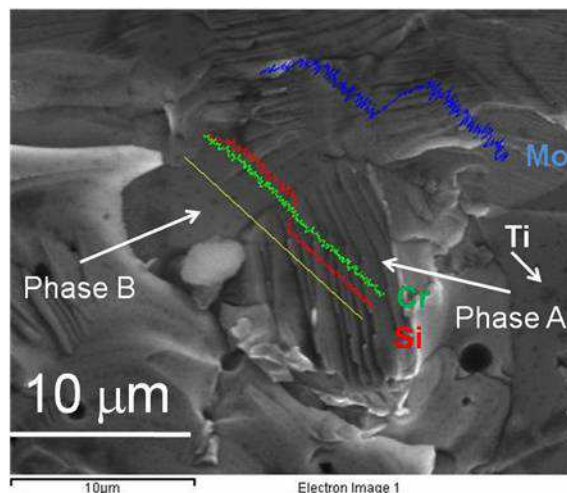


Fig. 5.41: Line scan over the fracture surface of alloy-1, showing the variation of Mo, Cr and Si along two phase region

Fig. 5.42 shows graphically, the effects of different concentrations of the alloying elements on the fracture toughness. The relative slopes of the linear regime indicate

significance of the different alloying additions. From the slopes of the different segments of plots it is seen that the fracture toughness is more sensitive (i.e. changes in fracture toughness) for the alloys having Cr concentration between 16–20 wt.% in comparison to 20–24 wt.% for all three levels of Si. Also, the fracture toughness is more sensitive for the alloy having Si concentration between 4–5 wt.% in comparison to 5–6 wt.% for all three levels of Cr.

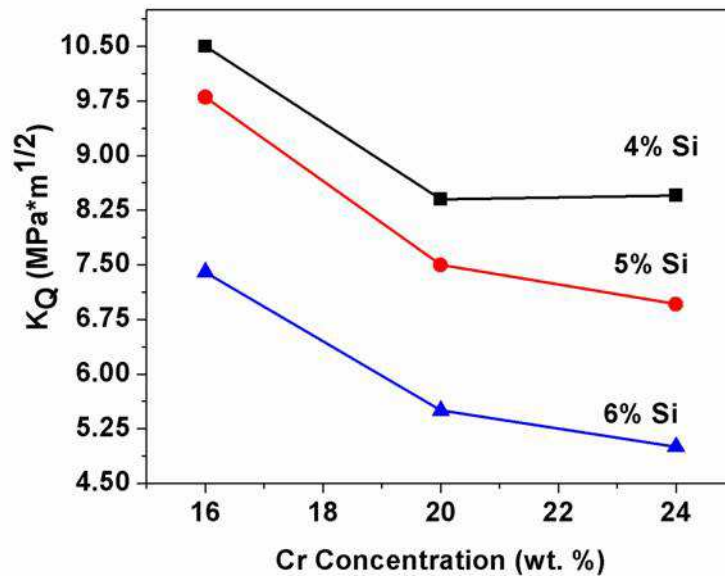


Fig. 5.42: Effects of different concentrations of the alloying elements on the fracture toughness

The effect of Si on the fracture toughness is directly related to the phase ratios of the constitutive phases. As the Si concentration increases, the volume percentage of silicide $(\text{Mo}, \text{Cr})_3\text{Si}$ phase also increases, results in decrease in fracture toughness decreases and vice-versa. Cr forms a solid solution with Mo and increase the resistance of dislocation movement. Thus, there is an increase in flow stress caused by the misfit in atomic sizes, resulting decrease in toughness.

Cr improves the oxidation resistance of the alloys by sacrificing room temperature fracture toughness. Marginal improvement in oxidation resistance, but a significant decrease in fracture toughness is observed for the alloy containing more than 16 wt.% Cr. It is not possible to choose a single alloy composition that exhibits both good oxidation resistances at high temperature as well as fracture toughness at room temperature. Therefore, optimization of the composition is necessary for achieving targeted properties. Mo–16Cr–4Si alloy

exhibits adequate oxidation resistance and fracture toughness, which can prevent catastrophic failure under oxidizing atmosphere and impact loading.

5.6.3 Effect of addition Ti on Mo–16Cr–4Si alloy

After understanding the effect of concentrations of Cr and Si on the properties of alloys, effect of Ti concentration has also been studied. Addition of Ti changes the properties of oxides, which improve their oxidation resistance by lowering oxidation rate and increasing spallation resistance [23]. However, this may apply only for small concentration alloying additions, which do not change the nature of the oxides in the scale. Therefore, the content of Ti was varied from 0.25 –1 wt. %, keeping Cr and Si at 16 and 4 wt. %. Three alloys having compositions of Mo–16Cr–4Si–0.25Ti, Mo–16Cr–4Si–0.5Ti and Mo–16Cr–4Si–1Ti were prepared by the same method as described earlier. Fracture toughness and oxidation behavior of the three alloys are shown graphically in Fig. 5.43.

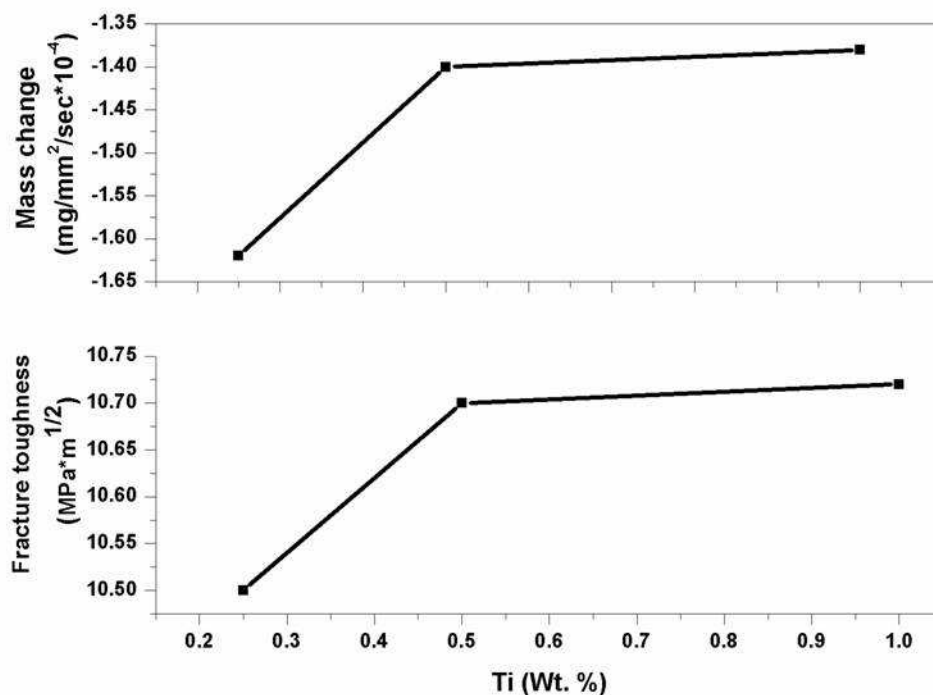


Fig. 5.43: Rate of weight change after oxidation and at 1273K and fracture toughness for the Mo-16Cr-4Si-xTi alloys, where x= 0.25, 0.5 and 1 wt. %

From the Fig. 5.43, it is seen that there is not much effect of Ti above the content 0.5 wt.% on both fracture toughness and oxidation rate. Thus, Mo–16Cr–4Si–0.5Ti alloy shows

optimum fracture toughness and oxidation resistance. Behaviour of Mo–16Cr–4Si–0.5Ti has further been studied in details to compare with Mo–Cr–Si alloy.

The load displacement curves of Mo–16Cr–4Si–0.5Ti alloy during the SENB test is shown in Fig. 5.44. Inset of Fig. 5.44 shows the SEM image of fractured surfaces of the alloy after bend test at room temperature. The fracture toughness of the Mo–16Cr–4Si–0.5Ti alloy ($10.7 \pm 0.5 \text{ MPa}\cdot\text{m}^{1/2}$) is much higher than the silicides Mo or Cr ($\sim 3 \text{ MPa}\cdot\text{m}^{1/2}$), mainly due to the crack arresting capability of the discontinuous (Mo, Cr, Ti)_{SS} phase. The fracture toughness of the system could be enhanced by the incorporation of the ductile phase; it is either by energy absorption by the deformation of ductile phase or crack blunting, branching, deflection or combinations of these processes.

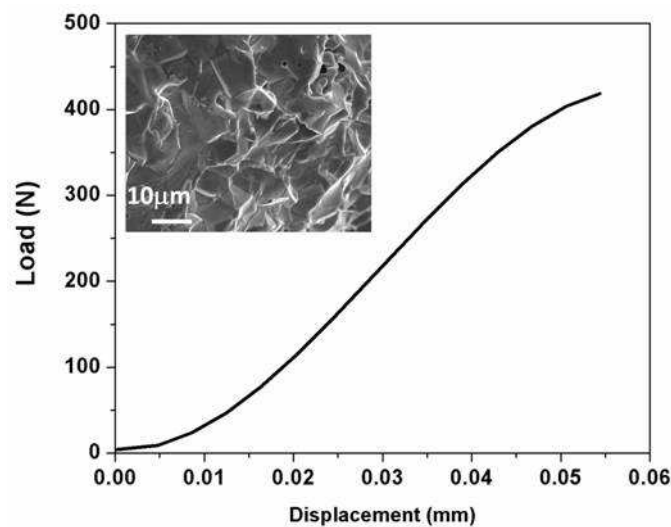


Fig. 5.44: Load–displacement curves of Mo–16Cr–4Si–1Ti during bending test. Insets show the SEM images of fractured surfaces of the alloys after bend test

The chemical compositions of the two phases of Mo–16Cr–4Si–0.5Ti alloy are: Si–1.19 wt.%, Cr–14.98 wt.% , Ti–0.46 wt.% and balance Mo for phase A and Si–8.96 wt.%, Cr–14.45 wt.%, Ti–0.33 wt.% and balance Mo for phase B. The addition of Ti has not improved the fracture toughness significantly. However a marked improvement was seen with respect to oxidation resistance. Weight loss of about $150 \text{ mg}/\text{cm}^2$ is observed during isothermal oxidation at 1000°C after oxidation for 50 hours, which is lower than the weight losses exhibited by alloys-9 ($250 \text{ mg}/\text{cm}^2$) and alloy-1($400 \text{ mg}/\text{cm}^2$), showing noticeable improvement in oxidation resistance by adding Ti as an alloying element. Fig. 5.45a and b show the cross section of the Mo-16Cr-4Si-0.5Ti alloy sample oxidized at 1273K for 1 hr and corresponding EDS line scan respectively, showing the variations of the elements. From the line scan it is seen that the oxide layer consists of silica and cromia.

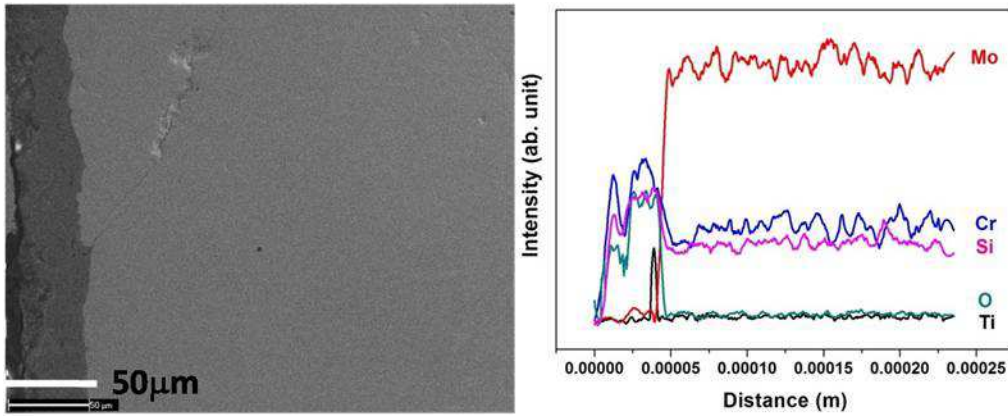


Fig. 5.45: (a) Cross sectional SEM image of the Mo-16Cr-4Si-0.5Ti alloy sample oxidized at 1273K for 1 hr (b) corresponding EDS line scan

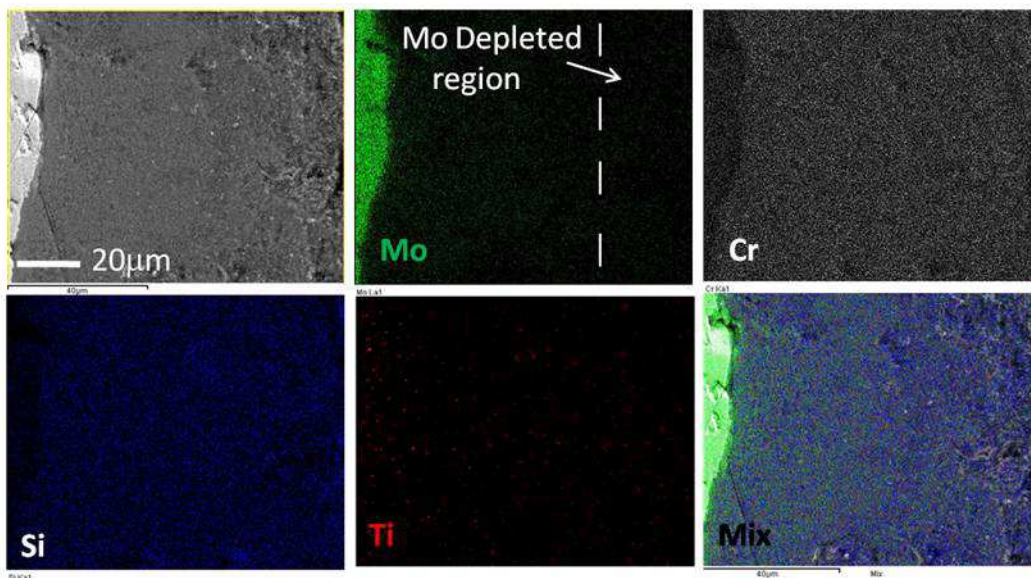


Fig.5.46: Elemental maps of the oxide region of the Mo-16Cr-4Si-0.5Ti alloy sample oxidized at 1273K for 5 hr.

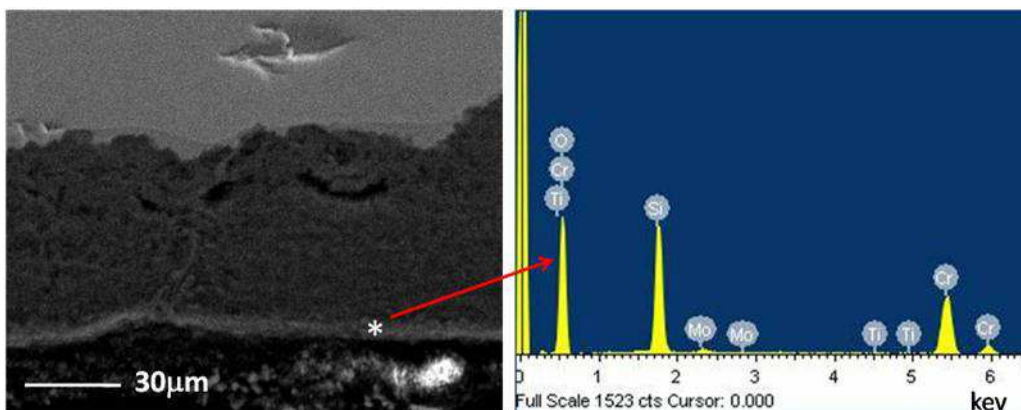


Fig.5.47: (a) Cross sectional SEM image of the Mo-16Cr-4Si-0.5Ti alloy sample oxidized at 1273K for 10 hr (b) corresponding EDS spectrum for the outermost layer.

Titanium oxide was found to be concentrated at the interface, which may be the probable reason for the high spallation resistance of the oxide layer. Fig. 5.46 shows the elemental map of the oxide region, showing the depletion of Mo from the outer layer from the Mo-16Cr-4Si-0.5Ti alloy sample oxidized at 1273K for 5 hr. Because of the depletion Mo, the outer layer becomes porous, but rich with Cr and Si. Actually, after evaporation of sufficient amount of Mo, the oxide layer become rich with Si and Cr, making the alloy oxidation resistant. Fig. 47 (a) shows the cross sectional SEM image of the Mo-16Cr-4Si-0.5Ti alloy sample oxidized at 1000 °C for 10 hr and Fig. 47(b) shows corresponding EDS spectrum for the outermost layer. The EDS spectrum shows the presence of broad peaks of Si and Cr along with oxygen, while the concentration of Mo is negligible. The XRD result also depicted that the oxide layer consisted of only silica and cromia. Thus, from the cross sectional examination of the oxide layer, it is seen that initially the oxide layer is porous and gradually the layer become denser and prevent the alloy from further catastrophic failure.

5.7 Development of oxidation resistant coating

Small specimens of dimensions 5 mm × 3 mm × 2 mm were cut from the Mo–16Cr–4Si–0.5Ti hot pressed alloy for conducting the coating experiments. The specimens were polished up to 1µm diamond finish followed by ultrasonic cleaning. The optimization of pack chemistries for the formation of silicide coatings have been reported earlier in chapter–4. Based on the experience of coating on Mo–30W alloy, the coating experiments were conducted at different temperatures from 1073K to 1573K for 6 h keeping pack chemistry of 20Si–2.5NH₄F–77.5Al₂O₃ (wt.%) fixed.

Fig. 5.48 shows the BSE images of the cross–sections of the specimens coated at 1073 K and 1373K for 6h. No cracks are observed in the coating layers. The inner layer of the coating shows fine grain structure, while columnar grains are seen in the outer layer. This indicates that the grain growth occurred parallel to the direction of the diffusion.

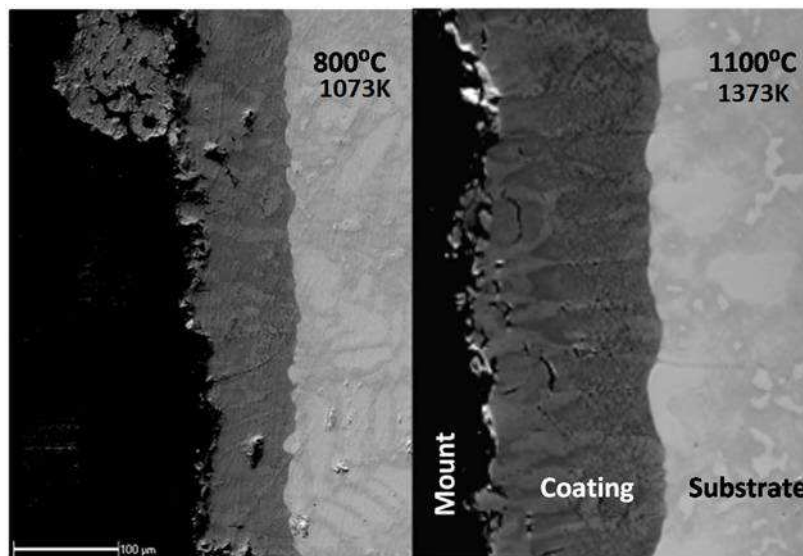


Fig. 5.48: Cross–section of the coated samples using coating temperature at 1073K and 1373K

The microstructure of the coating layer consists of three regions, namely white, grey and black. White and grey regions have been identified as silicide phases having higher concentrations of Mo and Cr respectively, while the black sub–micron sized particles have been identified as Si rich phase. The sub–micron sized particles are found dispersed uniformly, within the (Mo, Cr)Si₂ layer, when seen at high magnification (Fig. 5.51). The average compositions of the different contrast regions within coating are tabulated in Table–5.10.

Table–5.10: Average compositions of the different contrasts regions within coating

Phases	Mo (at. %)	Cr (at. %)	Si (at. %)	Ti (at. %)
White	14.20	10.04	75.16	0.6
Grey	3.51	24.57	71.61	0.31
Black	2.5	4.5	93	Nil
Overall	16.26	11.26	72.08	0.4

The Mo and Cr rich regions exist in the microstructure of the coating layer due to partitioning of CrSi_2 and MoSi_2 as shown in the isothermal section of the phase diagram of Mo–Cr–Si proposed by Ageev [87, 88] shown in Fig.5.49. It is noteworthy to mention here that there were no such Cr and Mo rich regions in the microstructure of the substrate. This is coherent to the phase diagram of Mo–Cr–Si (Fig. 5.49), which predicts that partitioning of CrSi_2 and MoSi_2 takes place in the system containing higher Si.

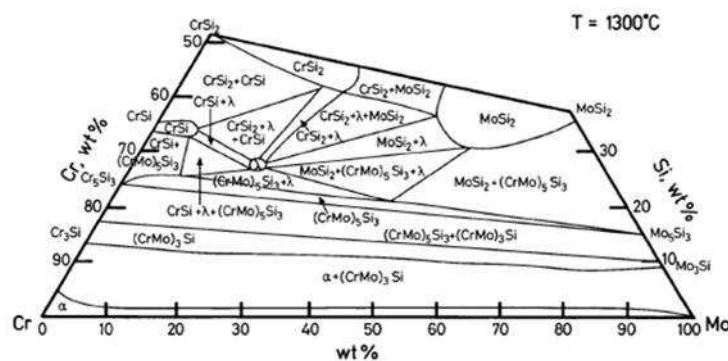


Fig. 5.49: Isothermal section of Mo–Cr–Si ternary phase diagram at 1573K [88]

From the phase diagram of Cr–Si [89] shown in Fig. 5.50, it is noticed that CrSi_2 is not a line compound; instead the concentration of Si in CrSi_2 increases with increasing temperature. Si concentration of coatings formed at 1573K is 72 at.% , which is higher than the stoichiometric value of 66 at. % for $(\text{Mo}, \text{Cr})\text{Si}_2$. Fig. 5.51 shows the qualitative line profile in the coating region of the sample coated at 1573K.

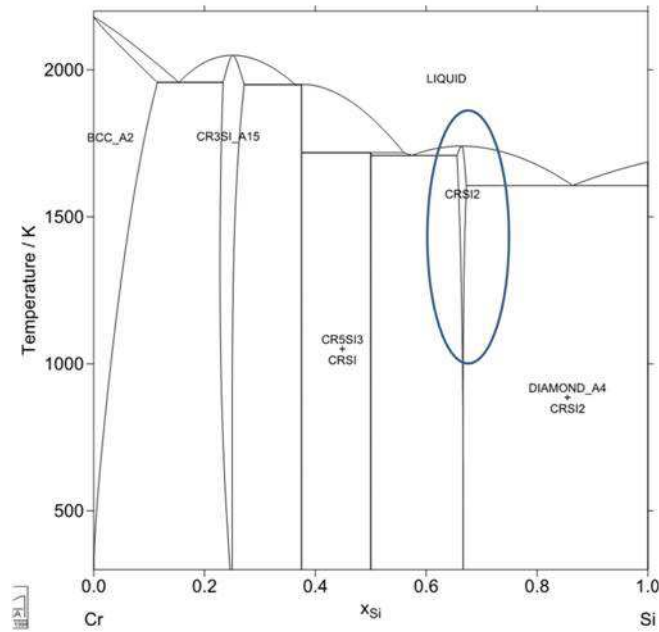


Fig. 5.50: Phase diagram of Cr–Si

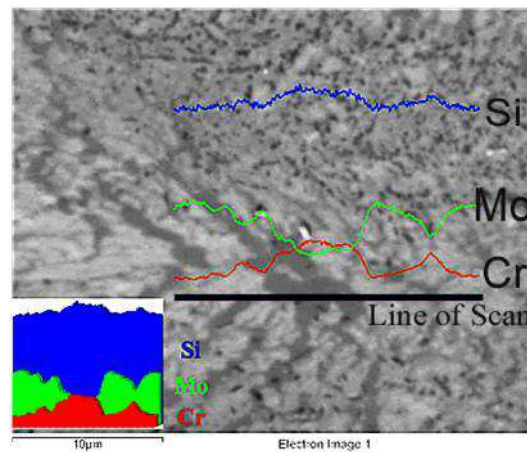


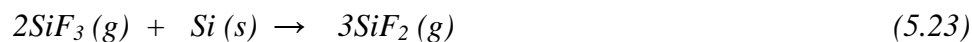
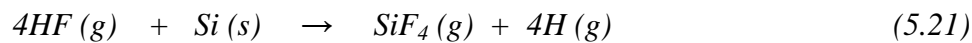
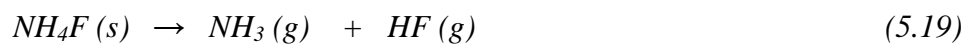
Fig. 5.51: Qualitative line profile in the coating area (Coating temperature =1573K), which shows that wherever Cr is more, Si is also more. Inset shows the same three dimensionally where the intensity is shows in arbitrary unit

The line profile reveals that the concentrations of Si are more in the Cr rich regions (grey regions in Fig. 5.51), corroborating the fact that Si concentration in CrSi_2 is more than 66 at.%. Since at the temperature of coating formation, solubility of Si in CrSi_2 is more, excess Si is expected to precipitate on cooling. Here, the precipitation takes place as sub-micron sized dispersoids. The EDS examination also showed very high silicon concentration in these dispersoids shown in Fig. 5.51. The oxidation resistance of this type of coating is due to the formation of silica and chromia layer. Moreover, Si rich dispersoid is expected to

enhance the oxidation resistance of the coating by acting as reservoir of Si to form silica layer.

5.7.1 Kinetics of growth of coating

In pack cementation process, the chemical potential gradient is the main driving force for the diffusion of halide vapors from the surroundings to the substrate surface in the pack. Activator, NH_4F dissociates into NH_3 and HF at temperatures above 573K, and subsequent reactions between HF and Si lead to the formation of the fluoride vapors such as SiF_4 , SiF_3 , SiF_2 , SiF depending on the local activity for molecular fluorine. The following reactions are likely to take place during the pack cementation process.



The standard free energies for the formation of different fluorides are -1428.3 , -1028.6 , -627.2 and -152.2 kJ/mole for SiF_4 , SiF_3 , SiF_2 and SiF , respectively [37]. Amongst the fluorides, SiF_4 and SiF_3 are very stable, while the vapor pressure of SiF is very low. The metal deficient fluorides SiF_4 and SiF_3 are assumed to be depleted species and their deposition is thermodynamically unfavorable, rather they carry fluorine back to the pack to re-form the lower fluoride species, which support deposition. On the other hand, partial pressure of SiF_2 is the maximum in the temperature range chosen in the present experimental campaign [38]. Therefore, the coating process is mainly dictated by the formation, migration and finally dissociation of SiF_2 . The most probable type of reaction for the siliconizing of the alloy using NH_4F activator can be illustrated as:



This is a disproportionation type reaction, where a lower halide (SiF_2) reacts with the active metallic surface to form a higher halide by depositing Si [90]. The coating (silicide) front moves inward enriching the substrate with Si and results in the formation of a silicide layer.

Tortorici and Dayananda [91, 92] reported that Mo₃Si layer could not form below 1623K, due to the nucleation difficulties, and the growth rate of MoSi₂ was much faster than that of Mo₅Si₃ in the temperature range of 1123–1623K. The present results are consistent with these earlier results that the phase formed in outer layer is of MoSi₂ type.

The thickness (h) of the coating layers, obtained at different coating temperatures and the corresponding weight gains (m) are given in Table–5.11. These results indicate the existence of a linear relationship ($h = 5.19 \times 10^{-4} m - 7.02 \times 10^{-6}$; $R^2=0.9989$) between coating thickness (h) and weight gain (m).

Table–5.11: Coating thickness and weight gain at different coating temperatures

Temperature (K)	1073	1273	1373	1573
Coating thickness (μm)	80	160	200	450
weight gain (kg/m^2) $\times 10^{-2}$	15.8	33.1	40.3	87.7

Therefore, for the pack siliconizing process, relationship between the coating thicknesses (h) with the processing parameters is governed by the equation–5.26 [37]

$$h = \frac{k_h}{T^{1/2}} W_{Si}^{1/2} W_{MF} t^{1/2} \quad (5.26)$$

Where k_h is a constant at constant temperatures, W_{Si} and W_{MF} are wt. % of Si and activator respectively. The variation of k_h with temperature can be given by,

$$k_h = k_0 \exp\left(-\frac{E_a}{RT}\right) \quad (5.27)$$

Where, E_a is the activation energy for the coating growth process, and k_0 is a constant. Finally substitution of k_h in equation–5.26 yields

$$h = \frac{k_0}{T^{1/2}} W_{Si}^{1/2} W_{MF} t^{1/2} \exp\left(-\frac{E_a}{RT}\right) \quad (5.28)$$

This is the ultimate kinetic equation for the coating growth process, relating the growth rate of the coating with temperature (T), time (t) and pack composition such as Si (W_{Si}) and activator content (W_{MF}). Equation-5.28 can be rewritten as:

$$\ln\left(T^{1/2}h\right) = -\frac{E_a}{RT} + \ln k_0 + \frac{1}{2}\ln(W_{Si}t) + \ln(W_{MF}) \quad (5.29)$$

At constant values of t , W_{Si} and W_{MF} , the activation energy of the silicide coating growth process can be obtained from the slope of the $\ln(T^{1/2}h)$ versus $1/T$ plot. Keeping the other parameters constant, the temperature of the coating process was varied from 1073 K to 1573K to determine the activation energy. The pack composition used for these experiments were fixed as 20Si-2.5NH₄F-77.5Al₂O₃ (wt.%) and soaking time (6h) was kept constant for all the experiments. Fig. 5.52 shows the linear fit of the plot for $\ln(T^{1/2}h)$ vs $1/T$. The activation energy obtained from the slope of the linear fit is 52.5 ± 5.15 kJ mol⁻¹. Similar activation energy was determined for the pack cementation coating process on a molybdenum base TZM alloy [38].

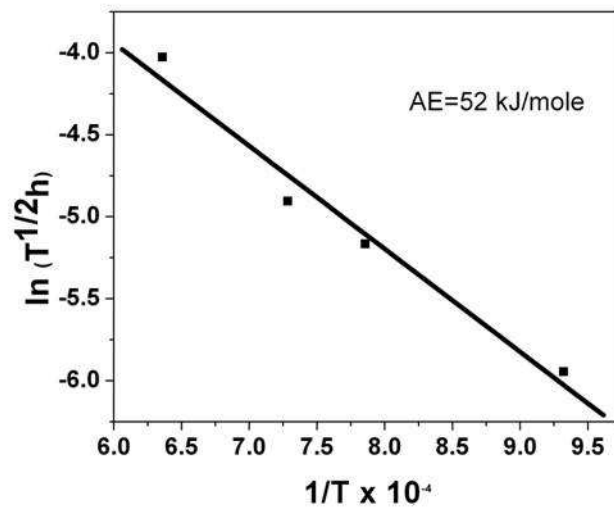


Fig. 5.52: Arrhenius plot of $\ln(T^{1/2}h)$ Vs $1/T$ for Mo-16Cr-4Si-0.5Ti alloy

5.7.2 Performance evaluation

Fig. 5.53 shows the TG plot for oxidation during continuous heating followed by isothermal holding at 1273K for the coated sample, showing a small mass gain due to the formation of SiO_2 and Cr_2O_3 layer. Fig. 5.54 shows the isothermal oxidation behaviour of the coated Mo-16Cr-4Si-0.5Ti alloy at 1273K for 50hr. During the isothermal oxidation at 1273K, a marginal weight gain of $3 \times 10^{-5} \text{ kg/m}^2$ is noted at the initial stage, followed by no change of weight, indicating the protective nature of the coating.

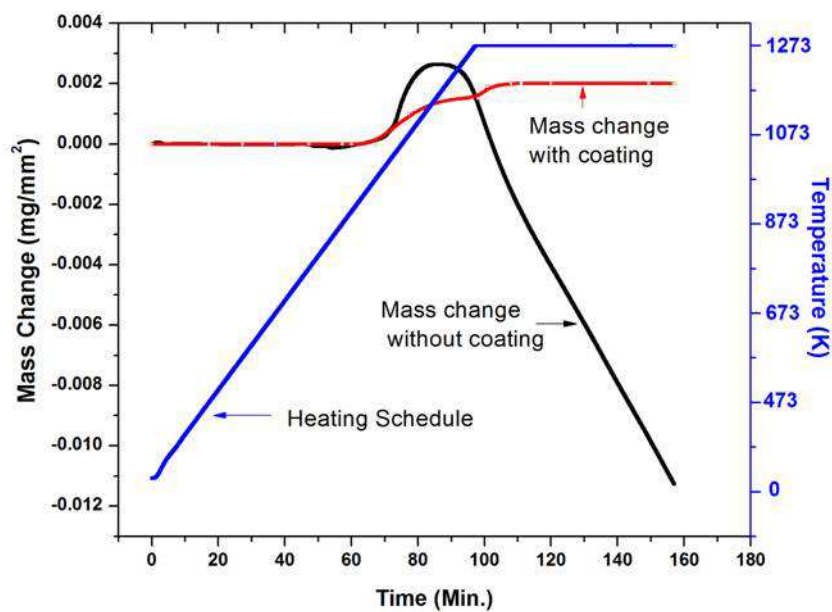


Fig. 5.53: TG plot showing the oxidation behavior of the sample with and without coatings

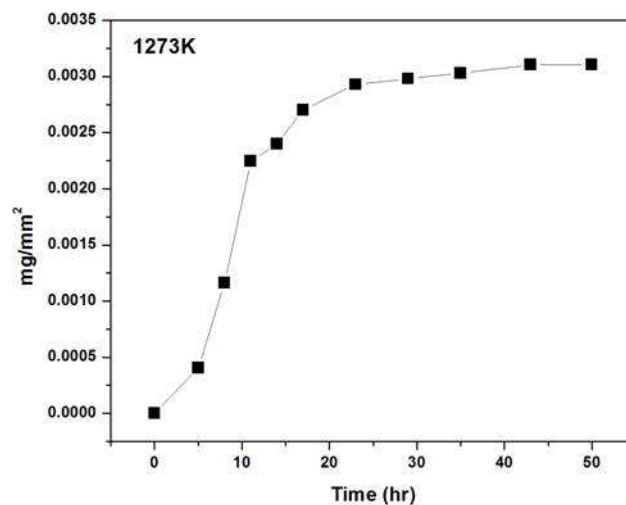


Fig. 5.54 Isothermal oxidation behaviour of the coated alloy for 50 h at 1273K

There was no chipping or peeling-off of the coating material from the coated surface after oxidation. Fig. 5.55 shows the line profile of the coated and then oxidized sample along the interfaces, showing qualitative variation of different elements across the cross section. The line profile shows the presence of Ti in the oxide scale, due to which the spalling resistance of the oxide layer is expected to improve. No change is observed in the composition of the (Mo,Cr)Si₂ layer even after oxidation at 1273K for 50h.

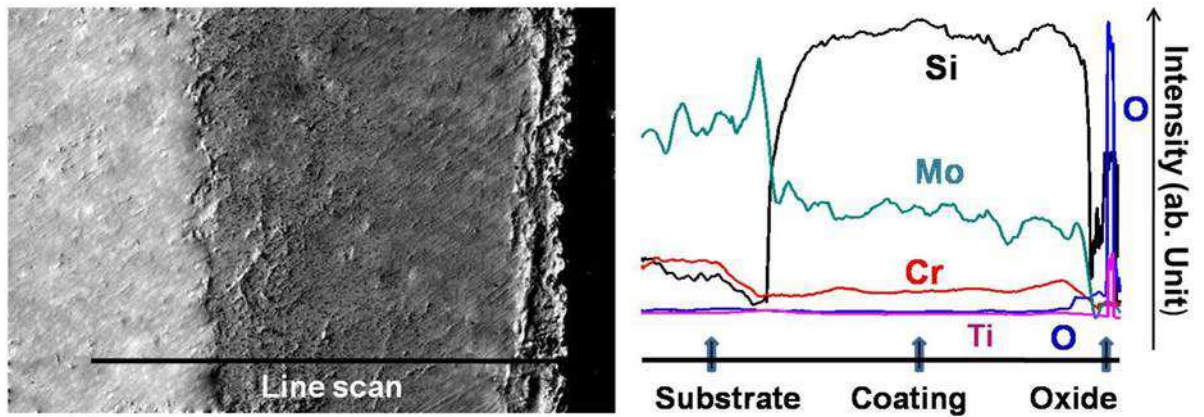


Fig. 5.55: BSE image of cross section of the coated sample after oxidation and the qualitative line profile across the cross section

5.8 Summary

The major findings of the present studies can be summarized as:

1. The present investigation demonstrates the technical feasibility of preparation of Mo based in situ composite alloys by reaction hot pressing and direct silicothermy co-reduction of mixed oxides of molybdenum and chromium.
2. In the co-reduction technique alloys were made in a single step with alloy yield of more than 85% by judiciously utilizing the heat of the reactions and experimental parameters.
3. Differential thermal analysis (DTA) studies conducted to find out the onset temperature for co-reduction reaction. The ignition temperatures for mixture of stoichiometric amount of MoO_2 , Cr_2O_3 and Si have been found to be 673K and 1673K with and without heat booster respectively.
4. Thermal studies have been carried out for the reduction of molybdenum oxide using silicon as reductants. The activation energy for the reduction of MoO_2 by silicon was evaluated to be 309 kJ/mole.
5. XRD analysis of the reduced mass confirmed the formation molybdenum as the metallic and SiO_2 as the slag phase after silicothermic reduction of MoO_2 .
6. The silicothermic reduced Mo-Cr-Si alloys was included by a ductile refractory solid solution phase of Mo and Cr containing 0.9-1.9 wt% Si and an intermetallic matrix of $(\text{Mo,Cr})_3\text{Si}$
7. Sintered density of more than 98% of theoretical density was achieved for the alloy Mo-16Cr-4Si-0.5Ti at hot pressing temperature of 1973 K under 10 MPa pressure for 3 h in vacuum.
8. Hot pressed Mo-16Cr-4Si-0.5Ti alloy consisted of a ductile refractory solid solution phase of Mo, Cr and Ti containing 0.9-1.9 wt% Si and an intermetallic matrix of $(\text{Mo,Cr,Ti})_3\text{Si}$. The volume percentage of the discontinuous $(\text{Mo, Cr, Ti})_{\text{ss}}$ phase was ~ 28%. The room temperature flexure strength and the fracture toughness of the alloy were 615 ± 15 MPa and 10.7 ± 0.5 MPa.m^{1/2} respectively.
9. Due to the crack hindrance and plastic deformation of the $(\text{Mo, Cr, Ti})_{\text{ss}}$ phase, together with crack deflection and interfacial de-bonding the toughness of the alloy is expected to enhance.
10. The Mo-Cr-Si alloy exhibited better superior oxidation resistance as compared to single phase Mo alloy. When oxidized at elevated temperature above 1073K

isothermally, the alloy shows an initial weight loss of the alloy in the form of MoO_3 . After sufficient evaporation of Mo from the surface, the Si and Cr concentration on the surface becomes high enough to form a protective layer against further oxidation.

11. A new method for determining oxidation kinetics is proposed. Oxidation kinetics of Mo and Mo–16Cr–xSi alloys were studied by this technique. The model was found to fit well with the weight change data of both Mo and Mo–16Cr–xSi alloys and hence validated its usefulness for oxidation studies of metal and alloys to evaluate the oxidation kinetics of and gives fairly reliable values of the activation energies using the thermogravimetry data of a single experiment. Effect of Si on the oxidation resistance was evaluated. The activation energy was found to be 167, 191 and 247 kJ/mole for the three alloys having Si 4, 5 and 6 wt.% respectively.
12. Effects of the different concentrations of the alloying elements – Cr, Si and Ti on room temperature fracture toughness and high temperature oxidation resistance were studied. The effect of Si on the fracture toughness and oxidation resistance is directly related to the phase ratios of the constitutive phases. As the Si concentration increases, the volume percentage of silicide $(\text{Mo}, \text{Cr})_3\text{Si}$ phase also increases, resulting in decrease in fracture toughness and vice-versa. Cr improves the oxidation resistance of the alloys by sacrificing room temperature fracture toughness. Marginal improvement in oxidation resistance, but a significant decrease in fracture toughness is observed for the alloy containing more than 16 wt.% Cr. The addition of Ti has not improved the fracture toughness significantly. However a marked improvement was seen with respect to oxidation resistance.
13. Mo-16Cr-4Si-0.5Ti was found to be the optimum alloy composition for achieving highest room temperature fracture toughness among the alloys studied, along with adequate oxidation resistance at 1273K.
14. The fracture toughness of the silicothermic reduced alloy was slightly higher than the hot pressed alloy because of higher density and finer distribution of Mo_{ss} phase in the matrix.
15. $(\text{Mo}, \text{Cr})\text{Si}_2$ based coating was developed, which showed excellent oxidation resistance at 1273K provided by reservoir of Si. The activation energy of the coating process was determined as 52.5kJ/mol.

References

- [1] D.M. Berczik. Method for enhancing the oxidation resistance of a molybdenum alloy and a method of making molybdenum Alloy. US Patent 5,595,616 (1997).
- [2] D.M. Berczik. Oxidation resistant Molybdenum Alloy. US Patent 5,693,156 (1997).
- [3] J.H. Schneibel, R.O. Ritchie, J.J. Kruzic, P.R. Tortorelli. Optimization of Mo–Si–B Intermetallic Alloys. *Metall. Mater. Trans. A* 36 (2005) 525–531.
- [4] M.K. Meyer, M.J. Kramer, M. Akinc. Compressive creep behavior of Mo_5Si_3 with the addition of boron. *Intermetallics* 4 (1996) 273–281.
- [5] H. Choe, J.H. Schneibel, R.O. Ritchie. Fracture and fatigue properties of Mo– Mo_3Si – Mo_5SiB_2 Refractory intermetallic alloys at ambient to elevated temperatures (25°C to 1300°C). *Metall. Mater. Trans. A* 34 (2003) 225–232.
- [6] V. Supatarawanich, D.R. Johnson, C.T. Liu. Effects of microstructure on the oxidation behavior of multiphase Mo–Si–B alloys. *Mater. Sci. Eng. A* 344 (2003) 328–334.
- [7] T.A. Parthasarathy, M.G. Mendiratta, D.M. Dimiduk. Oxidation mechanisms in Mo–reinforced Mo_5SiB_2 (T2)– Mo_3Si alloys. *Acta Mater.* 50 (2002) 1857–1868.
- [8] P. Jehanno, M. Heilmaier, H. Saage, H. Heyse, M. Boning, H. Kestler, J.H. Schneibel. Superplasticity of a multiphase refractory Mo–Si–B alloy. *Scr. Mater.* 55 (2006) 525–528.
- [9] P. Jehanno, M. Heilmaier, H. Saage, M. Boning, H. Kestler, J. Freudenberger, S. Drawin. Assessment of the high temperature deformation behavior of molybdenum silicide alloys. *Mater. Sci. Eng. A* 463 (2007) 216–223.
- [10] D. Sturm, M. Heilmaier, J.H. Schneibel, P. Jehanno, B. Skrotzki, H. Saage. The influence of silicon on the strength and fracture toughness of molybdenum. *Mater. Sci. Eng. A* 463 (2007) 107–114.
- [11] P. Jehanno, M. Heilmaier, H. Kestler. Characterization of an industrially processed Mo–based silicide alloy. *Intermetallics* 12 (2004) 1005–1009.
- [12] K. Yoshimi, S. Nakatani, S. Hanada, H. Ko, Y.H. Park. Synthesis and high temperature oxidation of Mo–Si–B–O pseudo in situ composites. *Sci. Technol. Adv. Mater.* 3 (2002) 181–192.
- [13] N. Nomura, T. Suzuki, K. Yoshimi, S. Hanada. Microstructure and oxidation resistance of plasma sprayed Mo–Si–B multiphase alloy coating. *Intermetallics* 11 (2003) 735–742.
- [14] K. Yoshimi, S. Nakatani, T. Suda, S. Hanada, H. Habazaki. Oxidation behavior of Mo_5SiB_2 –based alloy at elevated temperatures, *Intermetallics* 10 (2002) 407–414.

- [15] J. A. Lemberg, M.R. Middlemas, T. Weingartner, B. Gludovatz, J.K. Cochran, R.O. Ritchie. On the fracture toughness of fine-grained Mo–3Si–1B (wt.%) alloys at ambient to elevated (1300 °C) temperatures. *Intermetallics* 20 (2012) 141–154.
- [16] A.P. Alur, N. Chollacoop, K.S. Kumar. High-temperature compression behavior of Mo–Si–B alloys. *Acta Mater.* 52 (2004) 5571–5587.
- [17] S. Burk, B. Gorr, H.J. Christ. High temperature oxidation of Mo–Si–B alloys: Effect of low and very low oxygen partial pressures. *Acta Mater.* 58 (2010) 6154–6165.
- [18] I.M. Gunter, J.H. Schneibel, J.J. Kruzic. Ductility and fracture toughness of molybdenum with MgAl₂O₄ additions. *Mater. Sci. Eng. A* 458 (2007) 275–280.
- [19] Y. Yang, H. Bei, S. Chen, E.P. George, J. Tiley, Y. A. Chang. Effects of Ti, Zr, and Hf on the phase stability of Mo_{ss} + Mo₃Si + Mo₅SiB₂ alloys at 1600°C. *Acta Mater.* 58 (2010) 541–548.
- [20] J. Das, R. Mitra, S.K. Roy. Oxidation behaviour of Mo–Si–B–(Al, Ce) ultrafine-eutectic dendrite composites in the temperature range of 500–700°C. *Intermetallics* 19 (2011) 1–8.
- [21] S. Burk, B. Gorr, V.B. Trindade, H.J. Christ. Effect of Zr Addition on the high-temperature oxidation behaviour of Mo–Si–B Alloys. *Oxid. Met.* 73 (2009) 163–181.
- [22] S. Ochiai. Improvement of the oxidation-proof property and the scale structure of Mo₃Si intermetallic alloy through the addition of chromium and aluminum elements. *Intermetallics* 14 (2006) 1351–1357.
- [23] P.R. Subramanian, M.G. Mendiratta, D.M. Dimiduk. High temperature melting molybdenum–chromium–silicon alloys. US Patent 5,683,524 (1997).
- [24] R.M. Aikin. The mechanical properties of in-Situ composites. *J Met* 49 (1997) 35–39.
- [25] Z. Chen, Y.W. Yan. Influence of sintering temperature on microstructures of Nb/Nb₅Si₃ in situ composites synthesized by spark plasma sintering. *J Alloys Compd* 413 (2006) 73–76.
- [26] C.L. Yeh, W.H. Chen Preparation of Nb₅Si₃ intermetallic and Nb₅Si₃/Nb composite by self-propagating high-temperature synthesis. *J Alloys Compd* 402 (2005) 118–123.
- [27] M.G. Mendiratta, D.M. Dimiduk. Strength and toughness of a Nb/Nb₅Si₃ composite. *Metall Mater Trans A*, 24 (1993) 501–504.
- [28] H. Saage, K. Kruger, D. Sturm, M. Heilmaier, J.H. Schneibel, E. George, L. Heatherly, C. Somsen, G. Eggeler, Y. Yang. Ductilization of Mo–Si solid solutions manufactured by powder metallurgy. *Acta Mater* 57 (2009) 3895–3901.

- [29] W.Y. Kim, H. Tanaka, A. Kasama, S. Hanada. Effect of Cr Addition on Microstructure and Mechanical Properties in Nb–Si–Mo Base Multiphase Alloys . *Intermetallics* 9 (2001) 827–834.
- [30] S. Ochiai. Improvement of the oxidation–proof property and the scale structure of Mo₃Si intermetallic alloy through the addition of chromium and aluminum elements *Intermetallics*, 14 (2006) 1351–1357.
- [31] W. Dautzenberg, Das metallothermische Verchutzen Ohne Zufuhr elements. elektrischer Energie, in: G. Volkart, K.D. Frank (Eds.): *Metallurgie der Ferrolegierungen*, 2nd edn., Springer, Berlin, 1972, pp. 59–76.
- [32] I.G. Sharma, S.P. Chakraborty, A.K. Suri. Preparation of TZM alloy by aluminothermic smelting and its characterization. *J. Alloy Comp.*, 393 (2005) 122–128.
- [33] S.P. Chakraborty, S. Banerjee, I.G. Sharma, Bhaskar Paul, A.K. Suri. Studies on the synthesis and characterization of a molybdenum–based alloy. *J. Alloy Comp.* 477 (2009) 256–261.
- [34] Z. Li, LM. Peng. Microstructural and mechanical characterization of Nb–based in situ composites from Nb–Si–Ti ternary system. *Acta Mater* 55 (2007) 6573–6585.
- [35] R. Sakidja, F. Rioult, J. Werner, J.H. Perepezko. Aluminum pack cementation of Mo–Si–B alloys. *Scr Mater* 55 (2006) 903–906.
- [36] R. Sakidja, J.S. Park, J. Hamann, J.H. Perepezko. Synthesis of oxidation resistant silicide coatings on Mo–Si–B alloys. *Scr Mater* 53 (2005) 723–728.
- [37] S. Majumdar, I.G. Sharma, S. Raveendra, I. Samajdar, P. Bhargava. In situ chemical vapour co–deposition of Al and Si to form diffusion coatings on TZM. *Mater Sci Eng A* 492 (2008) 211–217.
- [38] S. Majumdar, I.G. Sharma, I.Samajdar, P.J. Bhargava. J. Relationship between pack chemistry and growth of silicide coatings on Mo –TZM alloy. *J Electrochem Soc* 155 (2008) 734–740.
- [39] S. Majumdar, I.G. Sharma. Oxidation behavior of MoSi₂ and Mo(Si, Al)₂ coated Mo–0.5Ti–0.1Zr–0.02C alloy. *Intermetallics* 19 (2011) 541–545.
- [40] J.S. Park, R. Sakidja, J.H. Perepezko. Coating designs for oxidation control of Mo–Si–B alloys. *Scr Mater* 46 (2002) 765–770.
- [41] B.C. Rathore, B. Pratibha. Theoretical optimisation of constitution of alloys by decoding their densities. *Mater lett* 61 (2007) 2956–2960.

- [42] I.H. Hall, Aluminothermic process, in: Ulmans Encyclopedia of Industrial chemistry, Verlag Chemie, Weinheim, 5th edn.,1985, pp. 447–452.
- [43] W. Dautzenberg, Aluminothermic, in: Ulmans Encyklopadie der Technischen Chemie, Verlag Chemie, Weinheim, 4th edn.,1974, pp. 351–361.
- [44] S. Majumdar, G.B. Kale, I.G. Sharma. A study on preparation of Mo–30W alloy by aluminothermic co–reduction of mixed oxides. *J. Alloys and Comp* 394 (2005) 168–175.
- [45] E.A. Brandes (Ed.): *Smithells Metals Reference Book*, 6th edn., 1983.
- [46] B. Sarangi, H.S. Ray, K.K. Tripathy, A. Sarangi. Determination of heats of aluminothermic redox reaction of V_2O_5 and MnO_2 . *J. Thermal Anal.* 44 (1995) 441–51.
- [47] O. Kubaschewski, C.B. Alcock. *Metallurgical thermochemistry*.5th ed. Pergamon press; 1979.
- [48] K.T. Jacob, V.S. Saji, J. Gopalakrishnan, Y. Waseda. Thermodynamic evidence for phase transition in $MoO_{2-\delta}$. *J. Chem. Thermodynamics.* 39 (2007) 1539–45.
- [49] M. Nagamori, J.A. Boivin, A. Claveau. Gibbs free energies of formation of amorphous Si_2O_3 , SiO and Si_2O . *J. Non–Crystall. Solids* 189 (1995) 270–76.
- [50] I. Barin. *Thermodynamic data of pure substances*. 3rd ed.VCH verlagsgesellschaft mbH, Weinheim FRG;1995.
- [51] B. Paul, S.P. Chakraborty, J. Kishor, I.G. Sharma, A.K. Suri. Studies on Synthesis and Characterization of Mo Based In Situ Composite by Silicothermy Co–reduction Process. *Met. Trans. B* 2011; 700 (42) 710–15.
- [52] R.H. Fan, H.L. Lu, K.N. Sun, W.X. Wang, X.B. Yi. Kinetics of thermite reaction in Al– Fe_2O_3 system. *Thermochim. Act.* 440 (2006) 129–131.
- [53] H. Friedman. Kinetics of thermal degradation of char–forming plastics from thermo–gravimetry. *J. Polym. Sci.* 6C (1963) 183–95.
- [54] H.E. Kissinger. The crystallization kinetics with heating rate in differential thermal analysis. *J. Res. Natl. Bur. Stand.* 57 (1956) 217–21.
- [55] T. Ozawa. Estimation of activation energy by iso–conversion methods. *Thermochim. Act.* 203 (1992) 159–65.

- [56] A. Ariffin, Z.M. Ariff, S.S. Jikan. Evaluation on non isothermal crystallization kinetics of polypropylene/kaolin composites by employing Dobreva and Kissinger methods. *J. Therm Anal Calorim.* 103 (2011) 171–177.
- [57] J.P. Elder. The general applicability of the Kissinger equation in thermal analysis. *J. Therm Anal Calorim.* 30 (1985) 657–669.
- [58] P. Budrugeac, E. Segal. Applicability of the Kissinger equation in thermal analysis. *J. Therm Anal Calorim.* 88 (2007) 703–707.
- [59] J. Farjas, N. Butchosa, P. Roura. A simple kinetic method for the determination of the reaction model from non-isothermal experiments. *J. Therm Anal Calorim.* 102 (2010) 615–625.
- [60] S. Majumdar, I.G. Sharma, I. Samajdar, P. Bhargava. Kinetic studies on hydrogen reduction of MoO_3 and morphological analysis of reduced Mo powder. *Met. Trans.* 39B (2008) 431–38.
- [61] M.J. Kennedy, S.C. Bevan. A kinetic study of the reduction of molybdenum trioxide by hydrogen. *J. L. Comm. Metals.* 36 (1974) 23–30.
- [62] T. Hoshino, Y. Nishioka. Inward Diffusion of Oxygen on a Silicon Surface. *Phys. Rev. Lett.* 84 (2000) 4633–4636.
- [63] V. Keryvin, V.H. Hoang, J. Shen. Hardness, toughness, brittleness and cracking systems in an iron-based bulk metallic glass by indentation. *Intermetallics* 17 (2009) 211–217.
- [64] J. T. Czernuszka, T. F. Page. Indentation behaviour of alloyed zirconia Ceramics. *J. Mater. Sc.*, 27 (1992) 1683–1689.
- [65] V.D. Krstic, P.S. Nicholson, R. G Hoagland. Toughening of Glasses by Metallic Particles. *J Am. Ceram. Soc.*, 64 (1981) 499–504.
- [66] M.F. Ashby, F.J. Blunt, M. Bannister. Flow Characteristics of Highly Constrained metal Wires. *Acta Metall.*, 37 (1989) 1847–57.
- [67] K.T. Venkateswara Rao, W.O. Soboyejo, R.O. Ritchie. Ductile-phase toughening and Fatigue–Crack Growth in Nb–Reinforced Molybdenum Disilicide Intermetallic Composites. *Metall Trans A*, 23A (1992) 2249–57.
- [68] C.L. Yeh, W.H. Chen. Preparation of Nb_5Si_3 intermetallic and $\text{Nb}_5\text{Si}_3/\text{Nb}$ composite by self-propagating high-temperature synthesis. *J Alloys Compd* 402 (2005) 118–123.

- [69] E. S. Jones, J. F. Mosher, R. Speiser, J. W. Spretnak. Molybdenum oxidation, Corrosion–Natn Ass Corros. Engr. 14 (1958) 20–26.
- [70] N. Floquet, O. Bertrand, J. J. Heizmann. Structural and morphological studies of the growth of MoO₃ scales during high–temperature oxidation of molybdenum. Oxid. Met. 37 (1992) 253–280.
- [71] E. A. Gulbransen, K. F. Andrew, F. A. Brassart. Oxidation of Molybdenum 550° to 1700°C. J. electrochem. Soc. 110 (1963) 952–959.
- [72] S. Paswan, R. Mitra, and S.K. Roy. Isothermal oxidation behaviour of Mo–Si–B and Mo–Si–B–Al alloys in the temperature range of 400–800 °C, Mater. Sci. Engg. A 424 (2006) 251–265.
- [73] T.A. Parthasarathy, M.G. Mendiratta, D.M. Dimiduk. Oxidation mechanisms in Mo–reinforced Mo₅SiB₂ (T2)–Mo₃Si alloys. Acta. Mater. 50 (2002) 1857–1868.
- [74] A K. Vijh. Relationship between activation energies for the thermal oxidation of metals and the semiconductivity of the oxides. J. Mater. Sc. 9 (1974) 985–989.
- [75] E. K. R. deal, O. H. Wansbrough. An investigation of the combustion of platinum. Proc. Roy. Soc. (London) A123 (1929) 202–208.
- [76] A. F. H. Ward, N. R. Bharucha. The relationship between the work function of a metal and its energy of activation for oxidation. Rec. Tray. Chim. Pays–Bas 72 (1953) 735–741.
- [77] D. Monceau, D. Poquillon. Continuous Thermogravimetry Under Cyclic Conditions. Oxid. Met. 61 (2004) 143–163.
- [78] J. Wang, R. Raj. Activation Energy for the Sintering of Two–Phase Alumina/Zirconia Ceramics. J. Am. Ceram. Soc., 74 (1991) 1959–1963.
- [79] K. Matsui, J. Hojo. Sintering kinetics at constant rates of heating: effect of GeO₂ addition on the initial sintering stage of 3 mol% Y₂O₃–doped zirconia powder. J Mater. Sci. 43 (2008) 852–859.
- [80] R. Yan, F. Chu, Q. Ma, X. Liu, G. Meng. Sintering kinetics of samarium doped ceria with addition of cobalt oxide. Mater. Lett. 60 (2006) 3605–3609.
- [81] G. Y. Meng, O. Toft. Sorensen, in: Y. Han (Ed.), Advanced Structural Materials, vol. 2 Elsevier Science Publishers B.V., Amsterdam, Netherlands, (1991) 369–374.
- [82] H. T. Wang, X. Q. Liu, F. L. Chen, G. Y. Meng. Kinetics and mechanism of a sintering process for macroporous alumina ceramics by extrusion. J. Am. Ceram. Soc. 81 (1998) 781–784.

- [83] Y. F. Liu, X. Q. Liu, S. W. Tao, G. Y. Meng, O. Toft. Kinetics of the reactive sintering of kaolinite–aluminium hydroxide extrudate. Sorensen, *Ceram. int.* 28 (2002) 479–486.
- [84] A. Thomaz, R. Guisard, S. Ae, H. Regina, M.–Castanho. Sintering studies on Ni–Cu–YSZ SOFC anode cermet processed by mechanical alloying. *Journal of Thermal Analysis and Calorimetry*, 97 (2009) 775–780.
- [85] B. Paul, D. Jain, A.C. Bidaye, I.G. Sharma, C.G.S. Pillai. Sintering kinetics of submicron sized cobalt powder. *Thermochim. Acta*, 488 (2009) 54–59.
- [86] B. Paul, D. Jain, S. P. Chakraborty, I. G. Sharma, C. G. S. Pillai, A. K. Suri. Sintering kinetics study of mechanically alloyed nanocrystalline Mo–30 wt.% W. *Thermochim. Acta*. 512 (2011) 134–141.
- [87] D. Yi, Z. Lai, C. Li, O.M. Akselsen, J.H. Ulvensoen. Ternary alloying study of MoSi₂. *Metall. Mater. Trans. A* 29 (1998) 119–129.
- [88] N. V. Ageev, D. Sostoianiiia, M. Sistem, editor. Moscow: Viniti Press; 1964;10:182–183.
- [89] HJ. Okamoto Cr–Si (Chromium–Silicon). *J. Phase Equilibria* 2001;22:593–593.
- [90] A. Mueller, G. Wang, R. A. Rapp, E.L. Courtright. Development and cyclic oxidation behaviour of a protective (Mo,W)(Si,Ge)₂ coating on Nb–base alloys. *J Electrochem Soc* 139 (1992) 1266–1275.
- [91] P.C. Tortorici, M.A. Dayananda. Growth of silicides and interdiffusion in the Mo–Si system. *Metall. Mater. Trans A*, 30 (1999) 545–550.
- [92] P.C. Tortorici, M.A. Dayananda Diffusion structures in Mo vs. Si solid–solid diffusion couples. *Scr. Mater* 38 (1998) 1863–1869.

Concluding Remark

Sintering kinetics of sub micron sized Mo–30 wt.% W alloy powder prepared through mechanical alloying was studied by both, constant rate of heating (CRH) and stepwise isothermal dilatometry (SID) technique. The observed experimental results demonstrated that the activation energy values calculated by SID method and CRH method are in good agreement. SID shrinkage data were analyzed by conventional and Mekipritti–Meng method to evaluate the sintering mechanism and activation energies. The Mekipritti–Meng model was found to fit well with the shrinkage data of Mo–30 wt% W alloy powder and hence validated its usefulness for sintering studies of alloys. Sintering in this alloy occurs through two dominant mechanisms with average activation energies of 230 and 480 kJ/ mole corresponding to grain boundary diffusion and lattice diffusion, respectively. The results are found to be consistent with the microstructural evaluation as studied by SEM analysis. Furthermore, the diffusivities calculated in this study agree well with previous reported values by high temperature tracer determinations.

To protect the Mo–30W alloy under oxidizing atmosphere, silicide based oxidation resistant coating were formed. Effects of activator content and temperature on coating were studied. Double layer coating consisting of $(\text{Mo,W})_5\text{Si}_3$ and $(\text{Mo,W})\text{Si}_2$ was formed at coating temperature of 1573K, whereas single layer coating consisting of $(\text{Mo,W})\text{Si}_2$ was formed at coating temperature below 1573K. The hardness values of the $(\text{Mo,W})\text{Si}_2$ phase ranged between 1250 ± 30 Hv for both the samples coated at 900 °C and 1300 °C, while the hardness value for $(\text{Mo,W})_5\text{Si}_3$ phase ranged between 726 ± 20 Hv. The wear rate of un-coated Mo–W alloy is significantly higher at all sliding speed as compared to $(\text{Mo,W})\text{Si}_2$ coated samples. Although wear rate of both coated samples is almost equal at all test conditions, double layer coating formed at 1300 °C showed improved crack resistance. Double layered coated alloy showed excellent oxidation resistant under cyclic oxidation test at 1273K for 50h.

The present investigation demonstrates the technical feasibility of preparation of Mo based in situ composite alloys by reaction hot pressing and direct silicothermy co-reduction of mixed oxides of molybdenum and chromium. In the co-reduction technique alloys were made in a single step with alloy yield of more than 85% by judiciously utilizing the heat of the reactions and experimental parameters.

Differential thermal analysis (DTA) studies conducted to find out the onset temperature for co-reduction reaction. The ignition temperatures for mixture of stoichiometric amount of

MoO₂, Cr₂O₃ and Si have been found to be 673K and 1673K with and without heat booster respectively. The thermodynamic and kinetics aspects of exothermic reactions were studied by TG-DTA. Thermal studies have been carried out for the reduction of molybdenum oxide using silicon as reductants. The activation energy for the reduction of MoO₂ by silicon was evaluated to be 309 kJ/mole. XRD analysis of the reduced mass confirmed the formation molybdenum as the metallic and SiO₂ as the slag phase after silicothermic reduction of MoO₂. The silicothermic reduced Mo–Cr–Si alloys was included by a ductile refractory solid solution phase of Mo and Cr containing 0.9-1.9 wt% Si and an intermetallic matrix of (Mo,Cr)₃Si

Sintered density of more than 98% of theoretical density was achieved for different alloys at hot pressing temperature of 1973 K under 10 MPa pressure for 1–3 h in vacuum. Effects of the different concentrations of the alloying elements – Cr, Si and Ti on room temperature fracture toughness and high temperature oxidation resistance were studied. The Mo–16Cr–4Si–0.5Ti was found to be the optimum alloy composition for achieving highest room temperature fracture toughness along with adequate oxidation resistance at 1000°C.

Hot pressed Mo–16Cr–4Si–0.5Ti alloy consisted of a ductile refractory solid solution phase of Mo, Cr and Ti containing 0.9–1.9 wt% Si and an intermetallic matrix of (Mo,Cr,Ti)₃Si. The volume percentage of the discontinuous (Mo, Cr, Ti)_{ss} phase was ~28%.

The Mo–Cr–Si alloy exhibited better thermal stability as compared to single phase Mo alloy. When oxidized at elevated temperature above 1073K isothermally, the alloy shows an initial weight loss of the alloy in the form of MoO₃. After sufficient evaporation of Mo from the surface, the Si and Cr concentration on the surface becomes high enough to form a protective layer against further oxidation.

An alternate method for determining oxidation kinetics is proposed. Oxidation kinetics of Mo and Mo-16Cr-xSi alloys were studied by this technique, where stepwise isothermal thermo-gravimetry (SITG) data were analyzed to get kinetics parameters according to the empirical rate equation.

$$\frac{dY}{dt} = nk(T)Y(1-Y)\left(\frac{1-Y}{Y}\right)^{1/n}$$

The model was found to fit well with the weight change data of both Mo and Mo-16Cr-xSi alloys and hence validated its usefulness for oxidation studies of metal and alloys to evaluate the oxidation kinetics of and gives fairly reliable values of the activation energies using the

thermogravimetry data of a single experiment. Effect of Si on the oxidation resistance was evaluated. The activation energy was found to be 167, 191 and 247 kJ/mole for the three alloys having Si 4, 5 and 6 wt.% respectively.

The room temperature flexure strength and the fracture toughness of the Mo-16Cr-4Si-0.5Ti alloy were 615 ± 15 MPa and 10.7 ± 0.5 MPa.m^{1/2} respectively. Due to the crack hindrance and plastic deformation of the Mo-phase, together with crack deflection and interfacial de-bonding the toughness of the alloy is expected to enhance. The fracture toughness of the silicothermic reduced alloy was slightly higher than the hot pressed alloy because of higher density and finer distribution of Mo_{ss} phase in the matrix.

Effects of the different concentrations of the alloying elements - Cr, Si and Ti on room temperature fracture toughness and high temperature oxidation resistance were studied. The Mo-16Cr-4Si-0.5Ti was found to be the optimum alloy composition for achieving highest room temperature fracture toughness along with adequate oxidation resistance at 1000°C.

Hot pressed Mo-16Cr-4Si-0.5Ti alloy consisted of a ductile refractory solid solution phase of Mo, Cr and Ti containing 0.9-1.9 wt% Si and an intermetallic matrix of (Mo,Cr,Ti)₃Si. The volume percentage of the discontinuous (Mo, Cr, Ti)_{ss} phase was ~28%. The alloy exhibited superior oxidation behavior in comparison with single phase molybdenum alloys. The room temperature flexure strength and the fracture toughness of the alloy were 615 ± 15 MPa and 10.7 ± 0.5 MPa.m^{1/2} respectively. Due to the crack hindrance and plastic deformation of the (Mo, Cr, Ti)_{ss} phase, together with crack deflection and interfacial de-bonding the toughness of the alloy is expected to enhance.

The fracture toughness of the silicothermic reduced alloy was slightly higher than the hot pressed alloy because of higher density and finer distribution of Mo_{ss} phase in the matrix.

(Mo, Cr)Si₂ based coating was developed, which showed excellent oxidation resistance at 1273K provided by reservoir of Si. The activation energy of the coating process was determined as 52.5kJ/mol.

Scope for further research

The present study opens up directions for further research in the field of development of high temperature material and coating of structural materials. Some of these are listed below:

1. In this work, only hot pressing and pressureless sintering was used for densification. Advanced processing technique, i.e. Spark Plasma Sintering (SPS) and hot isostatic pressing (HIP) can be attempted in future for the densification of these alloys.
2. Creep and fatigue behavior of the developed Mo-Cr-Si based alloys need to be studied.
3. In this work, room temperature fracture toughness test was carried out for the Mo-Cr-Si based alloys. Fracture toughness tests at elevated temperature could be performed.
4. The oxidation tests in this study have been carried out either in flowing oxygen or air. Oxidation behavior of the alloys under more aggressive environment such as in the presence of moisture, toxic gases etc. need to be explored.
5. Recent studies showed that the addition of the rare-earth elements lanthanum (La) and yttrium (Y) improves the oxidation resistance of the material significantly in a wide temperature range. The effect of the addition of the rare-earth elements is another area of research.
6. In the present study, silicide coating has been explored over Mo-30W and Mo-16Cr-4Si-0.5Ti alloys. Molybdenum alumino-silicide $\text{Mo}(\text{Si}, \text{Al})_2$ is reported to exhibit good oxidation resistance at high temperatures and no pest disintegration at the intermediate temperatures. The development of composite coating consisting of alumino-silicide over the Mo-30W and Mo-16Cr-4Si-0.5Ti alloys could be studied.

List of Publication

1. Microstructure and mechanical properties of hot pressed Mo–Cr–Si–Ti in-situ composite and oxidation behavior with silicide coatings; **Bhaskar Paul**, S. Majumdar and A.K. Suri ; **International journal of refractory metal and hard materials**, **38** (2013) 26–34.
2. Thermal analysis on conversion of MoO₃ to MoO₂ and its silicothermic reduction; **Bhaskar Paul**, Jugal Kishor, S.P. Chakraborty and A.K.Suri; **Journal of Thermal Analysis and Calorimetry**, **112** (2013) 31–36.
3. Formation of Silicide Based Oxidation Resistant Coating Over Mo–30 wt% W Alloy; **Bhaskar Paul**, S.P. Chakraborty, A.K. Suri; **Transactions of the Indian Ceramic Society** **72** (2013) 39–42.
4. A novel approach to determine oxidation kinetics of Mo–16Cr–xSi (x=4–6 wt.%) Si alloy using stepwise isothermal thermo–gravimetry; **Bhaskar Paul**, S. Kole, A.K. Suri; **Thermochimica Acta** **549** (2012) 57– 62.
5. Sintering kinetics study of mechanically alloyed nanocrystalline Mo–30 wt% W; **Bhaskar Paul**, Dheeraj Jain, S.P.Chakraborty, I. G. Sharma, C. G. S. Pillai and A.K.Suri, **Thermochimica Acta** **512** (2011) 134–141.
6. Studies on Synthesis and Characterization of Mo Based In Situ Composite by Silicothermy Co–reduction Process; **Bhaskar Paul**, S.P. Chakraborty, Jugal Kishor, I.G. Sharma and A.K. Suri published in **Metallurgical and Materials Transactions B**, **42** (2011) 700–710.
7. Studies on the synthesis of a Mo–30 wt% W alloy by non–conventional approaches; S.P. Chakraborty, S. Banerjee, G. Sanyal, V.S. Bhave, **Bhaskar Paul**, I.G. Sharma, A.K. Suri; **Journal of Alloys and Compounds**, **501** (2010) 211–217.

8. Microstructure and wear properties of silicide based coatings over Mo–30W alloy
Bhaskar Paul, P.K. Limaye, R.C. Hubli, A.K. Suri, **International Journal of Refractory Metals and Hard Materials**, **44** (2014) 77–83.
9. Mechanical and oxidation properties of hot pressed Mo–Cr–Si and Mo–Cr–Si–Ti in-situ composites, **Bhaskar Paul**, R.C. Hubli and A.K. Suri, Communicated for publication in **Metallurgical and Materials Transactions B**.

List of Publication in Conferences

1. **Best poster award** for the article titled “Formation of Silicide Based Oxidation Resistant Coating Over Mo–30 wt.% W Alloy” Authored: **Bhaskar Paul**, S. P. Chakraborty, A. Awasthi , in National conference “Materials and processing, **MAP–2012**, organized by MRSI(Material research society of India)
2. Microstructure evolution of Mo–16Cr–4Si alloy, Bhaskar Paul, S.P.Chakraborty, R.C.Hubli and A.K.Suri, Presented in EMSI–2011
3. Studies on preparation of Mo–30W alloy by co–precipitation followed by co–reduction
Bhaskar Paul, A. Awasthi, A. Prajapat, R.C. Hubli; Presented in **Thermans–2013**
4. Oxidation behavior of hot pressed Mo–Cr–Si in–situ composites
Bhaskar Paul, Jugal Kishor, R.C. Hubli; Presented in **Thermans–2013**

Replies to the queries of examiners

Comment: As a candidate material, Bhaskar has clearly pointed out the biggest competitor of Mo is Nb. Would appreciate a summary table comparing relative merits/demerits of the two alloy system

Reply: A table for comparing the Nb and Mo based alloys has been added

Properties	Nb Base Alloy	Mo Base Alloy
Density	++	+
DBTT	++	+
Ductility	+++	+
Weldability	++	+
High Temperature Strength	+	++
Liquid Metal Corrosion	+	+++
Oxidation Resistance – With Coating	+	+++
Without Coating	++	+
Thermal Conductivity	+	++
O ₂ Solubility	+	++

Comment: Figure 2.4 needs to be changed with a better figure. The same applies to figure 3.3, 3.9. If the original figure is not good enough, please replace it with appropriate schematic.

Reply: I have replaced the figures (2.4, 3.3, 3.9) by either schematic or better figures.

Comment: How did you obtain figure 4.1? Is it your own data? Then more details are needed. If it is from literature; then details must be given.

Reply: Figure 4.1 is taken from literature. The reference is now added (Ref: <http://www.plansee.com/>).

Comment: The initial shrinkage (Fig 4.1) is extremely interesting. Please comment further on the two possibilities mentioned.

Reply: Model equations proposed by Young and Cutler for determining the activation energy of initial stage of sintering were used for non isothermal shrinkage data. The shrinkage data was limited to 1473 K (i.e. up to ~ 5% of shrinkage). The plots of $\ln(yT \cdot dy/dT)$ versus $1/T$ and $\ln(y^2T \cdot dy/dT)$ versus $1/T$, that are shown in Fig. 6 together, allow the calculation of activation energy and the frequency factor for volume diffusion and grain boundary diffusion, respectively. The similarity in the two Arrhenius plots suggests that the mechanism for sintering here could be either volume diffusion or grain boundary diffusion or simultaneous occurrence of both. Actually, the diffusion rate is determined by temperature, powder characteristics and the specific structure of material. Further, the diffusion rate determines the paths of diffusion, through the volume or the boundaries of crystals, dislocations, or the surfaces. Volume diffusion in crystals is the most difficult material transport mechanism with the highest activation energy barrier associated with it. The path then becomes easier for diffusion through dislocations, boundaries and surfaces. However, in the present system, the calculated activation energy for volume diffusion (190 kJ/mole) seems to be erroneous (towards a lower side) since the reported activation energy value for pure Mo is much higher (~400 KJ/mole). Also the activation energy for the self diffusion of Mo and W are in the range of 350 KJ/mole. Thus the model for the initial stage of sintering employed here does give an idea about the dominant mechanism during the initial stage of sintering, which is grain boundary diffusion with activation energy of ~230 kJ/ mol.

Comment: Many of SEM images (example 4.13) are substandard: cannot you do something to improve them?

Reply: Figure 4.13 along with other substandard figures have been replaced with better SEM images.

Comment: Putting the EDS spectrum in several places does not really serve any purpose.

Reply: I have deleted many EDS spectrum from the thesis where there were other evidences present for chemical analysis.

Comment: I believe from the 3D wear profiles, more meaningful data could be obtained. Did you try?

Reply: I agree with the comment. I have tried to find out more information from the 3D wear profile. I have found out wear depth, scar shape, wear volume etc. from the 3D profile. These are incorporated in the thesis.

Comment: Typos need to be corrected. For example fig 5.8 pits “haet” instead of “heat”.

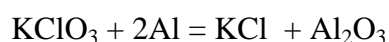
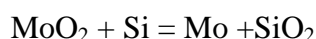
Reply: I have done proofreading to eliminate the typos and other mistakes and corrections were made wherever required.

Comment: The picture of Mo and SiO₂ (slag phase) is bit simplistic-what about other reaction products? Please expand further on poor and excellent slag-metal separation further.

Reply: The co-reduced product consists of two parts - one is metallic and other is non metallic (slag). The reduced metallic mass being heavier settled down or partitioned, because of density difference (in the molten state). All the other reaction products go in to the slag phase.

In the reaction campaign the reactant were: MoO₂, Si, KClO₃, Al, CaO

The probable reactions are:



Comment: A discussion, from existing knowledge, on the improvements in oxidation resistance and fracture toughness (with alloying additions) will be appreciated.

Reply: A discussion part is added on the improvements in oxidation resistance and fracture toughness with alloying additions and same has been summarized in the tabular form as:

Exp. No. (alloy)	Mo	Cr	Si	Hot pressing time At 1600°C, 10Mpa	Theoretical density (g/cc)	Sintered density	K _Q (MPa.m ^{1/2})	Δmg/mm ² /sec (x 10 ⁻⁴)
1	80	16	4	300 min	8.49	8.24	10.5	-1.620
2	79	16	5	240 min	8.24	8.03	9.8	-1.220
3	78	16	6	180 min	7.98	7.82	7.4	-1.160
4	76	20	4	270 min	8.35	8.14	8.4	-1.310
5	75	20	5	240 min	8.09	7.92	7.5	-1.398
6	74	20	6	180 min	7.93	7.81	5.5	-0.977
7	72	24	4	270 min	8.19	7.99	8.45	-1.392
8	71	24	5	240 min	8.04	7.87	5.2	-1.022
9	70	24	6	180 min	7.81	7.69	5.0	-0.950